Imperial College London

100 years of living science

MICRO-CT IMAGING AND PORE NETWORK EXTRACTION

A DISSERTATION
SUBMITTED TO THE DEPARTMENT OF
EARTH SCIENCE AND ENGINEERING OF
IMPERIAL COLLEGE LODON
IN PARTIAL FULFILMENT OF THE
REQUIREMENTS
FOR THE DEGREE OF
DOCTOR OF PHILOSOPHY

Hu Dong

2007

Abstract

Pore network models that simulate two and three-phase flow can predict multi-phase flow properties, such as relative permeability, once the pore geometry and wettability are known. Micro-CT scanning, as a non-destructive technique, provides a three-dimensional image of the pore space at a resolution of several microns. However, these images cannot be directly input into network models.

We develop a maximal ball algorithm to extract topologically equivalent networks of pores and throats from images of porous media that can used as input to network models. The algorithm is discussed in detail and is validated on images where networks have been extracted using other methods. Full networks with parameterized shapes for pores and throats have been generated on micro-CT images scanned during this PhD project and used as input to a pore-scale model (Valvatne and Blunt, 2004) to simulate single and two-phase flows. Good agreement is obtained on both the network structures and predicted single- and two- phase transport properties against benchmark data.

Acknowledgements

I would like to sincerely express my deepest gratitude to my supervisor Professor Martin J. Blunt for his constant support, guidance, patience and encouragement during the study. Without his assistance, the work would never have been done.

I thank Imperial College Consortium on Pore-scale Modelling for their financial support and samples provided for this study. Numerical Rocks AS, particularly Dr. Pål-Eric Øren and Stig Bakke are thanked for sharing and calculating data, and helpful discussions and suggestions throughout this project. I also thank them for offering me the opportunity to continue the pore-scale work in their team. Shell International E&P and Saudi Aramco, particularly Dr. Bob Smits, Dr. Xudong Jing, Dr. Nabeel Al-Afaleg and Dr. Mustafa Touati are thanked for recruiting me for summer internship, making me acquainted with industrial excitement and many useful advices provided during the course.

I would like to thank every member in the Department of Earth Science and Engineering at Imperial College London for their constant support and excellent academic environment provided. The gratitude extends to the XMT lab at the Department of Materials at Imperial College and SYRMEP lab at Elettra Synchrotron for their outstanding technical aids, particularly to Stefano Favretto, Prof. Gianni Schena, Dr. Mariela G. Araujo Fresky and Dr. Carlos A. Grattoni for their constant help in experimental work during the course. Dr. Feng Huang at the University of Science and Technology of China is specially thanked for his invaluable help to improve the program efficiency.

Further I would like to thank my fellow colleagues for providing friendly and intellectual environment, particular to Nabil Al-Bulushi, Dr. Mike Ale, Dr. Anwar Al-

Kharusi, Saif S.J. Alsayari, Dr. Branko Bijeljic, Dr. Ginevra Di Donato, Prof. Zhenliang Guan, Nasiru Idowu, Dr. Stefan Iglauer, Dr. Xavier Lopez, Dr. Huiyun Lu, Dr. Hiroshi Okabe, Dr. Mohammad Piri, Ran Qi, Saleh Mansoori, Dr. Matthew Rhodes, Dr. V. Sander Suicmez, Taha Sochi, Olumide Talabi, Dr. Per Valvatne, Congjiao Xie, etc.

My gratitude is also expressed to Prof. Peter D. Lee from Imperial College London and Dr. Kejian Wu from Heriot-Watt University, for serving on my examination committee.

I also thank you who are interested in my work and reading my thesis.

Finally I would like to thank my parents, wife and new born child. Thanks for your unconditional love and immense support!

Contents

List of figures

List of tables

1 Introduction

Accurate determination of petrophysical parameters and flow properties in porous media are of importance not only in petroleum engineering, but also in hydrology and environmental engineering (Blunt, 2001). It is possible to conduct experiments to obtain such macroscopic properties, for example, the capillary pressure and relative permeability, that are required to model fluid transport occurring in hydrocarbon production especially in enhanced oil recovery, transport of non-aqueous phase liquids (NAPL) in contaminant clean-up processes or designing underground nuclear waste repositories. However, these experiments are often difficult to perform for the full range of displacement processes. For instance, experiments on three-phase flow are of extreme difficulty and the results are not reliable in the low saturation region (Oak, 1990). Besides, there is an infinite number of possible fluid arrangements in terms of saturations and sequences of displacement to constitute a comprehensive set of experimental measurements. The almost universal practice in the oil industry is to measure relative permeability for only two-phase flow at one initial condition and use empirical models, of limited accuracy, to predict the behavior for other cases (Blunt, 2001).

Pore-scale modeling, where fluid displacement is simulated in a model of the porous medium, has been used as a platform to study multi-phase flow at the pore scale. Several authors have reviewed recent advances in pore-scale modeling (Celia et al., 1995; Blunt, 2001; 2002). The pore space in a rock is represented by a network of pores (corresponding to the larger void spaces) and throats (the narrow openings connecting the pores) with parameterized geometries, through which multi-phase flow can be simulated by solving for flow and multi-phase displacement semi-analytically.

The first use of a simple network was described by Fatt in 1956 (a, b, c). He randomly assigned radii on two-dimensional (2D) regular lattice and predicted

capillary pressure and relative permeability of drainage. For the calculation, he used a physical network of electrical resistors due to computational limitations at that time, where electrical current was used as an analogue of fluid flow. He found that the simulation results on a network lattice gave closer agreement to experimental measurements than assuming the porous media was a bundle of parallel tubes.

The next major advance in pore-scale modeling did not occur because of the bottleneck of computing power until in the1970s, Chatzis and Dullien (1977) revisited the assumptions made by Fatt and showed that 2D pore network models poorly represent real porous media compared to three-dimensional (3D) models because they are unable to reproduce the spatial interconnectivity of pore systems.

From then on, extensive studies on the structural properties of the pore space have been carried out to develop predictive models of multi-phase flow. The importance of topology of the structure, size distribution of pore bodies and throats and their spatial correlations has been noted by many authors (Chatzis and Dullien, 1977; Jerauld and Salter, 1990; Lowry and Miller, 1995; Dixit et al., 1997). However, those pore networks were mostly based on regular lattices and were consequently unable to reflect the real topology and geometry of natural materials.

Research on networks extracted from a real porous material was pioneered by Bryant et al. (1992; 1993a; 1993b). Bryant et al. assumed that the porous medium could be represented by a random close packing of uniform spheres, including consideration of compaction and cementation effects. The sphere packing was then tessellated into tetrahedral cells where pores are found in the cells and throats are assigned on the boundaries of the cells. The hydraulic conductivities of the network were spatially correlated in their study and good predictions were made of the trend in permeability with porosity for Fontainebleau sandstone (Bourbie and Zinszner, 1985). Bryant and Blunt (1992) used this model to predict relative permeability for a sand pack and a sandstone with good agreement with experiment.

This approach was later extended by Øren and Bakke (1998; 2002; 2003) who considered packings of spheres of different sizes. They simulated the processes by which the rock was formed, including sedimentation, compaction and diagenesis to construct synthetic sedimentary rocks. Pore networks were extracted from these images using a similar Voronoi tessellation approach to Bryant (1992; 1993a; 1993b) on the pore space, since the centers of the grains were known.

These models derived from process-based images that reproduce the topology of geological materials have been able to make many successful predictions of single and multi-phase flow and transport properties including two and three-phase relative permeability and capillary pressure (Øren et al., 1998; Patzek, 2001; Øren and Bakke, 2002; 2003; Valvatne and Blunt, 2004; Piri and Blunt, 2005a; 2005b).

Based on these pore networks extracted from a process-based model, Valvatne and Blunt (2004) developed a methodology to modify the network to represent a system of interest using easily obtained properties such as pore throat size distribution inferred from capillary pressure curves. Then successful predictions of multi-phase properties were made for a range of porous media.

Although these process-based models are able to generate representative pore structures where the sedimentary processes can be simulated, to widen the range of samples for which predictions of multiphase properties may be made, it is necessary to develop a network extraction technique that can be generally applied to any 3D image of interest. This is particularly important for carbonates that typically have a very complex sedimentary and diagenetic history that is not easy to be reproduced using a process-based model.

First a 3D image of the rock has to be obtained. There are several ways to do this. The first is through direct imaging, such as serial sectioning (Lymberopoulos

and Payatakes, 1992; Vogel and Roth, 2001; Tomutsa and Silin, 2004), confocal laser scanning microscopy (Fredrich et al., 1995) and micro X-ray computerized tomography (micro-CT) (Dunsmuir et al., 1991; Coenen et al., 2004). Among these techniques, micro-CT allows samples a few mm across to be imaged non-destructively in 3D at a resolution of a few microns using a laboratory micro-CT scanner and down to sub-micron resolutions using a synchrotron micro-CT (Coenen et al., 2004). Micro-CT imaging provides a practical way with reasonable time and cost to obtain information on the structure of porous media including cores and even rock cuttings when cores plugs are not available.

In the oil industry, 2D thin section high-resolution images using electron microscopy are routinely obtained from core samples. Statistical methods are then used to create 3D images that attempt to capture the structural properties inferred from the 2D image. To reproduce the connectivity and typical shapes of the pore structure, multiple-point methods have recently been proposed (see, for instance, Okabe and Blunt, 2004). A related but different method was proposed by Wu et al. (2004) who developed an efficient reconstruction algorithm using a Markov chain Monte-Carlo method to generate a wide range of pore structures by scanning and predicting neighborhood patterns in a 5-point stencil.

The third method is the geological process-based method mentioned previously (Bakke and Øren, 1997; Øren et al., 1998). The grain size distribution is obtained from 2D thin sections and the packing of these grains with subsequent compaction and diagenesis is simulated. This method successfully reproduces the geological realities of natural rocks in terms of statistical morphology and topology and predicts absolute permeability and formation factors (Øren and Bakke, 2002; 2003). More importantly, as discussed above, pore networks derived from this method has been used to successfully predict transport properties for multi-phase flow.

All the imaging methods described above can produce images representing the

rocks of interest. While it is possible to simulate single-phase flow directly in 3D pore-scale images (Chen and Doolen, 1998; Manwart et al., 2002), to date most success in predicting capillary-controlled multi-phase flow has been achieved using network models. Once the images are available, pore networks can be derived from 3D images directly. In Chapter 2, I will review the literature on different imaging methods and pore network generation algorithms.

Chapter 3 will describe the principles and apparatus of micro-CT imaging. Imaging processing to generate a usable format for network extraction work is also introduced and the micro-CT images acquired during the course will be shown in this chapter.

The details of the maximal ball algorithm that we developed to extract an effective pore network will be presented in Chapter 4. The subroutines for building maximal balls, removing redundant balls, clustering balls into family trees, segmenting the pores space and calculating relevant parameters will be presented in this chapter.

Chapter 5 will give a brief description of all the samples studied in this project including images of five sphere packings, reconstructed Fontainebleau sandstone and Berea sandstone as benchmark images as well as another 12 images of various porous rocks to compare the absolute permeability and formation factors computed from the pore-scale models and the voxelized images directly.

The validations of the method and results will be discussed in Chapter 6. The topological and geometrical properties are compared against the benchmark data. The transport properties are predicted and analyzed by comparing to calculations directly on images, benchmark networks and experimental data.

In Chapter 7 the extracted networks will be used to predict relative

permeability, formation factor, capillary pressure and relative permeability and compared to experimental data, and results from other networks, where available.

Conclusions and suggestions for further work will be presented in Chapter 8.

2 Literature review

2.1 Pore space imaging

As mentioned in the Introduction, there are two types of method to generate a 3D image of the pore space. The first is direct imaging, which produces 3D images mapping the real interior structure of its original sample, such as the destructive approach of cutting and stacking serial 2D sections, confocal laser scanning microscopy and non-destructive X-ray micro-tomograhpy (micro-CT); the second category includes various reconstruction methods to construct synthetic 3D rock images from high resolution 2D thin sections using statistical methods or geological process simulation.

2.1.1 Serial sectioning

As an established technique, serial sectioning provides a direct way to visualize 3D microstructures when successive layers of materials are removed and exposed surfaces are imaged at high resolution. The 3D image of pore space can be obtained by stacking serial sections (Lymberopoulos and Payatakes, 1992; Vogel and Roth, 2001). However, the method is extensively time consuming due to the laborious polishing and slicing driven by the destructive processes. Only 5-20 slices per hour can be obtained using fully automated approach reported by (Spowart, 2003), which is not ideal for imaging representative rock volume with heterogeneity. Besides, crevices parallel to the slices are difficult to image. The work flow of conventional serial sectioning is illustrated in Fig. 2.1.

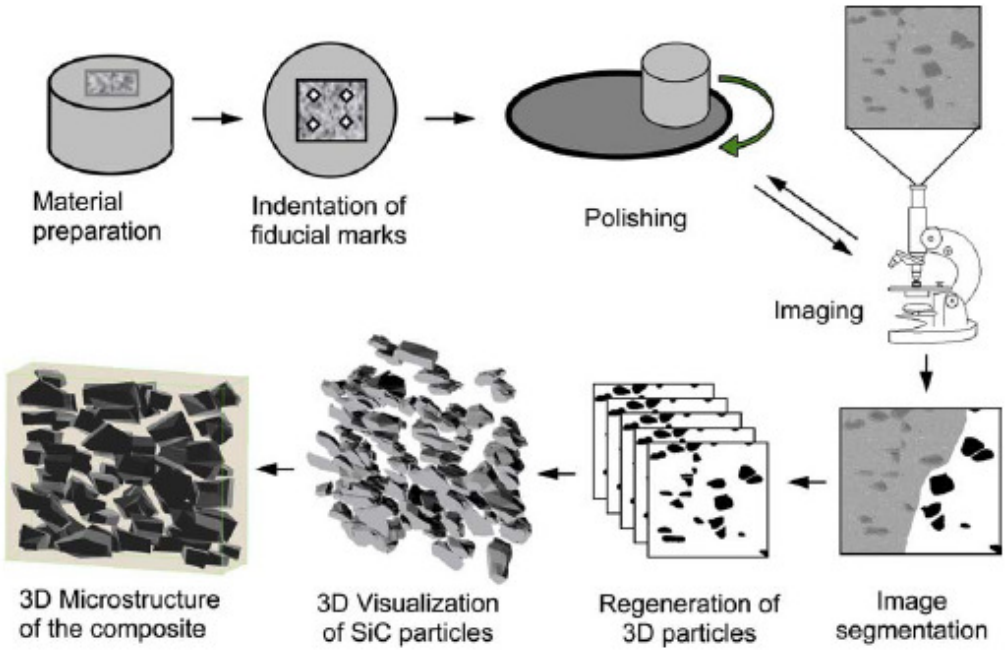

Figure 2.1. Flow chart of serial sectioning to obtain 3D images of porous media. (Chawla et al., 2006)

Recently, an innovative 3D imaging method which combines serial sectioning and focused ion beam (FIB) technology(Tomutsa and Radmilovic, 2003; Tomutsa and Silin, 2004; Tomutsa et al., 2007) has emerged to image microstructures of geological materials, Figs. 2.2 and 2.3. A FIB uses a focused beam of gallium ions (Ga+) accelerated to an energy of 5-50 keV and then focused onto the sample by electrostatic lenses. A modern FIB can deliver tens of nanoamps of current to a sample, or can image the sample with a spot size on the order of a few nanometers (http://en.wikipedia.org/wiki/Focused_ion_beam).

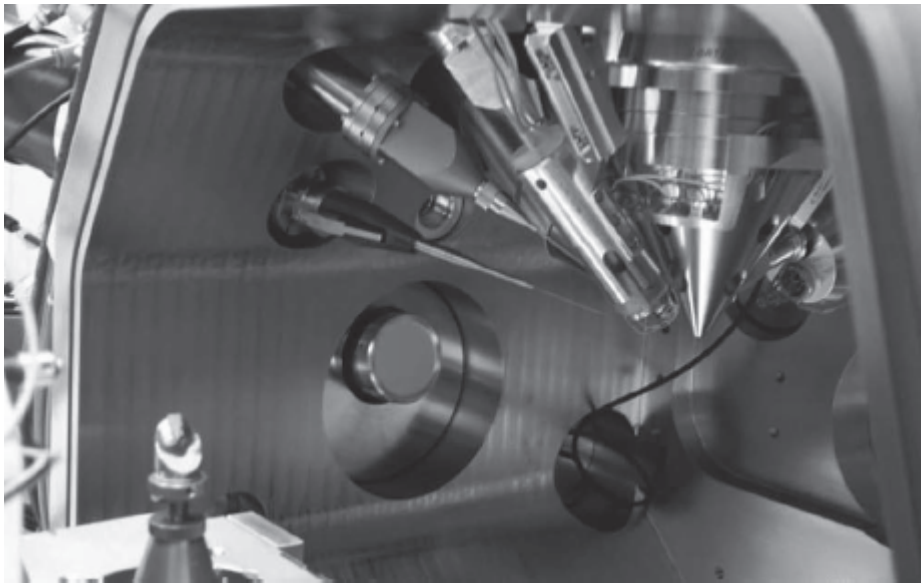

Figure 2.2. FIB sample chamber with sample mounted on a 45 ° stage. (Tomutsa et al., 2007)

The time required for ion currents of few thousands pA to mill an area of 50 μm by 50 μm with a depth of 0.1μm is of the order of minutes, which depends strongly on the current and the sample material. Higher energy cuts faster but produces rougher surfaces resulting in a poor quality image. Although this method provides great potential in imaging hydrocarbon bearing rocks at high resolution and produces images with better quality than the electron beam imaging due to less charging of the surface, it is still significantly time consuming due to the refocusing between milling and imaging as well as the sample repositioning (Tomutsa et al., 2007).

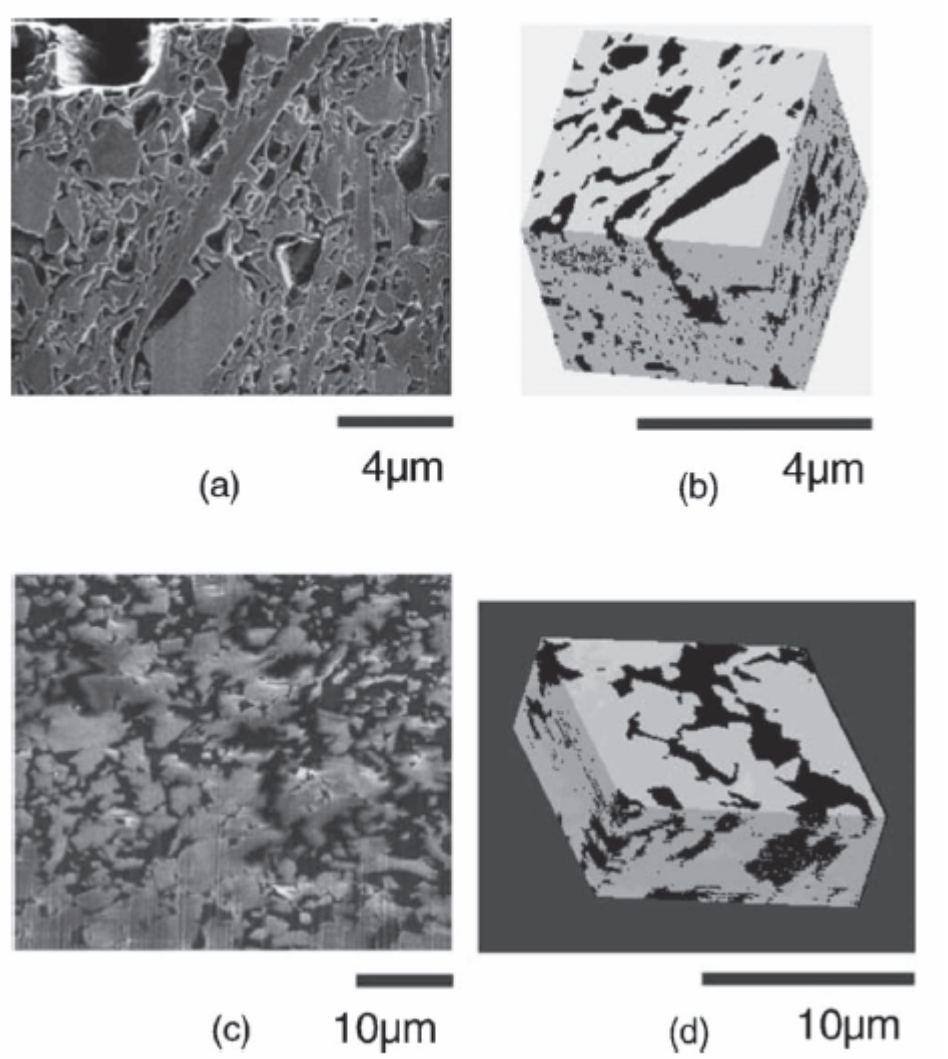

Figure 2.3. 2D FIB image of diatomite (a) and chalk (c) and their 3D reconstruction images based on FIB serial sectioning (b, d). The reconstructions are from successive binarized FIB images spaced at 0.1μm. The pore space is black (Tomutsa et al., 2007).

2.1.2 Confocal laser scanning microscopy

Confocal laser scanning microscopy can provide sub-micron resolution, but is limited to a certain thickness and the resolution of the isolated pore space (Fredrich et al., 1995). The sample is impregnated with epoxy doped by fluorechrome with an excitation wavelength to fluorescence. Any dye particles in the focal region under a laser beam are excited and detected by a photomultiplier. The detected region can be

precisely controlled by computer and shifted either along the surface or with a different depth. A 3D image of the pore structure is therefore recorded.

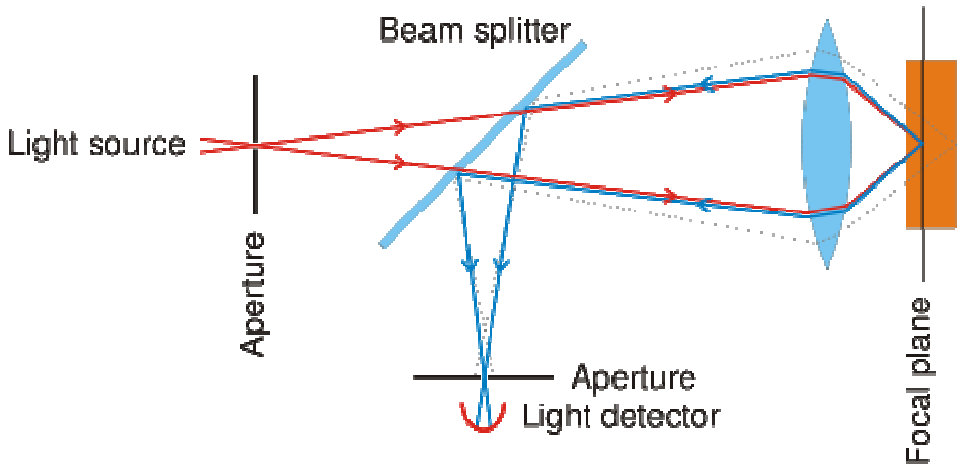

Figure 2.4. Schematic picture of confocal laser scanning microscopy (http://en.wikipedia.org/wiki/Confocal_laser_scanning_microscopy).

As can be seen in the schematic picture Fig. 2.4, a laser beam passes a light source aperture and then is focused into a small focal volume within a fluorescent specimen by an objective lens. The emitted fluorescent light mixed with reflected laser light from the illuminated spot is then recollected by the objective lens. A beam splitter separates the light mixture by allowing only the laser light to pass through and reflecting the fluorescent light into the detector where the fluorescent light is detected by a photo-detection device transforming the light signal into an electrical one and recorded by a computer. The light not coming from the focal point is obstructed and thus suppressed by the detector aperture, as shown by the dotted gray line in Fig. 2.4. (http://en.wikipedia.org/wiki/Confocal_laser_scanning_microscopy).

Fig. 2.5. gives some examples of the resultant pore space images at high resolution down to a couple of hundred nanometers. Although this technology provides enhanced resolution with optical level quality, it is usually pseudo 3D rather than allowing thick, opaque objects to be scanned.

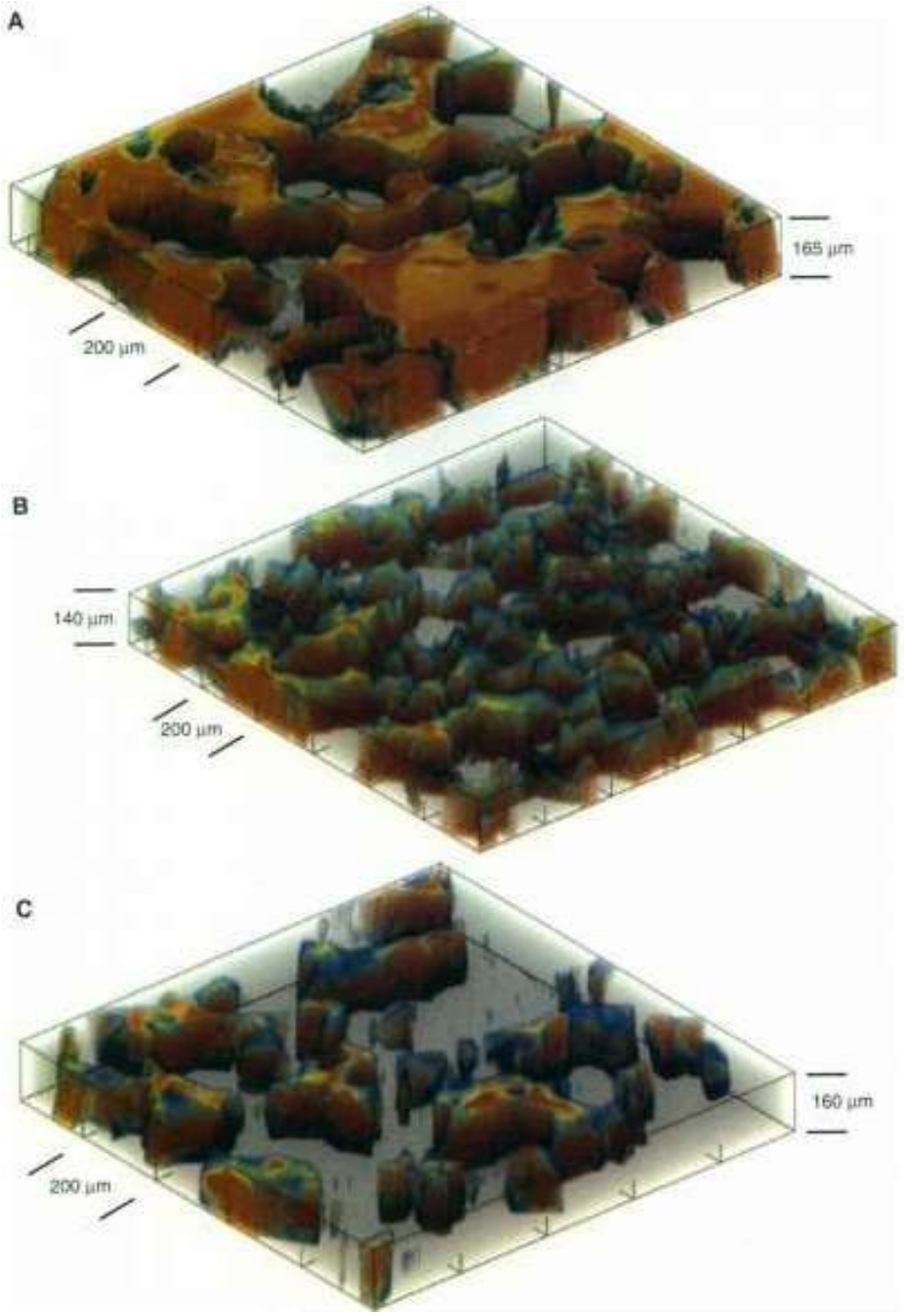

Figure 2.5. Pore space imaged by confocal laser scanning microscopy. The pore space is colored and the solid is transparent. A, B and C show sample images with different cementation and pore sizes (Fredrich et al., 1995).

2.1.3 Stochastic reconstruction using statistical methods

2D pore space images are routinely available at high resolution. 3D images

can be reconstructed using statistical methods with information obtained by analyzing 2D thin sections.

Methods based on a truncated Gaussian random field are often used with the geometrical properties of the original pore space to reconstruct 3D images (Adler and Thovert, 1998). These geometrical properties include porosity (also called one-point correlation function) and two-point correlation function (measuring the probability of finding two points separated by a certain distance within the same phase), which are basic quantities used to characterize pore structures. The idea is to generate a random phase function of space *Z(x)* that is equal to zero in the solid phase and one in the pore space. *Z(x)* must satisfy the one and two-point correlation function of a reference sample where the thin section is from.

However, the one and two-point correlations are insufficient to replicate the topological information of the porous media (Quiblier, 1984; Adler et al., 1992; Roberts, 1997; Adler and Thovert, 1998; Levitz, 1998; Liang et al., 1998; Yeong and Torquato, 1998a; 1998b; Ioannidis et al., 1999; 1999; Roberts and Torquato, 1999; Bekri et al., 2000; Ioannidis and Chatzis, 2000). Yeong and Torquato (1998a; 1998b) used a combination of the two-point correlation function and the distribution of linear path, which is the probability of finding a line segment with certain length in the void space as a descriptor to characterize the pore geometry. Hilfer (1991) introduced local porosity distribution and local percolation probability to improve the geometrical characterization. Local porosity is the probability density of finding the local porosity ϕ in the range $\phi \pm \Delta\phi$ in a cell of edge length *L*. Local percolation probability is to measure the fraction of cells with edge length *L* percolating in a given direction as an indicator of connectedness. Other descriptors, such as pore chord length that is the length in the void between two solid voxels with a given direction, are also very useful to characterize the structure to generate 3D images (Serra, 1982; Torquato and Lu, 1993; Levitz, 1998; Roberts and Torquato, 1999). The combination of one- and

two-point correlation functions with these geometrical descriptors improves the reconstruction of connectedness and predictions of macroscopic properties such as permeability.

Despite this, these methods still fail to reproduce the long-range connectivity of the original pore space. Yeong et al. (1998a; 1998b) developed a stochastic method based on simulated annealing extended later by Manwart et. al (2000). This method is based on moving pore space voxels around to minimize the objective function and they obtained the correct porosity. This method offers the promise to match not only one- and two- point correlation functions but also multi- point correlation functions.

Okabe and Blunt (2004; 2005) developed a multi-point statistical method to reconstruct the 3D volume from thin sections, which enables the typical patterns of the void space seen in 2D and consequently preserves the long-range connectivity, Figs. 2.6 and 2.7.

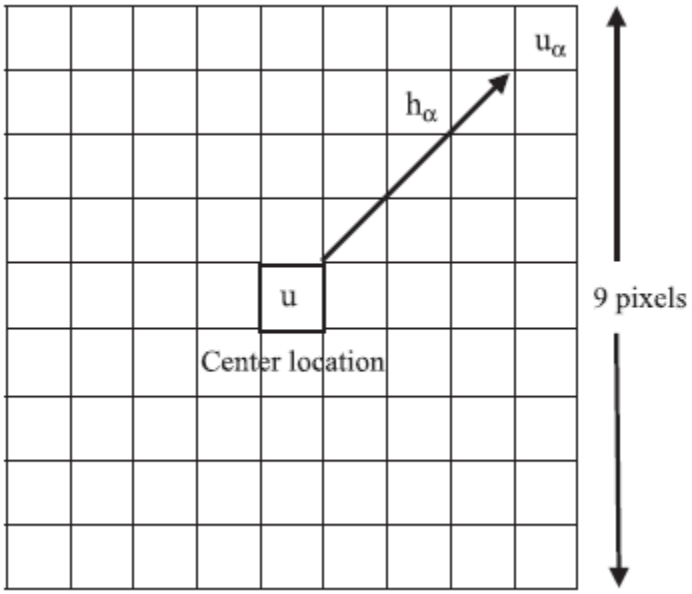

Figure 2.6. A 9 × 9 template to capture multiple-point statistics. The training image (a 2D input) is scanned and each occurrence of any possible pattern of void and solid is recorded. (Okabe and Blunt, 2005)

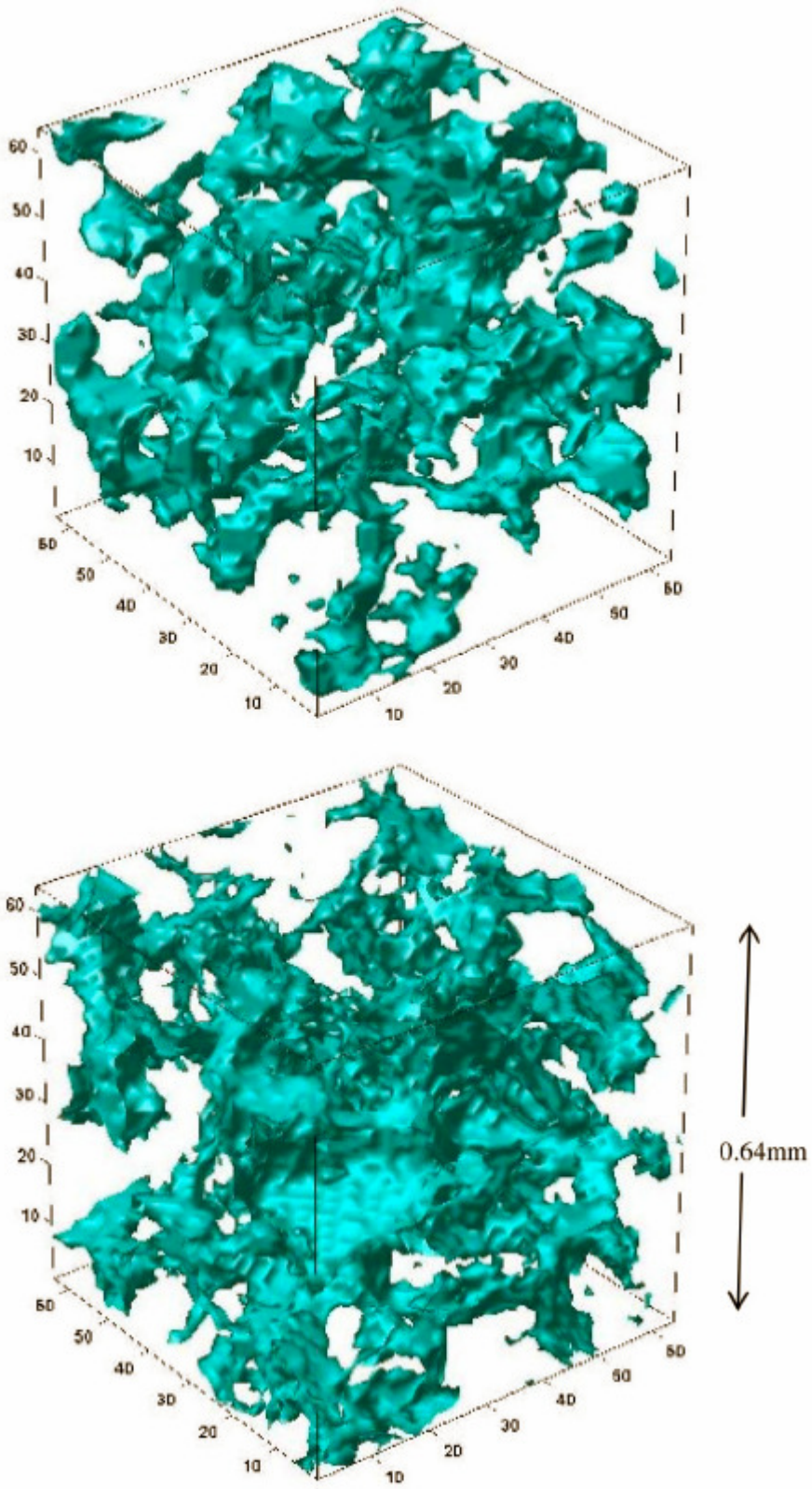

Figure 2.7. Comparison of micro-CT image of Berea sandstone and the reconstructed image using a multi-point statistical method. (Okabe, 2004)

A method based on a Markov Random Mesh statistical model was developed by Wu et al. (2004; 2006) using 5-point stencil to measure the probability of neighboring pixels, Figs. 2.8 and 2.9. This is a fast and efficient method to reconstruct the pore space preserving the long-range connectivity. This method identifies all the transition probabilities between the voids and solids of the medium for a given local training lattice stencil used for stochastic reconstruction.

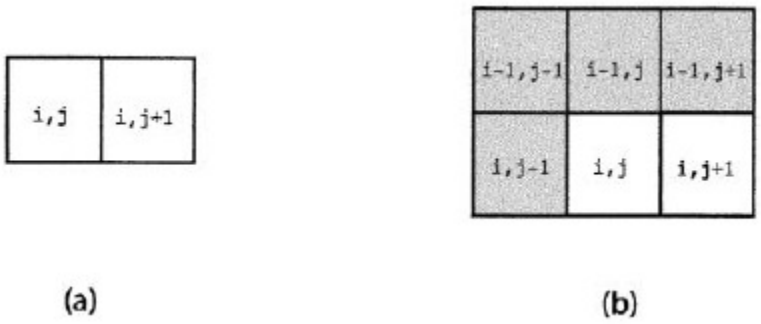

Figure 2.8. Two pixel neighborhood (a) and five pixel neighborhood (b).(Wu et al., 2004) .

These statistical methods discussed above produce high resolution 3D images derived from their original 2D inputs with similar morphological statistics. The other advantage of statistical reconstruction, compared to a geological process-based model discussed in the next section, is that it can generate the 3D structures when the sedimentary processes are not clear, for instance, in carbonates. The disadvantage is that, to date, most of the models assume that the pore structure is isotropic.

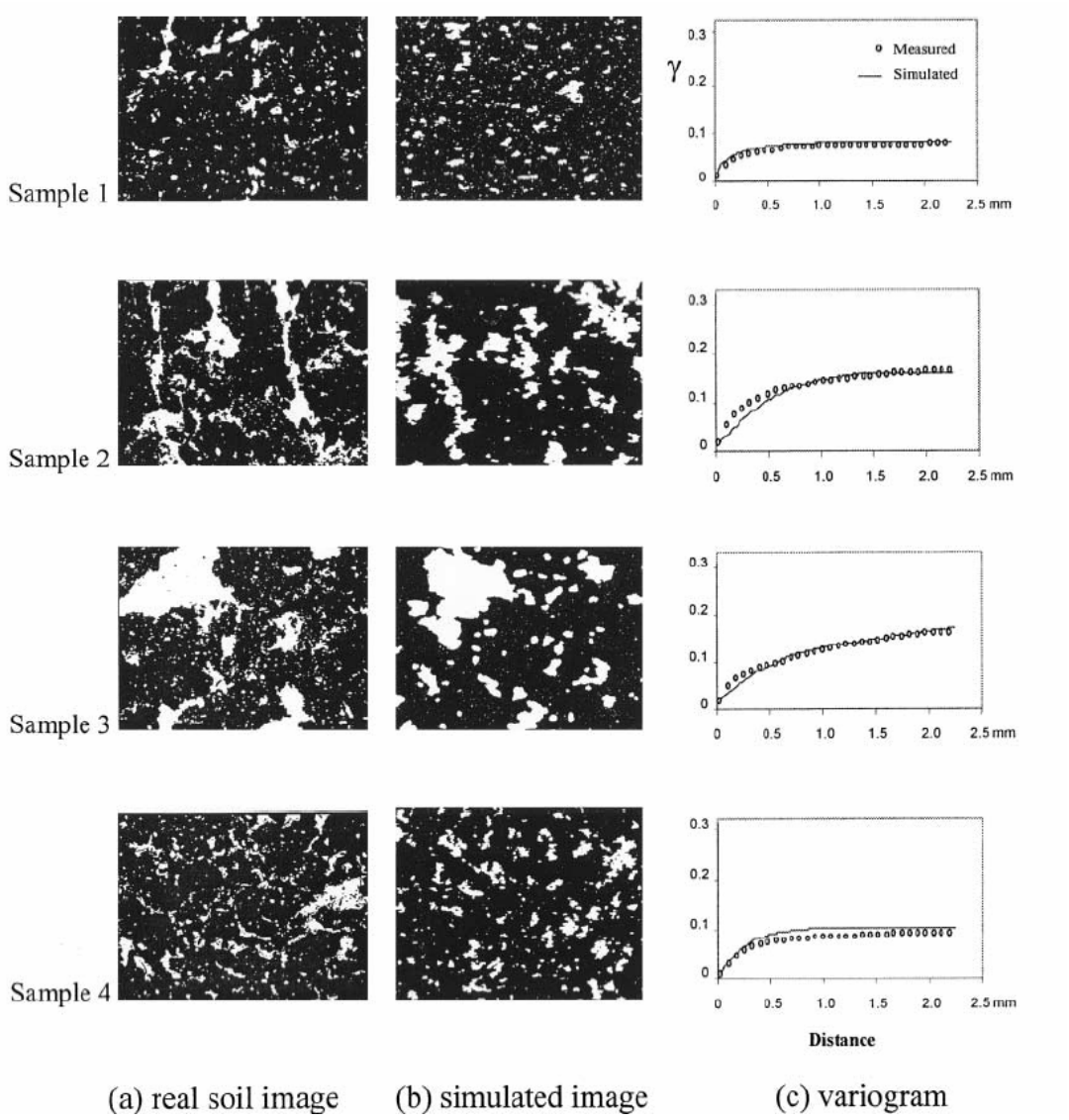

Figure 2.9. Reconstructed images (each image size is 1.6 by 1.2 cm) using Markov chain Monte-Carlo by (Wu et al., 2004). (a) Original thin sections of soil; (b) Relevant reconstructed images; (c) Semivariograms of pore space in original and simulated images.

2.1.4 Process-based reconstructions

Bryant et al. (1992; 1993a; 1993b; 1995) simulated close packing with equally-sized spheres followed by processes such as swelling the spheres uniformly

and allowing them to overlap and compacting by vertically moving the centers. This is a reasonable approximation of the process of quartz cementation. A major triumph was made in pore-scale modeling since the pore space can be tessellated into cells and pore networks can be generated by assigning cells as pores and cell faces as throats. Transport properties were able to be predicted on water-wet sandpacks, sphere packs and a cemented quartz sandstone.

Later the method was extended by Øren and Bakke (1998; 2002; 2003) including different sized spheres to simulate more sophisticated geological processes, such as sedimentation, compaction and digenesis processes. The grain size distribution can be obtained from analyzing 2D thin sections of rocks. The sedimentation allows the grains to be deposited successively in a gravitational field to a stable position with a local or global minimum in potential energy. The compaction process moves the grain centers in a vertical direction and allows the grains to overlap. During the diagenesis process, quartz cements grow and clay content is introduced. More minerals and clay are introduced to simulate the composition observed in thin sections. The simulated rock images produce good agreement with micro-CT images of Fontainebleau and Berea sandstones, see Fig. 2.10, in terms of the morphological properties, such as two-point correlation functions, local porosity distributions and local percolation probabilities and petrophysical properties such as absolute permeability and formation factors.

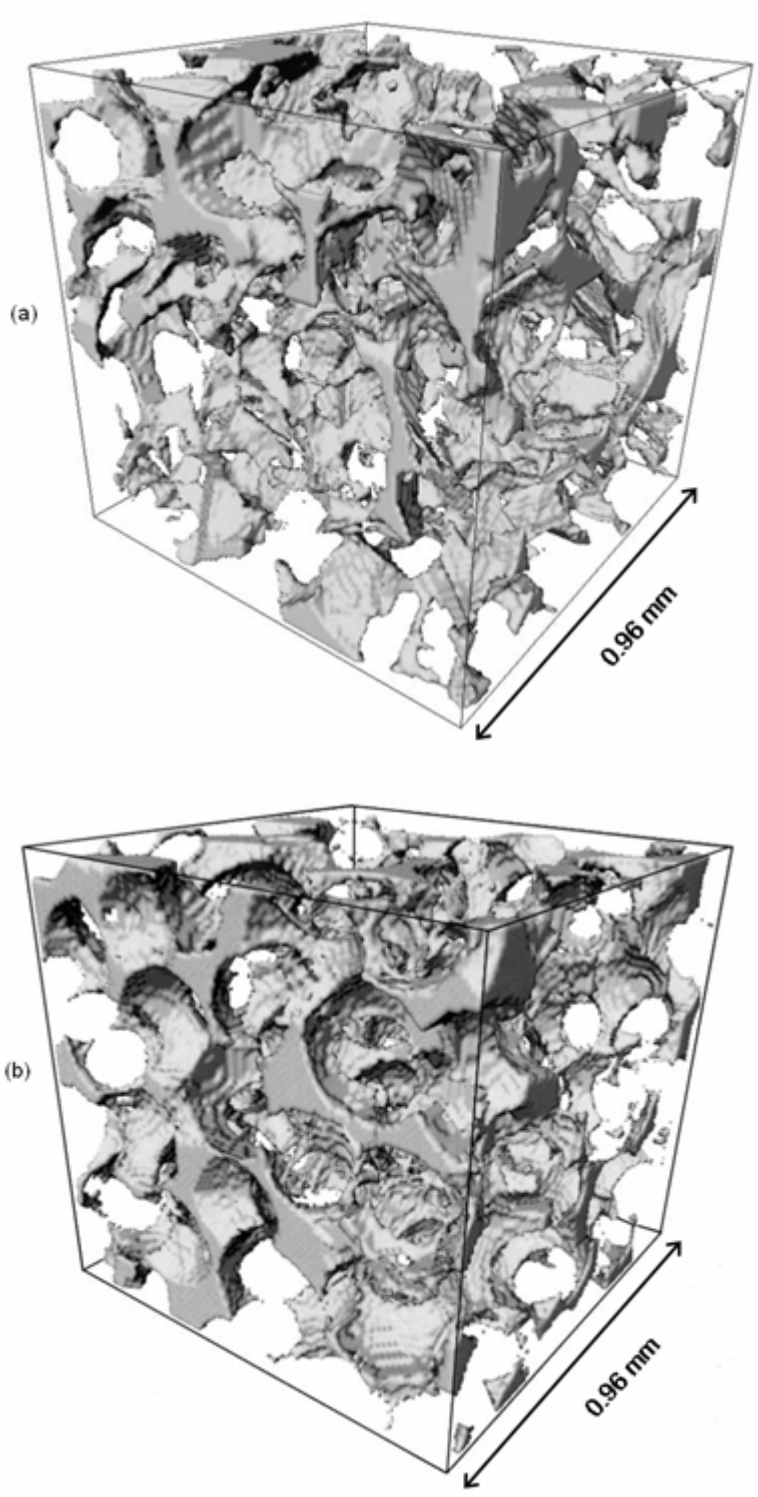

Figure 2.10. Comparison of micro-CT image (a) and process based image (b) of a Fontainebleau sandstone. (Øren and Bakke, 2002)

More importantly, pore networks can be extracted from process based images using Voronoi tessellation. Successful predictions were made using these geological

process-based models (Øren et al., 1998; Patzek, 2001; Øren and Bakke, 2002; 2003; Valvatne and Blunt, 2004; Piri and Blunt, 2005a; 2005b).

2.1.5 X-ray computed micro-tomography (micro-CT)

All the imaging techniques discussed above aim to generate 3D images with similar properties of the real structure of the porous media. However, each of them have their own limitations as discussed in previous sections.

In the last two decades after the first micro-CT system was conceived and built by Jim Elliott in the early 1980s (Elliott and Dover, 1982), micro-CT technology has been developed and extended to the petroleum industry (Dunsmuir et al., 1991) to provide high resolution 3D images with a resolution down to the pore scale, namely, the micron and sub-micron domain (Coenen et al., 2004). This is a non-destructive and truly 3D imaging technique.

To image geological porous materials at the micro-scale, two types of micro-CT systems are common in use. One is a desktop micro-CT scanner using an industrial X-ray generation tube and the other is synchrotron X-ray micro-tomography. Although most of the state-of-art desktop micro-CT scanners provide a resolution down to 5 microns or finer, the best image resolution has been achieved and reported in the literature by using synchrotron micro-CT. For example, a resolution of 700 nm was reported by Conean (2004). Some manufacturers of desktop micro-CT, for instance, SkyScan claims their Nanotomography scanner (SkyScan 2011 nano-CT) has a range of 150 to 250 nanometers per pixel with a resolution of 400 nm and a field of view (FOV) of 200 micrometers (http://en.wikipedia.org/wiki/Nanotomography).

A digital core laboratory (Knackstedt et al., 2004) was built at the Australian National University (ANU) in 2004. Extensive study (Arns et al., 2005) on pore space imaging has been carried out using their self-built micro-CT system, which enables

core plugs up to 5 cm diameter to be imaged within the maximum field of view of 55 mm of the system and with a resolution down to 2μm. The 3D reconstruction algorithm based on the Feldkamp (1995) technique has been parallelized and takes a cluster computer of 128 CPUs approximately 4 hours to generate 2048^3 voxel tomogram for the ANU group. Fig. 2.11 gives some examples of micro-CT images of porous media.

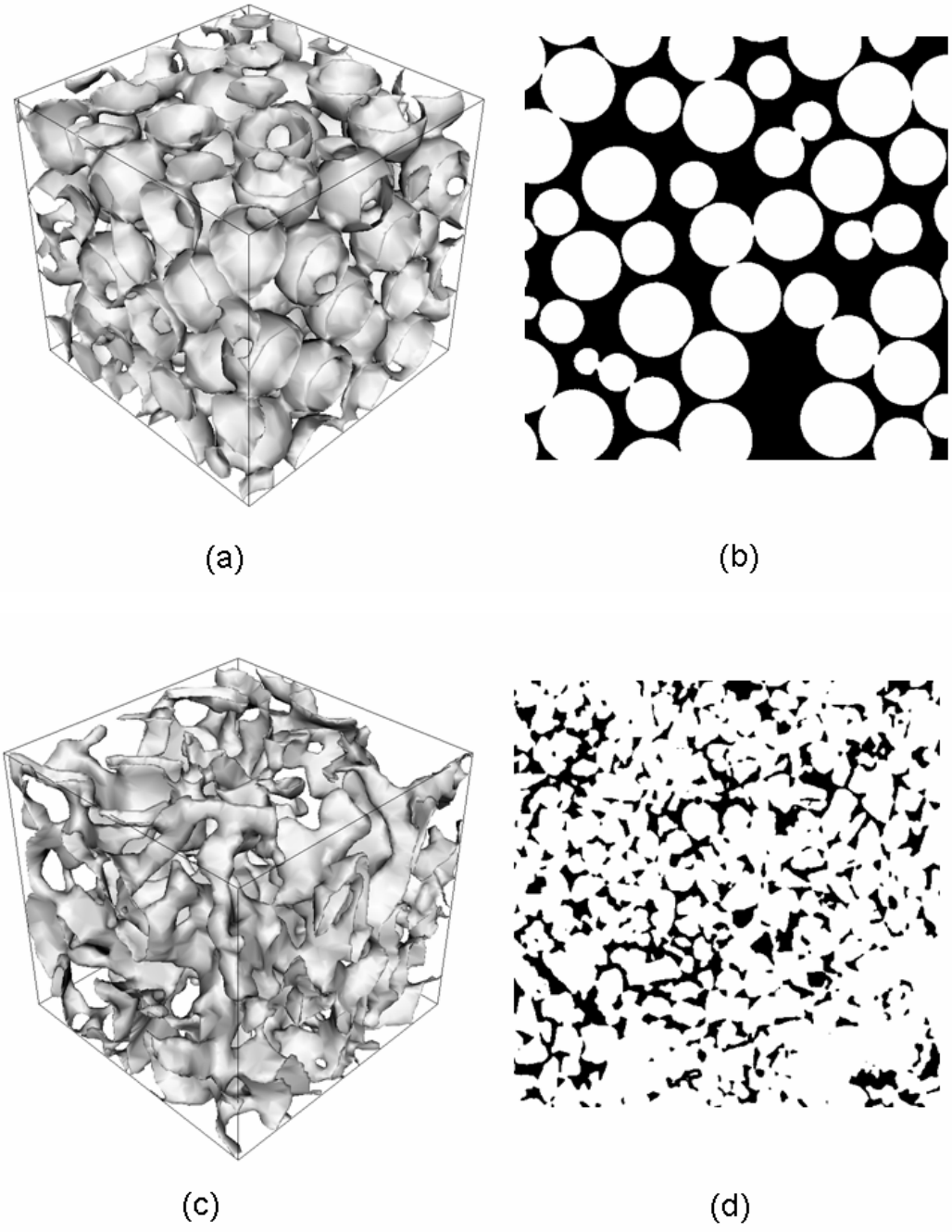

(Figure 2.11, to be continued)

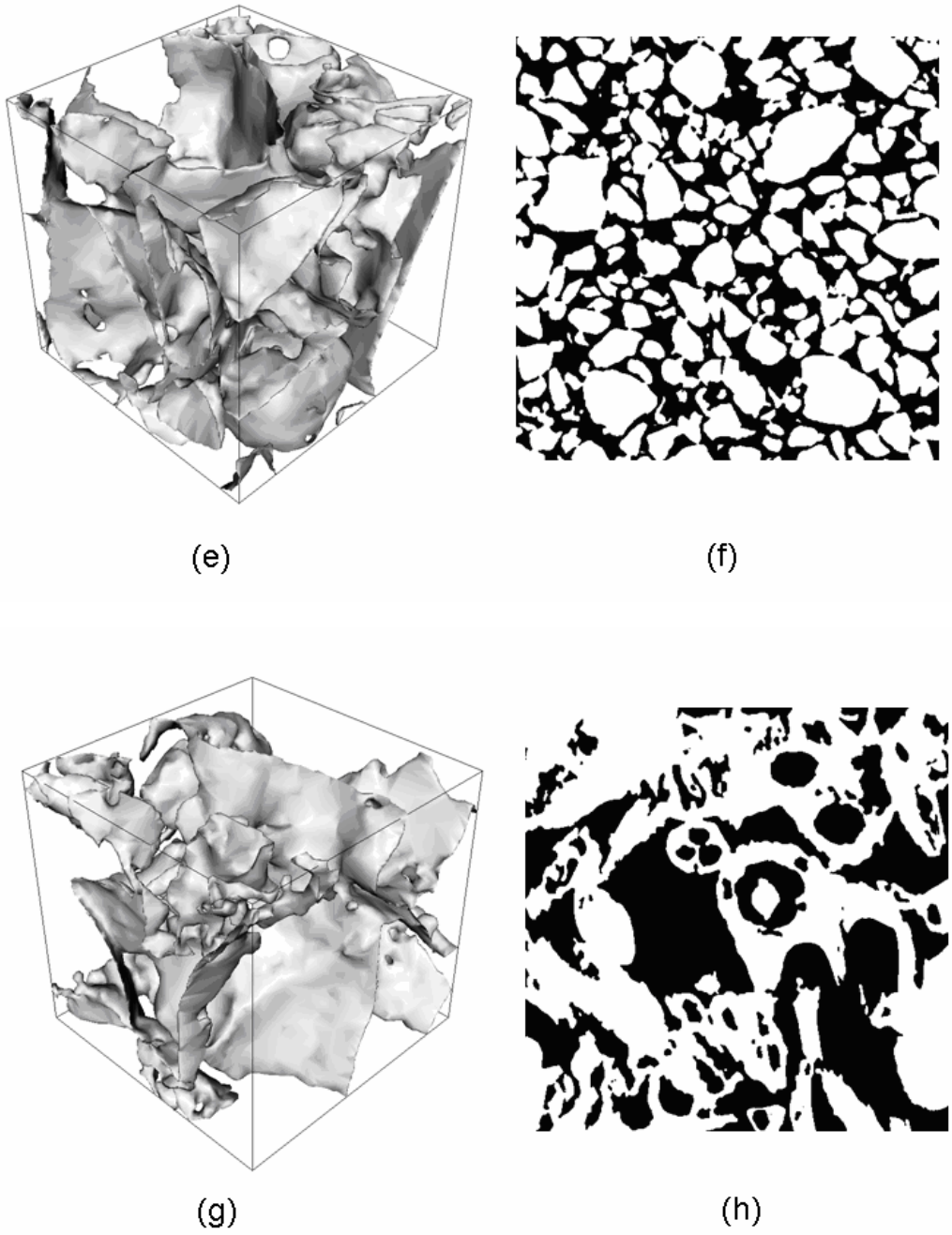

Figure 2.11. Micro-CT images of porous media imaged at the XCT lab at the Australian National Universtiy (http://xct.anu.edu.au/network_comparison); (a) and (b) are the 3D view and a cross-sectional image respectively of a silica sphere pack with a void volume fraction (porosity) of 37.9 %. The diameter of the beads is 1.59 mm and the dimensions are 512 × 512 × 512 with a voxel side length of 17.472 µm ; (c) and (d) are of sample Castlegate outcrop sandstone, from southeastern Utah, USA. The

segmented image porosity is 20.6 %. The dimensions are 512 × 512 × 512 voxels with a voxel side length of 5.6 µm; (e) and (f) are the images of a poorly sorted unconsolidated fluvial sandpack from southern Australia. The segmented image has a porosity of 36.3 % (void phase). The dimensions are 512 × 512 × 512 voxels with a voxel side length of 9.184 µm; (g) and (h) are from a sample of a very porous (43% void) fossiliferous outcrop carbonate - Mt Gambier limestone - from South Australia. The dimensions are 512 × 512 × 512 voxels with a voxel side length of 3.024 µm and a segmented porosity of 43.6%.

A virtual permeametry has been developed at ANU to compute absolute permeability and formation factors based on the micro-structure provided by micro-CT using a lattice Boltzmann simulation (Arns et al., 2004a) and solving for the Laplace equation on voxels respectively. Besides, their study on micro-CT imaging also extends to rock fabric and texture identification, three-phase flow visualization and pore network extraction (Arns et al., 2005; Saadatfar et al., 2005).

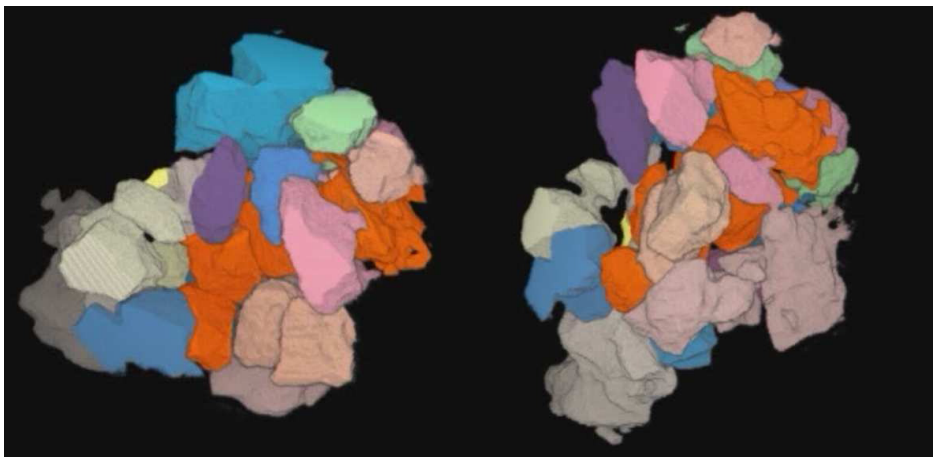

Figure 2.12. Two images of a highly coordinated grain and its neighboring grains. (Saadatfar et al., 2005)

Micro-CT provides fair resolution to distinguish initial and residual fluid distribution in pore space, see Fig. 2.13, which is important for IOR (improved oil

recovery) and EOR (enhanced oil recovery) applications.

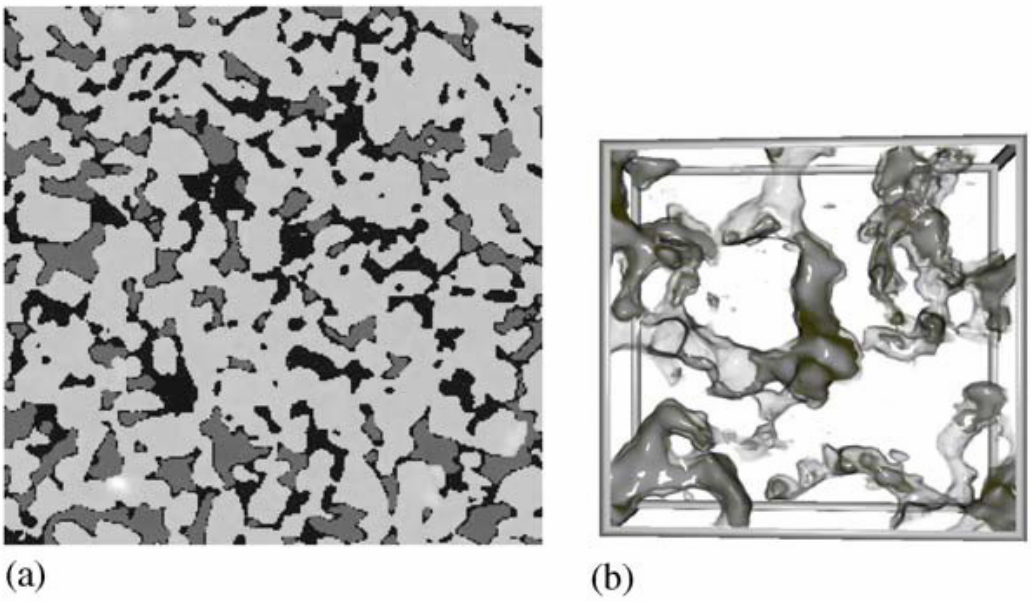

Figure 2.13. (a) and (b) are the 2D and 3D images of experimental two-phase fluid configuration during drainage in Berea sandstone at 60% wetting phase saturation. The image resolution is 9μm. In (a), the black is the wetting phase; the dark gray is the non-wetting phase; the lightest are the grains. (b) shows the wetting phase (dark) and the non-wetting phase (light) within a subsection of the core (grain removed). (Turner et al., 2004)

The image resolution from a common desktop micro-CT scanner is sufficient for poorly consolidated sandstones. For consolidated materials and carbonates where the sub-micron porosity may dominate the flow, it is possible to use Synchrotron X-ray micro-CT. However, Synchrotron micro-CT cannot be used as a routine examination for industrial application due to the cost and sporadic accessibility. These obstacles can be overcome with developing advances in micro-CT technology and the improving computing power to handle huge image datasets.

Details on micro-CT scanning will be discussed in Chapter 3.

2.2 Pore network extraction methods

As discussed above, there are different methods that can generate 3D images of either real or synthetic pore space images. However, it is not practical to simulate fluid flow directly based on these images especially for multi-phase flow until an equivalent network is found, as mentioned in the Introduction.

Attempts to extract pore networks from generic and arbitrary 3D images have been tried for more than a decade. The major algorithms include the multi-orientation scanning method, the medial axis based method, the maximal ball method and the Voronoi diagram based method.

2.2.1 Multi-orientation scanning

Zhao et al. (1994) developed an algorithm using multi-orientated plates scanning along the pore channels to detect pore bodies and pore throats, Fig. 2.14. Overlapping plates during the scanning from different directions give indications of local minima which defines the throats. However, this method has difficulties locating pore bodies. The concept of orientation plates was later adopted by Baldwin et al. (1996) and Liang et al. (2000) to find the hydraulic radius along the pore space skeleton predefined using thinning algorithms.

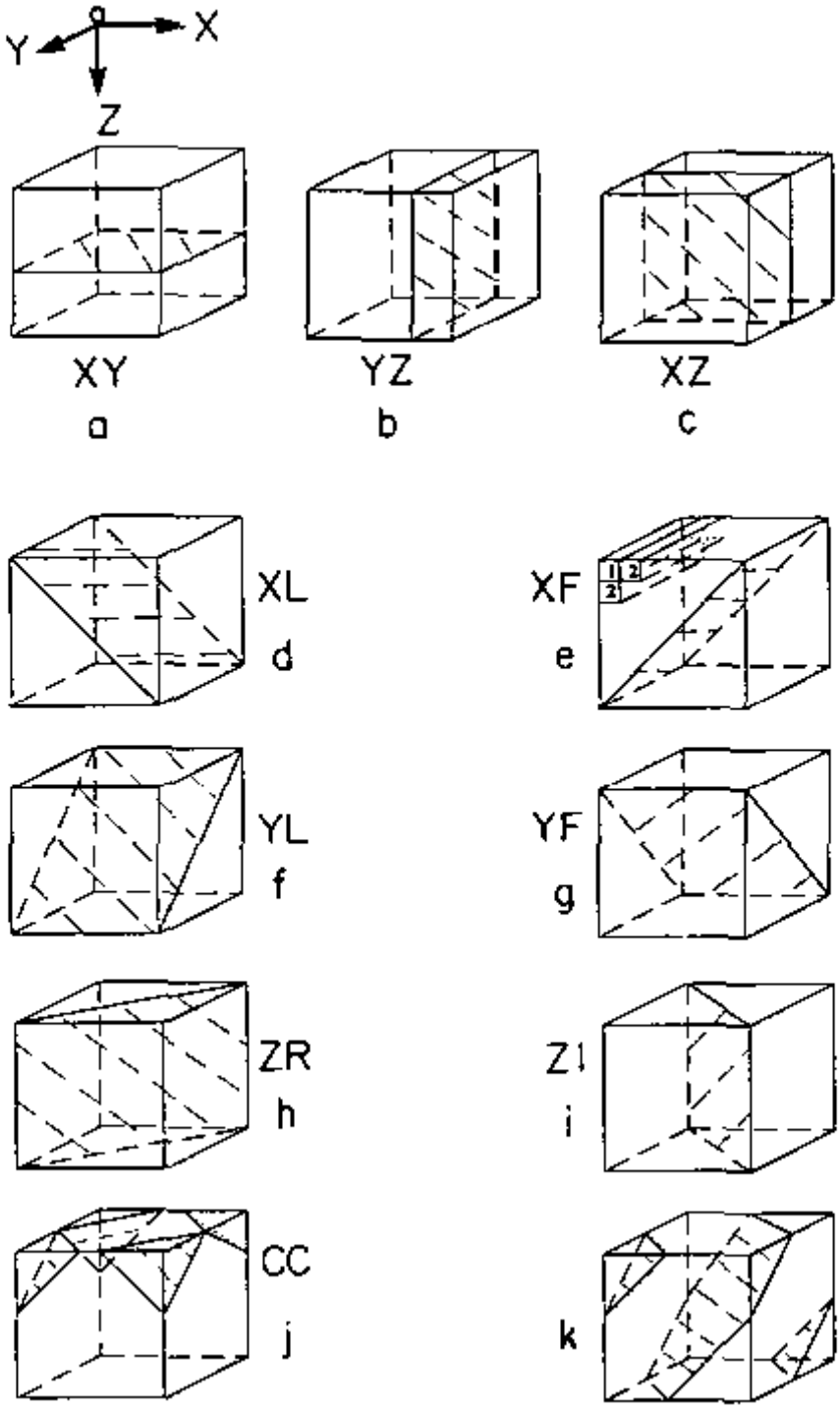

Figure 2.14. Planar serial sections along different directions. (a)-(c) are three orthogonal orientation; (d)-(i) are the diagonal orientations; (j) represents four corner to corner scanning and (k) shows serial sections viewed from a corner-to-corner direction. (Zhao, 1994)

2.2.2 Medial axis based algorithms

The medial axis based methods transform the pore space into a medial axis that is the reduced representation of the pore space acting as a topological skeleton roughly running along the middle of pore channels. Pore space partitioning can be validated along the skeleton to decide the pore throats by local minima along branches and pore bodies at the nodes (Lindquist et al., 1996; Lindquist and Venkatarangan, 1999; Sheppard et al., 2005; Shin et al., 2005; Prodanović et al., 2006).

The medial axis can be obtained by a thinning algorithm (Baldwin et al., 1996; Liang et al., 2000) or a pore space burning algorithm (Lindquist et al., 1996). The pore space is eroded from the grain surfaces until the burning from different directions ends up in one voxel. A burn number is recorded for each voxel on the meidal axis, which defines the radius of the largest inscribed sphere centered at that voxel.

The medial axis mathematically preserves the topology of the pore space. However, it is difficult to identify pores unambiguously, since, first the clean-up processes need to be performed to remove the trifling details on the skeleton due to the intrinsic sensitivity of the algorithm to noise in digitalized images (Venkatarangan, 2000), especially to that in the form of the *bumps* on the surface (Shin et al. 2005); second, they normally encompass more than one junction of the medial axis and various merging algorithms have to be developed to reasonably trim the skeleton and fuse the junctions together whilst avoiding unrealistically high coordination numbers (Sheppard et al., 2005; Shin and Lindquist 2005).

Fig. 2.15 gives an example of the effects before and after the cleaning-up process.

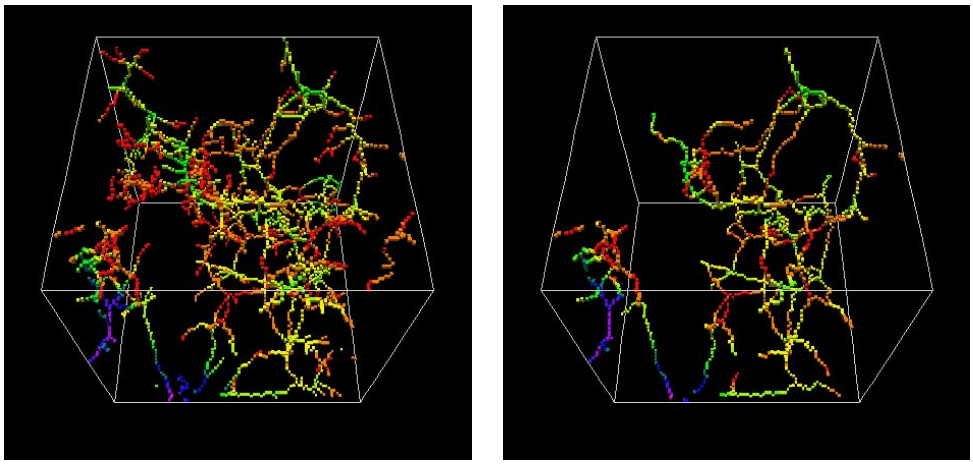

Figure 2.15. The medial axis algorithm is highly sensitive to the irregularity in the void-grain surface and disconnected voxel clusters due to misidentification in segmentation. The left picture shows the medial axis extracted from a small region of a Berea sandstone image (voxel side length is 4.93 μm); the right one is the set of medial axis after trimming all dead ends where no fluid flow through. The colors represent, in rainbow scale, distance to the closest (at least two) grain voxels. (http://www.ams.sunysb.edu/~lindquis/3dma/3dma_rock/3dma_rock.html)

Silin and Patzek (Silin and Patzek, 2006) illustrated some problems of pore and throat identification of medial axis based algorithms. In Fig. 2.16, (a) is considered as four distinct pore bodies with the coordination numbers equal to 3, while it is suggested as one pore by human intuition; (b) is a rectangular parallelepiped that is regarded as four nodes if only being judged by skeleton, but again it is viewed as one pore intuitively.

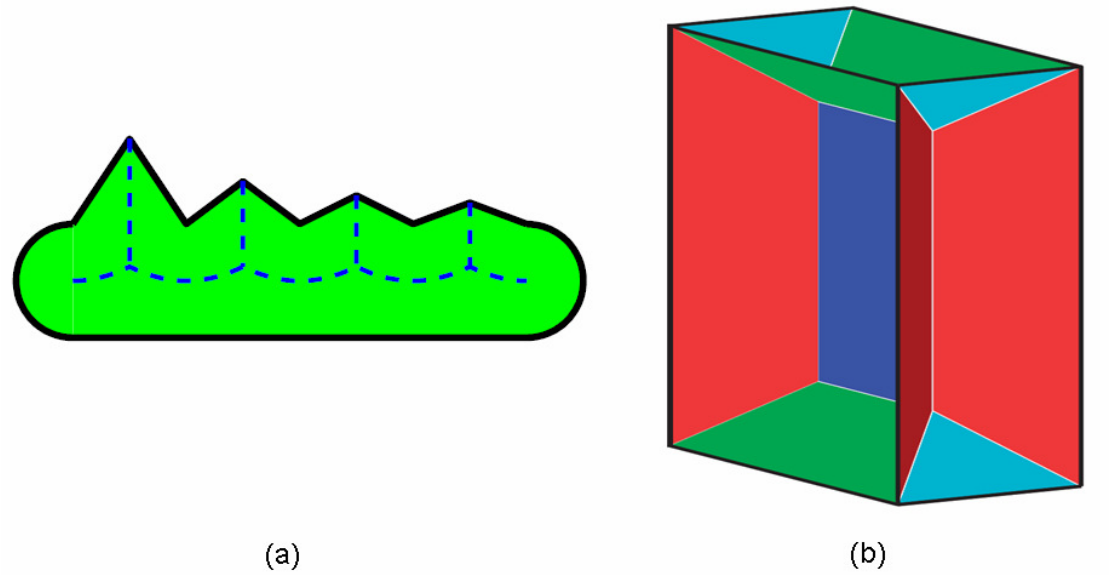

Figure 2.16. (a) shows the skeleton of a 2D object with perturbed boundary. (b) shows the skeleton of a simple 3D objects (Silin and Patzek, 2006).

Shin et al. (2005) developed a method to distinguish the spurious branch connecting to the surface bumps from the ones passing through a contact surface of two pores by judging the distances from the node to the nearest solid M and to the end of the branch L. For those end-segments in Fig. 2.17 (a), if $L \le M$, L is declared to be spurious. For the segments linking two nodes, the minimum of M_1 and M_2 measured at different nodes is used to determine the true skeleton. If $L > \min(M_1, M_2)$, the segment is assumed to pass between two pores, otherwise it is lie solely within one pore. These measures give good solutions to eliminate some obviously spurious throats. However, it is only applicable to the distinctive waist configuration, i.e. high aspect ratio cases, which is not necessarily found in reservoir rocks.

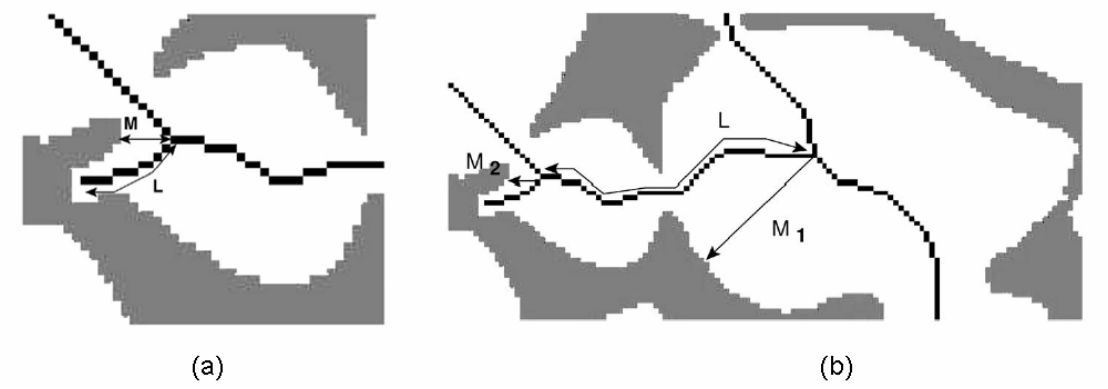

Figure 2.17. In Shin et al.'s model (2005), the length *L* of a branch-leaf segment is used to judge the spurious throats connecting to a bump in one pore (a) or passing through a contact surface between real two pores (b).

To minimize the number of spurious throats derived from the medial axis, Sheppard et al. (2005) developed a pore merging algorithm according to the quality of candidate throats to be removed. A series of quality evaluation criteria were also proposed in their merging algorithm to truncate the high coordination numbers, where throats with less influence to network topology will be removed and the preliminary connected individual pores will be merged. The quality of each throat is quantified as a non-linear combination of its *constriction ratio* and *length-width ratio*. The constriction ratio is the smaller aspect ratio of a throat, i.e. the ratio of the smaller inscribed radius of the two pores linked by the throat to the radius of throat. The length-width ratio is the distance of pore to pore centers to the minimum throat width linking the two pores. They assume a very short throat has poor quality, while a very constrictive throat is of high quality. A threshold is given to remove low quality throats. Since many spurious throats is caused by the noise level of the original image in the first place, a Gaussian smoothing kernel is used to depress the noise before the medial axis is extracted to the distance map that calculates the number of steps from the voxel to the grain surface, which reduces the complexity in the *clean-up* process in the medial axis based algorithms. As a consequence, the resultant medial axis contains fewer spurious features. Some example networks are given by Sheppard et al.

(2005).

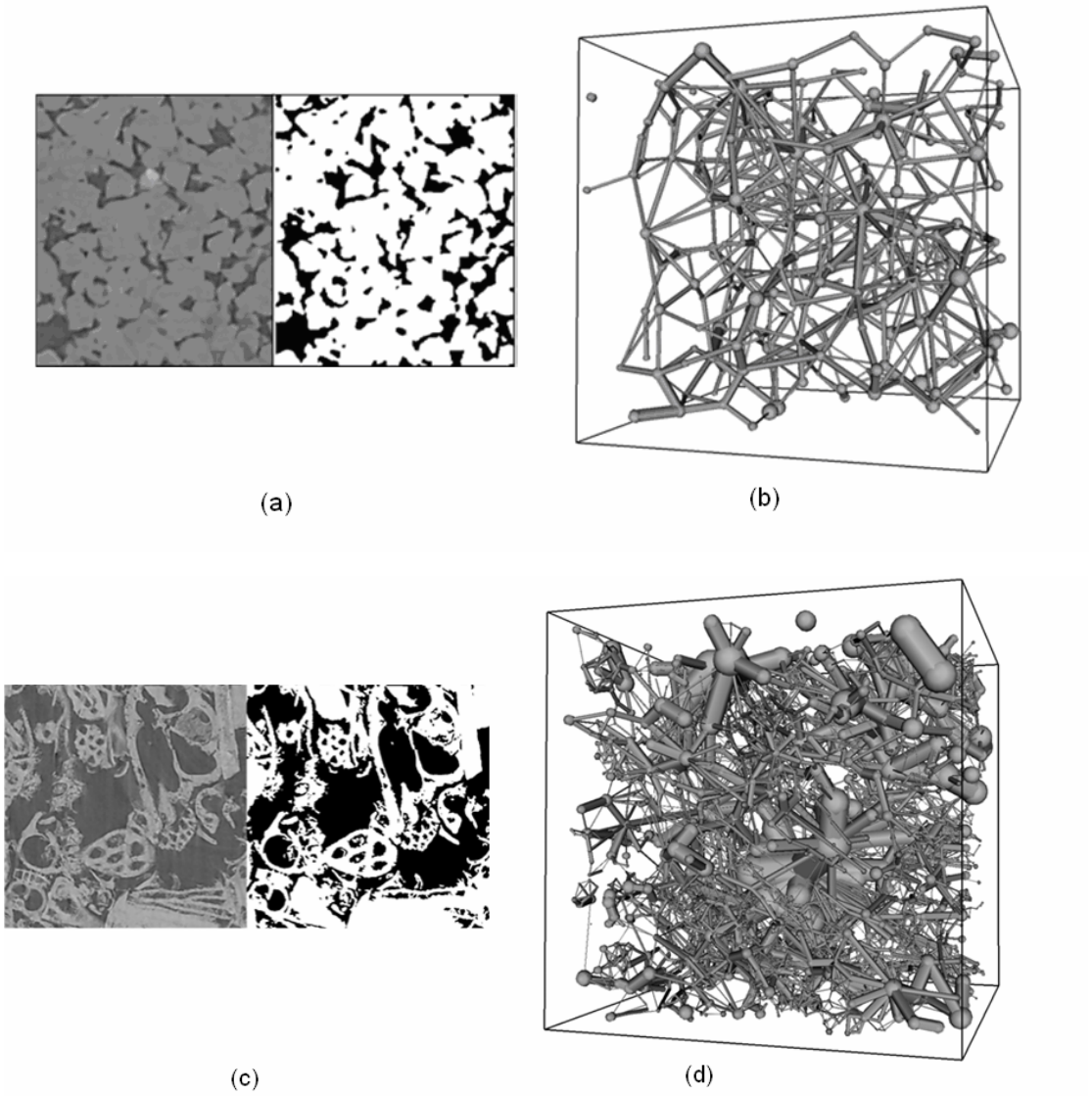

Figure 2.18. (a) shows the gray scale and segmented images of a sandstone; (b) is the network of this sandstone extracted using the medial axis algorithm; (c) shows the gray scale and segmented images of a carbonate sample and (d) is the corresponding network. (Sheppard et al., 2005)

The medial axis based method is promising with properly developed merging criteria. However, the choice of threshold value for throat quality qualification can be problematic without being examined by real flow simulations.

In conclusion, medial axis algorithms readily capture the interconnectivity of the pore spaces but encounters problems in identifying pores.

2.2.3 Voronoi diagram based algorithms

When geological process based images have been built, since the grain centers are known, it is possible to extract pore networks using the Vonoroi diagram (Bryant and Blunt, 1992; Bryant et al., 1993a; 1993b; Bryant and Raikes, 1995; Øren et al., 1998; Øren and Bakke, 2002; 2003). An ultimate dilation of the grains can be performed to tessellate the pore space using Voronoi polyhedra. The voxels that have neighboring voxels from four or more different grains can be regarded as the pores of the network. The edges of the polyhedra consist of voxels that have neighboring voxels from three different grains define the links between pores. Pore networks extracted from these methods have been proved successful in pore-scale simulation.

Delurue (2002) developed a methodology using the Voronoi diagram to find the skeleton from general 3D images to partition the pore space. Seeds for tessellation are selected on the border of grain and void to create discrete segments (Yu et al., 1998). Then the skeleton can be extracted based on a selection of Voronoi branches after the Voronoi diagram is generated based on these predefined segments (Fig. 2.19). Local apertures are calculated along the skeleton to find the pore size distribution (Fig. 2.20). Non-overlapping maximal balls are defined to divide the pore space into sub-objects. These sub-objects are eventually classified into nodes and links for pore networks. The equivalent conductivity has been successfully compared with the hydraulic conductivity measured experimentally in saturated soil (Delerue and Perrier, 2002). However, the topology is poor compared to the Berea network generated by Øren and Bakke (2003) when applying the Delurue model to a Berea sandstone sample tested by Okabe and Blunt (2004).

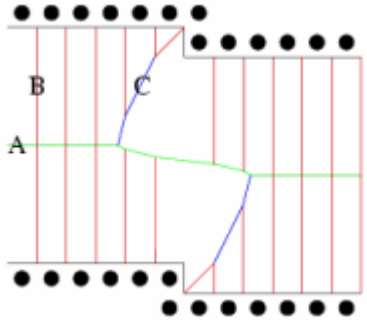

Figure 2.19. The skeleton extraction is based on a selection of Voronoi branches (black points are seeds) in the Voronoi diagram. In the skeleton, A and C should be kept but B should be removed. (http://www.bondy.ird.fr/~delerue/these.html)

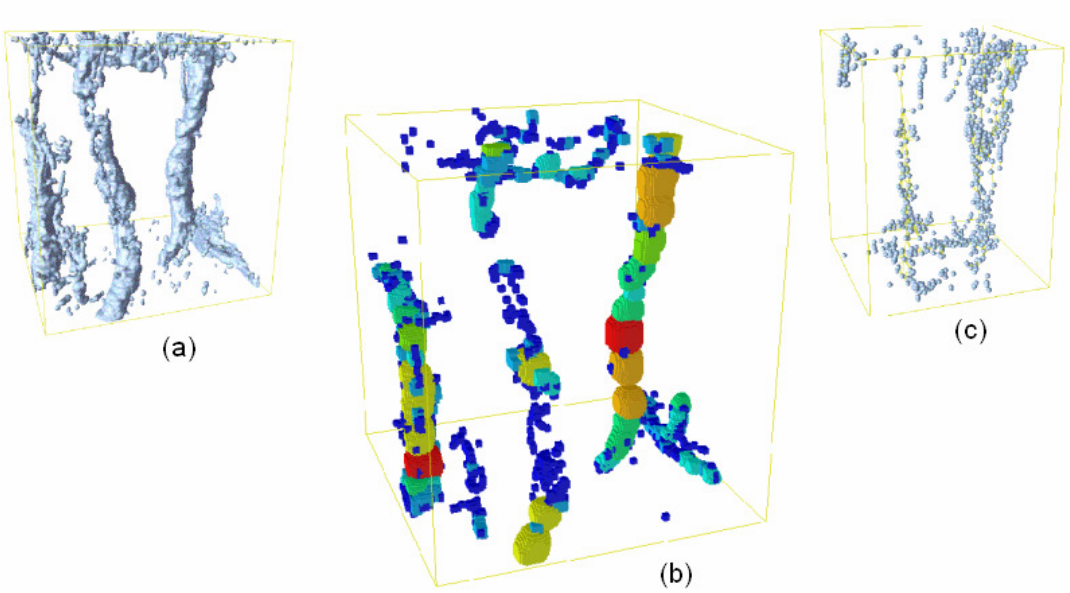

Figure 2.20. (a) is the original image of an example pore space; (b) is the non-overlapping maximum spheres in the pore space measuring the pore sizes; (c) is the pore centers in their original positions in the image. (http://www.bondy.ird.fr/~delerue/these.html)

2.2.4 Maximal ball algorithm

The maximal ball algorithm (Silin et al., 2003; 2006) starts from each voxel in the pore space to find the largest inscribed spheres that just touch the grain or the boundary, Figs. 2.21 and 2.22. Then those included in other spheres are viewed as

inclusions and removed; the rest are called maximal balls and describe the pore space without redundancy. Locally the largest maximal balls identify pores while the smallest balls between pores are throats. The maximal balls were used in Silin's work (2003, 2006) only to find dimensionless capillary pressures rather than to extract a pore network from the image.

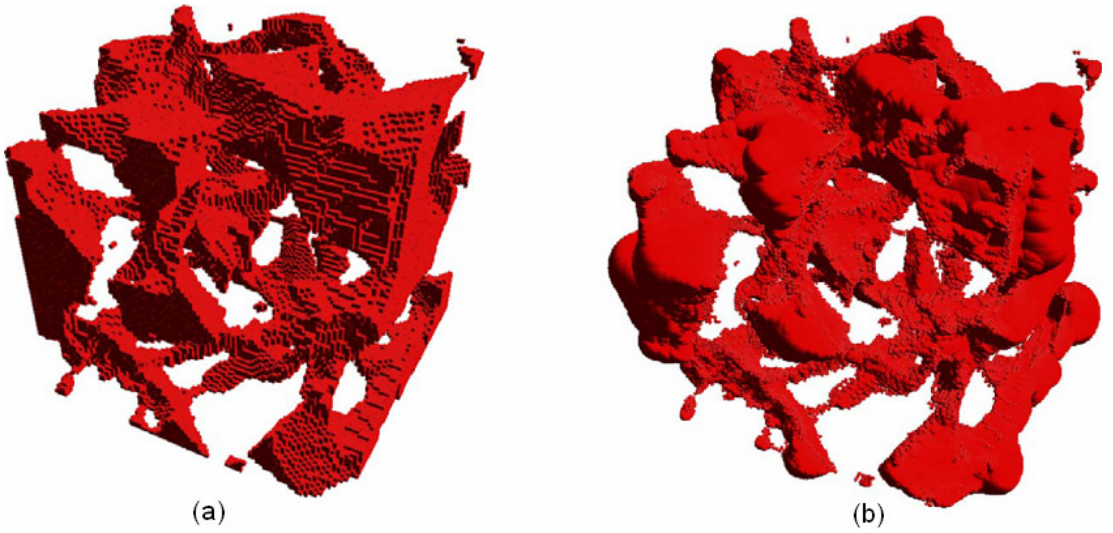

Figure 2.21. (a) is the pore space image of a Fontainebleau sandstone with a porosity of 17%; (b) is maximal balls in the pore space. The dimensionless sizes of the images are 200 × 200 × 200 counted in voxels. (Silin and Patzek, 2006).

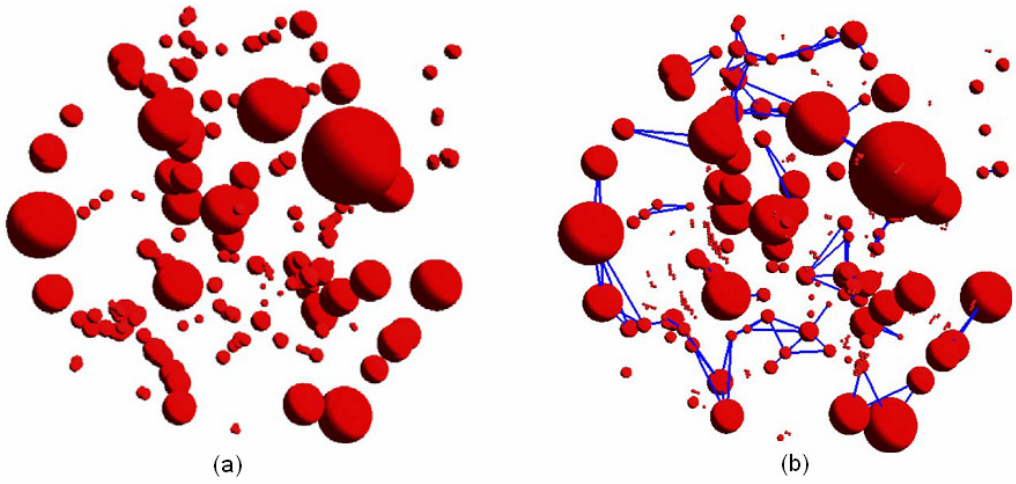

Figure 2.22. (a) shows master balls (pores) found in Fig. 2.21 (a); (b) is the pores and their connectivity of the pore space. (Silin and Patzek, 2006)

Al-Kharusi and Blunt (2007) extended this method to study the pore space of sandstone and carbonate samples. Starting from the same point of finding maximal balls at each voxel, Al-Kharusi and Blunt developed a more comprehensive set of criteria to determine the maximal ball hierarchy. In Silin et al.'s work, only two types of relationship are defined, *masters* and *slaves*, which is the bigger and smaller balls respectively compared to their neighbors. Al-Kharusi and Blunt added a new relationship, the *cluster* to accommodate the adjacent maximal balls at the same size, Fig. 2.23. This resolved the problems of ambiguity caused by the identical balls that are not trivial after transforming the pore space to maximal balls from voxels. Pore networks are extracted from the pore space images and used for single- and multi-phase simulations. Absolute permeability was successfully predicted. However, their work requires tremendous memory usage and hence was limited to relatively small systems containing fewer than a thousand pores.

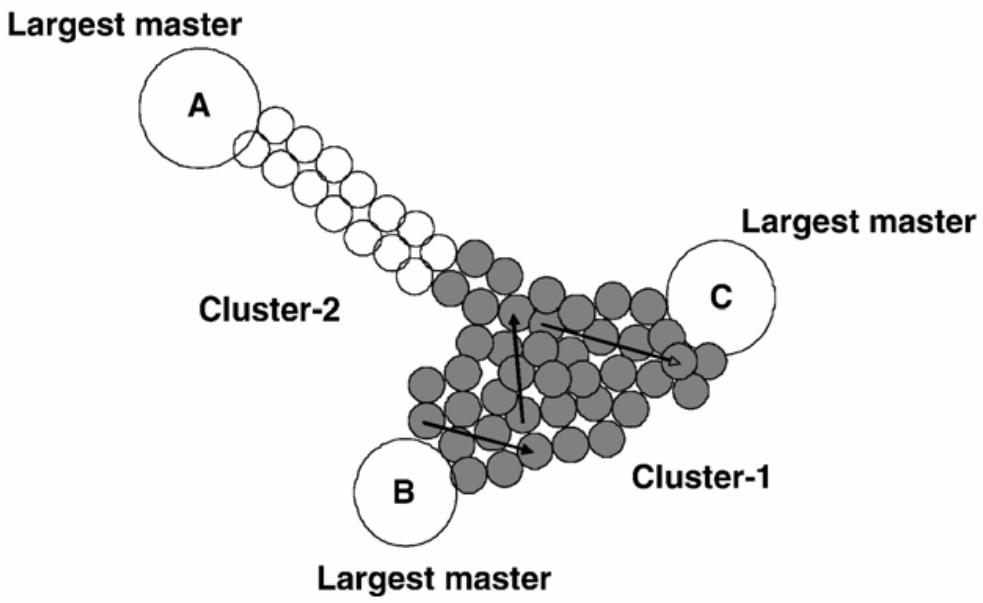

Figure 2.23. Clusters are defined to fuse the identical spheres in the pore space. (Al-Kharusi and Blunt, 2007).

In this study, we will refine Silin et al's method of maximal balls and develop an efficient algorithm to extract pore networks. The major differences of this work from Silin et al.'s and Al-Kharusi and Blunt's include the following:

1. The method to construct the maximal balls.

In stead of inflating a digital sphere by one voxel increment in radius, we developed a two-step searching algorithm to find the nearest interface of void and solid to define a ball.

2. The hierarchical arrangement of maximal balls.

To avoid the confusion caused by the identical maximal balls and the misjudgment of individual balls for their strategic positions during the analysis, we don not consider *masters*, *slaves* and *clusters* but invented a *clustering process* to define pores and throats by affiliating the maximal balls into family trees according to their size and rank (the sequence being connected to earlier defined branches on the family trees). The concept of a *cluster* is not exactly same in this PhD thesis from Al-Kharusi and Blunt's work, which in this work is defined in Section 4.1.2. The ancestor of each family tree defines the pore and the common child defines the throats (or part of the throat if the two trees joint at a clump). Instead of comparing each pair of neighboring balls, we start from the largest maximal ball in the image as a pore and go the next biggest one. Thus the ancestors are always found before visiting their children with a smaller size. This process is in conformity to the pore recognition by human intuition, by which the main features of the pore space are recognized before noticing the puny details. The description of the algorithm is given in chapter 4.

3 Micro-CT imaging

A series of measurements of the structures of various porous rocks has been carried out during this PhD project using X-ray micro-tomography (also called micro-CT, MCT, XMT or μCT). As a non-destructive technique, micro-CT provides a direct way to image the pore space as a volumetric (3D) representation of structures. A micro-CT scanner uses X-rays to penetrate from different view points a 3D object and create attenuated projection profile, also known as shadow images that are later reconstructed using a filtered back projection algorithm (Kak and Slaney, 2001) to form the interior volume of the sample as a stack of 2D slices with a resolution of a few microns without destroying the original model.

Micro-CT allows a comprehensive insight of rock structure that is used to extract the pore network which preserves the topology of pore space and parameterizes the geometrical features of the prototype. In this chapter, the working principles of micro-CT, the spatial resolution, imaging and image processing will be discussed and micro-CT images will be shown in the chapter.

3.1 Apparatus and working principles

Two different micro-CT systems have been used for the imaging work in this study. One is the laboratory micro-CT, also called desktop micro-CT; the other is Synchrotron X-ray micro-tomography.

The desktop micro-CT scanner 'v|tome|x' was used in the XMT lab at the Department of Materials, Imperial College London, Fig. 3.1. v|tome|x is an high-resolution μCT system manufactured by Phoenix|x-ray in Germany and equipped with

an image acquisition and processing software, SIXTOS. The X-ray tube of this nano-focus system has a focal spot size less than 1 µm. However, in practice, we use 1.5 µm focal spot size to obtain sufficient photon flux passing through the rock samples and responsed by the detector. The 16-bit digital X-ray detector of this system is a flat panel detector, Perkin Elmer RID 512-400 based on an 8" amorphous silicon sensor with a pixel size of 400µm and a field of view of 512 × 512 pixels.

Figure 3.1. Micro-CT scanner, Phoenix v|tome|x, at Imperial College.

The synchrotron micro-CT scanner is at the beamline of SYnchrotron Radiation for MEdical Physics (SYRMEP) at Elettra Synchrotron, Trieste, Italy, Fig. 3.2. The X-ray is generated by the synchrotron and the detector is a 2048×2024 pixel CCD detector with a pixel size 14µm and dynamic range 16-bit.

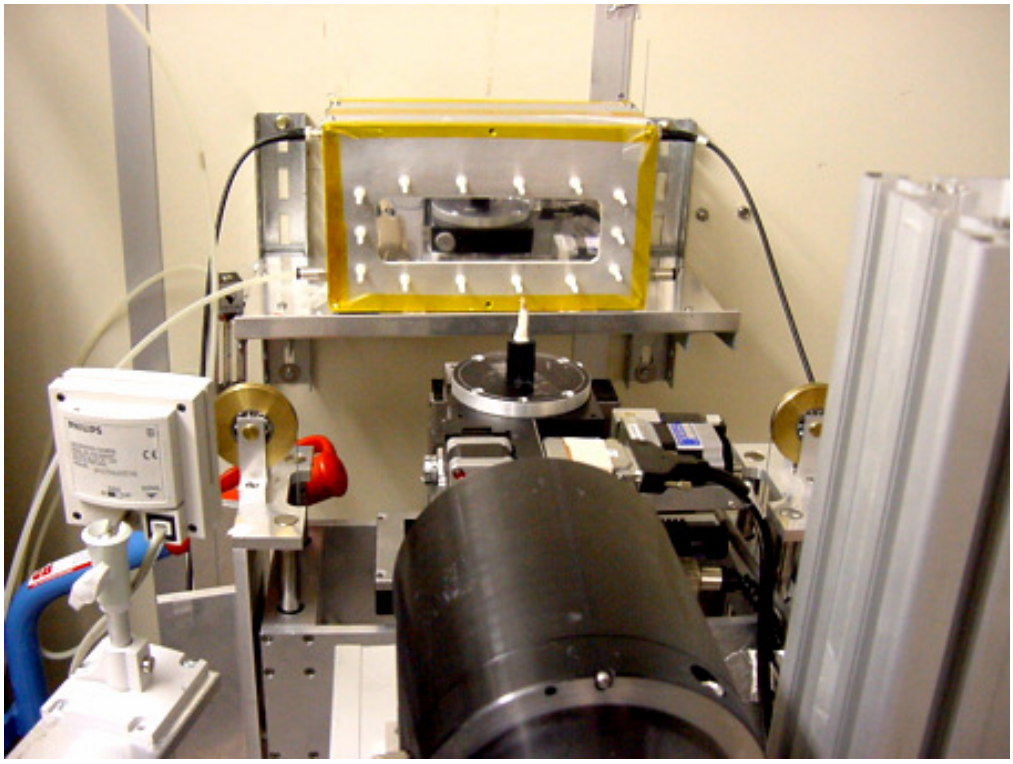

Figure 3.2. X-ray microtomography at SYRMEP at Elettra Synchrotron, Trieste, Italy.

The fundamental differences of the two systems are the X-ray sources. Nevertheless, they share the same conceptual working principles as computed tomography. In this section, the basic setup, X-ray source, X-ray attenuation and the reconstruction will be described.

3.1.1 Basic setup

Both the two systems, Figs. 3.3, 3.4, have similar components in their basic setups, the X-ray source, a manipulator sample stage that can position and rotate the sample with high precision and a detector to receive the attenuated profiles as raw information for reconstruction. Besides, computers are used to control the X-ray source and the scanning parameters as well as to perform the reconstruction software to transform the radiographic images (attenuation profiles, Fig. 3.5) to the interior volumetric view of the sample.

Figs. 3.3 and 3.4 illustrate the setups of the desktop micro-CT scanner at Imperial College and the Synchrotron micro-CT in Elettra respectively. The desktop scanner uses an industrial tube to generate a bundle of X-rays as a cone beam. The sample has to be imaged at least every half degree and rotated 360 degrees during the scan for a comprehensive set of radiographic profiles for the reconstruction. The Synchrotron produces a parallel beam by which only 180 degrees are needed for the rotation, for the beam symmetry gives mirror information from opposite positions.

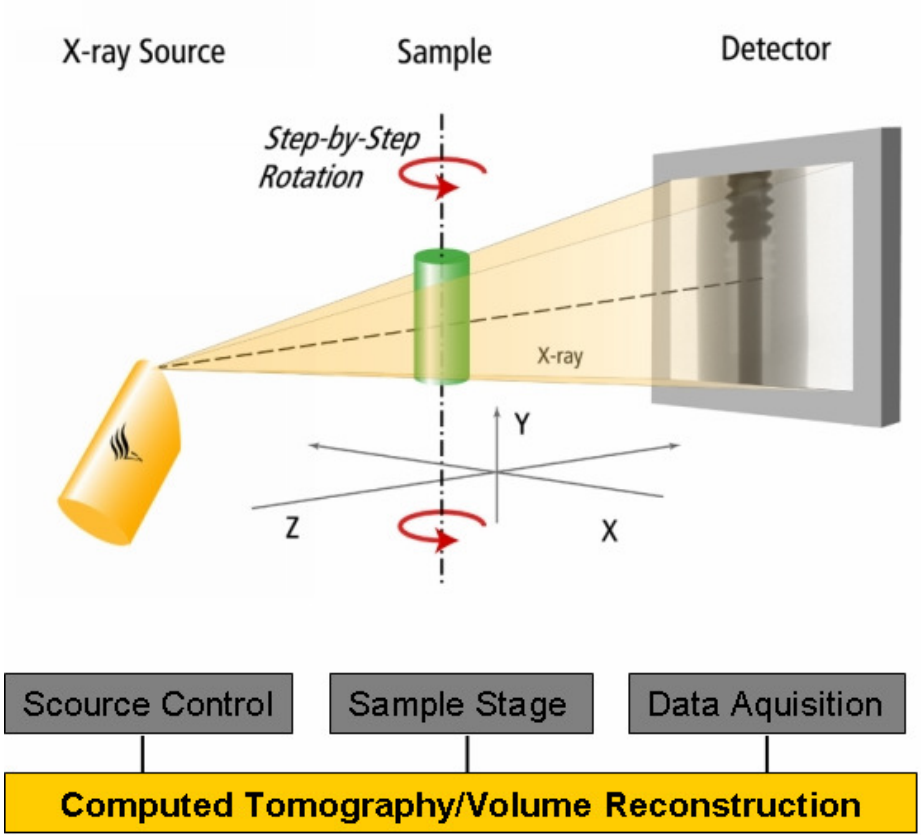

Figure 3.3. The schematic picture of basic components of a micro-CT scanner from the manual of the v|tome|x system. The system uses X-rays to penetrate sample that is rotated during the scanning and project the X-ray attenuation profiles on the detector from different view points. These attenuation profiles are used for reconstructing 3D image of the interior volume of the sample.

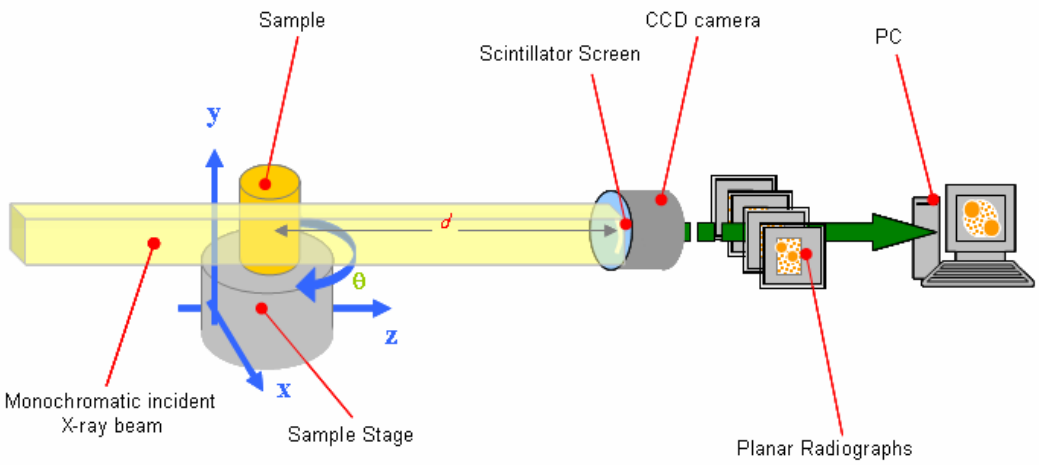

Figure 3.4. The basic setup of Synchrotron X-ray source micro-CT (http://www.ts.infn.it/physics/experiments/syrma/SYRMEP/Home_syrmep.html).

3.1.2 X-ray attenuation

During scanning, the X-ray radiation from the source penetrates and is attenuated by the specimen depending on the material composition, density and thickness along the beam direction. The attenuation of X-rays through a homogenous material can be calculated using Beer's law (Kak and Slaney, 2001),

$$I = I_0 e^{-\mu x} \tag{3.1}$$

where I_0 is the initial X-ray intensity; I/I_0 is the attenuation of X-ray intensity per unit length of a given material; μ is the linear attenuation coefficient for the material being scanned (units: 1/length); and x is the length of the X-ray path through the material.

The equation for composite materials is

$$I = I_0 e^{-\sum_i \mu_i x_i} \tag{3.2}$$

where the increment i reflects an individual material with attenuation coefficient μ_i over a linear extent x_i. In this study, the most distinguishable materials are air (or the mixture of Epoxy and Struers Caldofix, see Section 3.2) in the void space and the minerals as solid phases.

The attenuated X-ray intensities (radiography) are received by the detector and transferred to the computer where the volume is reconstructed using the 2D projections. Fig. 3.5 gives an example of an attenuation profile.

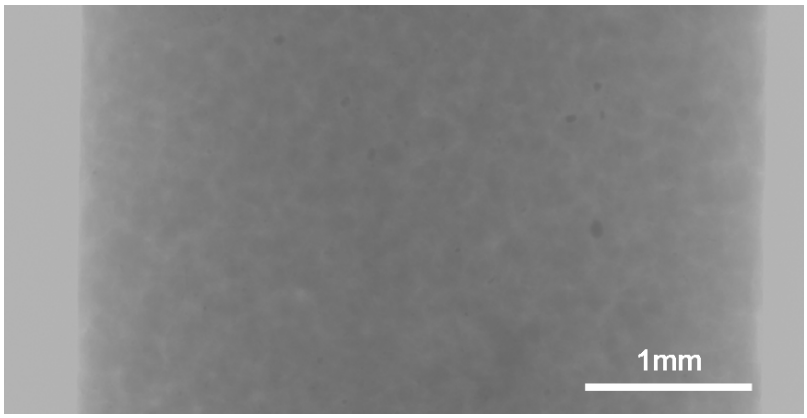

Figure 3.5. The projection profile of attenuated X-ray radiation through a sandstone received by the detector.

3.1.3 X-ray sources

The tabletop scanner in the laboratory uses an industrial X-ray generation tube. The electrons emitted from a cathode by thermionic emission are accelerated by high voltage in order to collide with the target metal anode. During the impinging, X-ray photons are emitted due to two atomic processes: Bremsstrahlung and characteristic photon emission.

Bremsstrahlung (German, "braking radiation" or "deceleration radiation") generates the continuous spectrum of X-ray photons, whose maximum energy is equivalent to the kinetic energy of the incident electrons decelerated at the anode.

Characteristic photon emission generates certain spectral lines depending on the target anode element used. When an incident electron interacts with an atom, it may impart sufficient energy to an electron at lower energy shell and knock it out of the original energy status. An electron from a higher energy shell drops into the hole and emits a characteristic photon depending on the energy level difference in this process.

X-rays can also be found in Synchrotron radiation which typically includes radio waves infrared light, visible light, ultraviolet light, and X-rays. Synchrotrons are now mostly used for producing monochromatic high intensity X-ray beams. The relativistic electrons (i.e., moving near the speed of light) are circulated in the storage ring after being accelerated by a synchrotron. X-ray radiation is produced by a bending magnet or an undulator and projected at a tangent to the electron storage ring and captured by a beamline. The crystal monochromator (in Elettra, a double-crystal Si (111)) is used to select the bandwidth of the energy giving a monochromatic X-ray beam to produce high quality images.

The laboratory X-ray source has a number of limitations compared to Synchrotron X-rays. First, the energy of the lab white (polychromatic) X-ray photons cover a range of wavelengths in the spectrum, so it introduces a relatively high noise level to the reconstructed image due to the non-linear attenuation of the polychromatic beam. When taking into account that the attenuation coefficient is a function of X-ray Energy E, equation 3.2 becomes

$$I = \int I(E)^{\sum(-\mu_i(E)x_i)} dE \tag{3.3}$$

In practice, most of the reconstruction methods for laboratory micro-CT use a single estimated energy rather than the precise measurements of the energy spectrum. Hence the image quality of tabletop scanner with a range of X-ray frequencies is evidently poorer compared to Synchrotron micro-tomography with monochramtic X-ray radiation – see Fig. 3.6.

Second, the high resolution imaging requires a beam focal spot size smaller than the voxel size. However, the reduced focal spot size of desktop micro-CT decreases the number of emitted photons, which again increases the noise level and decreases the flux of X-ray photons. On the contrary, the high intensity of synchrotron sources is advantageous to produce a high X-ray photon flux for rapid data accumulation and improved detail levels.

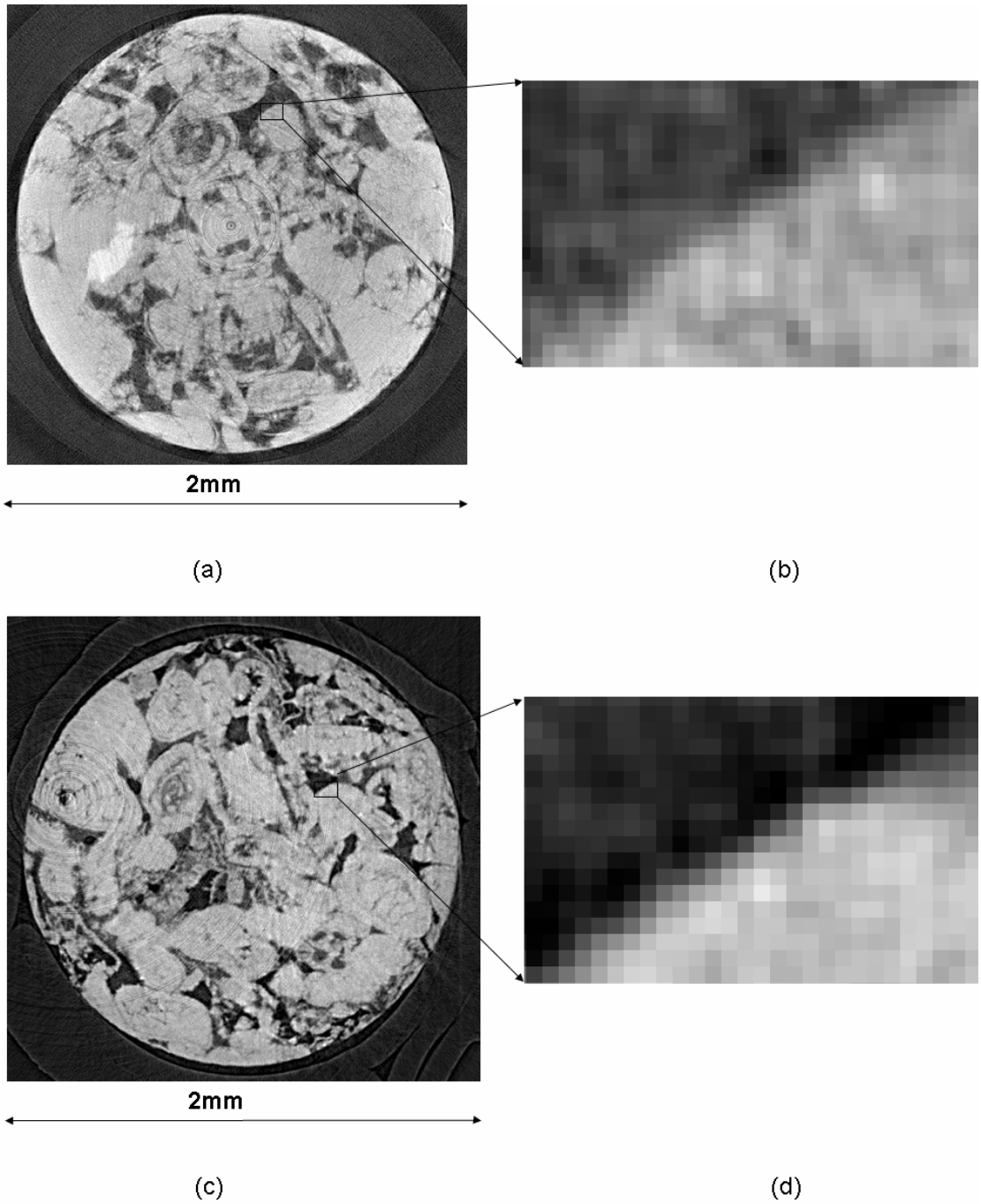

Figure 3.6. (a) and (c) are cross-sections of micro-CT images of a limestone sample imaged at the desktop μCT and Synchrotron μCT respectively. (b) and (d) are the highlighted details of similar patterns from the two images.

It is evident that the synchrotron μCT provides higher quality images in terms of signal-to-noise ratio compared to the desktop μCT. The boundaries in Fig. 3.6 are obvious and high purity of the void and solid is observed in the Synchrotron image.

3.1.4 3D reconstruction

The attenuation profiles are continuously measured and collected from different angles of view. Each view represents a rotational interval equal to 360 degrees (or 180 degrees with a parallel beam) divided by the total number of views.

Reconstruction is a mathematical process of converting attenuation profiles into a volume as serial two-dimensional slice images. The most widespread reconstruction technique is called filtered back-projection. For each projection, an intensity map is recorded in the XY detector plane. The projections are submitted to filtering procedures. In the filtration process, horizontal projection profiles are ramp-filtered in the Fourier domain after zero padding. In the back-projection process, an image volume is reconstructed by back-projecting filtered data along X-ray paths with appropriate weights. The weights are the beam length considering the different paths of the rays through the object.

3.1.5 Spatial resolution

The eventual purpose from acquiring a pore space image is to extract a topologically equivalent network where the pore space is replaced by pores and throats. Therefore, two aims need to be achieved by the imaging work: 1. to identify the boundary of the solid phase and void phase; 2. to recognize the smallest crevices. The most important achievable parameter to accomplish the aims is the spatial resolution since the contrast is relatively good between the void and solid for porous rocks.

The image spatial resolution is the ability to distinguish high contrast phases (void and solid, in this study) that are close to each other. To simplify the problem and make easy comprehension, if it is not specified in the thesis, we use the term

resolution for both the voxel side length and the real spatial resolution that is the minimum distance that two objects are separable in the image.

In general, we expect to obtain the highest possible resolution to image sedimentary rocks. In practice, we require the resolution of 15~20 microns for coarse sandstone, 5~15 microns for unconsolidated sandstone and <5 microns for consolidated sandstone and most carbonates. An even finer resolution is required for many carbonates since sub-micron pore throats have a significant impact on transport. Examples are given in Figs. 3.7-3.9.

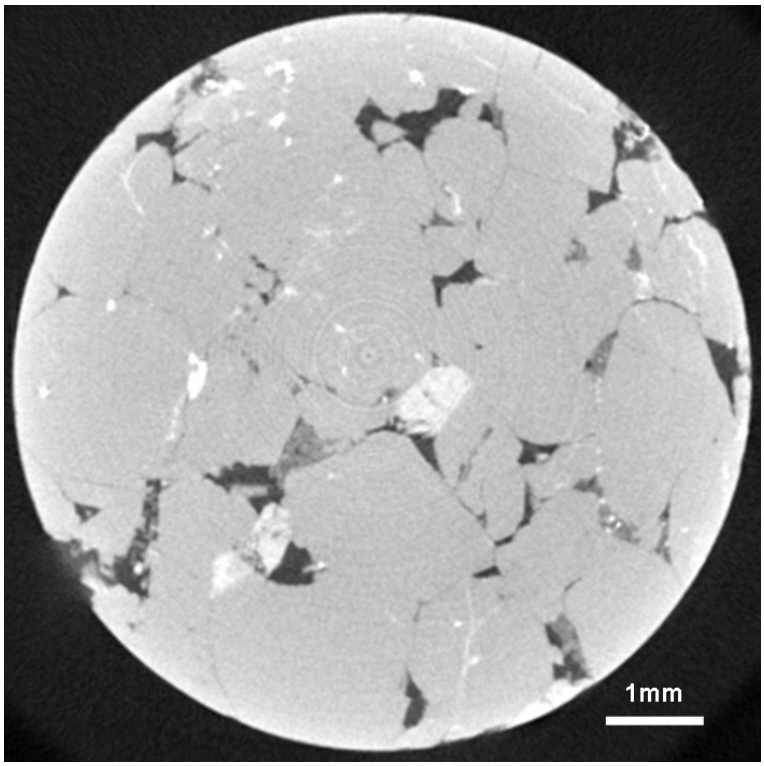

Figure 3.7. An example of coarse sandstone image with a resolution of 19 μm.

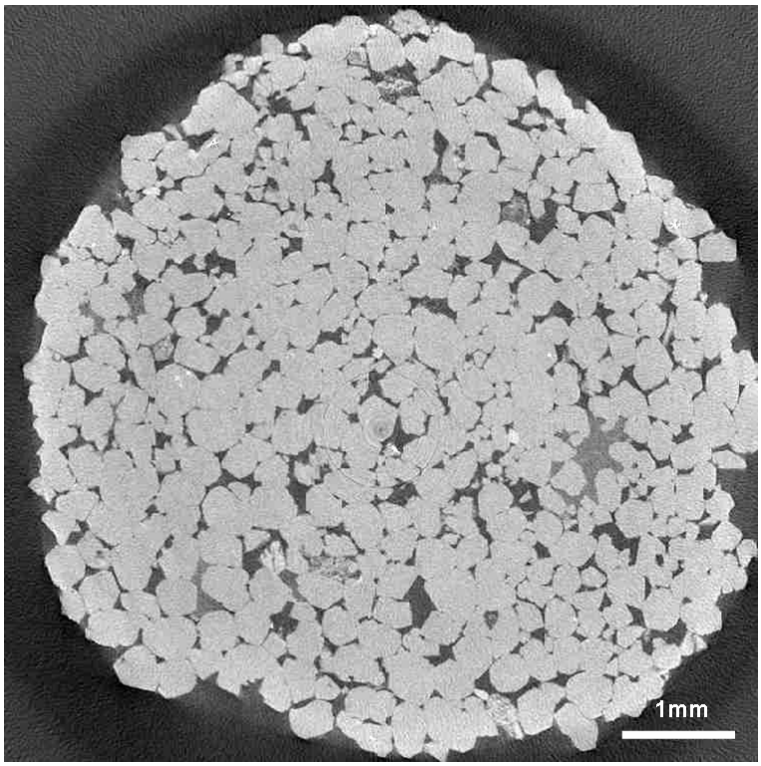

Figure 3.8. An example of unconsolidated sand image with a resolution of 8 μm.

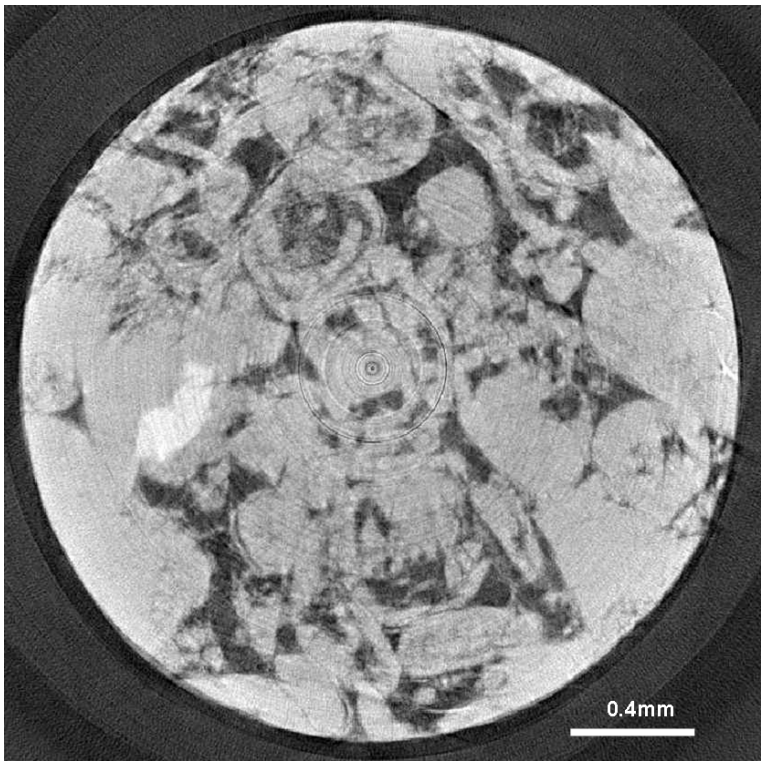

Figure 3.9. An example of limestone image with a resolution of 2.9 μm.

The desktop scanners give magnification depending on the geometry of the cone beam. It is assumed that the source is a point, which projects the sample onto the large detector. Therefore the sample should be placed very close to the focal spot of X-ray source and far from the detector for higher magnification factors. In the Phoenix v|tome|x system, the projection image size is equal to the number of sensors on detector, 512×512, which can be doubled when using virtual detector mode which moves the detector horizontally acting as 1024×512. Since during the scanning the sample has to be thoroughly observed in the field of view (FOV), the full width of the sample at any angle of view will be projected onto the detector; thus the resolution can be estimated:

$$resolution \approx \frac{D}{L} \tag{3.4}$$

where D is the diameter of sample to be scanned; and L is the number of pixels along the long edge of detector. In practice, a margin effect must be considered as the edges of specimen must be seen in the projection profile ensuring that the sample is in the FOV. When 75% of the detector is covered by the sample projection, the approximate resolution of this v|tome|x system can be found using Fig. 3.10.

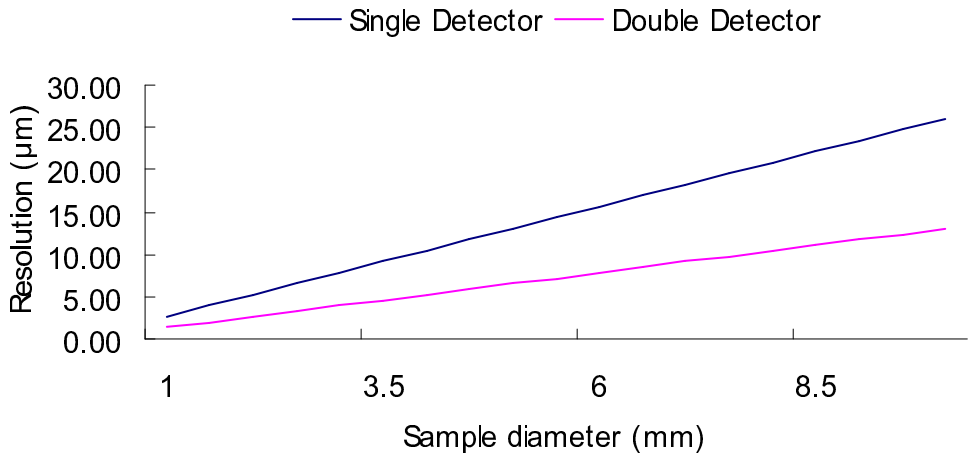

Figure 3.10. The estimated relationship of resolution and sample size. (data are provided by Prof. P. D. Lee.)

In Synchrotron micro-CT, since the beam is parallel giving no geometrical magnification itself; the resolution is dependent on the pixel size of the detector. In SYRMED the pixel length of the CCD used in this project is 14 μm. Nevertheless, when operated with a tapered fibre optic device between the sample and detector, the system magnification provides an improved image voxel size of 3.85 μm.

3.2 Sample preparation

Considering both the factors of detector coverage during the sample rotation and the relation between sample size and resolution, the mounted specimen must be small and well shaped to obtain the maximum use of the detector to acquire the highest possible resolution. We drill small cylinders out of larger core samples and align them vertically onto the sample stage for best resolution acquisition.

To maintain the integrity of some unconsolidated sandstones during the physically destructive drilling to obtain small size samples from the core plug, we impregnate the samples with a mixed resin of Epoxy resin and Struers Caldofix which is typical for embedding of materialographic specimens and vacuum the pore space to introduce the resin. The mould containing the mixture and sample is kept at atmospheric pressure at 60ºC for 8 hours for the core plug to be cured. After this pre-processing, the pore space is embraced by hardened resins with very low attenuation coefficient that can be easily distinguished from the solid phase in the image.

3.3 Imaging

A brief summary of the parameters undertaken to obtain raw X-ray attenuation

profiles using Phoenix v|tome|x system provided by the XMT lab at Imperial is given below. The detailed procedures for synchrotron micro-CT scanning can be found on Elettra website (http://www.ts.infn.it/physics/experiments/syrma/SYRMEP/Home_ syrmep.html).

1. Sample positioning

The specimen must be positioned using the control panel of the system so that the specimen fills the field of view as fully as possible while retaining a band of clear air to the left and right of the specimen *throughout the rotation*. Quick scans are taken for every 45^{o} to make sure the edges of the specimen is more than 20-25 pixels from the edge of the detector at each view. To obtain the highest possible resolution, the sample has to be regulated and aligned as well as possible.

2. Sensor Calibration

First, the energy of X-ray has to be decided by tuning the voltage. A value of 90kV is sufficient to penetrate the minerals and makes good contrast between void and solid. The resultant current is around 100μA.

Then, the correction images have to be acquired to remove inhomogeneity in the background images i.e. images with only air between source and detector. Two such images are required, one with the X-rays on and one with the X-rays off (also called flat and dark field in Synchrotron micro-CT). The flat field is necessary to account for the non-uniformities in the X-ray beam and the non-uniform response of the detector.

3. Operational parameters

Parameters such as the number of images to average for one projection image,

the metal thickness to reduce the beam hardening effects (for desktop μCT which uses polychromatic beam) etc. are defined for the scanning operation. One important factor affecting the image quality is the number of projections which should be similar or greater to the width of the object in pixel.

4. Reconstruction

The software SIXTOS is used in the XMT lab at Imperial College London for reconstruction. A calibration factor (also called 'Dejust' or 'Djust') needs to be found in this step by visual inspection to compensate for any difference between the center of the specimen and the center of the reconstruction.

3.4 Images

3.4.1 Pore space images

During this project, rock samples provided by Saudi Aramco, Shell, Total and Imperial College have been imaged using the desktop μCT scanner at Imperial College and the Synchrotron μCT scanner at SYRMEP, Elettra. Table 3.1 shows 18 cross-sections of micro-CT images of 13 samples that have been selected to validate our algorithm. The images with a name ending up with '–S ' were imaged by the Synchrotron μCT scanner at Elettra. Sample names, sizes of datasets and image resolutions are given in Table 3.1. Pore networks are extracted from the images whose petrophysical properties were computed at Numerical Rocks AS, Norway by Øren and Bakke (2002, 2003) on the voxelized images; and the results calculated from pore network predictions and voxel grids are compared in Chapter 7.

Table 3.1. Cross-sections of micro-CT images of samples. –S indicates samples imaged using the Sychrotron; all other images used a desktop XMT system.

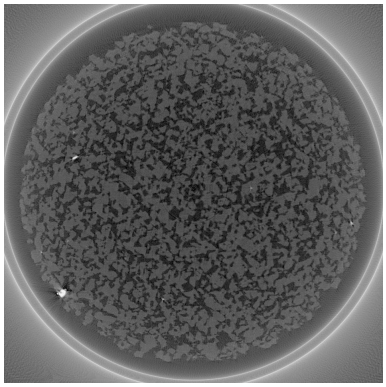

Synthetic A1

Voxels: 584×585×444

Resolution: 4.747 µm

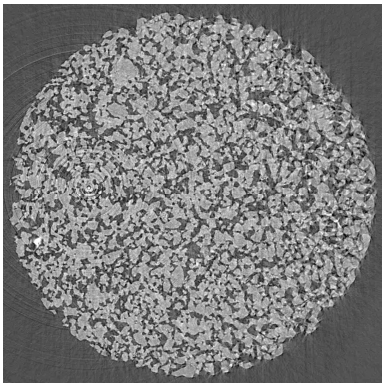

Synthetic A1-S

Voxels: 800×775×400

Resolution: 3.85 µm

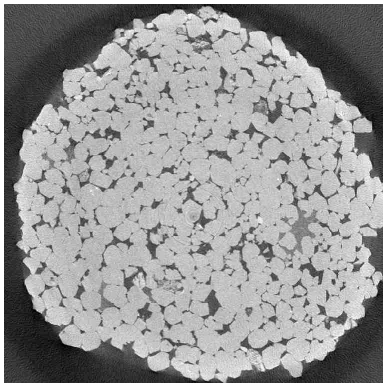

Sandstone S1

Voxels: 850×850×400

Resolution: 8.638 µm

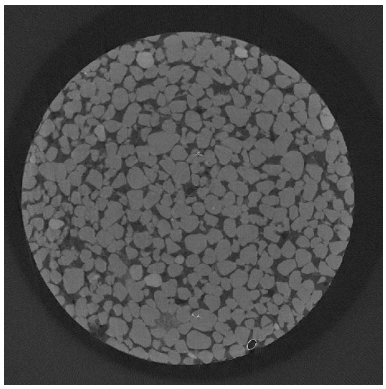

Sandstone S2

Voxels: 950×950×300

Resolution: 4.956 µm

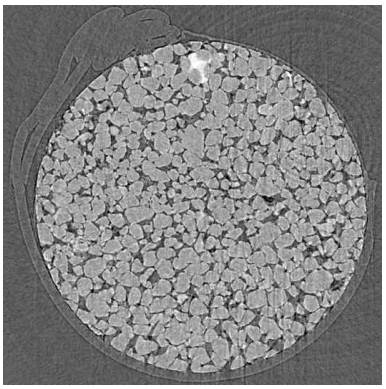

Sandstone S2-S

Voxels: 530×530×285

Resolution: 3.85 µm

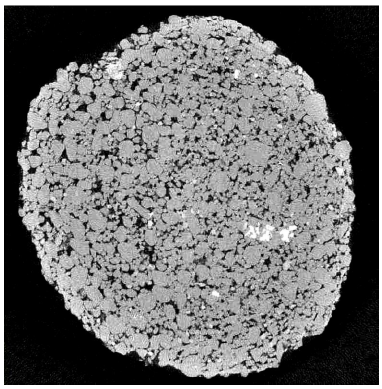

Sandstone S3

Voxels: 875×900×400

Resolution: 9.1 µm

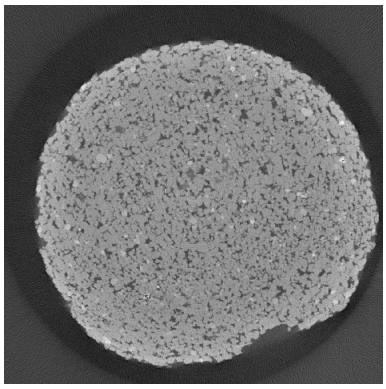

Sandstone S4

Voxels: 550×550×512

Resolution: 8.960 µm

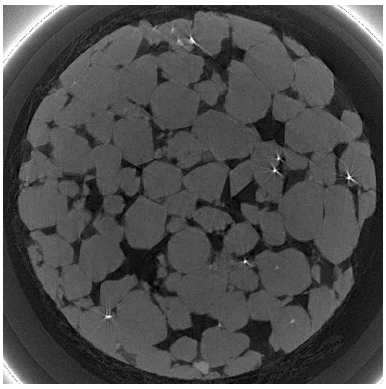

Sandstone S5

Voxels: 775×750×400

Resolution: 3.997 µm

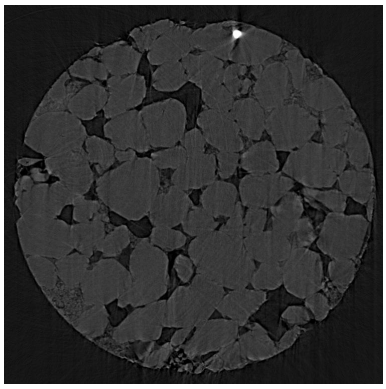

Sandstone S5-S

Voxels: 796×796×800

Resolution: 3.85 µm

(Table continued)

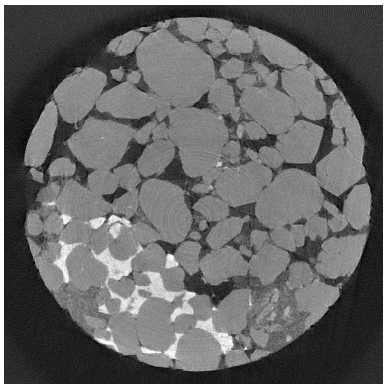

Sandstone S6

Voxels: 875×875×400

Resolution: 5.1 µm

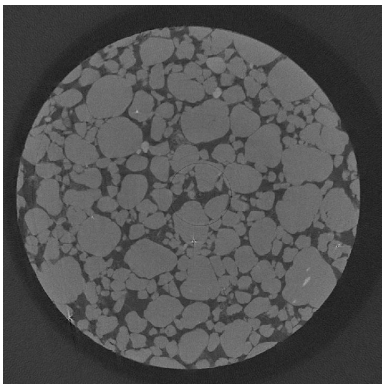

Sandstone S7

Voxels: 950×950×350

Resolution: 4.803 µm

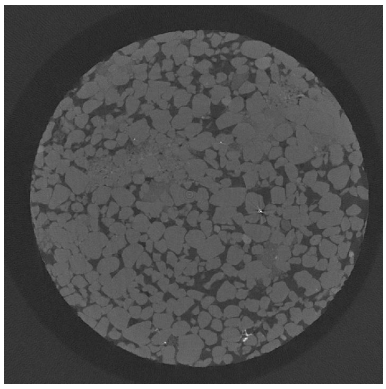

Sandstone S8

Voxels: 950×950×350

Resolution: 4.892 µm

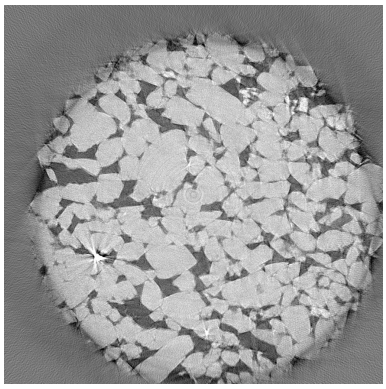

Sandstone S9

Voxels: 512×512×512

Resolution: 3.40 µm

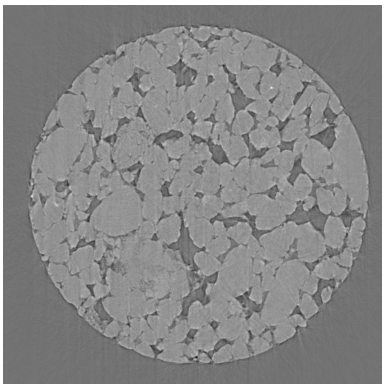

Sandstone S9-S

Voxels: 742×742×500

Resolution: 3.85 µm

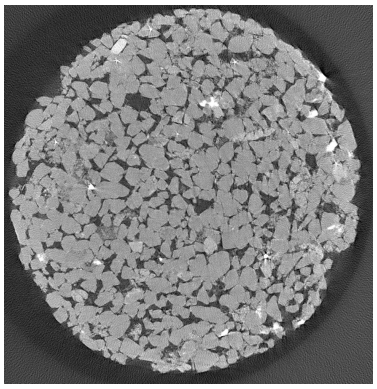

Sandstone Berea

Voxels: 950×950×350

Resolution: 5.345 µm

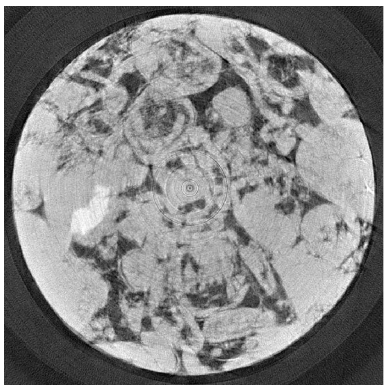

Carbonate C1

Voxels: 750×750×400

Resolution: 2.857 µm

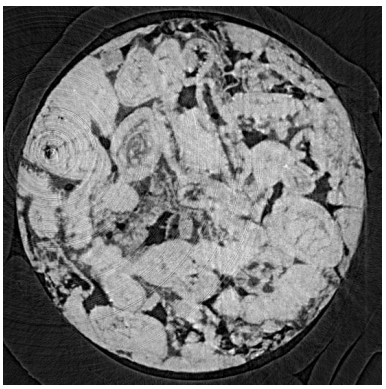

Carbonate C1-S

Voxels: 569×569×400

Resolution: 3.85 µm

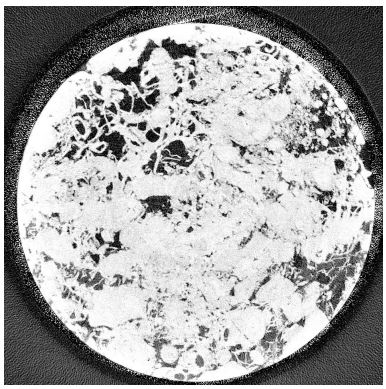

Carbonate C2

Voxels: 600×600×512

Resolution: 5.345 µm

These micro-CT images are part of our image library which will accommodate a wide range of sandstone and carbonate μCT images in the future. This work has two aims. One is to carry on extensive study on pore space images and the derived networks to work out a comprehensive set of criteria to decide the definitive scanning parameters such as sample size, resolution, representative elementary volume, the proper filtering and thresholding values for the image processing etc. The other object is that after the completion of this library, to predict the transport properties for new samples, we only need to find the samples in the library with similar structures and do some minor change to the network parameters, such as pore sizes, throat sizes, aspect ratio, porosity etc. (see examples in Valvatne and Blunt, 2004) for predictions.

3.4.2 Trapped oil images – two phase flow visualization

To extend the application of micro-CT in pore-scale modeling, a preliminary study on the visualization of two-phase flow in porous media was carried out in cooperated with Stefano Favretto and Prof. Gianni Schena at University of Trieste using the SYRMEP μCT system. The experimental setup illustrated in Fig. 3.11 was equipped at the SYRMEP lab allowing multi-phase flow observed in-situ in the porous sample during the scanning.

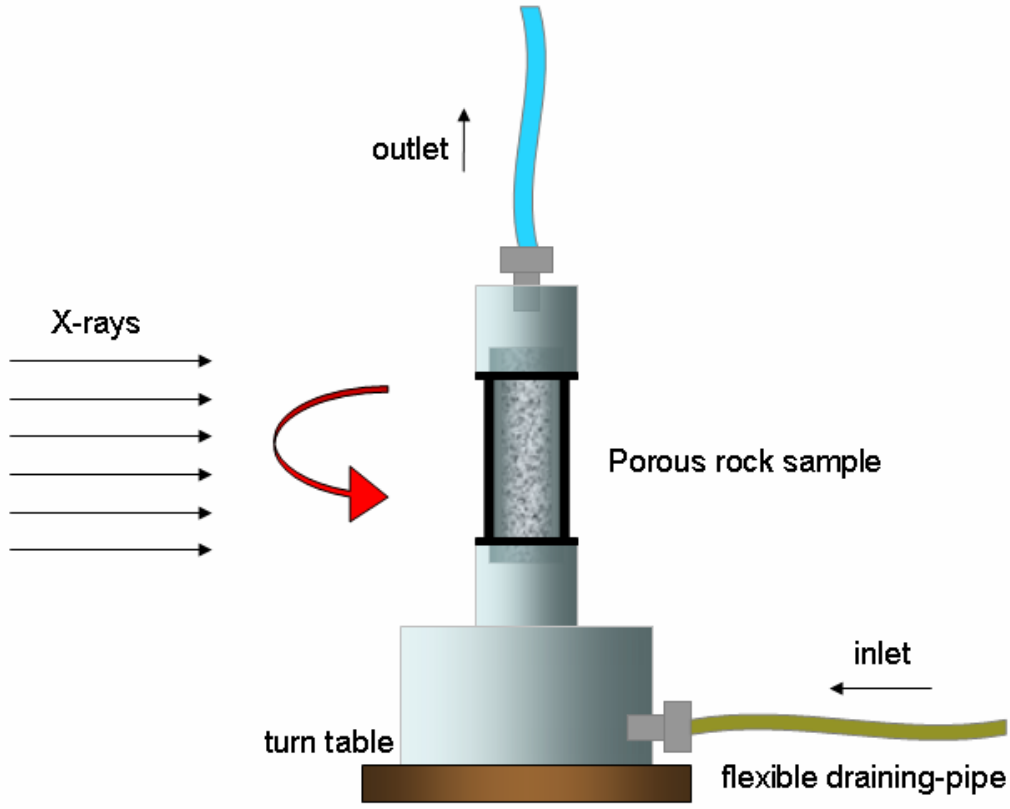

Figure 3.11. Schematic picture of the experiment for two-phase flow.

A high porosity (23.52%) and permeable (2200mD) rock sample was chosen from the Petrophysics Lab at Imperial College London for the experiment. It is pink sandstone called Doddington, from Doddington Hill quarry in Northumberland, and is a Carboniferous fell sandstone with fine-medium grains mainly quartz (98%) and minor feldspar (2%) (Al-Harthy, 1999).

To distinguish the wetting phase (brine) from the non-wetting phase (decane) by judging the gray scale of the micro-CT image, a doping agent, iodide is added to the brine (KI solution with a concentration of 13% in weight), which endues sufficient contrast in gray scales to rock minerals and oil phase due to its high absorption to X-rays. Figs. 3.12 and 3.13 show the trapped oil by brine in the pore space after water flooding.

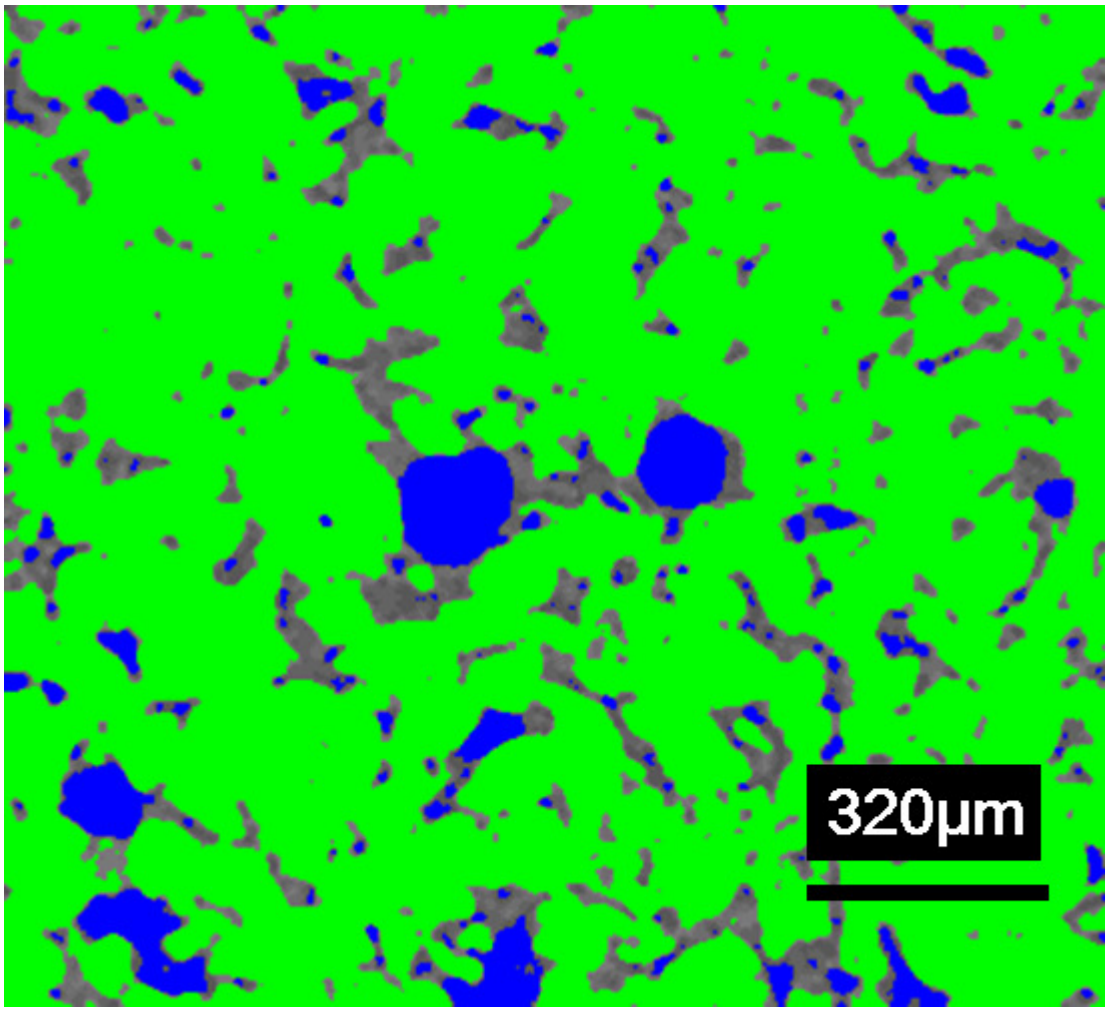

Figure 3.12. This cross-sectional picture shows the trapped oil after the water flooding. The trapped oil is in blue and the rock matrix is in green. The gray is water phase doped by KI. The non-wetting phase is trapped in the centers of big pores while the water occupies the corners and small pores.

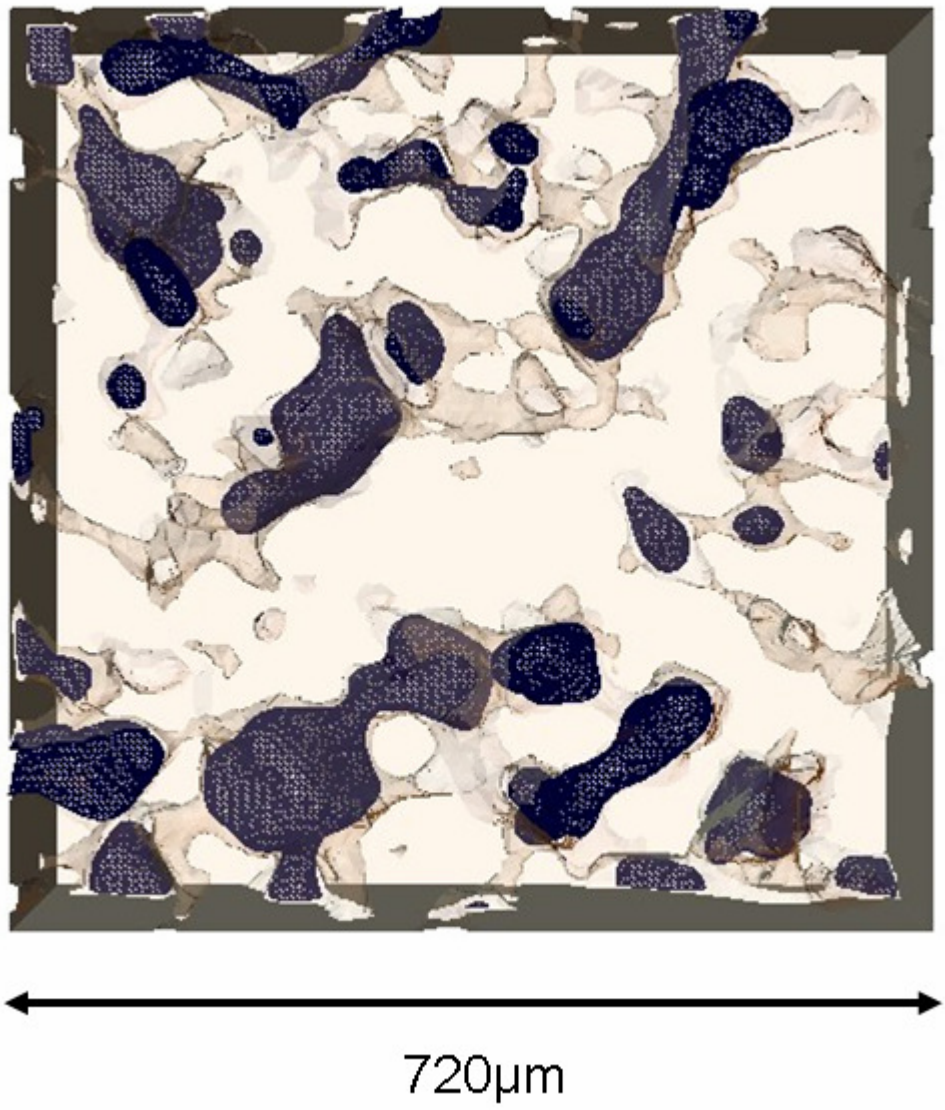

Figure 3.13. A 3D view of trapped oil in the pore space after water flooding. The blue gridded objects are the oil drops surrounded by the water phase (semi-transparent) in the pore space.

This example shows that micro-CT technology can visualize the phase configuration in porous media and has the potential to study the pore-scale physics of multi-phase flow based on the micro-scale images. However, this thesis will be mainly concerned with network extraction and so we will only consider grain/void images from now on.

3.5 Post-processing

Mirco-CT outputs a 3D image which is a 3D array of gray scales. In order to obtain the pore space to quantitatively define the pore geometry and topology, the gray scales must be segmented into black and white representing the void and solid. Filters must be applied to the images to enhance the contrast of different materials and remove the noise.

3.5.1 Median filter

As a cornerstone of modern image processing, the median filter is used extensively in smoothing and to remove noise. The idea of a median filter is to replace the gray scale value of a voxel by the median value of the nearest 26 surrounding cells. We apply median filter to the gray scales to despeckle the image without introducing new gray values into the scale.

In Fig. 3.14, the effects of median filtering are demonstrated by applying to a sandstone image. The image resolution is 5.0 μm. (a) is a cross section of the original micro-CT image of the sample. After segmentation, the noises in the raw image become small grain voxels in the void or the holes in grains shown in (c). (b) is the effects of being smoothed by using a median filter and (d) is the binarized black-and-white image. Comparing (c) and (d), we find the median filter preserves the integrity of the grains and the pore space.

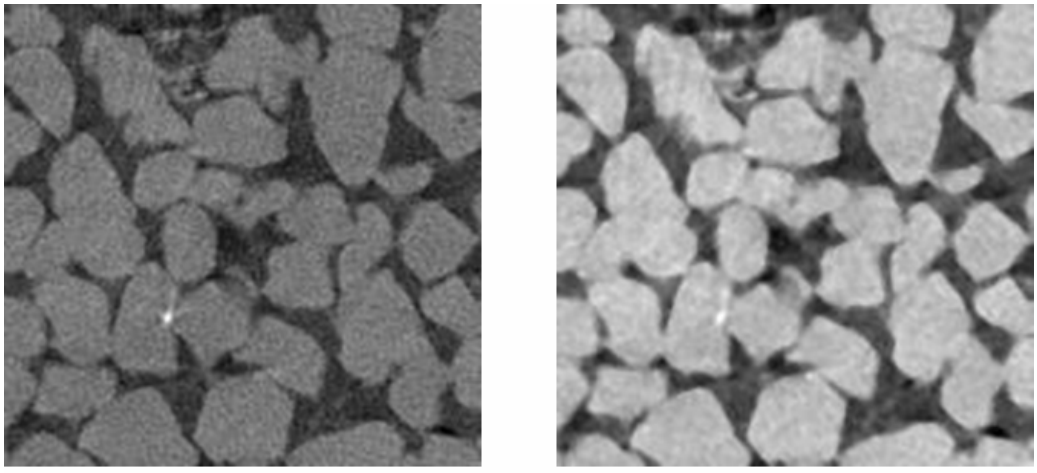

(a) (b)

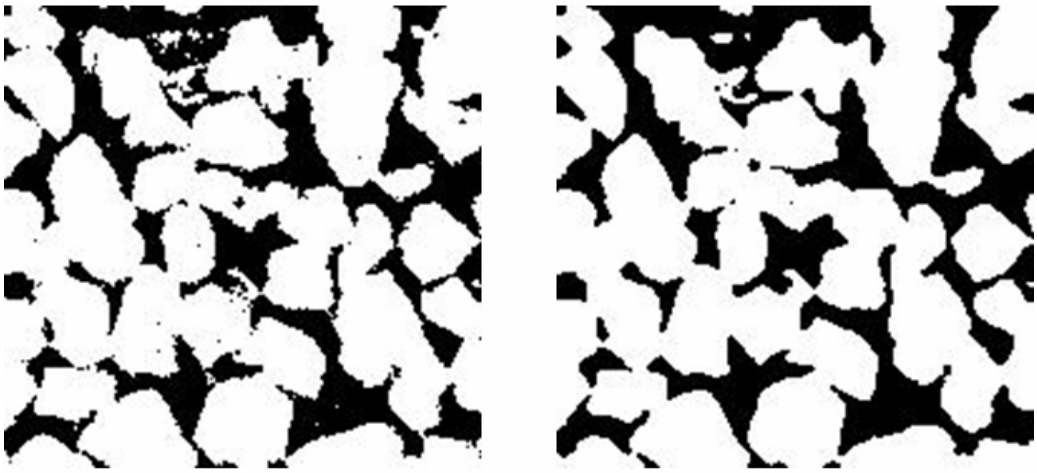

(c) (d)

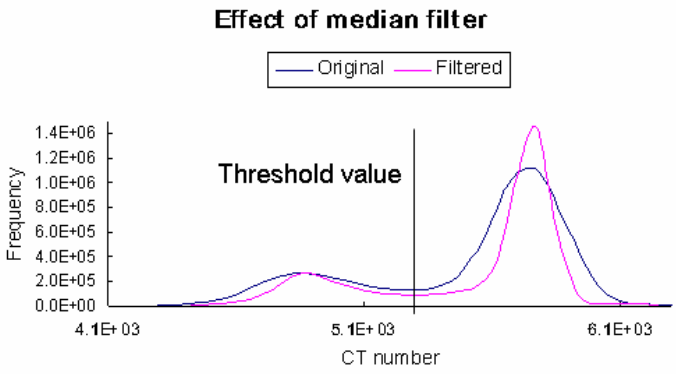

(e)

Figure 3.14. (a) A cross section of the raw image of a sandstone; (b) is the median filtered image of (a); (c) is the segmented image of (a); (d) is the segmented image of (b). The side length of the four cross section images is 0.75mm; (e) shows the effect of median filtering on the gray scale histogram and where the threshold value is set. The two peaks representing two phases (void and solid) are more distinguished after

the filtering.

3.5.2 Imaging segmentation

In order to obtain the pore space from the matrix, a segmentation process is required to binarize the gray scale into two scales, black (void) and white (solid), based on the gray scale histogram, shown in Fig. 3.14 (e).

The bimodal histogram suggests that the image contains two peaks representing the void and solid respectively. A threshold value is chosen at the valley to divide the image into two phases. We use the function of *threshold* provided in ImageJ (more details about using ImageJ can be found in Appendix A). An automatic thresholding integrated in ImageJ is applied to select the thresholding value, which is an iterative procedure based on the *isodata* algorithm (Ridler and Calvard, 1978). Briefly, this algorithm divides the image into objects and background by taking an initial threshold; then the averages of the pixels at or below the threshold and pixels above are computed. The averages of those two values are computed, the threshold is incremented and the process is repeated until the threshold is larger than the composite average, which is given by:

threshold = (average background + average objects)/2 (3.5)

If the automatic thresholding is not satisfied by visual inspection, a minor adjustment will be manually performed to minimize the unreal grain voxels in the void and the holes in the grains.

4 Pore network extraction algorithm

In this chapter, the details of the algorithm to extract pore networks from generic 3D images will be presented. First, we introduce the concepts of maximal ball (MB) and MB clustering used in this algorithm, for they are basic building blocks for pores and throats converted from the voxels in the void. A clustering algorithm is then proposed with a grading system, by which the maximal balls are grouped into pores and throats without ambiguity. The volumes, lengths and shape factors of the pores and throats are calculated to extract a full network with the same format as used in Øren et al.'s work (1998; 2002; 2003), which is taken as input format of the multi-phase simulation codes at Imperial College (Valvatne and Blunt, 2004; Piri and Blunt, 2005a; 2005b).

4.1 Basic concepts

4.1.1 Maximal balls

MBs are the basic elements used in our method to define the pore space and detect the geometrical changes and connectivity. As a set of voxels assembling a largest sphere, a MB must touch the grain surface and so MBs cannot be a subset of any other MB. Therefore, every MB is in possession of at least one voxel that is not contained in any other MB. The aggregate of all MBs defines the void space in a rock image without redundancy.

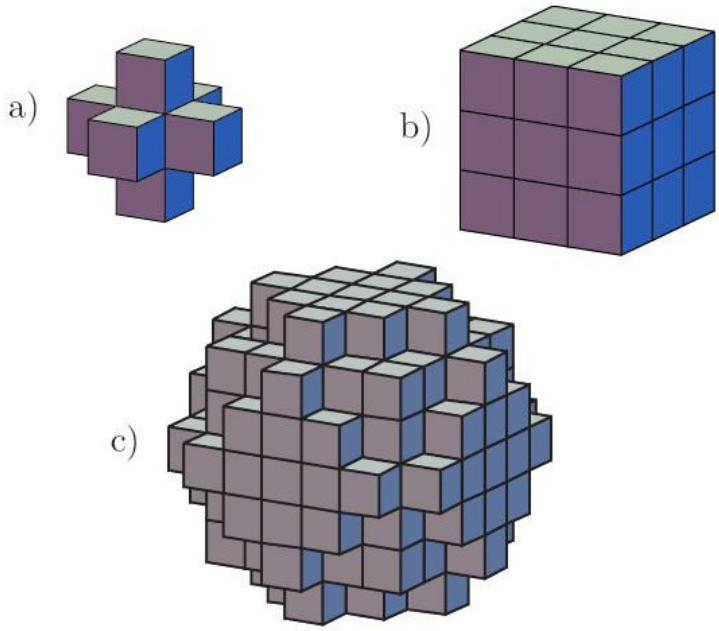

Figure 4.1. Assembly of discrete voxels mimics digital balls: (a) R=1; (b) R=$\sqrt{3}$; (c) R=$\sqrt{13}$. (Silin et al., 2003).

In a continuum description, a sphere is defined by a center C and a radius R. However, in a discrete image, it is difficult to define a precise radius due to the discontinuity caused by individuality of voxels, Fig. 4.1. We therefore introduce the lower and upper limits to define a range instead of a single radius. We define the radius squared in the algorithm. Let $R^2{}_{LEFT}$ and $R^2{}_{RIGHT}$ denote the squares of the lower and upper limits. We have $R^2{}_{LEFT} \le R^2 < R^2{}_{RIGHT}$. $R^2{}_{RIGHT}$ is the square of the Euclidian distance from the center $C(x_c, y_c, z_c)$ to the nearest grain voxel $V_g(x_g, y_{g,} z_g)$:

$$R^2{}_{RIGHT} = dist^2(C, V_g) = (x_g - x_c)^2 + (y_g - y_c)^2 + (z_g - z_c)^2, C \in S, V_g \in S_g \tag{4.1}$$

where S and S_g denote the voxelized void and solid space respectively.

R^2_{LEFT} is defined by a void voxel $V(x, y, z)$ existing in the R_{RIGHT} sphere with a maximum distance from the center:

$$R^2_{LEFT} = \max\{dist^2(V,C) \mid dist^2(V,C) < R^2_{RIGHT}, V \in S, C \in S\} \quad (4.2)$$

The difference between R^2_{LEFT} and R^2_{RIGHT} is no more than 2 voxel lengths squared in most cases, but this difference is significant for small balls. R^2_{LEFT} and R^2_{RIGHT} can only be the sums of three square numbers by definition. For example, if $R^2_{RIGHT} = 0^2 + 2^2 + 2^2 = 8$, R^2_{LEFT} must only be 6 ($R^2_{LEFT} = 1^2 + 1^2 + 2^2$) where a existing voxel can be found with the maximum distance from the same center. Fig. 4.2 gives an example of two digital spheres whose radius squared is 6 and 8.

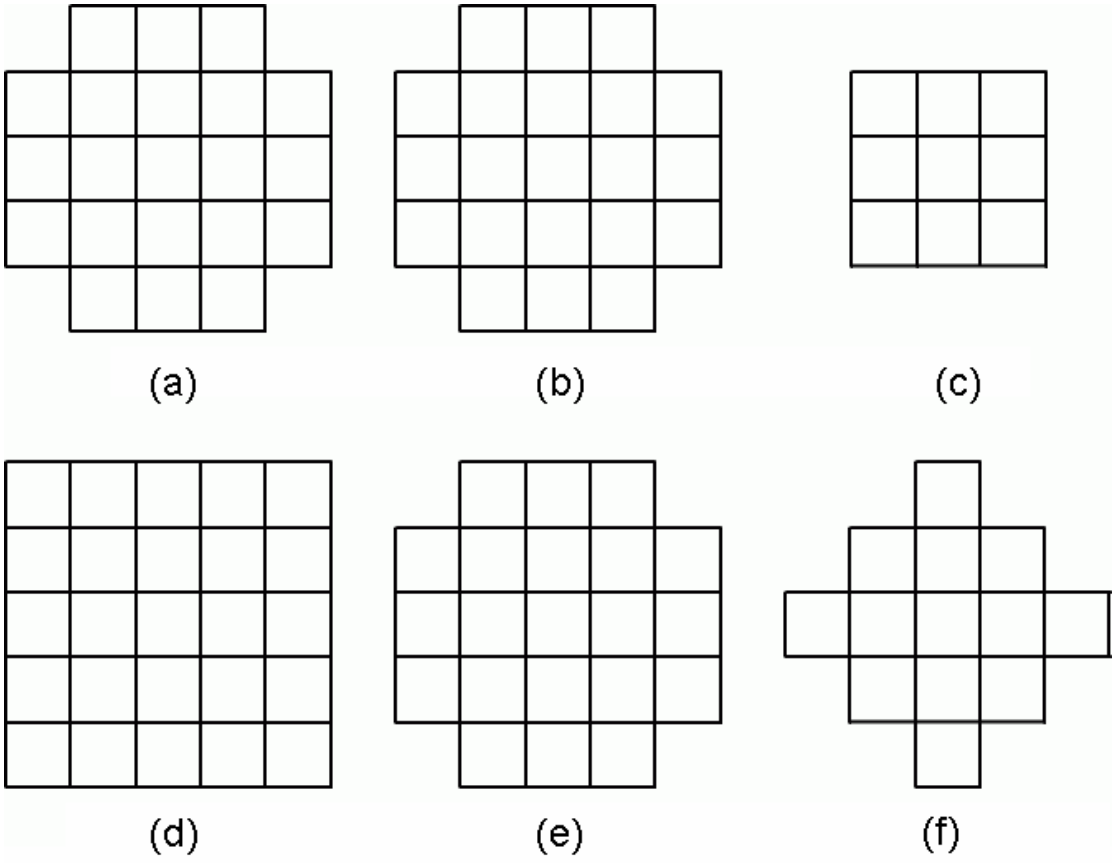

Figure 4.2. Example of digital spheres whose radius squared is 6 and 8 voxel units. (a)-(c) are respectively the central disk, lateral disks with distance 1 and 2 to the center of the sphere with a radius of $\sqrt{6}$; (d)-(f) are respectively the central disk, lateral disks with distance 1 and 2 to the center of the sphere with a radius of $\sqrt{8}$. If the radius $\sqrt{8}$ sphere defines R_{RIGHT}, R_{LEFT} must be $\sqrt{6}$ due to the discontinuity of the sum of three square numbers.

R_{LEFT} is similar to the MB radius defined in Silin et al. (2003). We will show later, however, that R_{RIGHT} is needed when we define pores and throats.

4.1.2 Clusters

MBs are found filling the entire void space measuring the local apertures not only in pore central spaces but also at highly irregular corners. To define the topology

we merge MBs into clusters. Two types of cluster are defined: single and multi clusters.

In a single cluster, a principal MB absorbs all its direct smaller neighbors in its domain. To find such neighbors, for an MB with a radius of R, as shown in Fig. 4.3, we define a spherical searching range twice the radius of the ball, which is sufficient to find smaller neighbors' centers. We select each MB that overlaps or touches the principal MB. It is added to the cluster if it has a smaller radius than the principal MB. We define overlapping using the larger definition of radius in case of losing connectivity when using R_{LEFT} :

$$dist(C_1, C_2) < R_{RIGHT1} + R_{RIGHT2} \quad C_1, C_2 \in S \tag{4.3}$$

where C_1, C_2 are the centers of balls.

We adopt the concept of family trees for the clusters. The principal MB is a parent and the absorbed MBs are children. Each of them has a generation rank number. Direct children rank 1 generation younger (numerically greater) than the parent.

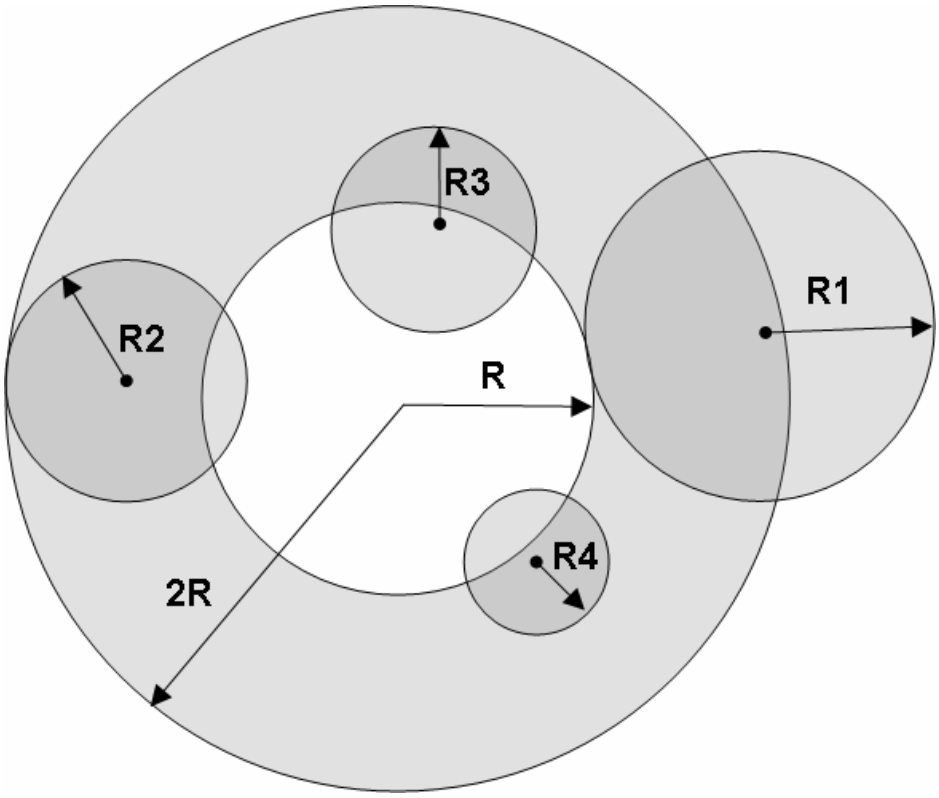

Figure 4.3. This is a schematic picture of a single cluster. The white ball is the parent and absorbs smaller children centered in a range of $2R$, $(R > R_1 > R_2 > R_3 > R_4)$. Any ball that overlaps or touches the parent ball with a smaller radius than the parent will be clustered as children. The children's generation number will be 1 greater than their parent.

We extend the concept of a single cluster to multi-clusters as follows. Any of the principal (ancestor)'s subordinates (children) can absorb their own smaller neighbors (grandchildren) and so on. In this case, the cluster becomes multi-cluster by introducing younger generations. Each node on the family tree follows the same rule to find direct offsprings centered in its $2R$ range around the parent. The clustering processes are reversible by knowing parents for each node so that the sub-level MBs can trace back until the common ancestor found.

In our algorithm, we sort the MBs in the pore space into interconnected clusters. The common ancestor of each cluster defines a pore. If a MB is connected to

two clusters – that is a child of parents with different common ancestors – then it defines a throat. An MB chain can be defined from the throat to pore by recognizing parents. As shown in Fig. 4.4, cluster A and B meet at the throat node indicated. Since the chains starts from a pore and ends at a throat, we call the chain a pore-throat chain. Pore-throat chains are used to define the topology of the pore space. MBs not contributing to the chains are not needed to define the topology but are important to describe the shape and sizes of pores and throats. They can be related to individual pores and throats by knowing the parenting hierarchy. Details of this clustering will be described in Section 4.3.

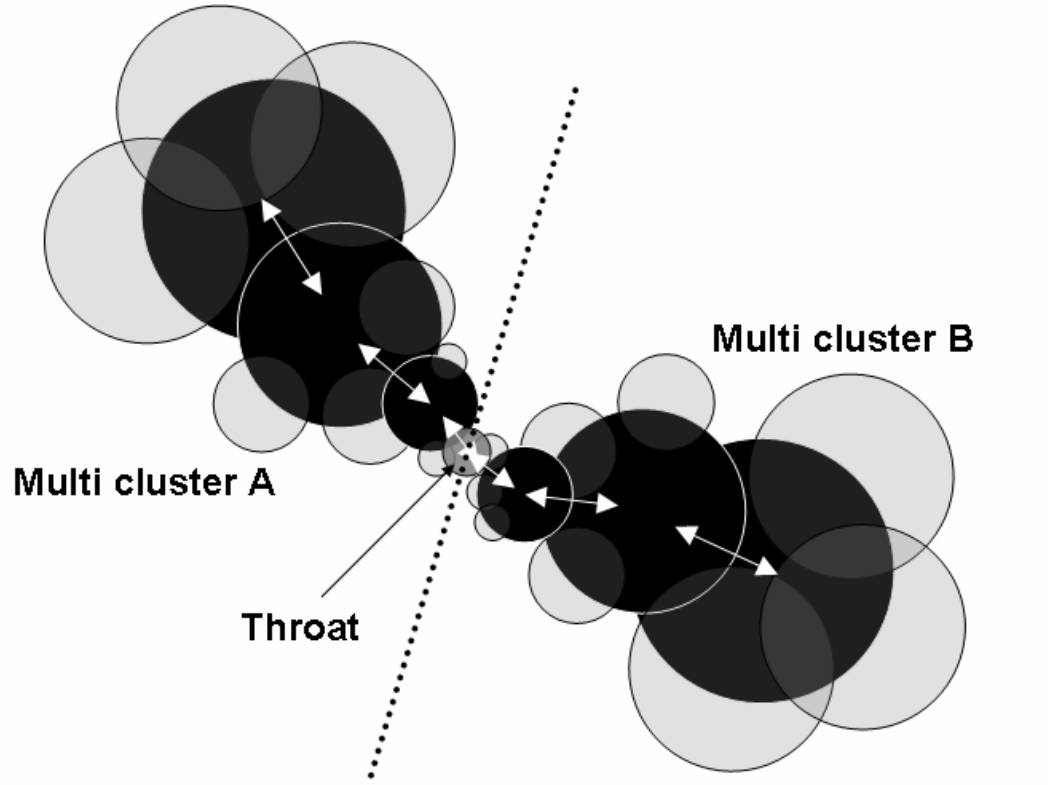

Figure 4.4. Single clusters extend as family trees. From an ancestor, the children and grandchildren are added to the multi-cluster by absorbing their own offspring centered in a 2R range. Generation number, family name and parent's name are used to keep the family tree traceable. When throat is found as a common child of different families, MB chains are defined (white arrows) and two pore-throat structures are formed.

4.2 Building maximal balls

4.2.1 Build inscribed balls

Regardless of the method to obtain a 3D image of the porous media, the input data for network extraction is a 3D array consisting of voxels with a value of either 1 or 0 which means grain or void respectively. We build inscribed spheres that touch the grain surface centered at each void voxel. A sphere found inside an existing ball is removed as an inclusion, which will be discussed in Section 4.2. To build such inscribed balls, we developed a two-step searching algorithm. Instead of attaching void voxels to the center one by one or layer by layer, assembling a ball until it hits a grain or boundary, we use an expanding search to define the potential search range followed by a shrinking search to find the genuine nearest solid voxel.

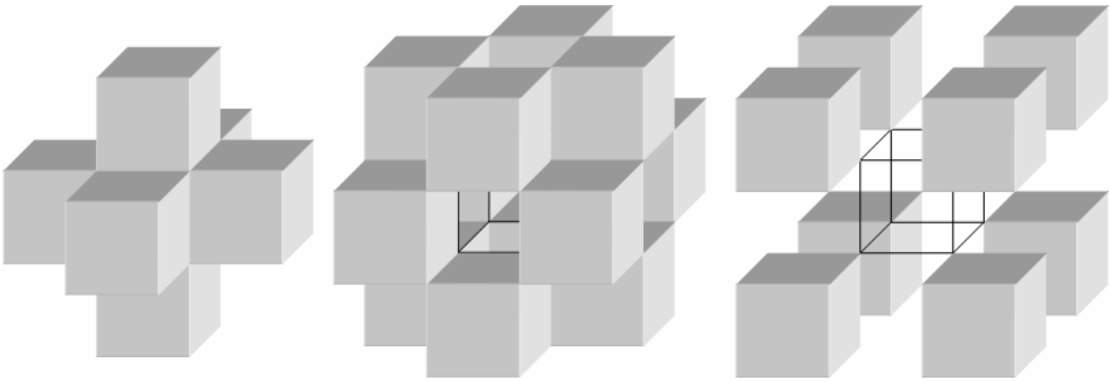

Figure 4.5. Three types of directional lines defined by the nearest-neighbor voxels of the central cell. The left picture shows the lateral lines, by which six directions are defined. Each step represents 1 voxel length. The middle figure defines 12 directions by diagonal lines. Each step is $\sqrt{2}$ voxel length. The right picture shows the 8 diametrical lines with a $\sqrt{3}$ step length.

During the expanding search, we search for solid or boundary voxels along 26 directional lines. The stop point defines the range for the second step where all voxels contained within the range are checked to find the nearest solid voxel. The search directions are shown in Fig. 4.5. The search directions are classified into three categories in Table 1 as they have different step lengths.

Table 4.1. Looping variables for directional lines.

Category	Looping variables
Lateral lines	(i++, j, k), (i--, j, k), (i, j++, k), (i, j--, k), (i, j, k++), (i, j, k--)
Diagonal lines	(i++, j++, k), (i++, j--, k), (i--, j++, k), (i--, j--, k), (i++, j, k++), (i++, j, k--), (i--, j, k++), (i--, j, k--), (i, j++, k++), (i, j++, k--), (i, j--, k++), (i, j--, k--)
Diametrical lines	(i++, j++, k++),(i++, j++, k--), (i++, j--, k++), (i++, j--, k--), (i--, j++, k++), (i--, j++, k--), (i--, j--, k++), (i--, j--, k--)

We can rapidly find the first grain or boundary voxel solely along the 26 directions and stop the expansion. We deem the distance from center of the MB to the found grain the range of the shrinking search. Every voxel inside this sphere has to be checked to find the real nearest solid (R_{RIGHT}) and a voxel with a maximum distance (R_{LEFT}) just less than R_{RIGHT}. We build inscribed balls on every void voxel before finding out the maximal ones among them.

$$B = B(C_i, R_i, R_{RIGHT\,i}) \quad B \subset S, C_i \in S, i = 1,2,3,...,n \tag{4.4}$$

where *n* is the number of void voxels in the 3D image.

4.2.2 Remove the inclusions

There are some inscribed balls completely embedded in another sphere, which provide no extra information to determine the void space. Such included balls must be removed since they are redundant. We denote C_A and C_B the centers of ball A and B with radius of R_A and R_B respectively. Ball B is included in A if the difference of radius is not less than the Euclidean distance of the centers, i.e. $dist(C_A, C_B) \leq | R_{LEFT\ A} - R_{LEFT\ B} |$.

However, this method still leaves some included balls, because of the discrete nature of the void space, as illustrated in Fig. 4.6. To remove such inclusions, we use R_{RIGHT} for the larger ball and R_{LEFT} for the small ball to let the inclusion be detected.

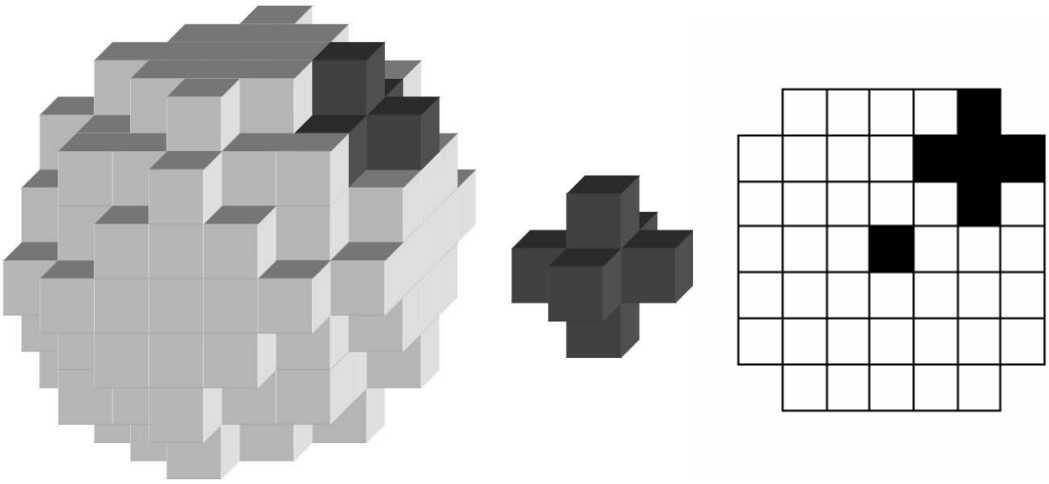

Figure 4.6. The radius of the larger ball on the left is $\sqrt{13}$ voxel lengths. The radius of the middle smaller ball is 1. The right picture shows the central cross-section of the balls put together. The small ball is clearly included in the larger one. However, the condition $dist(C_A, C_B) \leq | R_{LEFT\ A} - R_{LEFT\ B} |$ cannot detect the inclusion. The difference of their radius is $\sqrt{13}$ -1, which is smaller than the distance between the centers $\sqrt{8}$.

Using R_{RIGHT} for the outer ball radius can overcome this problem.

After the inclusions are removed, the overlapping *maximal* balls contain the entire void space without a redundancy. Accordingly, we transform the space of discrete voxels into one of overlapping MBs. Every voxel in the image is contained in one or more MBs. We classify MBs into pores and throats by clustering them.

4.3 Clustering and identifying pores and throats

To implement pore and throat identification, we developed a fast clustering algorithm with a grading system. The procedures are described below:

1. We sort all the MBs from the largest to the smallest, and then divide them into subsections according to size. Each group contains MBs of the same size. Let *M* denote the number of MBs in the first group, representing the largest balls. All the MBs are initially given infinite rank.

2. Starting from the first ball A in the image with the largest radius, we define it as a pore and rank it 1st as an ancestor. All its smaller overlapping neighbors are absorbed by A and ranked 2nd generation. Every ball in this cluster remembers that A is its ancestor and parent.

3. We collect the same sized balls left in the first group and sort these *M-1* balls by their rank. Starting from the first, ball B absorbs its smaller unranked neighbors and ranks them one generation younger. The clustered balls inherit the family name of ancestor and know B as parent. If the B's rank was infinite before being processed, B defines a new pore as an ancestor. If not, B is regarded as part of its ancestor's pore body and ready to transfer the family name to children. If B absorbs any MBs from two families, B's common child

defines a throat. Once a throat is found, two pore-throat chains are constructed from the throat to ancestors by visiting parents layer upon layer.

4. The same sorting and clustering processes apply for the next MB that has the same size. After all the balls in this group are processed, we move to the next group with a smaller size.

5. The same sorting and clustering processes apply for all the groups until we reach the minimum size set for a pore. Below this threshold, the MBs may provide connections (be throats) but cannot be pores. In general, we define the minimum pore a 3D cross with 7 voxels illustrated in Fig.4.7, while a single voxel can only be a throat rather than a pore.

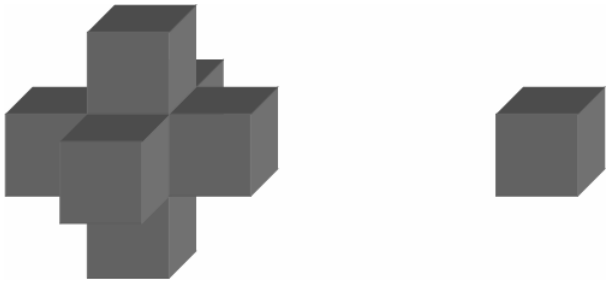

Figure 4.7. The left picture shows the minimum pore defined by default in this algorithm consisting of 7 voxels ($R_{LEFT}=1$ and $R_{RIGHT}=\sqrt{2}$). The right one is a single voxel that can only be used as throat bricks rather than representing a pore. The user can also define an arbitrary minimum pore size according to the image resolution and the level of detail required.

The grading system of the clustering avoids the ambiguity caused by the equal sized small pores since they can be distinguished by generation rank rather than size alone.

In the clustering process, the locations and sizes are defined for every pore and throat. To associate voxels to them, the pore space is segmented into pore blocks and throat blocks.

4.4 Pore space segmentation

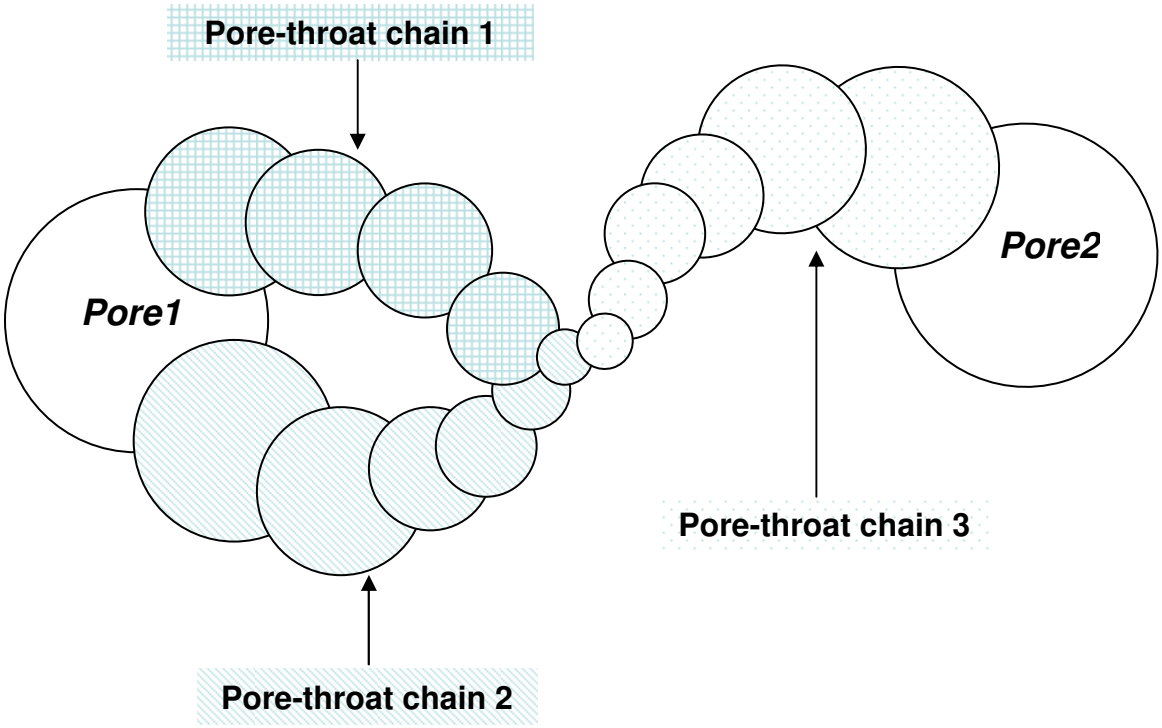

Figure 4.8. Parallel pore-throat chains wind in one channel.

After the clustering, pore-throat chains have been constructed throughout the pore space as bundled skeletons. The remaining MBs can be associated to the chains as flesh to describe the profiles of the pore space using the parenting hierarchy established during clustering. The chains capture the topology of the pore space. However, it is quite common that there is more than one pore-throat chain linking the same two pores in the same channel, Fig. 4.8.

We segment the pore space into pores and throats according to these chains. What is a pore and what constitutes a throat is somewhat arbitrary; in topological

terms all we need to assign is the connectivity of the void space. However, as we discuss later, how we divide the void space into pores and throats does have an impact on the prediction of transport properties.

On a pore-throat chain with known ancestor size, we set the initial border between pore and throat blocks where a MB can be found having a radius of 0.7 times the ancestor's radius, Fig. 4.9. This is clearly an arbitrary division, but note that the method consistently gives the same coordination number to each pore, regardless of this pore and throat segmentation.

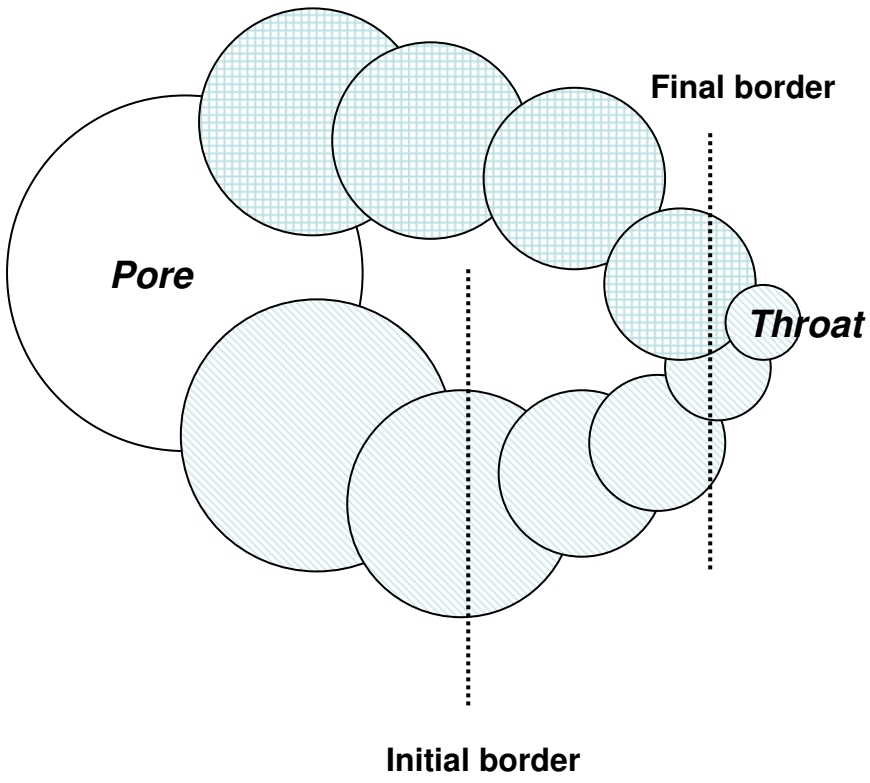

Figure 4.9. Pore throat segmentation. The maximal ball on the initial border has a radius 0.7 times of the ancestor's radius. The final border is where all the chains join together before approaching to the throat.

We compare these chains linking the pore and throat and move the border to

where the two (or more) chains merged. Voxels are assigned to either pores or throats according to the new border of the pore throat. Eventually every voxel in the image is assigned a unique pore or throat label.

The advantage of this pore segmentation method is that each maximal ball can be easily attached to the pore-throat chains without upsetting the parenting relationship. However, the lengths of throats tend to be underestimated and so the pore lengths are overestimated as witnessed by the throat length comparisons, see Fig. 4.10. A higher frequency of short throats are defined in the MB network than in the PB approach, especially for a throat length equal to one voxel (see Fig. 6.16), which indicates that during the pore space segmentation, many pore-throat chains join at single voxels. The underestimated throat lengths can result in an overestimation of the overall conductance of flow (Section 7.1.1, Equation 7.4) since the pore conductance is weighed excessively due to these overrated lengths.

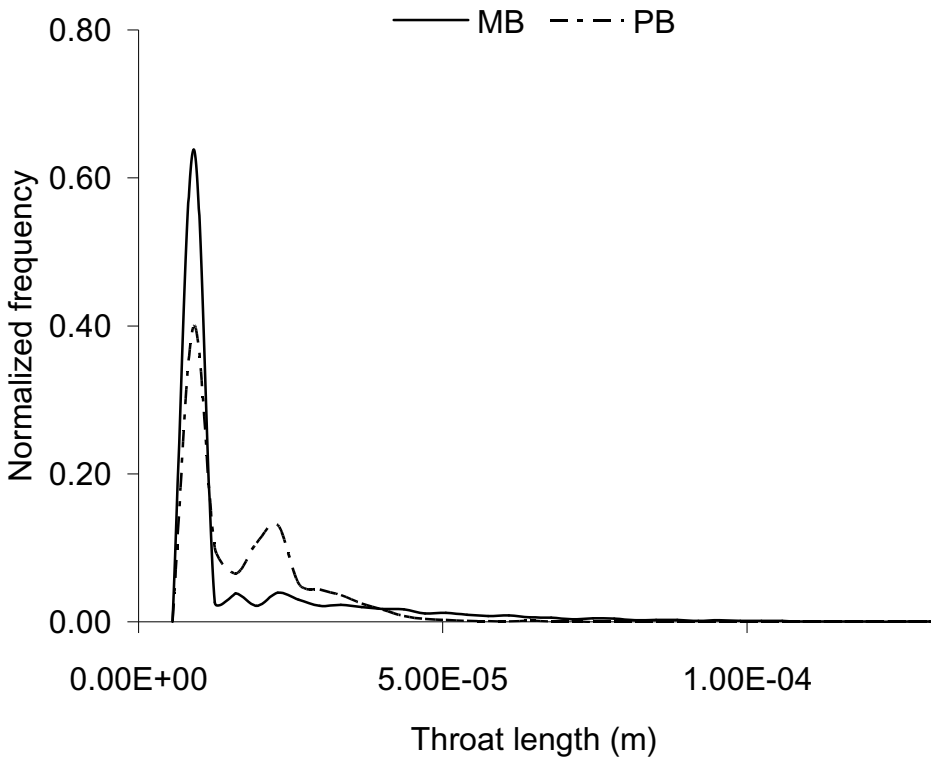

Figure 4.10. Comparison of throat length distributions of PB network and that derived

from the original definition of the MB method on the reconstructed Fontainebleau sandstone.

Therefore, we correct the length of throat by equation 4.5- 4.7 similar to that given by Øren and Bakke (2003), Fig. 4.11.

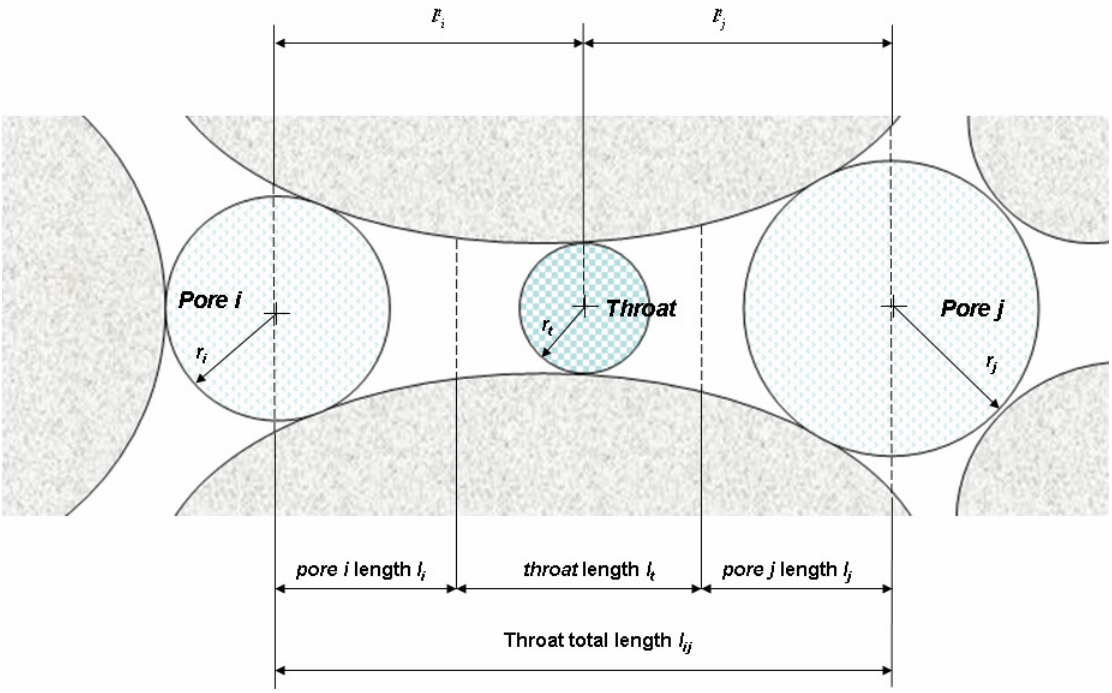

Figure 4.11. Schematic picture of the length correction for pores and throats.

The throat length l_t is defined by subtracting the two pore lengths (l_i and l_j) from the total throat length l_{ij} (the distance from *pore i* center to *pore j* center).

$$l_t = l_{ij} - l_i - l_j \tag{4.5}$$

The pore length l_i and l_j are defined by

$$l_i = l_i^t (1 - 0.6\frac{r_t}{r_i}) \tag{4.6}$$

$$l_j = l_j^t (1 - 0.6\frac{r_t}{r_j}) \tag{4.7}$$

where r_i, r_j and r_t are the radii of *pore i*, *pore j* and *throat* respectively; l^t_i and l^t_j are the distances between the centers of *pore i* and *pore j* to the throat center. The comparison

of the throat length distributions after the correction can be seen in Section 6.2.5.

4.5 ***Calculating other pore network parameters:*** size, volume and shape factor

1. Size:

Theoretically, the size of a pore is defined as the inscribed radius of the ancestor MB. The radius of a throat is the inscribed radius of the biggest throat MB in the pore-throat chains linking two pores.

To suppress the discontinuity in the prediction of properties that depend directly on throat size – such as capillary pressure – caused by the discrete nature of the computed radii, we randomly distribute the radius defined by a range whose lower limit is ($R_{left}-1$) and whose upper limit is R_{right}. The minimum size is set to 0.1 times of the voxel side length. The criterion for size treatment is verified by comparing the capillary pressure curves produced by the PB (abbreviation for process-based method; Øren and Bakke, 2003) and MB networks and good agreement is found in Fig. 4.12. The same criterion was applied to all the samples in this study to extract networks and compute the absolute permeability and formation factors in Chapter 7.

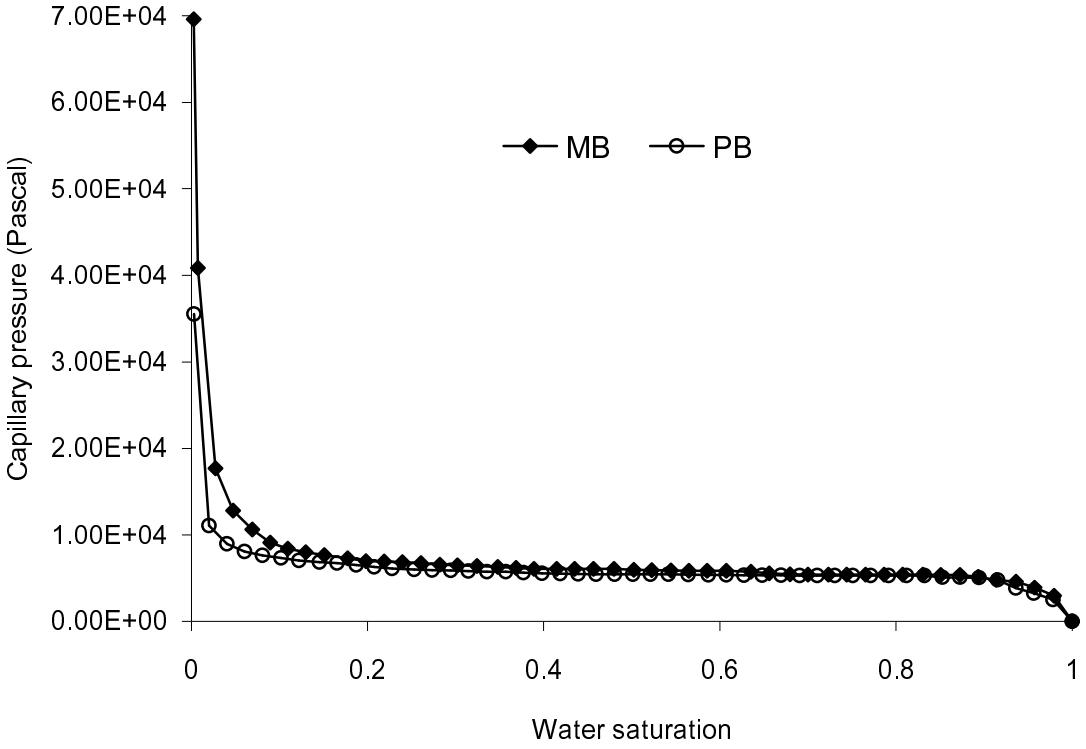

Figure 4.12. Capillary pressure curves of PB and MB networks of the reconstructed Fontainebleau sandstone. Good agreement is found despite the discrepancy at low saturation, which indicates different size treatments resulting in dissimilarity only on the smallest throats less than one voxel wide.

In practice, especially for future work, it is suggested to compare the processed throat size against the throat size distribution translated from mercury injection experiments and pore size distribution from NMR results to depress the uncertainties associated with the image processing and the blurring effects from micro-CT images. Systematic study on criteria chosen for size treatment related to the image resolution and geological structures is also highly recommended.

2. Volume:

The volumes of a pore or throat are found by counting the number of void blocks associated with each pore or throat block defined.

3. Shape factor:

Real pores and throats have complex and high irregular geometrical profiles. We approximate them as cylindrical capillaries with a constant but arbitrary cross-section with a dimensionless factor shape *G*,

$$G = \frac{VL}{A_s^{\,2}} \tag{4.8}$$

where A_s is the surface area of the pore or throat block – this is found by counting the number of surfaces between void and solid in each element; *V* is block volume; and *L* is the block length.

This is an equivalent to

$$G = \frac{A}{P^2} \tag{4.9}$$

where *A* is the cross-sectional area and *P* is perimeter (Mason and Morrow, 1991) as shown in Fig. 4.13.

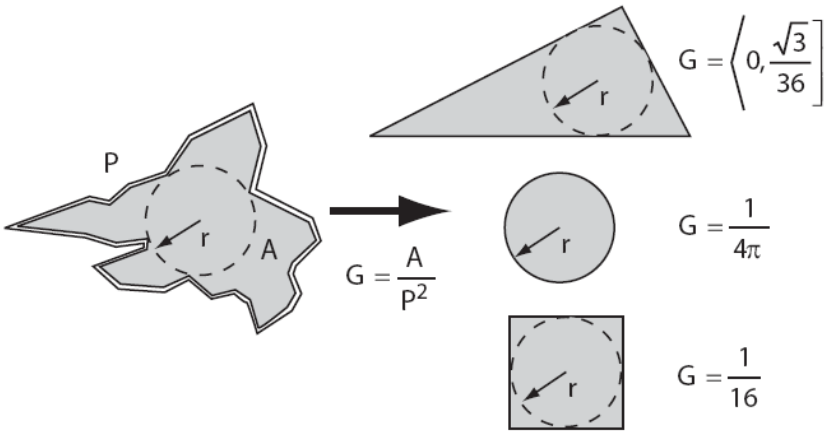

Figure 4.13. The dimensionless shape factor of network elements (Mason and Morrow, 1991).

The resultant network is then output in a form suitable for input into current pore-scale network simulators that can compute single and multiphase flow properties (Øren et al., 1998; Øren and Bakke, 2002; 2003; Valvatne and Blunt, 2004; Piri and Blunt, 2005a; 2005b).

5 Samples

5.1 Benchmark samples

The benchmark samples include five regular packings with number of pores known, a process-based reconstructed Fontainebleau sandstone image with an equivalent pore network generated from a process-based algorithm and a Berea sandstone micro-CT image that can be compared to a process-based Berea network (Øren and Bakke, 2003; Valvatne and Blunt, 2004; Piri and Blunt, 2005a; Piri and Blunt, 2005b) with associated experimental data on relative permeability (Oak, 1990).

5.1.1 Regular packings

Five images of regular packings of equally-sized spheres were provided by Øren and Bakke using the process-based method (Bakke and Øren, 1997). The packings are cubic, orthorhombic, tetragonal-sphenoidal, rhombohedral-pyramidal and rhombohedral-hexagonal packs, Fig. 5.1.

In these packs, each sphere has a diameter of 50 times the voxel length. Each image consists of 120^3 voxels and contains fewer than a hundred pores, Figs. 5.2-5.6. The small datasets allow us to inspect the individual pores visually. The numbers of pores were also given along with the datasets by Øren and Bakke for the network comparison in Chapter 6.

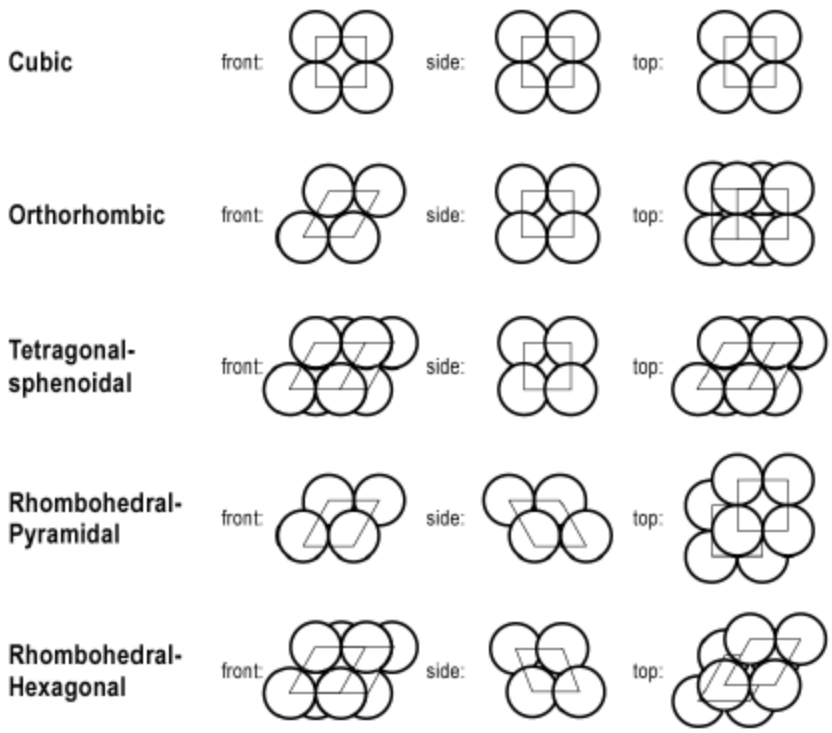

Figure 5.1. Five basic regular packing arrangements, characterised by the smallest possible cells to represent the packing. The rectangular and rhombic shapes indicate the faces of unit cells (Alberts, 2005).

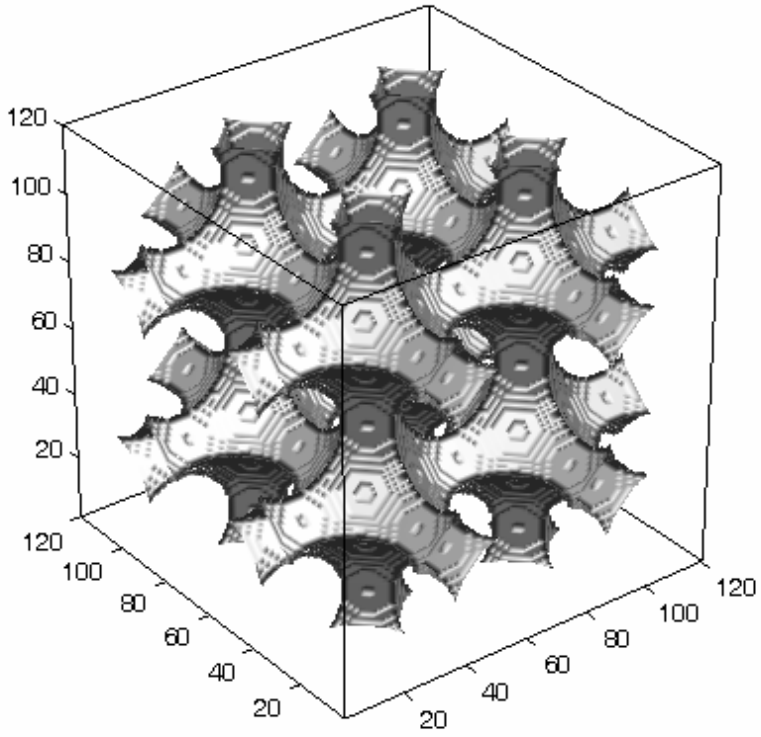

Figure 5.2. 3D view of the cubic packing (120^3 voxels).

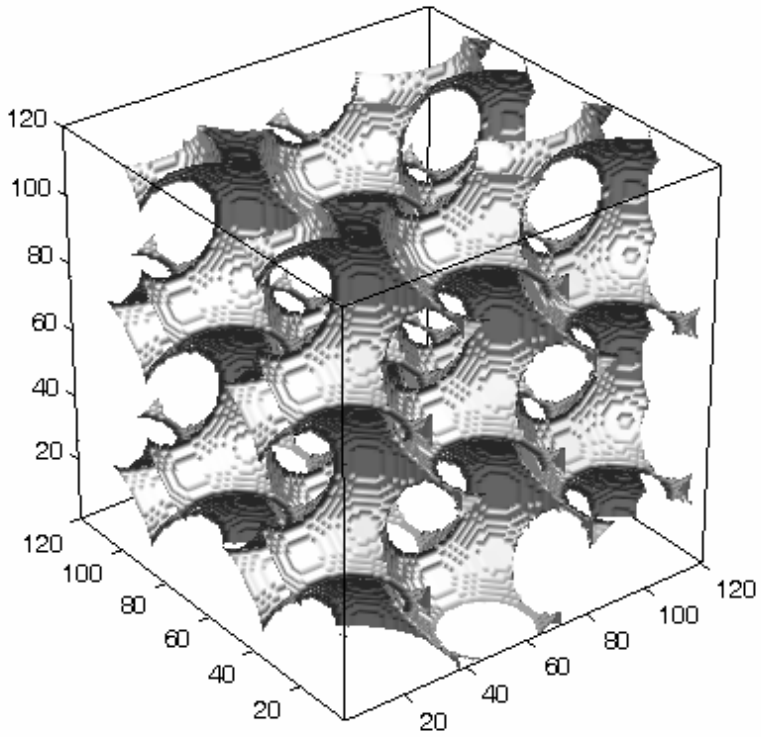

Figure 5.3. 3D view of the orthorhombic packing (120^3 voxels).

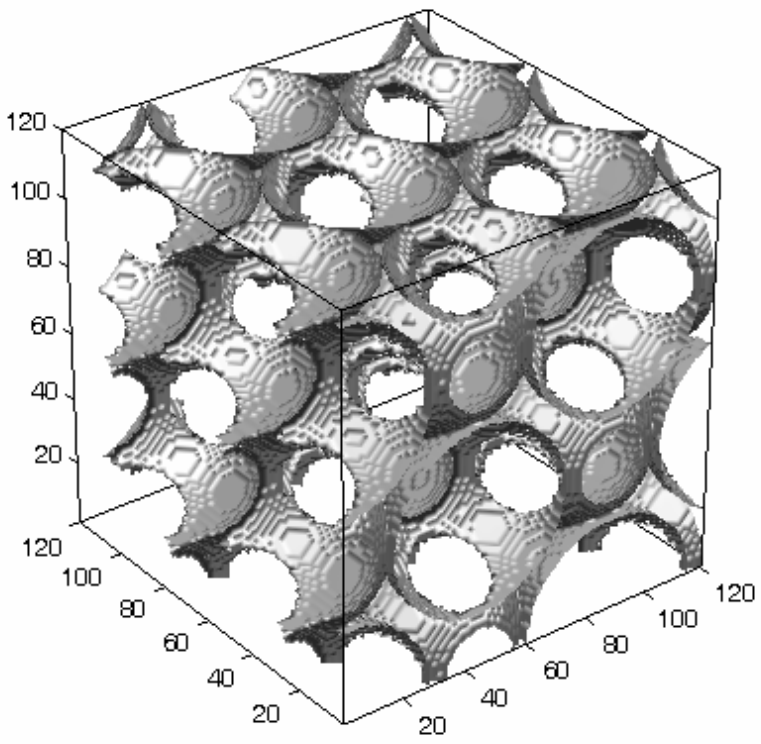

Figure 5.4. 3D view of the tetragonal-sphenoidal packing (120^3 voxels).

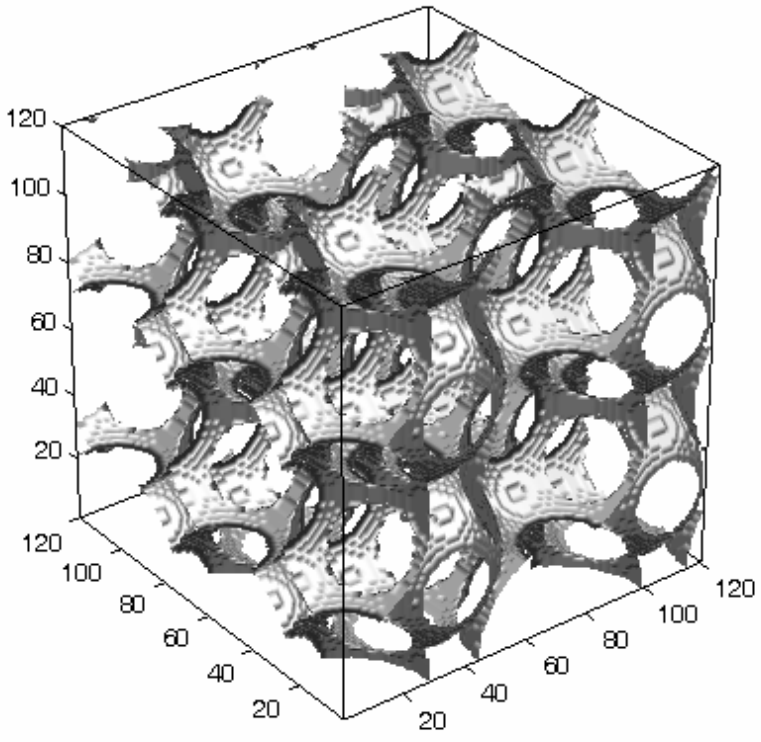

Figure 5.5. 3D view of the rhombohedral-pyramidal packing (120^3 voxels).

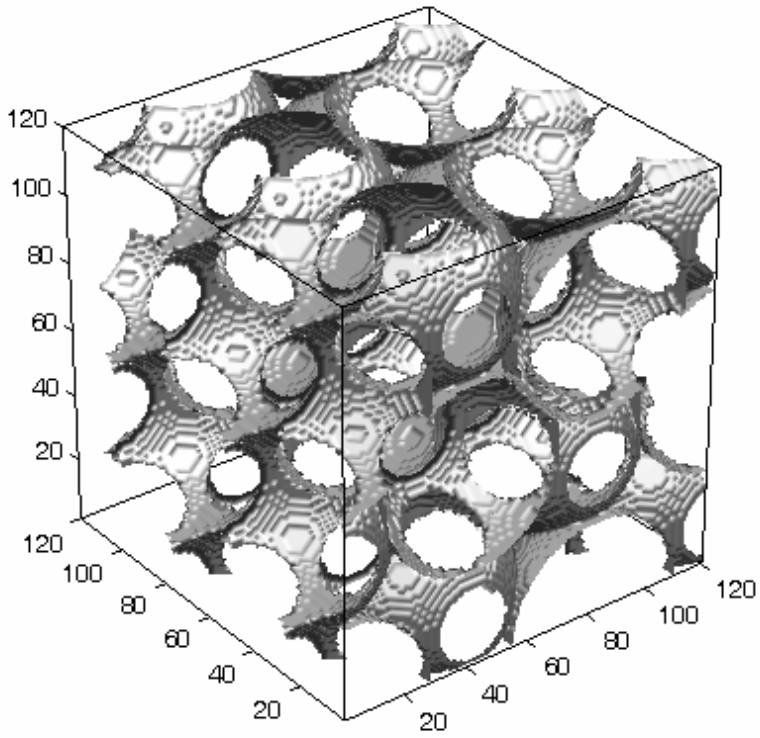

Figure 5.6. 3D view of the rhombohedral-hexagonal packing (120^3 voxels).

5.1.2 Fontainebleau sandstone

Fontainebleau sandstone is an ideal granular system without clay content consisting of monocrystalline quartz grains that have been well rounded through transport for long periods before being deposited (Bourbie et al., 1987). This sandstone is found in the Ile de France region around Paris, which is pure sandstone of Oligocene age (Stampian). This well sorted sandstone has a grain size around 250 μm. The porosity varies from 2% to 30% depending on the degree of compaction and diagenesis without noticeable grain size modification (Okabe and Blunt, 2004). The relation between porosity and permeability had been studied by Bourbie and Zinszner (1985) and expressed as

$$k = 0.303\phi^{3.05} \quad (5.1)$$

for high porosities ($\phi > 8-9\%$), where ϕ is the total porosity and k is the absolute permeability in millidarcies ($\approx 10^{-15}$ m^2).

For low porosity ($\phi < 8-9\%$) samples, the absolute permeability k (in milidarcies) is

$$k = 2.75\times 10^{-5}\phi^{7.33} \quad (5.2)$$

In this study, we used a reconstructed image by the PB method of Fontainebleau sandstone to extract pore networks. The porosity of the reconstructed image is 13.57% consisting of 300^3 voxels across a volume of 11.39 mm^3. Figs. 5.7-5.9 give the visual comparison of the PB reconstructed image and a micro-CT image of Fontainebleau sandstone. The PB reconstructed images reproduces the morphology and topology of the original rock sample (Øren and Bakke, 2002).

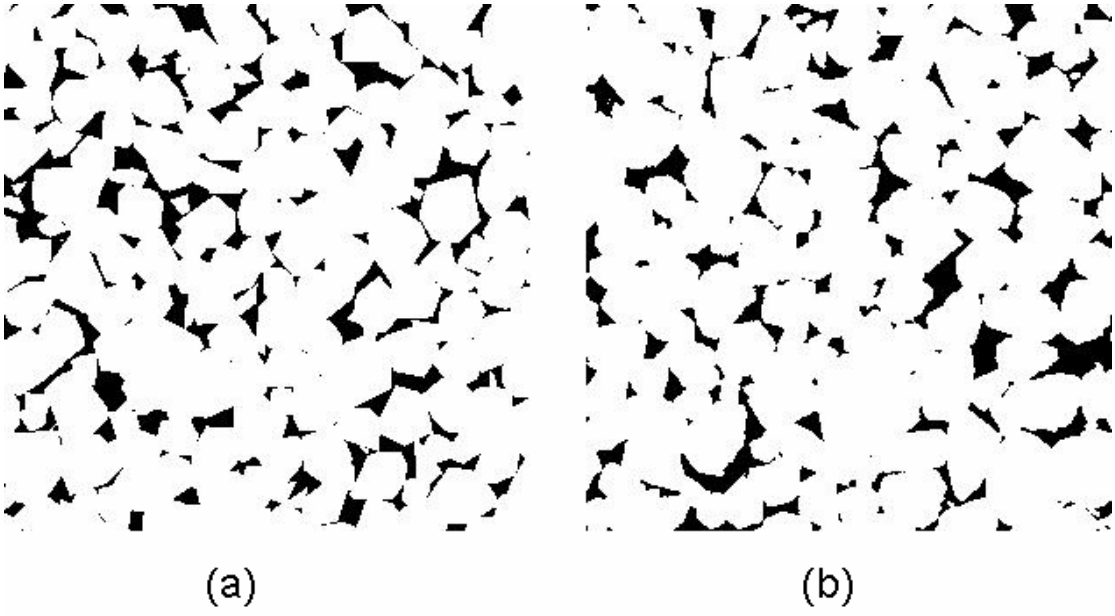

Figure 5.7. Cross-sectional images of (a) reconstructed Fontainebleau image by the

process-based method and (b) micro-CT image of Fontainebleau (Coker et al., 1996; Øren and Bakke, 2002).

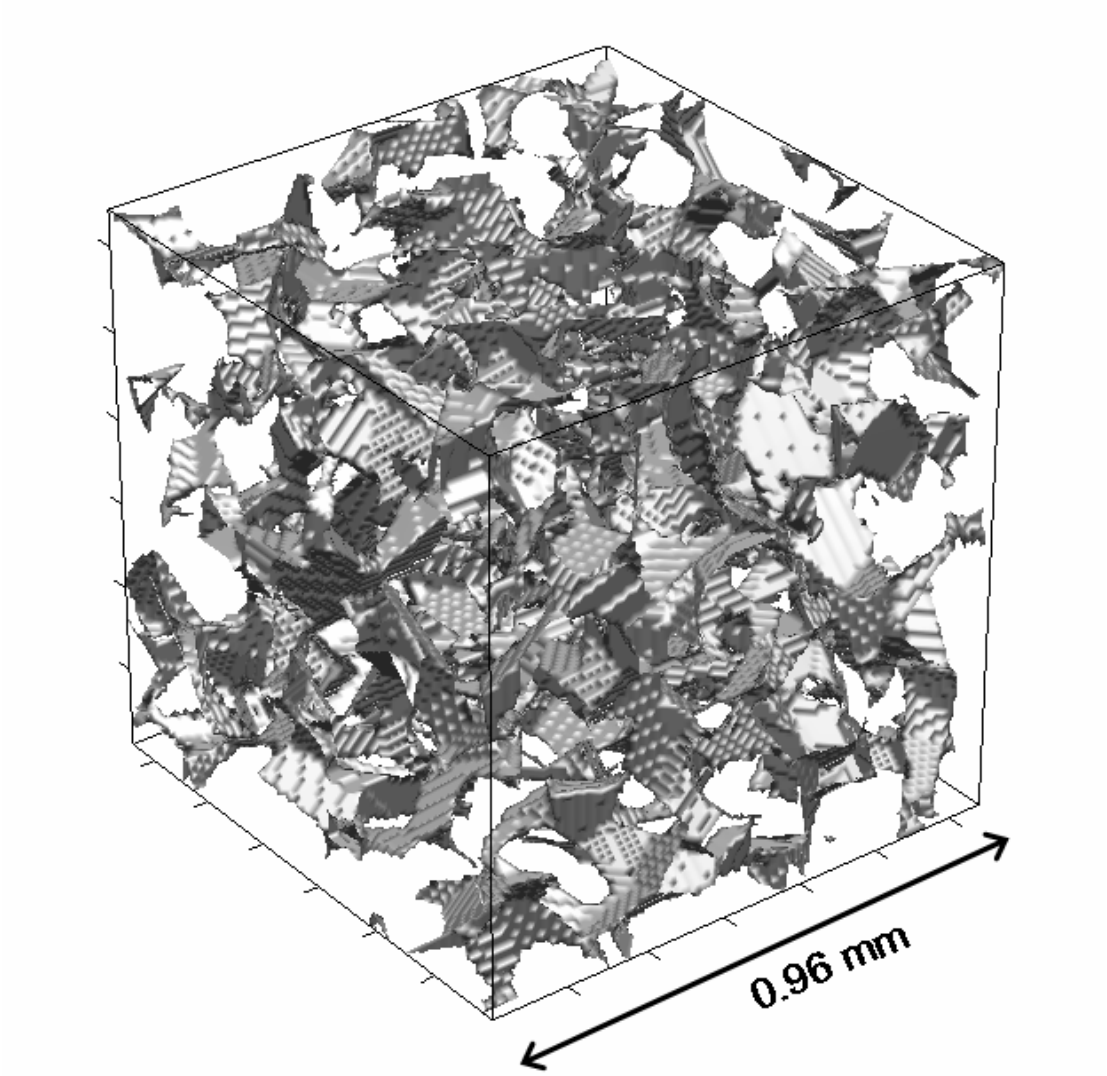

Figure 5.8. 3D view of a subsample of the reconstructed Fontainebleau image.

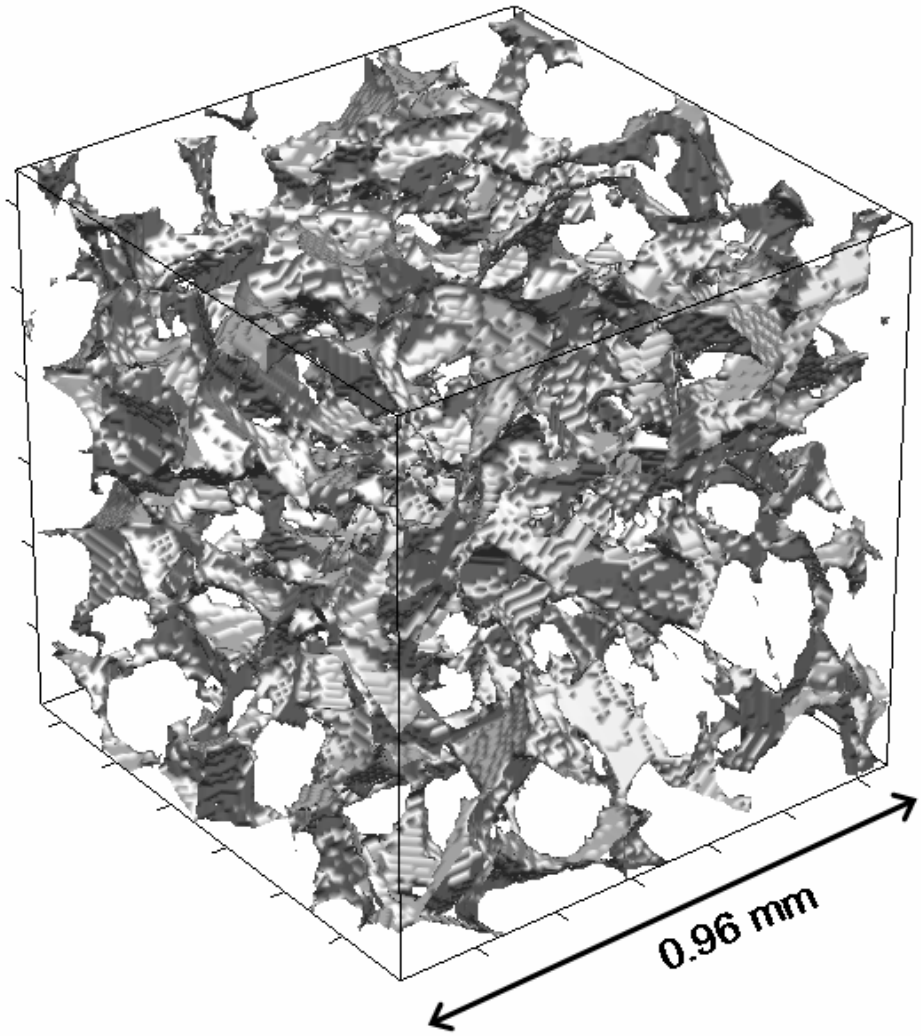

Figure 5.9. 3D view of a subsample of the micro-CT Fontainebleau image.

The algorithm is validated on the reconstructed Fontainebleau image. The network extracted is compared against the PB network in terms of topological and morphological parameters (in Chapter 6) and petrophysical properties and transport properties (in Chapter 7).

5.1.3 Berea sandstone

Berea sandstone is another standard material containing minor amounts of feldspar, dolomite and clays (Fig. 5.10). The sandstone found in Berea, Ohio was

formerly quarried for construction due to its durability and now is also widely used for core analysis (Churcher et al., 1991; Dullien, 1992). This sandstone also occurs in the oil and gas producing formation in the Michigan Basin. Berea sandstone forms the middle layer of the Waverly group of geological rock formations in Ohio during the Mississippian geological period (360-325 million years ago) and it was deposited in the channel and sandwiched between two other layers: red Bedford limestone below and Berea Shale above. Two distinct units comprise this sandstone formation: the lower, referred to as Orange Berea, is high angle cross-bedding, coarser-grained and more poorly-sorted than the upper unit; the upper unit of Berea sandstone is frequently used in core flooding experiments (for instance, Oak, 1990) due to its fine-grained, well-sorted characteristics with closely spaced planar bedding. (Okabe and Blunt, 2004)

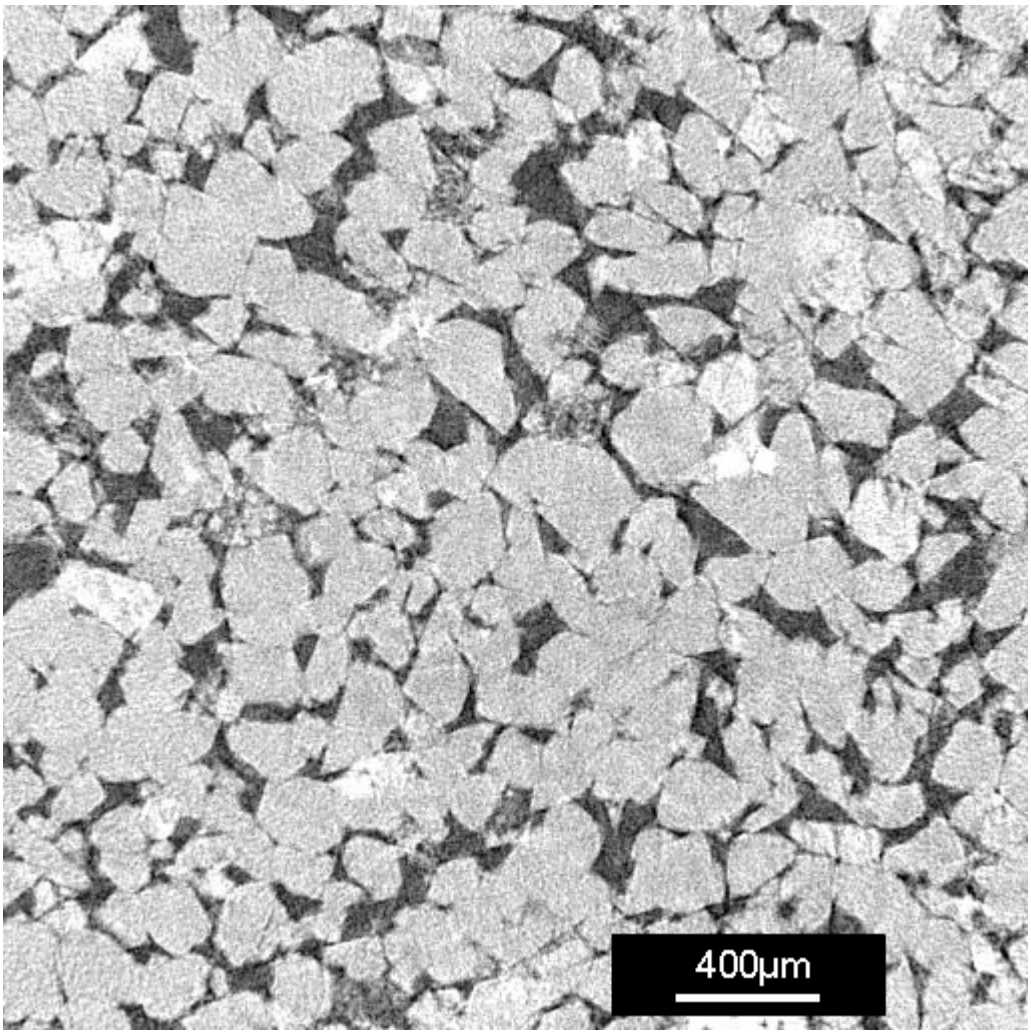

Figure 5.10. A cross-section of a micro-CT image of Berea sandstone imaged at Imperial College London. The resolution of the image is 5.345µm.

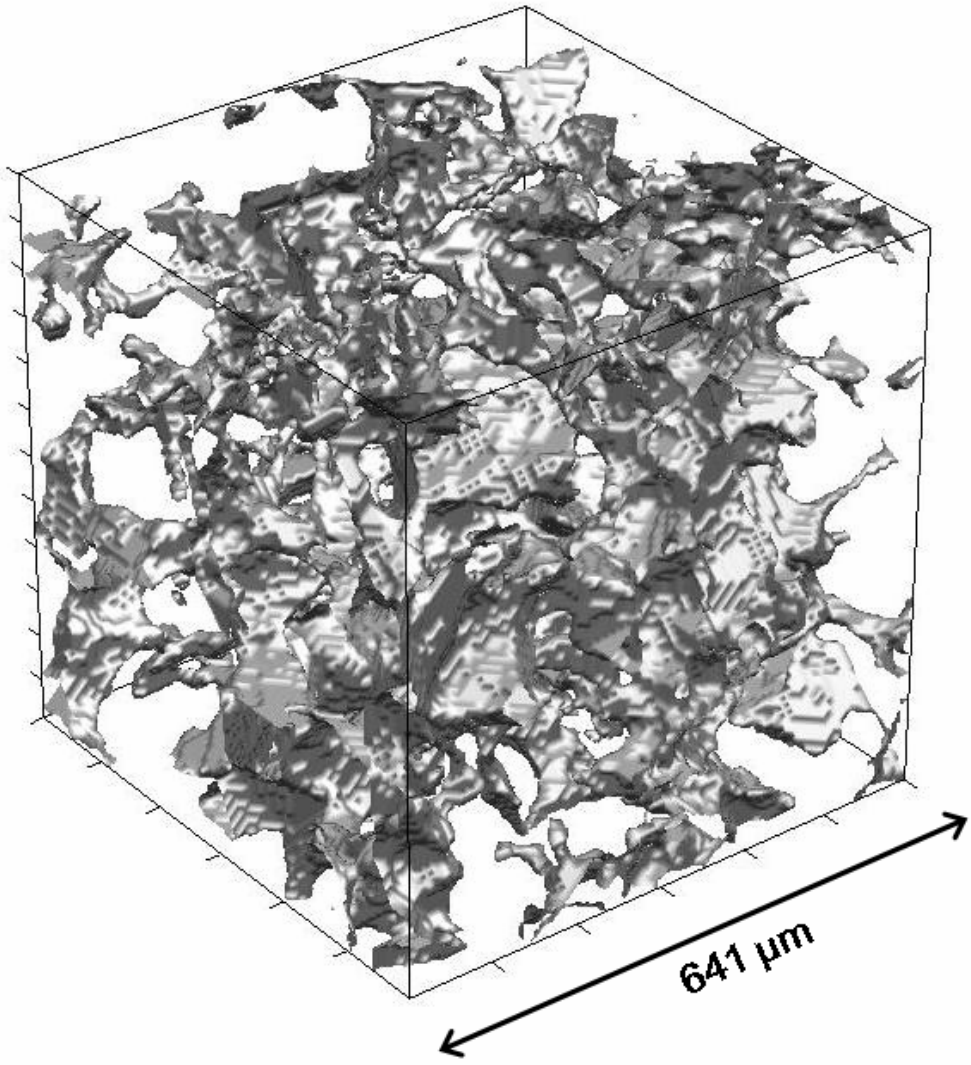

Figure 5.11. 3D view of a subsection of the micro-CT image of this Berea sandstone.

A subsection consisting of 400^3 voxels with a porosity of 19.6% partitioned from a micro-CT image of Berea sandstone is used in this study to extract a pore network to compare the transport properties against the results of multi-phase flow experiments with a water-wet Berea sandstone performed by Oak (1990).

5.2 Other test samples

A series of sandstone, carbonate and synthetic samples have been imaged during

this project (Section 3.4) compositing our image library, among which, 13 images (including Berea sandstone image in Section 5.1.3) of good quality were selected from the library and sent to Numerical Rocks AS (Trondheim, Norway) to calculate the basic petrophysical properties, (i.e. absolute permeability and formation factors) based on their micro-structures (i.e. directly on the micro-CT images) for benchmarking the results of pore-scale simulations across the networks extracted using the maximal ball algorithm.

In this preliminary study, for carbonates, we use images containing 400^3 voxels due to its heterogeneity and images consisting of 300^3 voxels for sandstone and synthetic samples. Fig. 5.12 gives an indication of pore sizes in the pore network pictures. The two-point correlation function of each image is calculated (Øren and Bakke, 2003) in this section, which measures the possibility of finding the two end points of a segment with a certain length in the same phase, pore or solid. The first decay length, at which the correlation function reaches zero for the first time, is used as an indication of the representative elementary volume (REV) of the rock image. Half of our images (A1, S1-4 and S8) have an image side length more than 10 times of its first decay length, which empirically is believed sufficient to contain a REV, which means that we can find statistically meaningful transport properties from them. It is suggested to carry on a study in the future to find out the necessary sizes of the models related to their structural and statistical properties. Representative 2D cross-sections, image resolutions, pictures of the networks and the two-point correlation functions for all the samples are shown in Figs. 5.13-5.36. The distributions of pore sizes, throat sizes and coordination numbers of each network will be extracted and presented in Section 6.4. The petrophysical properties, such as porosity, absolute permeability and formation factors are computed and discussed in Section 7.3.3.

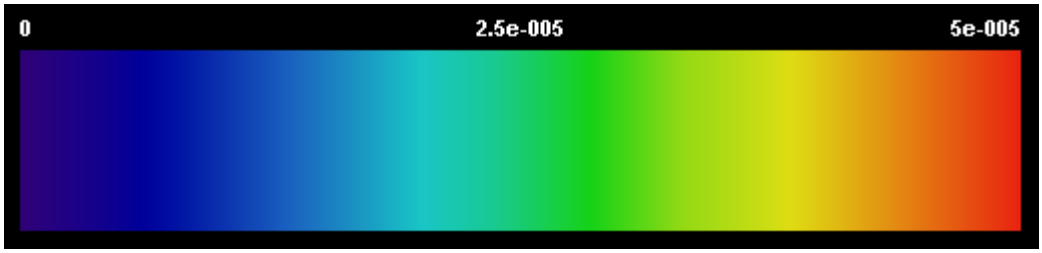

Figure 5.12. Colormap indicates the size of pores (in meters) in the pore network pictures.

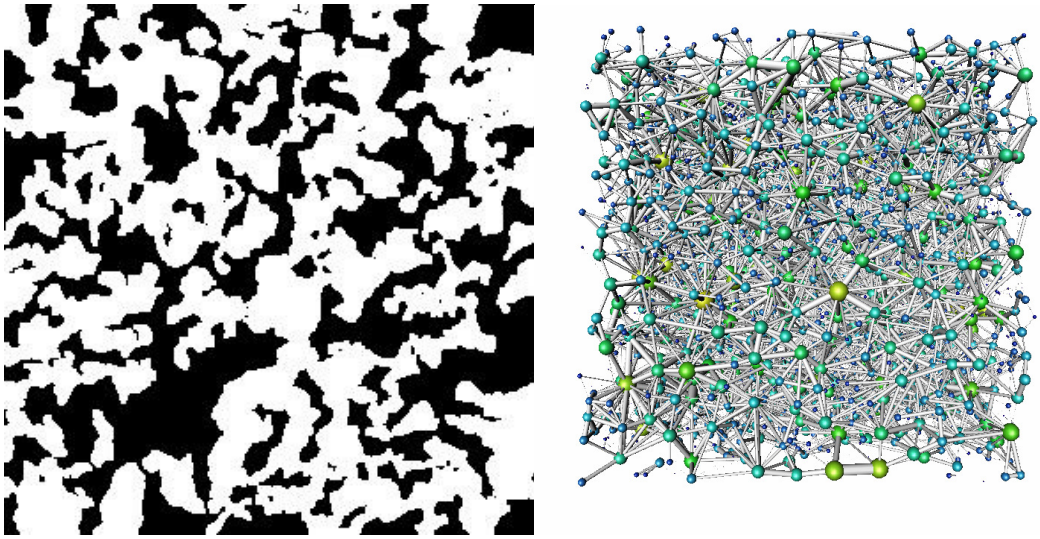

Figure 5.13. Cross-section and pore network of synthetic silica sample A1. The image resolution is 3.9 µm. The side length of the 3D image and the pore network is 1170 µm.

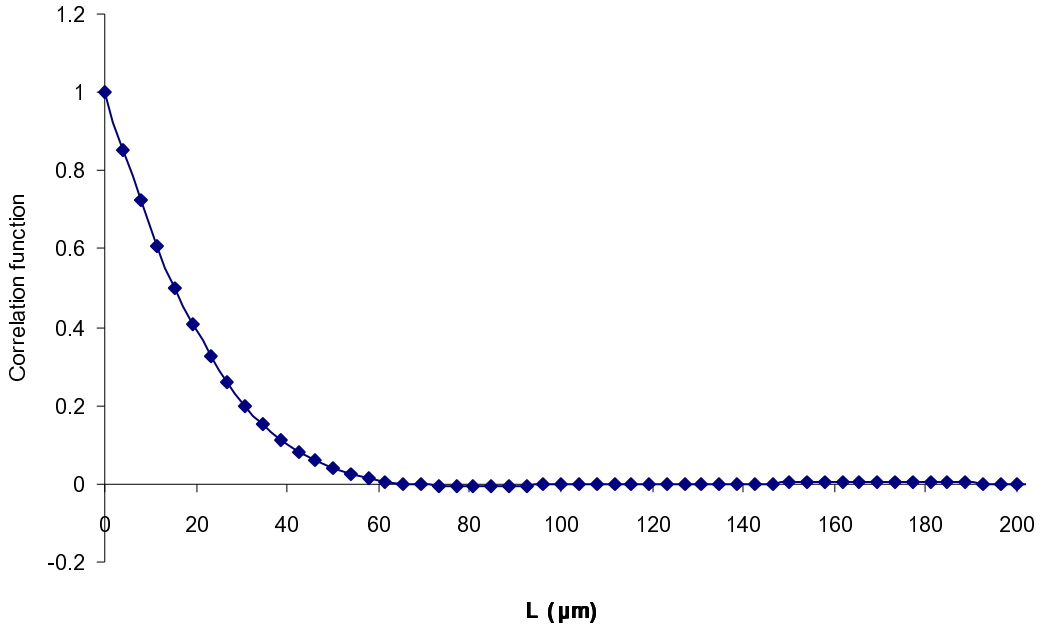

Figure 5.14. Two-point correlation function (average of X, Y and Z directions) for sample A1. The first decay length is 70 µm for sample A1.

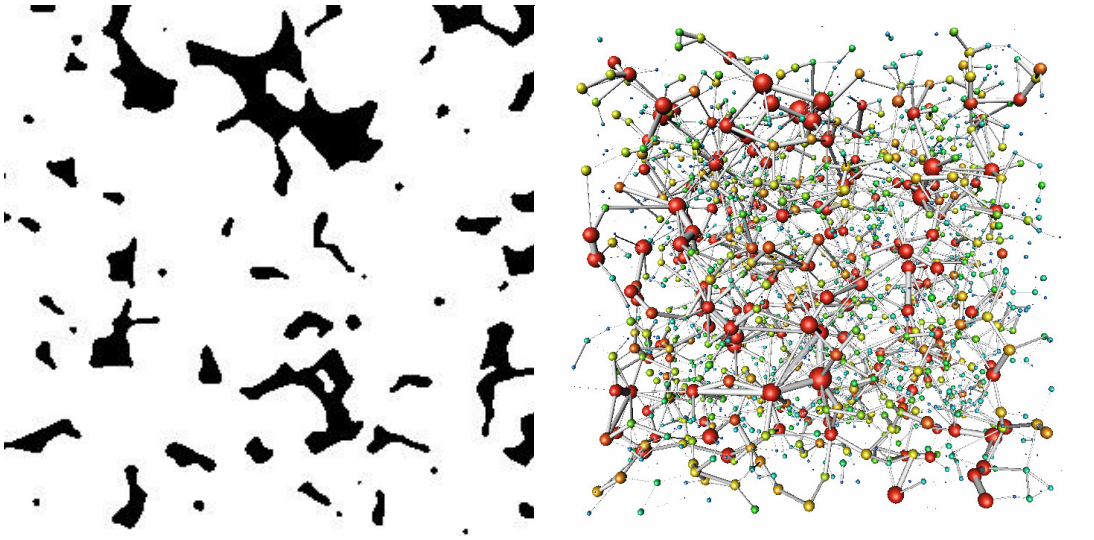

Figure 5.15. Cross-section and pore network of sandstone S1. The image resolution is 8.7 µm.The side length of the 3D image and the pore network is 2610 µm.

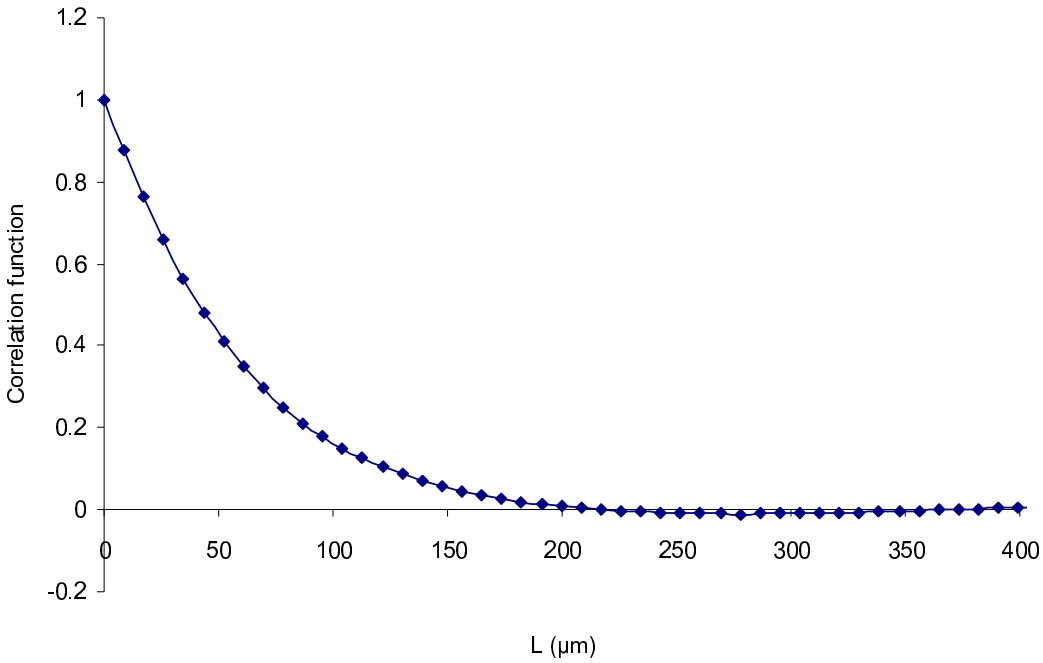

Figure 5.16. Two-point correlation function (average of X, Y and Z directions) for sample S1. The first decay length is 220 microns for sample S1.

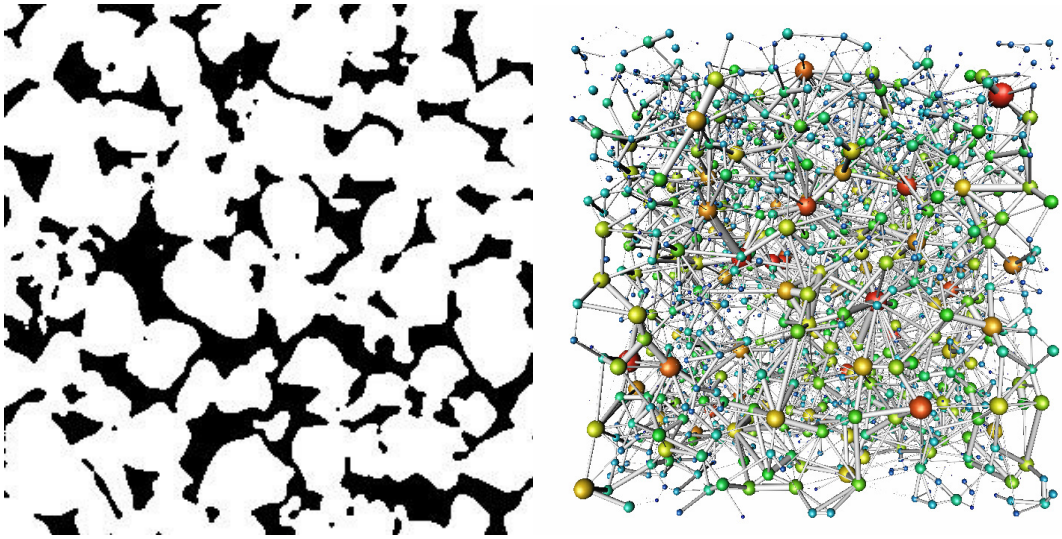

Figure 5.17. Cross-section and pore network of sandstone S2. The image resolution is 5.0 µm. The side length of the 3D image and the pore network is 1500 µm.

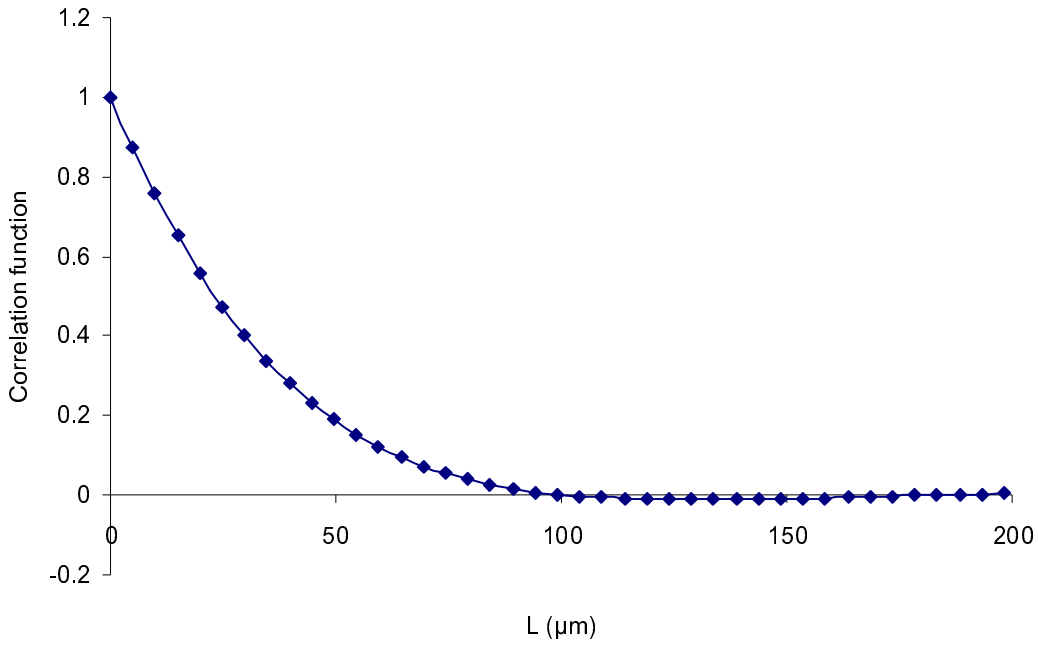

Figure 5.18. Two-point correlation function (average of X, Y and Z directions) for sample S2. The first decay length is 100 microns for sample S2.

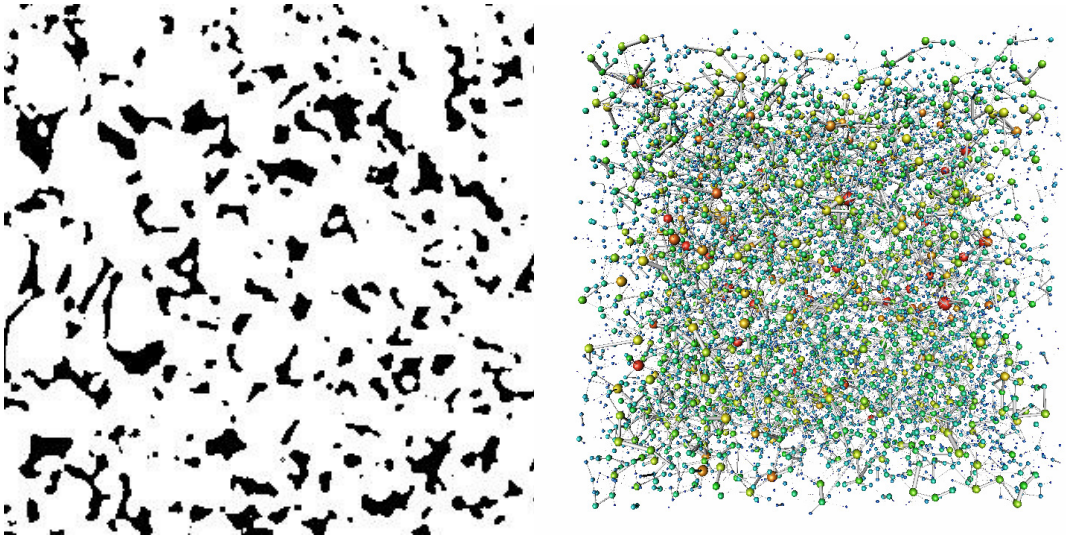

Figure 5.19. Cross-section and pore network of sandstone S3. The image resolution is 9.1 µm. The side length of the 3D image and the pore network is 2730 µm.

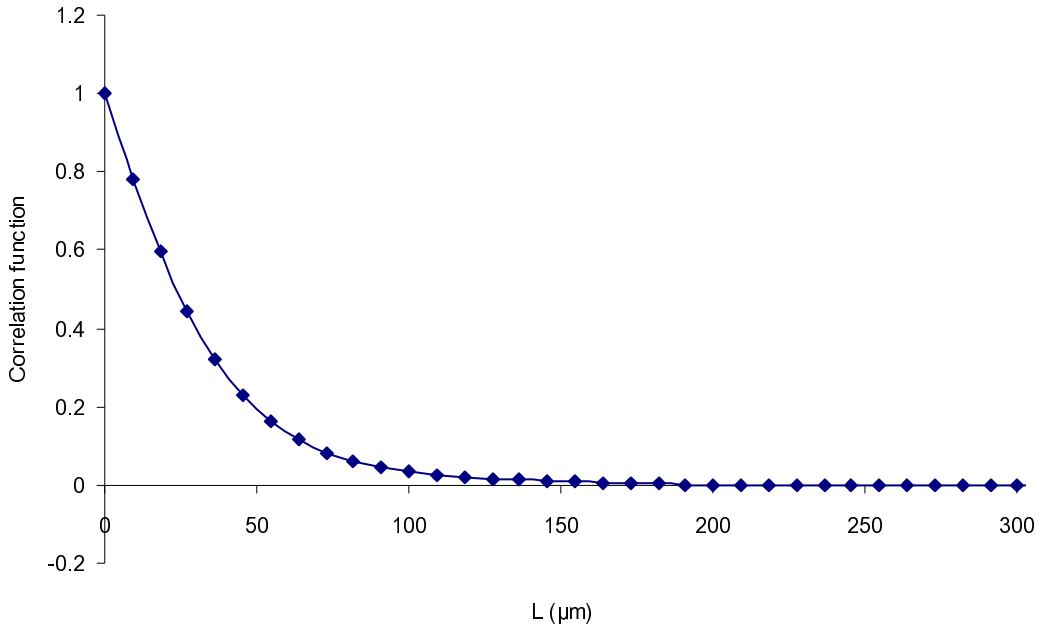

Figure 5.20. Two-point correlation function (average of X, Y and Z directions) for sample S3. The first decay length is 170 microns for sample S3.

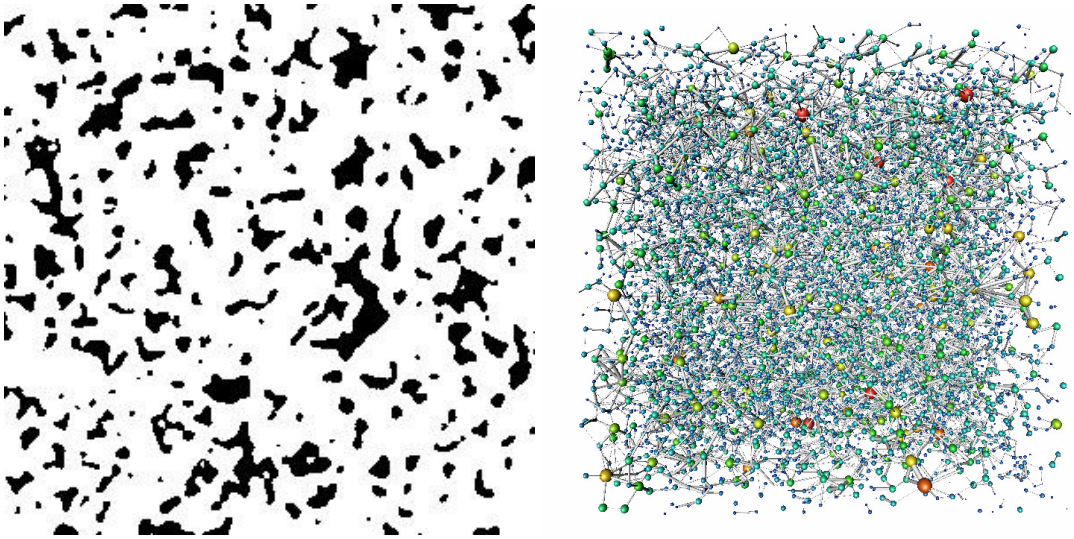

Figure 5.21. Cross-section and pore network of sandstone S4. The image resolution is 9.0 µm. The side length of the 3D image and the pore network is 2700 µm.

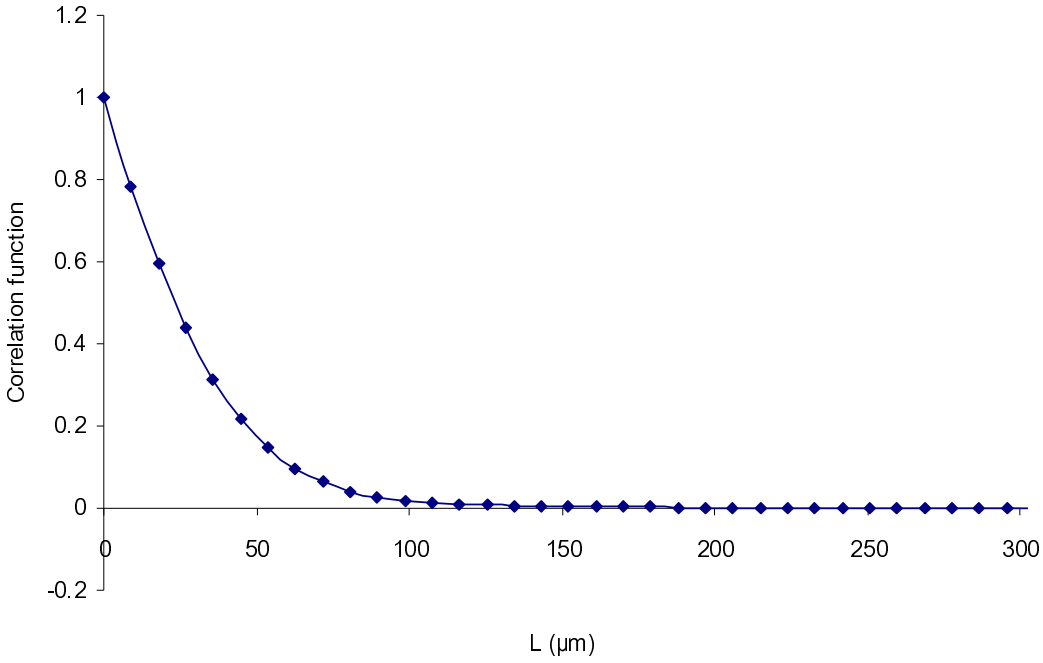

Figure 5.22. Two-point correlation function (average of X, Y and Z directions) for sample S4. The first decay length is 232 microns for sample S4.

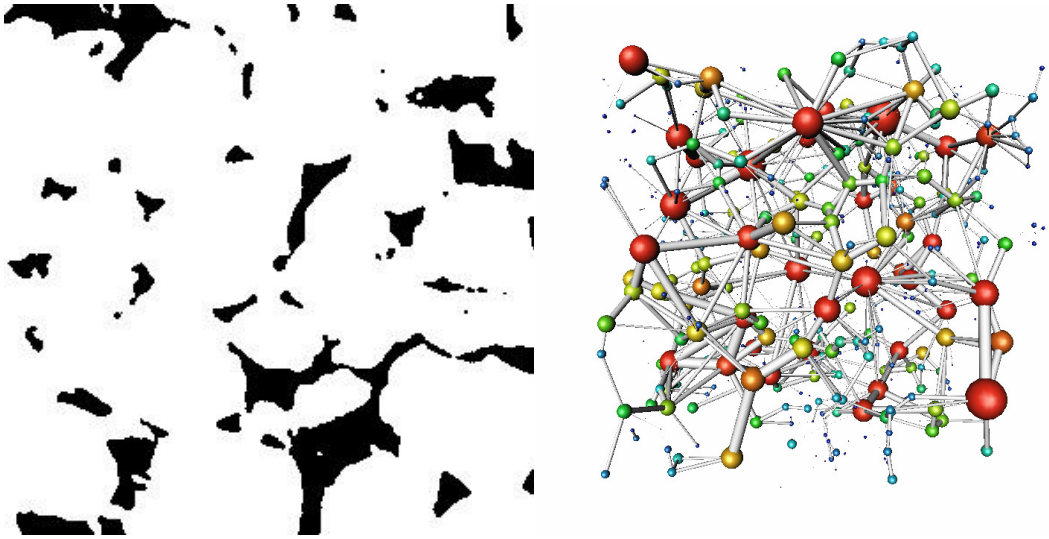

Figure 5.23. Cross-section and pore network of sandstone S5. The image resolution is 4.0 µm. The side length of the 3D image and the pore network is 1200 µm.

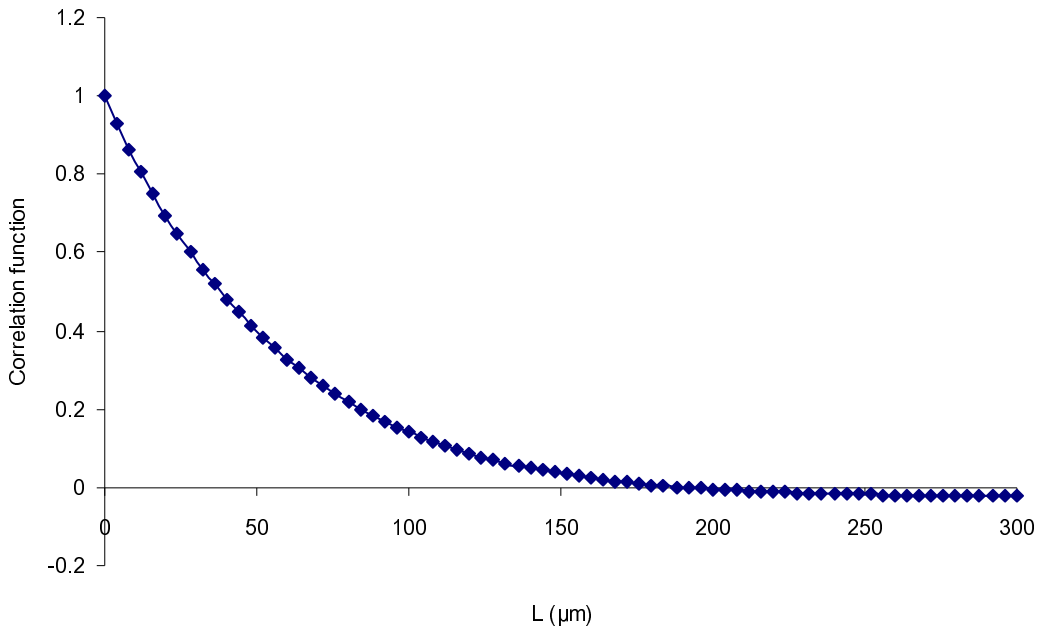

Figure 5.24. Two-point correlation function (average of X, Y and Z directions) for sample S5. The first decay length is 180 microns for sample S5.

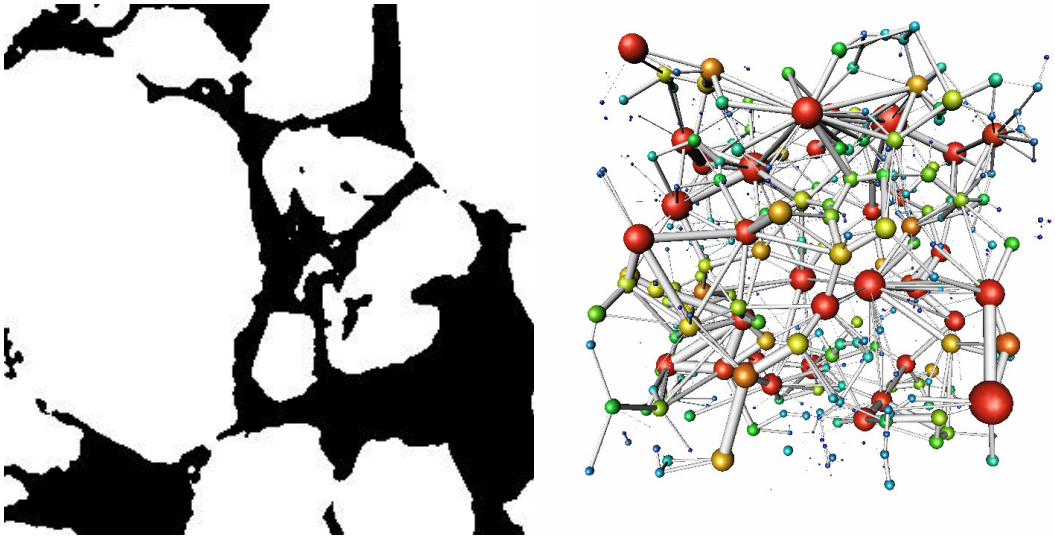

Figure 5.25. Cross-section and pore network of sandstone S6. The image resolution is 5.1 µm. The side length of the 3D image and the pore network is 1530 µm.

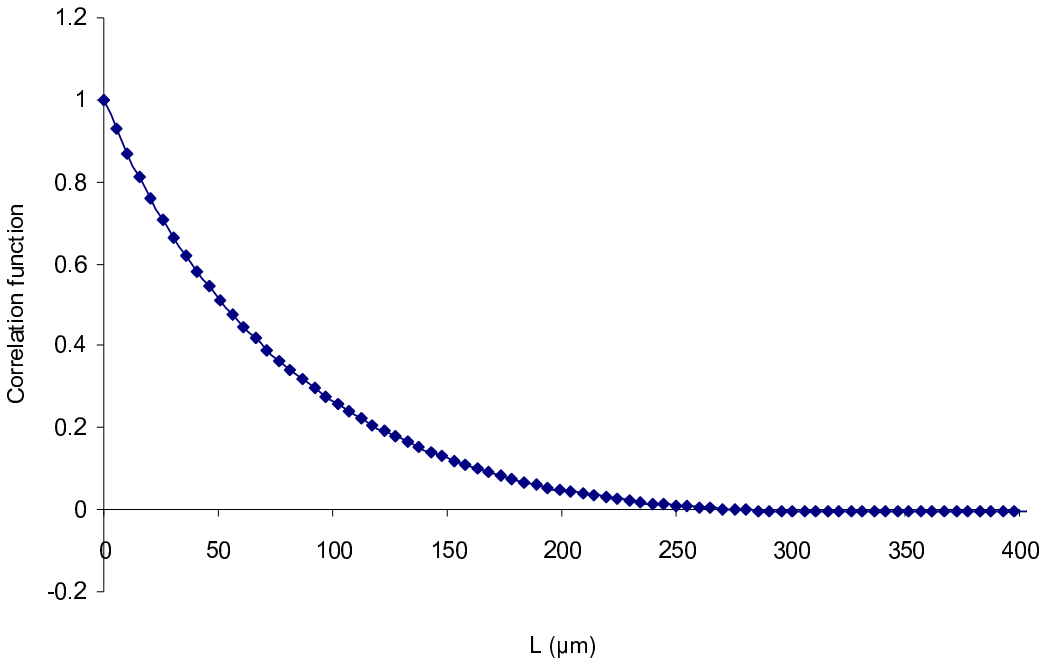

Figure 5.26. Two-point correlation function (average of X, Y and Z directions) for sample S6. The first decay length is 270 microns for sample S6.

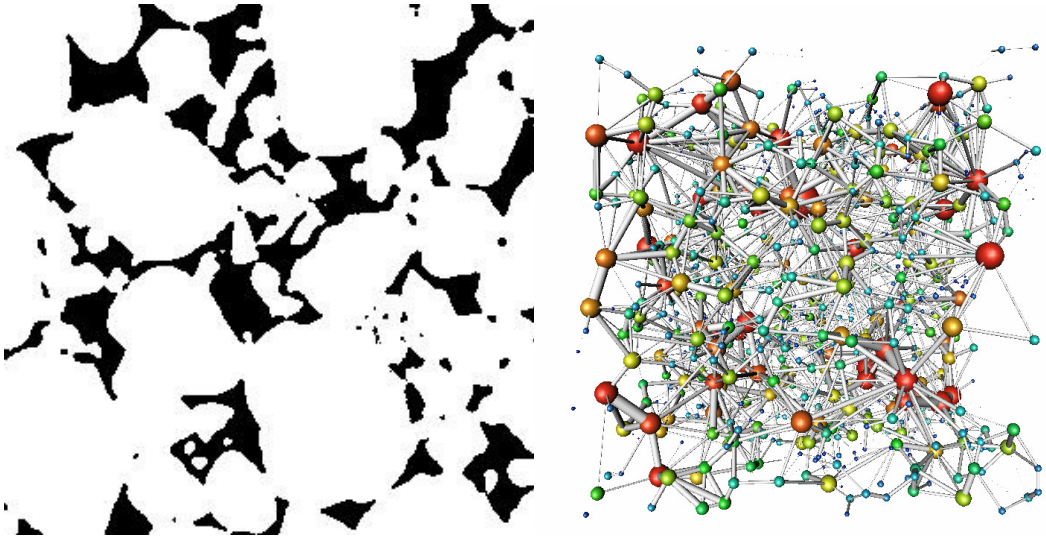

Figure 5.27. Cross-section and pore network of sandstone S7. The image resolution is 4.8 µm. The side length of the 3D image and the pore network is 1440 µm.

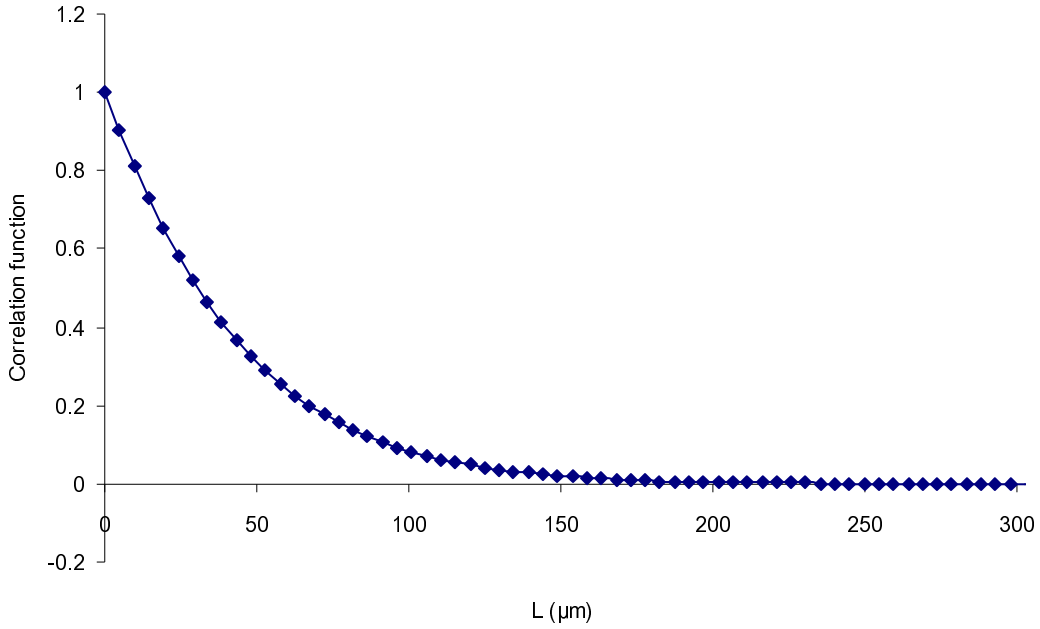

Figure 5.28. Two-point correlation function (average of X, Y and Z directions) for sample S7. The first time decay length is 185 microns for sample S7.

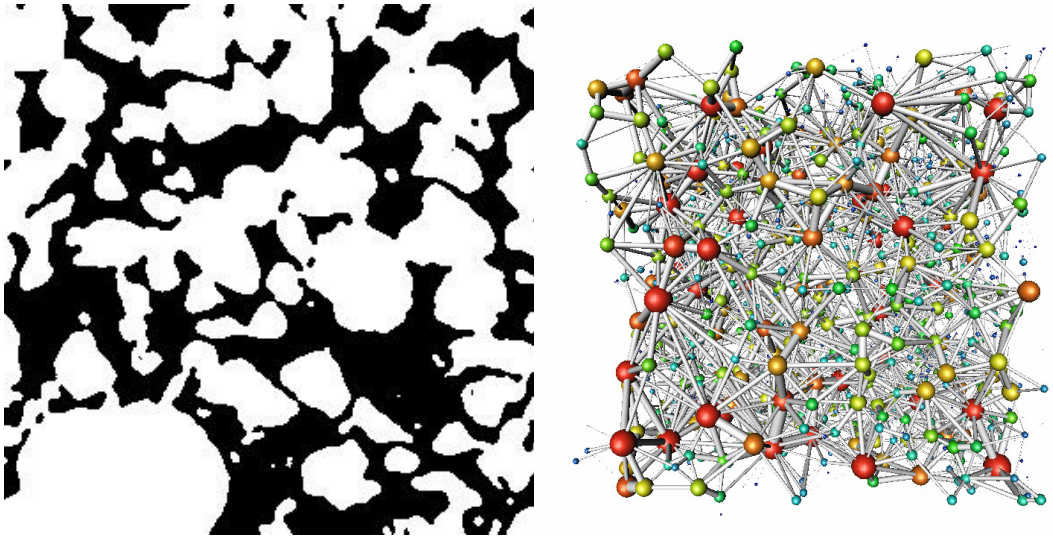

Figure 5.29. Cross-section and pore network of sandstone S8. The image resolution is 4.9 µm. The side length of the 3D image and the pore network is 1470 µm.

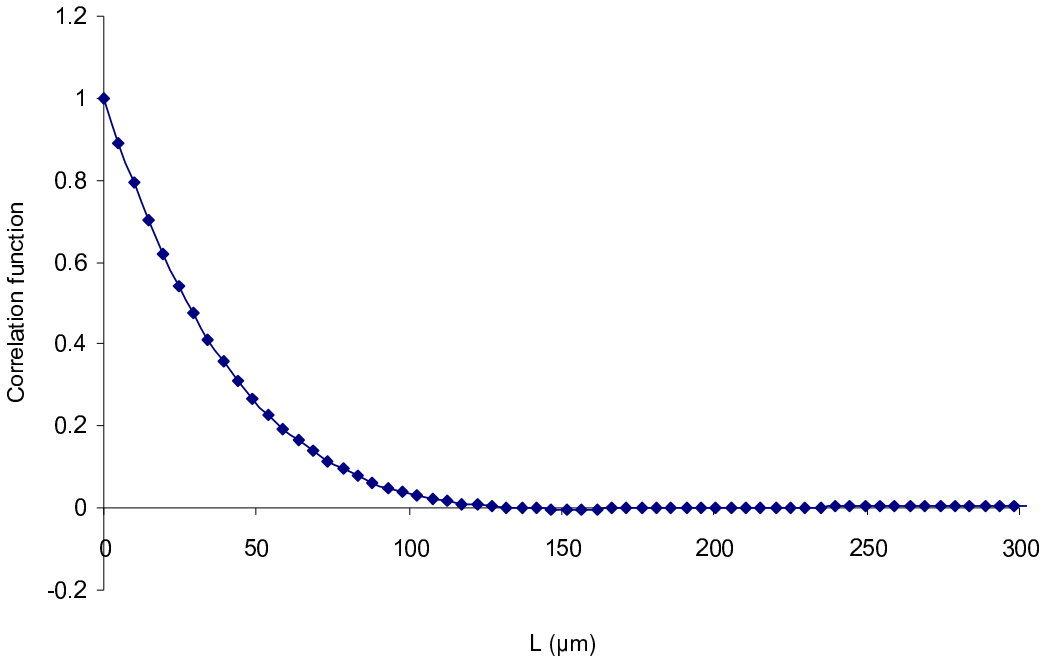

Figure 5.30. Two-point correlation function (average of X, Y and Z directions) for sample S8. The first decay length is 135 microns for sample S8.

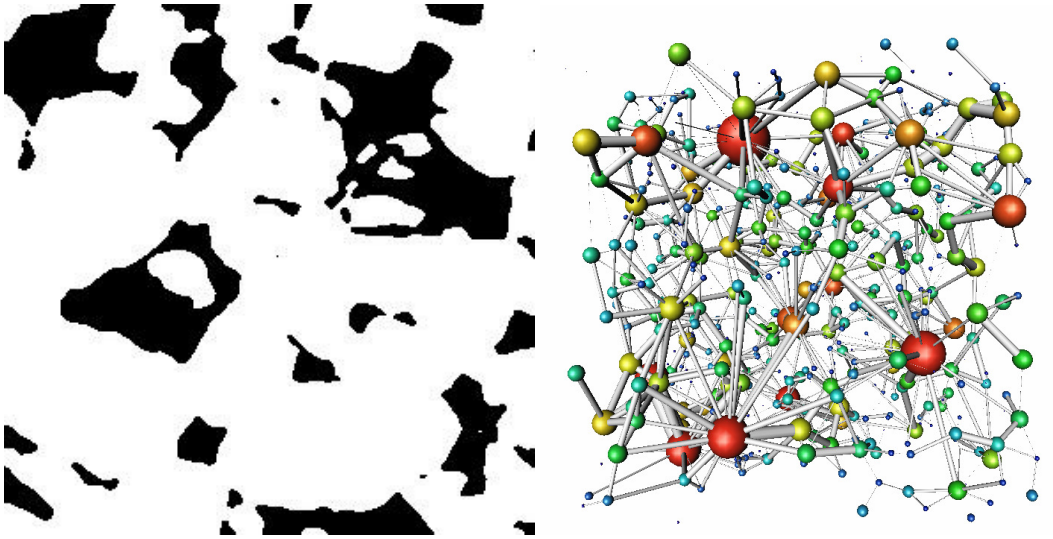

Figure 5.31. Cross-section and pore network of sandstone S9. The image resolution is 3.4 µm. The side length of the 3D image and the pore network is 1020 µm.

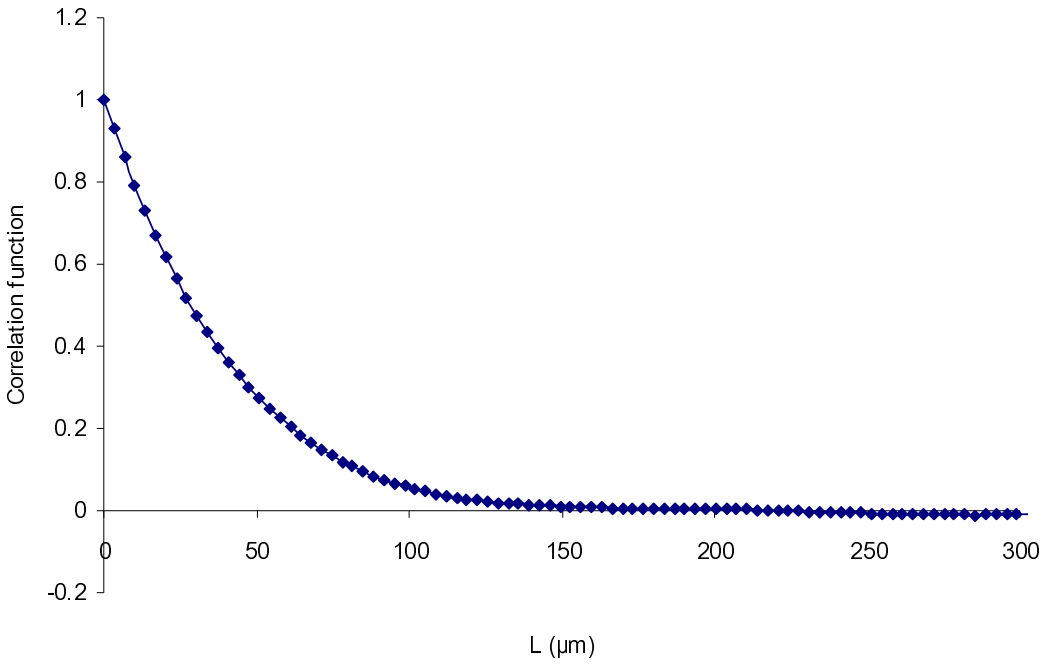

Figure 5.32. Two-point correlation function (average of X, Y and Z directions) for sample S9. The first decay length is 225 µm for sample S11.

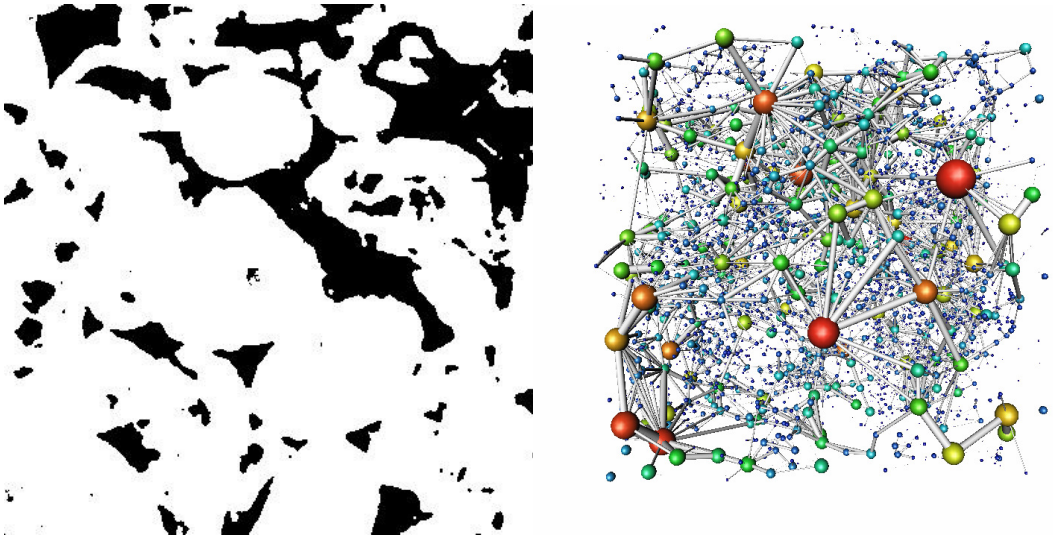

Figure 5.33. Cross-section and pore network of carbonate C1. The image resolution is 2.9 µm. The side length of the 3D image and the pore network is 1160 µm.

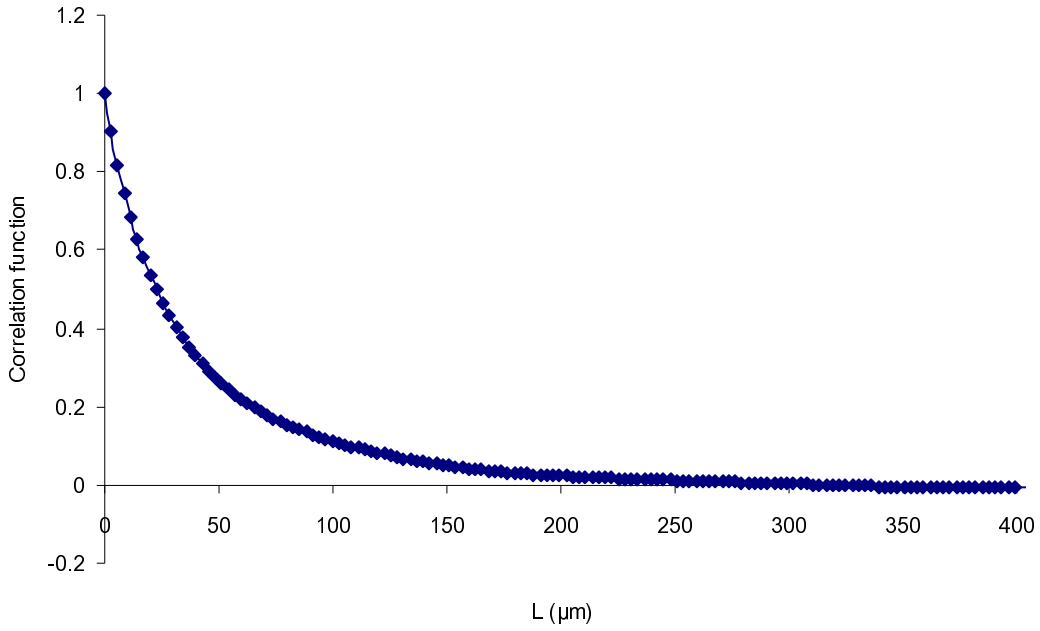

Figure 5.34. Two-point correlation function (average of X, Y and Z directions) for sample C1. The first decay length is 260 µm for sample C1.

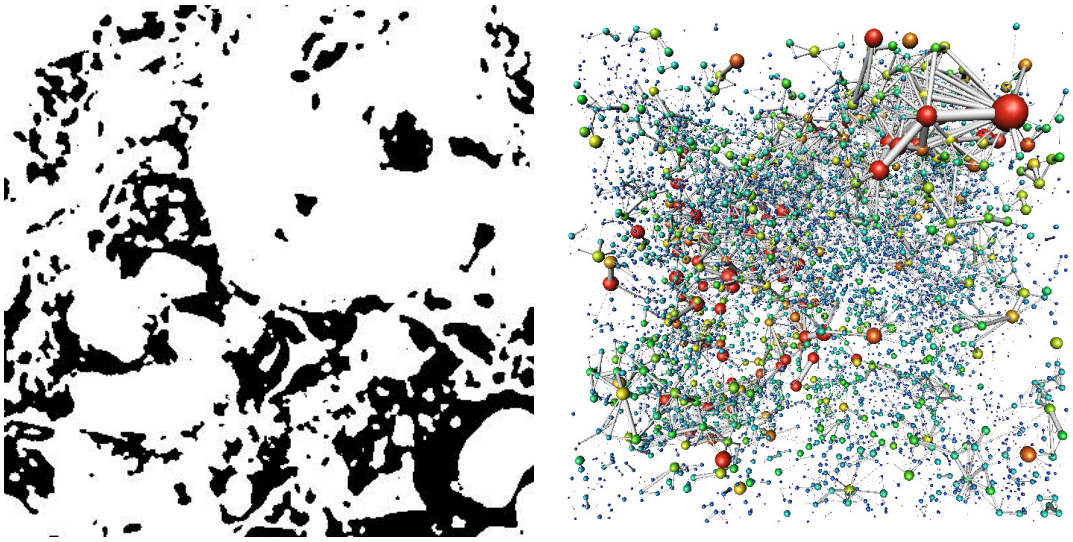

Figure 5.35. Cross-section and pore network of carbonate C2. The image resolution is 5.3 µm. The side length of the 3D image and the pore network is 2120 µm.

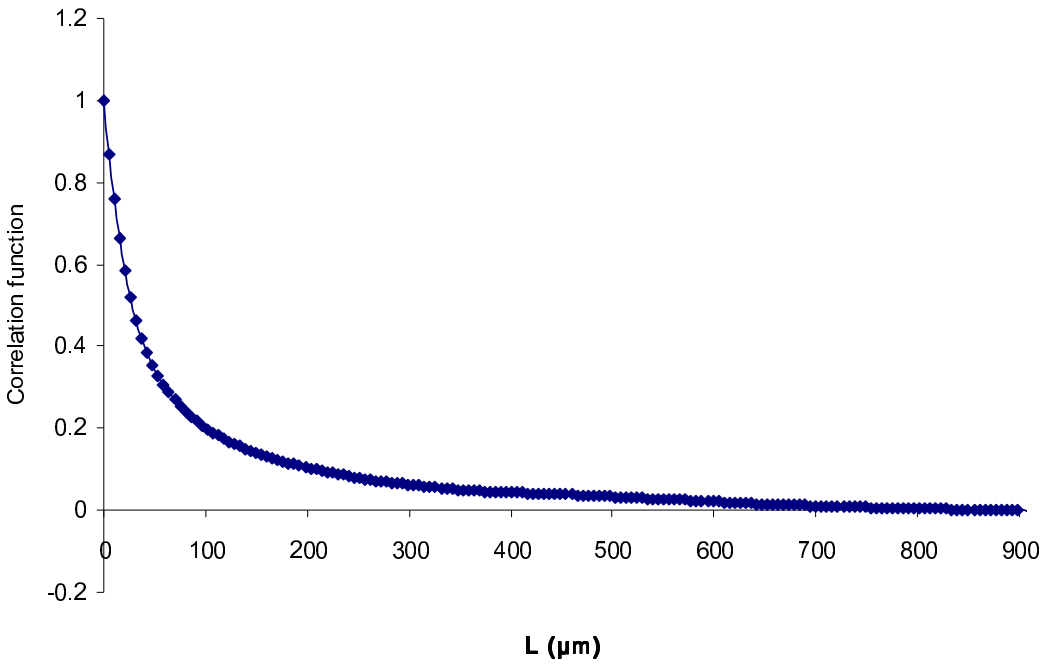

Figure 5.36. Two-point correlation function (average of X, Y and Z directions) for sample C2. The first decay length is 881 µm for sample C2.

6 Image analysis of samples

In this chapter, to verify the maximal ball algorithm, we validated our method on benchmark images. First, several 3D images of regular packings of equally sized spheres are used. The number of pores is compared with theoretical solutions and networks from the PB method (Øren and Bakke, 2003).

We then extracted a pore network from a PB reconstructed Fontainebleau sandstone image and benchmark our MB network against the PB network from the same image.

We also extract a network from a micro-CT image of Berea sandstone and compare our MB network with the classic Berea network widely used from a PB reconstructed Berea sandstone image (Øren and Bakke, 2003).

6.1 Validation on sphere packings

6.1.1 Datasets

We first validated our method on regular packings of equally-sized spheres (Section 5.1.1). The packs were provided by Øren and Bakke using the process-based method. They are cubic, orthorhombic, tetragonal-sphenoidal, rhombohedral-pyramidal and rhombohedral-hexagonal packs. The numbers of pores in the packs were provided along with the image datasets.

6.1.2 Number of pores

Due to differences on how different extraction methods treat the boundary of

the packs, we compared pores in the interior only.

The first dataset is a cubic packing. The basic structure is shown in Fig. 6.1. One pore can be defined by 8 grains periodically. The porosity of an infinite packing is 47.6% and the number of pores is

$$N = (X-1)(Y-1)(Z-1) \tag{6.1}$$

where *X, Y, Z* are the number of grains in three directions respectively.

In this section studied, *X*=*Y*=*Z*=3 and it is visually apparent that there are 8 interior pores – these are found by our method and by the PB method, as shown in Fig. 6.1.

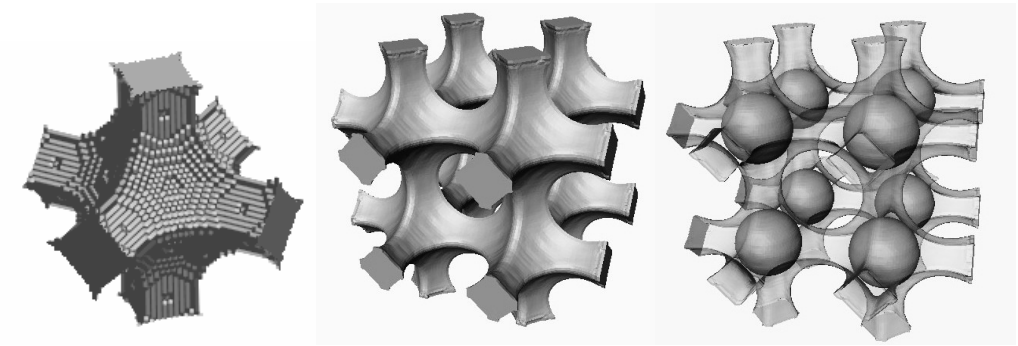

Figure 6.1. The left picture shows the basic structure containing a pore defined by 8 spherical grains for a cubic packing; the middle picture is the pore space that we study; the right shows the pores we defined that are superimposed on the pore space image.

In an orthorhombic packing, every 8 grains defines two pores in the structure as shown in Fig. 6.2. The porosity of infinite packing is 39.5% and interior number of pores is twice of that of a cubic packing: $2(X-1)(Y-1)(Z-1)$. For the section studied, X=Y=Z=3 and both methods found 16 interior pores, Fig. 6.2.

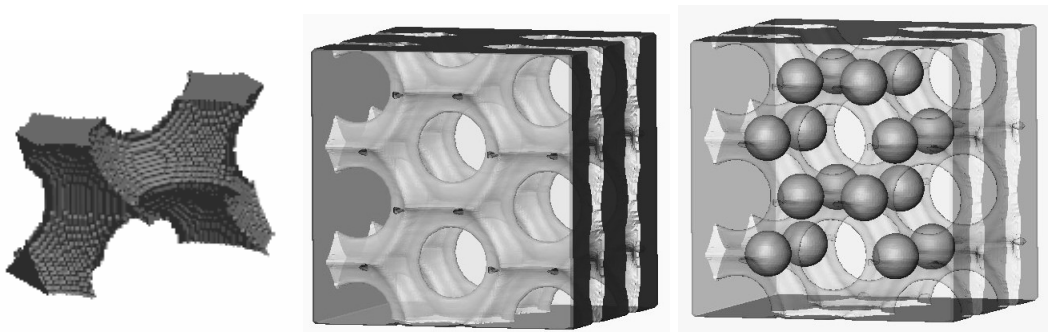

Figure 6.2. The left picture shows the basic structure for an orthorhombic packing containing two pores defined by 8 spherical grains; the middle picture is the pore space that we study; the right shows the pores we defined superimposed on the pore space image.

For the rest of the packings, the two methods found 86, 36 and 42 interior pores in tetragonal-sphenoidal, rhombohedral-pyramidal and rhombohedral-hexagonal packings respectively. In all cases both methods gave results identical to theoretical predictions.

6.2 Validation on a reconstructed Fontainebleau sandstone image

We used a reconstructed Fontainebleau sandstone image generated from the PB method to compare the PB and MB network generation methods. The image consists of 300^3 voxels with a voxel edge size of 7.5 μm representing a volume of 11.39 mm^3, Fig. 6.3. The porosity measured on the image is 13.5%. Fontainebleau sandstone serves as basis for many petrophysics experiments due to its monocrystalline type (Bourbie et al., 1987), so that the image only consists of quartz grains with no clay porosity causing intragranular pores. We compare the properties of the two networks, Figs. 6.4 and 6.5, in terms of topological and geometrical

parameters and simulate single- and two-phase flow through the networks to compare their transport properties. The results of the static network properties are tabulated and followed with the statistical comparisons in the next sections. The transport properties are presented and discussed in Chapter 7.

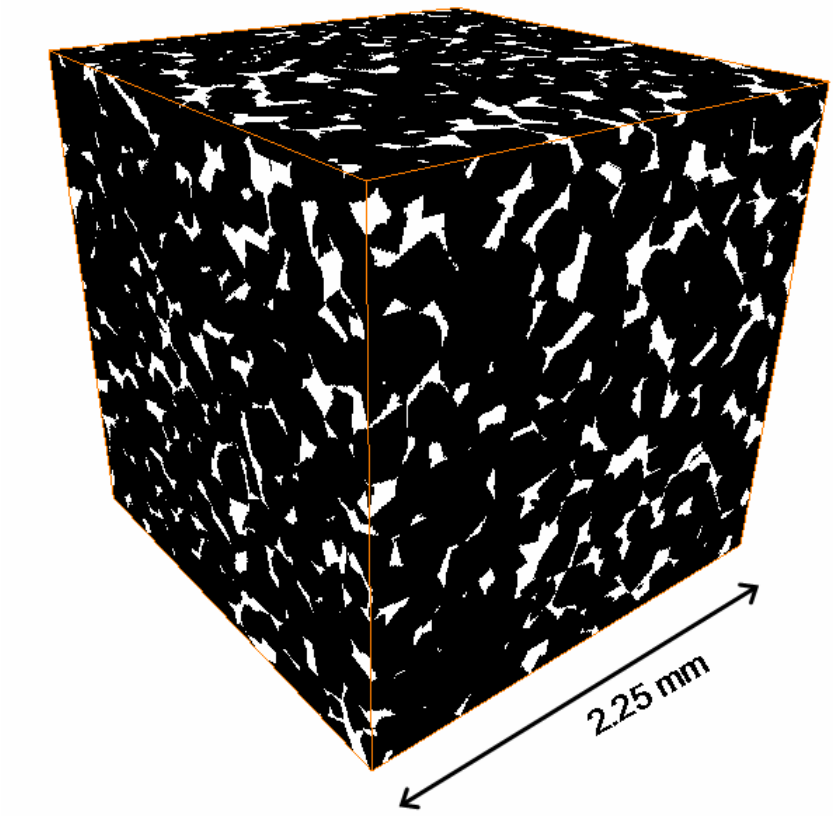

Figure 6.3. The 3D image of reconstructed Fontainebleau sandstone.

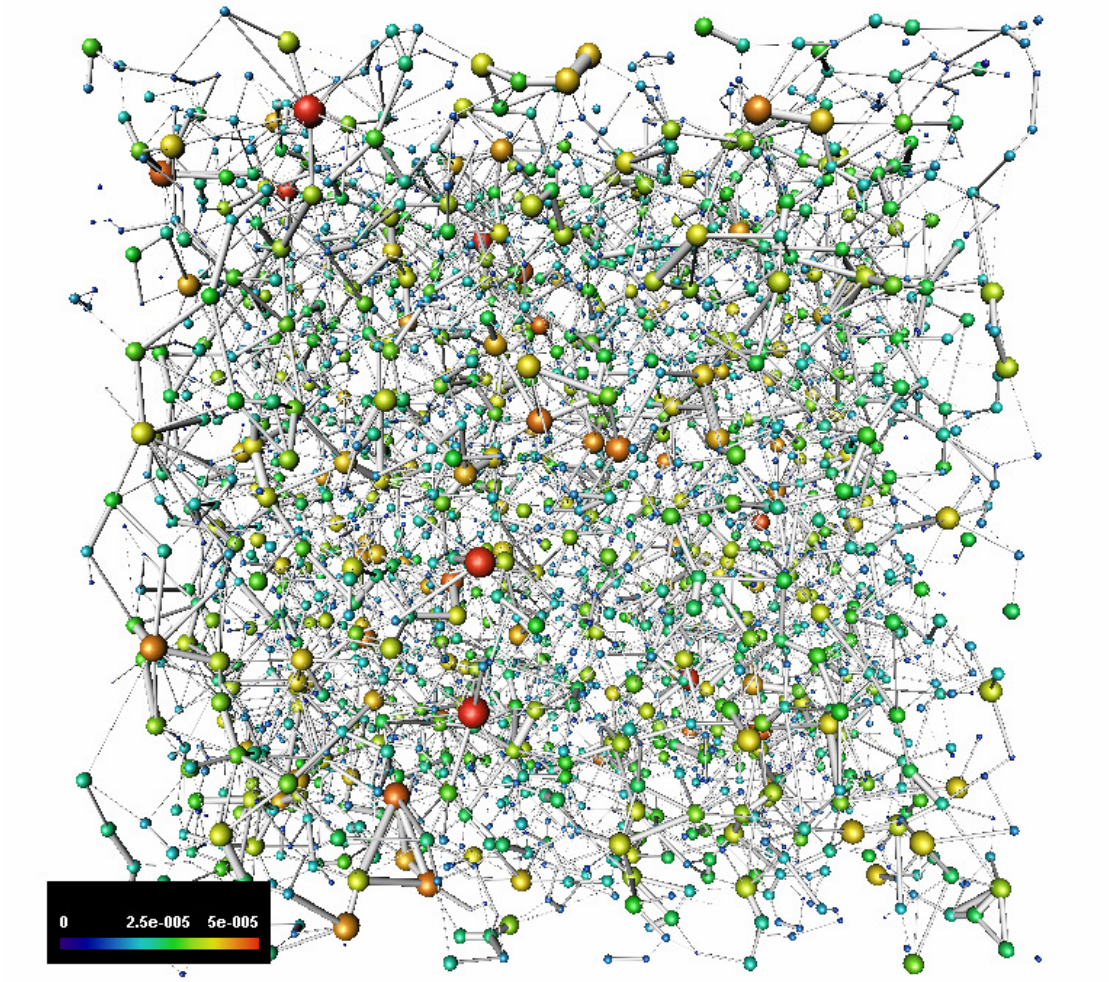

Figure 6.4. The extracted network using the maximal ball algorithm. The color map shows the size of the pores in the network in meters.

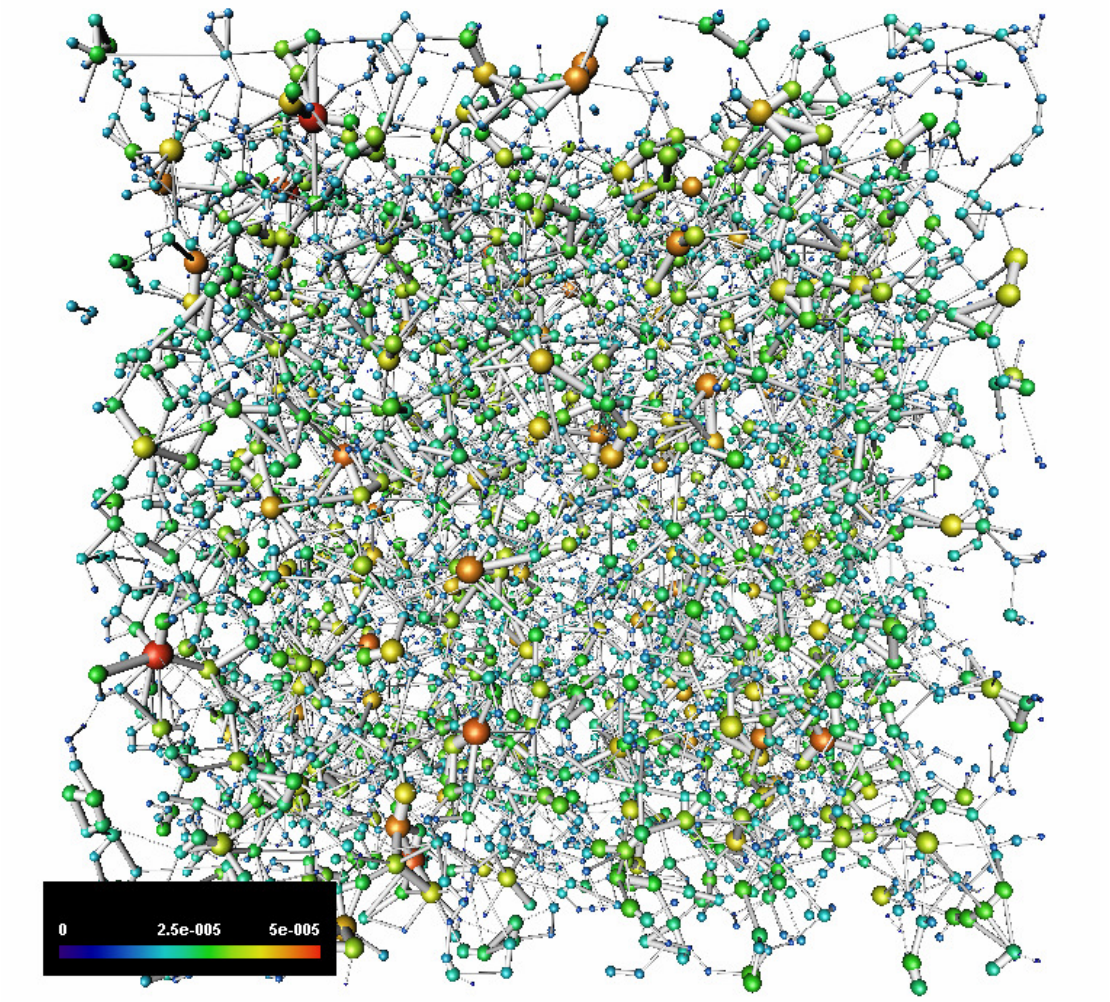

Figure 6.5. The extracted network using the process-based algorithm. The color map shows the size of the pores in the network in meters.

6.2.1 Number and positions of pores

First, we compute the MB network and compare the number of pores and throats as well as their position distribution with the PB network.

It is found in Table 6.1 that the PB method defines more pores and throats than MB method, especially on the surface of the model. There are two reasons for the discrepancy. One is the boundary effect. The MB method regards boundaries as solid

while the PB method tends to think them open. The second reason is the different consideration for merging neighboring pores.

Table 6.1. Properties of Fontainebleau sandstone networks: number of pores and throats.

Number of elements	**PB**	**MB**
No. of pores	4997	3101
No. of throats	8192	6112
No. of surface pores	433	289

We plot the number of pores as a function of position in Fig. 6.6. The MB method defines fewer pores uniformly in the interior region of the image. On the boundary, more dissimilarity is observed due to different definition of boundary pores, but this alone does not explain the difference in the total number of pores.

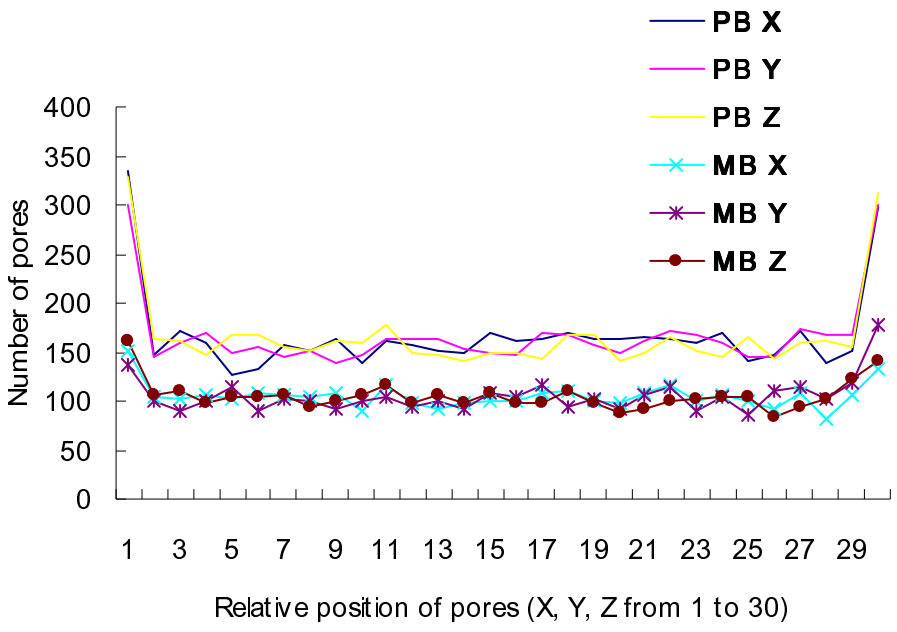

Figure 6.6. Comparison of pore relative positions defined by PB and MB methods on a reconstructed Fontainebleau image.

To explain this discrepancy, Fig. 6.7 shows how overlapping pores in the PB method are fused as one.

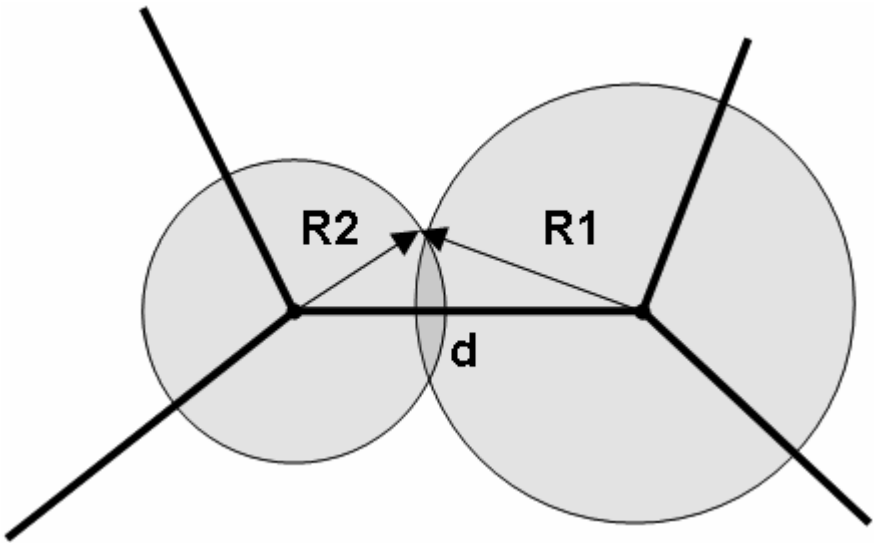

Figure 6.7. Pore fusion in the PB method. Overlapped pores on the skeleton are merged as one pore.

In the MB method, there are no explicit fusions. During the clustering (the concept of clusters can be found in Section 4.1.2), the narrow regions of the pore space are ignored when pore-throat chains are constructed. For example in Fig. 6.8, $R_1 \geq R_2 > R_3$. R_3 is centered in the $2R_1$ range and absorbed by R_1. If R_2 is a free MB (not from another family tree) but touches R_3, R_2 will be part of the pore body fathered by R_1. The narrow R_3 is therefore not a throat but is treated as pore extension linking R_1 and R_2. However, in the PB method, R_3 could represent a throat with R_1 and R_2 representing separate pores. This is the reason why the MB method gives fewer pores. It is not apparent what is a strictly correct definition; what matters is how well the networks predict transport properties, and this is discussed later.

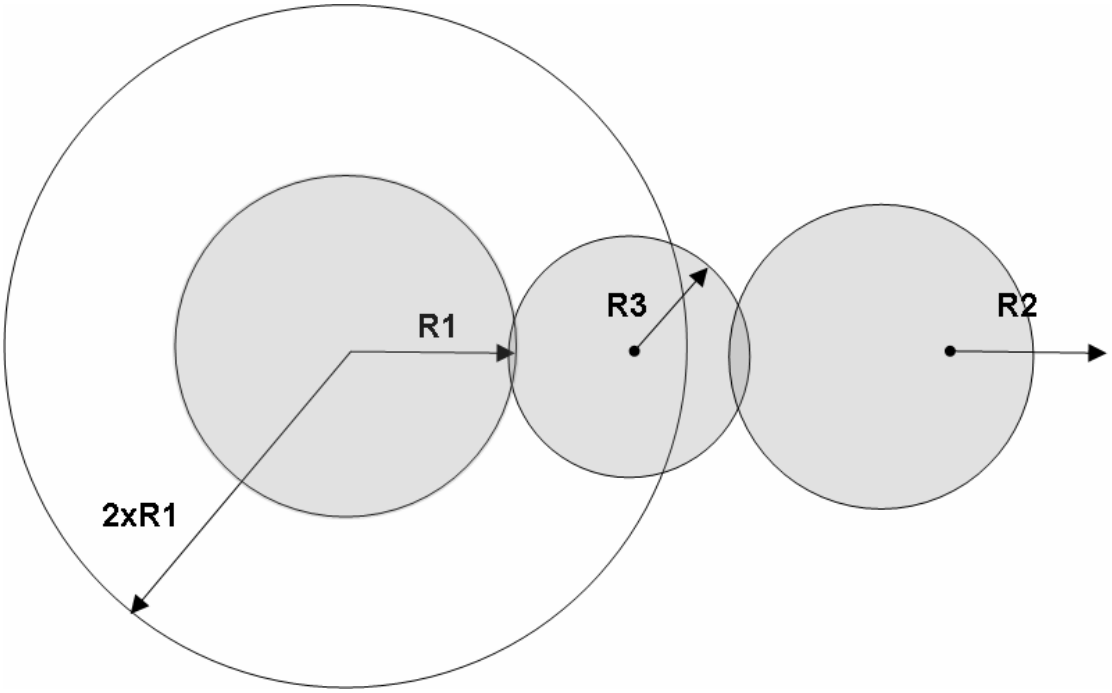

Figure 6.8. R_2 is fused to R_1 and bridged by R_3 during the clustering: the whole entity is classified as a single pore, while other extraction methods could label R_3 a throat connecting two separate pores centered at R_1 and R_2.

In the regular packings, this dissimilarity cannot be seen due to the long distance of connections between pores and the significant change of size from throats to pores. However, the discrepancy is not significant as long as the pore network is capable to capture the topology of pore space and predict transport properties.

6.2.2 Connectivity

Coordination number Z (also called connection number) is the number of independent throats linked to a pore. The distribution of coordination numbers is a measure of pore network connectivity, which has critical influence on transport properties (Arns et al., 2004b; Mahmud et al., 2007). We compare the distributions for PB and MB networks of the reconstructed Fontainebleau.

Table 6.2. Properties of Fontainebleau sandstone networks: connectivity.

Connectivity	**PB**	**MB**
Average connection number	3.19	3.85
Minimum connection number	1	0
Maximum connection number	10	12
No. of connections to inlet	227	146
No. of connections to outlet	206	143
No. of isolated elements	46	35

The average coordination number is close and so is the maximum coordination number. The minimum coordination number is 0 in the MB network and 1 in the PB network. However, both networks find some physically isolated elements in the networks when simulating fluid flow through the network using the two-phase simulator developed by Valvatne and Blunt (2004).

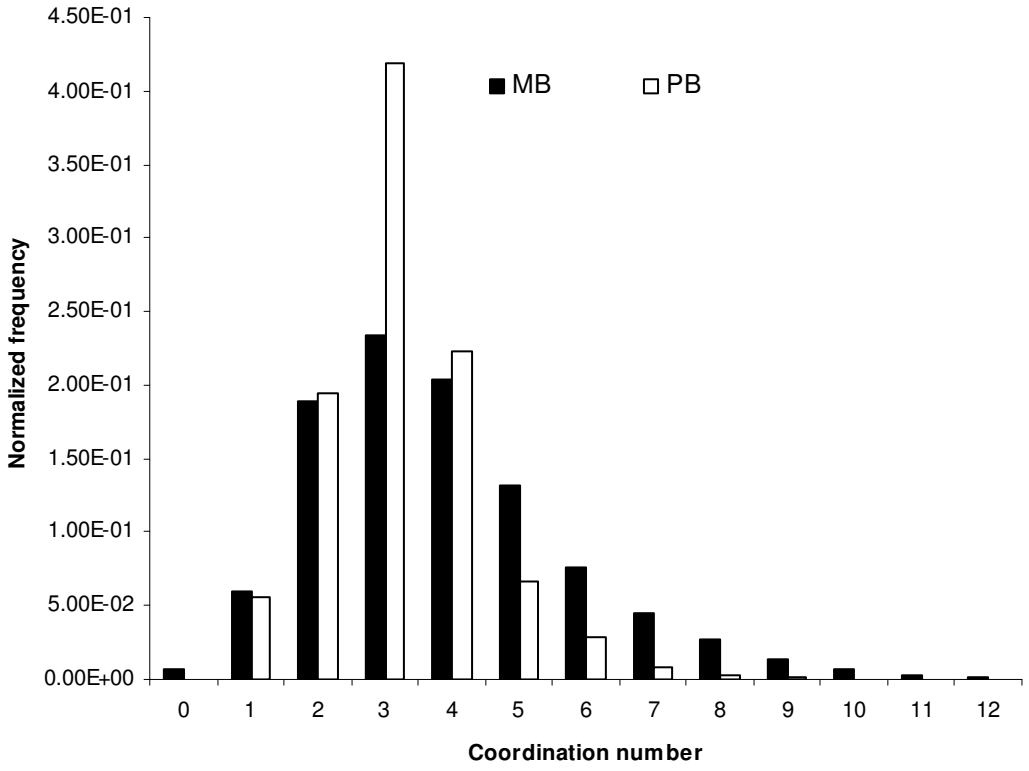

Figure 6.9. Comparison of coordination number distributions of PB and MB methods

on a reconstructed Fontainebleau image.

In the distribution, both the methods found the single peak value 3, although the MB method defines more pores with a higher *Z*.

The result is consistent with the MB method finding fewer pores. From the schematic picture below, it can be seen if the two pores from the PB method are defined (or merged) as one pore in MB, their coordination numbers are added up for a new (and higher) coordination number of the MB pore.

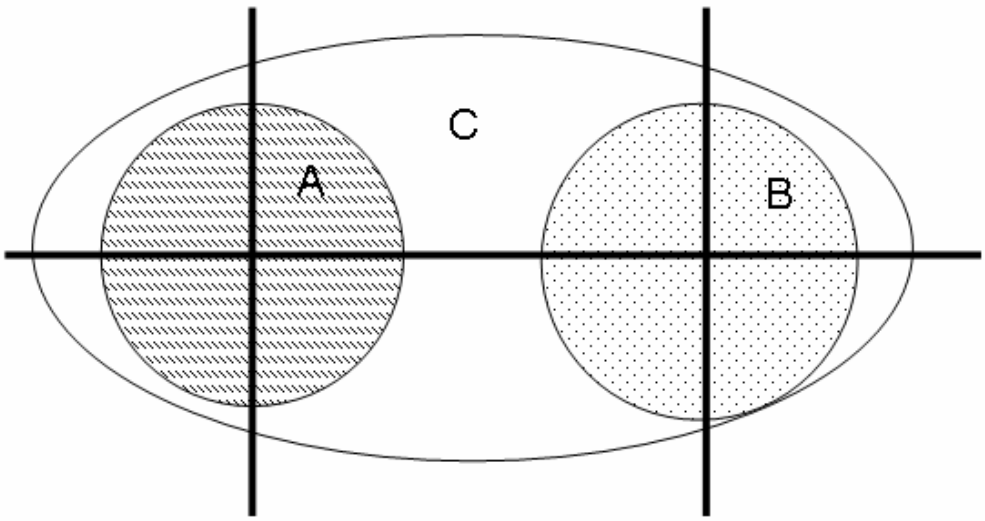

Figure 6.10. Schematic picture of coordination number increasing. Pores A and B both have a coordination number of 4 (four throats) in a PB network. In the MB method, it is possible for them to be merged as one pore as explained previously in Fig. 6.7 and 6.8. The new pore C will have a coordination number 6. This merging contributes to the offsets of coordination number distributions seen in Fig. 6.9.

6.2.3 Pore and throat sizes

1. Pore size

The sizes of the network elements are defined by their inscribed radii. The statistical comparison is tabulated in Table 6.3 and plotted in Fig. 6.11 in this section.

Table 6.3. Properties of Fontainebleau sandstone networks: pore size.

Pore size	**PB**	**MB**
Average pore radius	19.89 μm	19.04 μm
Minimum pore radius	2.727 μm	0.77 μm
Maximum pore radius	49.92 μm	54.07 μm

The statistics of the pore inscribed radii indicates a good agreement especially for mean and maximum values, although discrepancy is found between the two methods on the minimum pore size (both are smaller than their theoretical minimum – the image resolution is 7.5 μm). This is due to different post-processing on sizes (for MB, see Section 4.5) to eliminate the discreteness caused by the voxelization of the image.

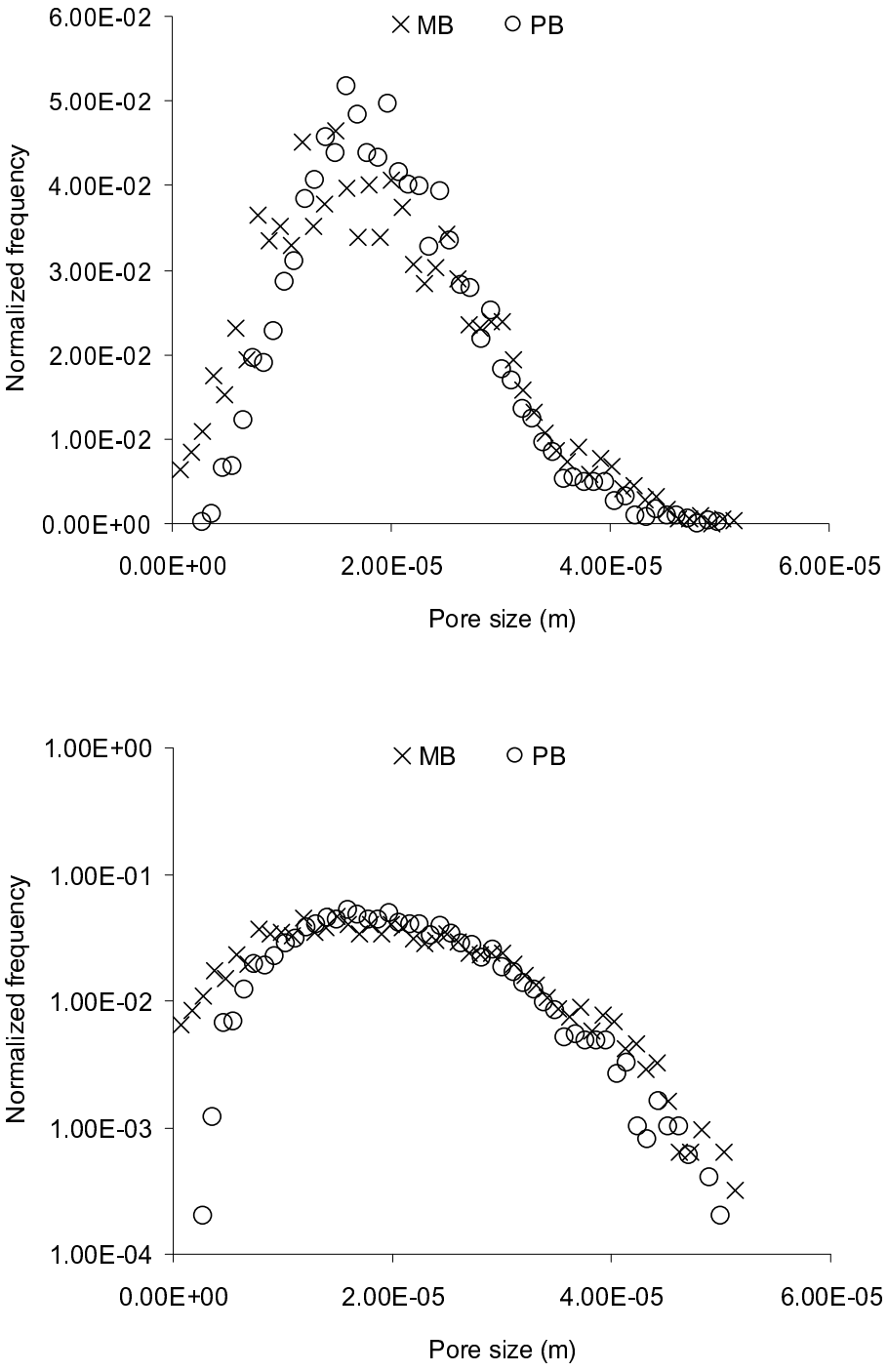

Figure 6.11. Comparison of pore size distributions (top) of MB and PB networks extracted from reconstructed Fontainebleau sandstone. On the lower figure, the pore size distribution is also plotted but with the frequency given on a logarithmic scale.

Fig. 6.11 shows similar pore size distributions from both methods, even

though the MB network distributes pore size with a slightly wider distribution than for the PB method, which is consistent with the differences in predicted drainage relative permeability shown in Section 7.4.1.

The different merging criteria and boundary pore definition contributes as well to the dissimilarity in size distribution, which can be significant when the network has a finite size (i.e. only a few thousands of pores in the network).

2. Throat size

Table 6.4 compares the throat size statistics of the two networks. The MB network defines smaller throats in terms of average, maximum and minimum values than the PB network.

Table 6.4. Properties of Fontainebleau sandstone networks: throat size.

Throat size	**PB**	**MB**
Average throat radius	11.22 μm	7.29 μm
Minimum throat radius	1.035 μm	0.75 μm
Maximum throat radius	40.05 μm	33.50 μm

Fig. 6.12 compares the distributions of the throat sizes of the networks. MB network defines more small throats and less large throats than PB.

The different minimum throat size comes from different size post-processing, since the theoretical minimum is the voxel size. The differences in the average and maximum throat sizes in Table 6.4 as well as the fractions of large throats in Fig. 6.12 is because large elements identified as ‘throats’ by the PB method are merged into pore-bodies in the MB method.

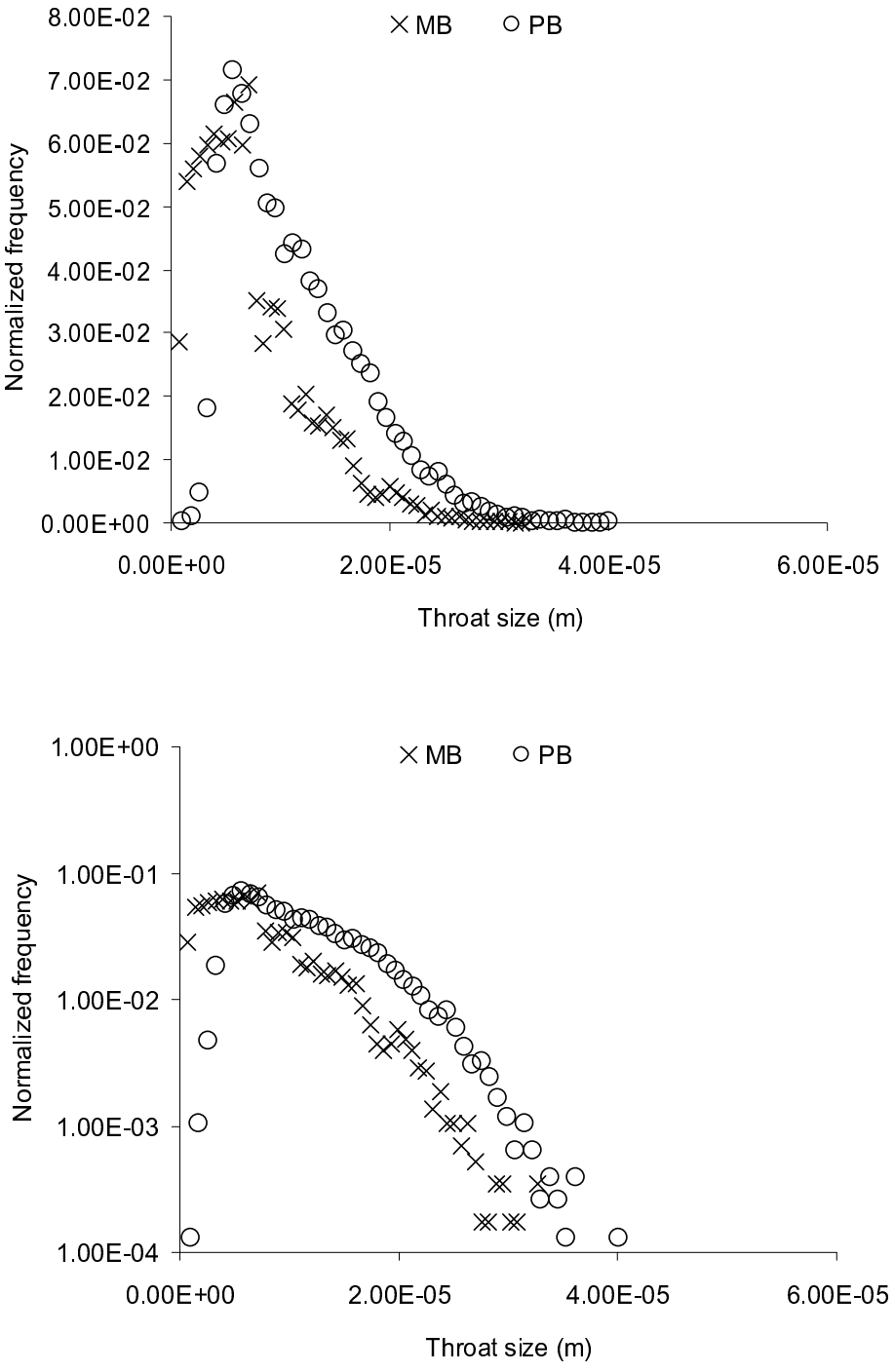

Figure 6.12. Comparison of throat size distributions (top) of MB and PB networks extracted from the reconstructed Fontainebleau sandstone. The lower figure shows the distribution but with the frequency on a logarithmic axis.

6.2.4 Pore and throat volumes

The statistics of pore and throat volumes are summarized in Table 6.5. As mentioned earlier in the algorithm description, the MB network gives volume to pores rather than throats. The throat volume is 13.7% of the total pore volume in the MB network while it is 27% in the PB network of Fontainebleau sandstone. Since the number of pores and throats in the MB network are fewer than in the PB network, the pore volumes are larger in the MB than in the PB network, which can be seen from the distributions in Fig. 6.13. Therefore, the throat volumes are relatively underestimated in the MB network even if apparent agreement is found in the distribution of absolute volume. This will make a difference for the calculation of water saturation in our transport predictions. The method of pore space segmentation needs to be refined to see what method gives the best predictions of multiphase properties.

Table 6.5. Properties of Fontainebleau sandstone networks: pore volume.

Pore volume	**PB**	**MB**
Total volume of pores (µm³)	1.13×10^{-9}	1.33×10^{-9}
Average pore volume (µm³)	2.25×10^{-13}	4.30×10^{-13}
Minimum pore volume (µm³)	4.23×10^{-16}	5.48×10^{-15}
Maximum pore volume (µm³)	3.24×10^{-12}	4.70×10^{-12}

Table 6.6. Properties of Fontainebleau sandstone networks: throat volume.

Throat volume	**PB**	**MB**
Total volume of throats (µm³)	4.20×10^{-10}	2.13×10^{-10}
Average throat volume (µm³)	5.41×10^{-14}	3.49×10^{-14}
Minimum throat volume (µm³)	4.23×10^{-16}	4.22×10^{-16}
Maximum throat volume (µm³)	8.8×10^{-13}	8.90×10^{-13}

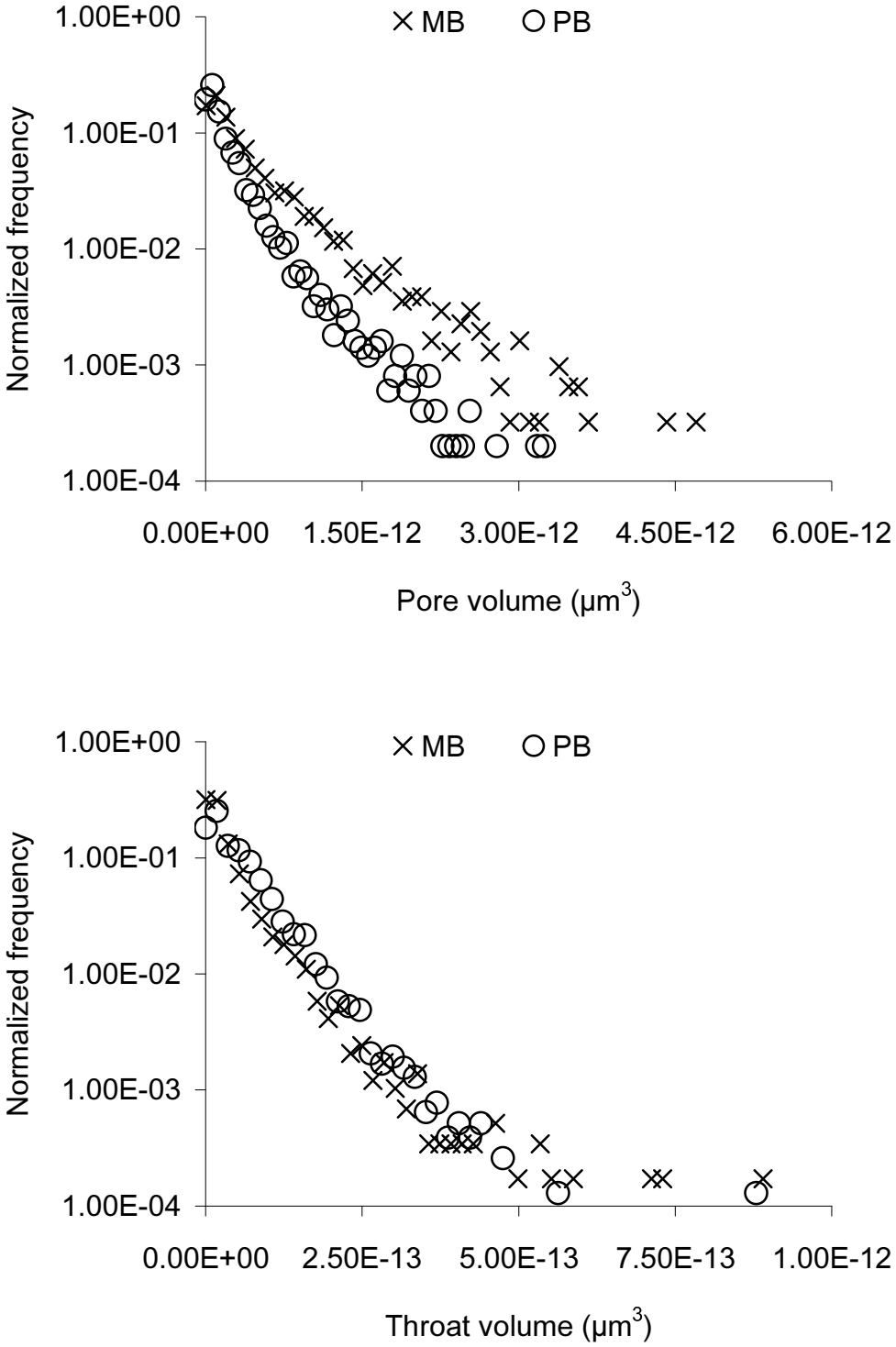

Figure 6.13. Comparison of volume distributions of pores and throats for MB and PB networks extracted from reconstructed Fontainebleau sandstone. (a) Pore volume distribution; (b) throat volume distribution.

6.2.5 The lengths of elements

1. Throat total length

The throat total length is the distance measured from two pore centers that are linked by this throat. This length is defined as l_{ij} in Section 4.4, Fig. 4.11. The distribution, Fig. 6.14, shows that the MB method tends to define longer connections than the PB method. This is because of the merging of what would be pores in the PB method, giving fewer, larger pores in the MB network.

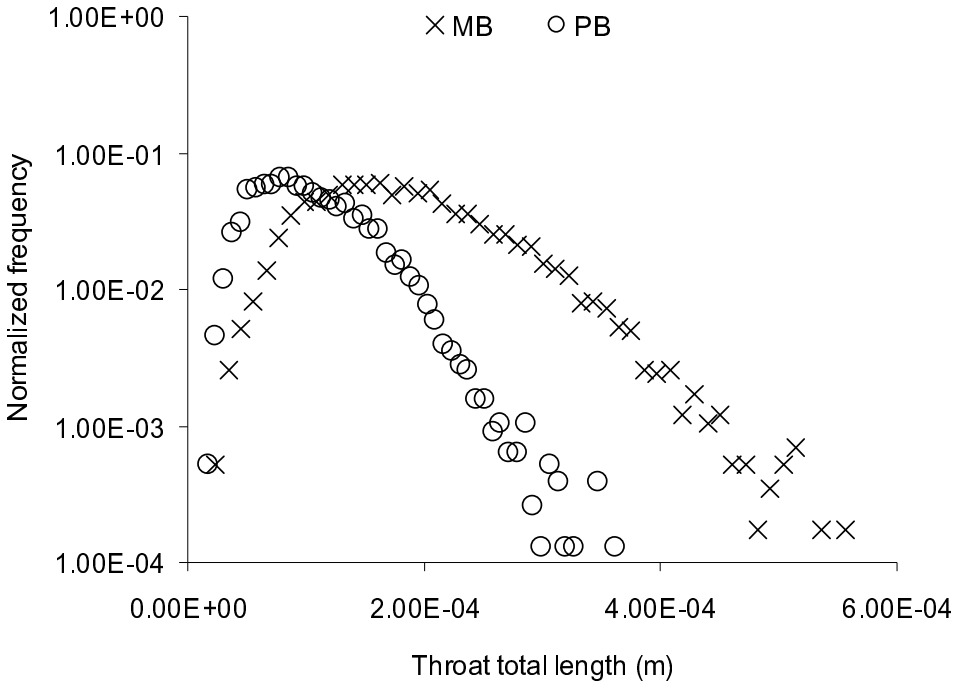

Figure 6.14. Comparison of throat total length distributions of MB and PB networks extracted from reconstructed Fontainebleau sandstone.

2. Pore length

The pore length is defined in Section 4.4 (Equations 4.5 and 4.6). The two networks have very similar distribution of pore lengths, although the MB network

tends to have slightly longer pores (less than 0.01%) shown in Fig. 6.15.

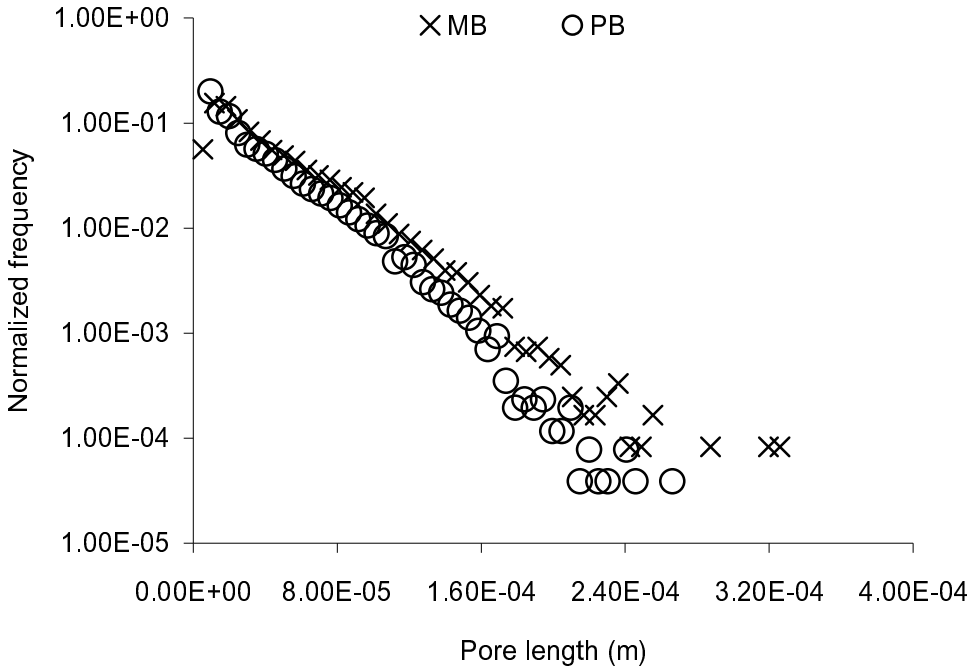

Figure 6.15. Comparison of pore length distributions of MB and PB networks extracted from reconstructed Fontainebleau sandstone.

3. Throat length

The throat length is the length of a pure throat defined as l_t in Section 4.4 (Fig. 4.11, Equation 4.5). The lengths of throats are compared in Fig. 6.16. The MB method defines longer throat lengths, which is in accord with longer throat total lengths.

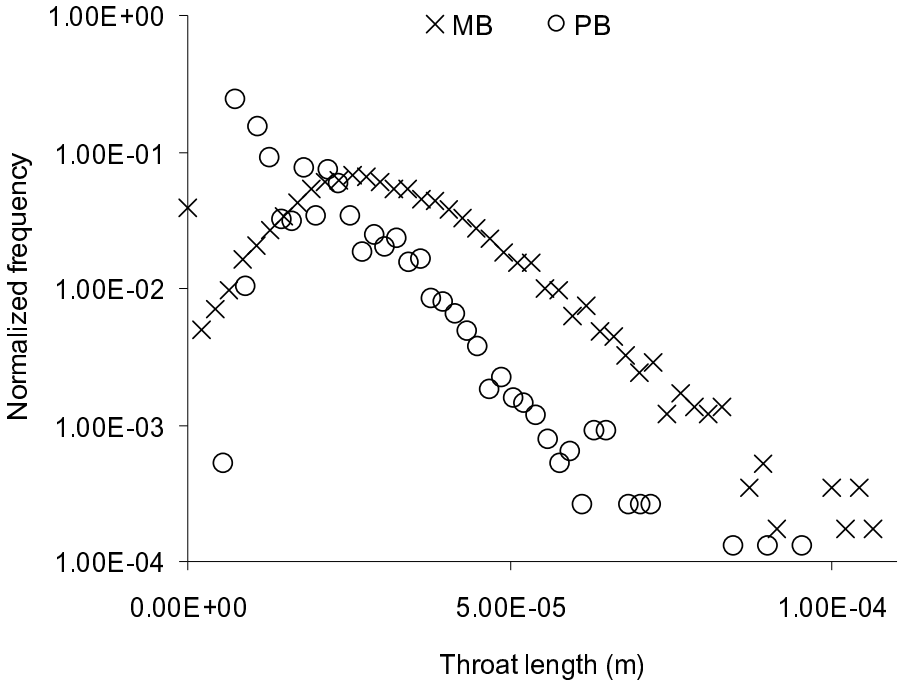

Figure 6.16. Comparison of throat length distributions of MB and PB networks extracted from reconstructed Fontainebleau sandstone .

6.2.6 Shape factors of pores and throats

The underestimation of throat volumes causes large uncertainty in the shape factor calculation influencing the computed conductance defined by Equation 7.5 and the corner half angles (Valvatne, 2004). Instead we use a normal distribution to randomly assign the throat shape factor in a reasonable range (0, 0.0625] as triangle and square throats and keep the pore shape factors as the computed values from the real pores (see in Section 4.4).

Table 6.7. Properties of Fontainebleau sandstone networks: number of shaped pores and throats.

Number of elements	**PB**	**MB**
No. of triangular shaped elements	13088	9204
No. of square shaped elements	103	11
No. of circular shaped elements	0	0

The MB method defines fewer square shaped elements than the PB method (0.12% and 0.79% respectively) due to different ways to calculate the shape factors.

In the shape factor distributions for both pores and throats, Figs. 6.16 and 6.17, a left-side offset can be found in the MB method compared to the PB method, which means a higher order of shape irregularity is defined for MB elements than PB. For the pores whose shape factors are computed, the distribution is consistent with the fact that more volumes tend to be assigned to pores rather than to throats in the current method, therefore the angularity of MB pores is increased. For the throats, we have arbitrarily assigned the distribution; we could have chosen one that more closely matched that obtained from PB modelling.

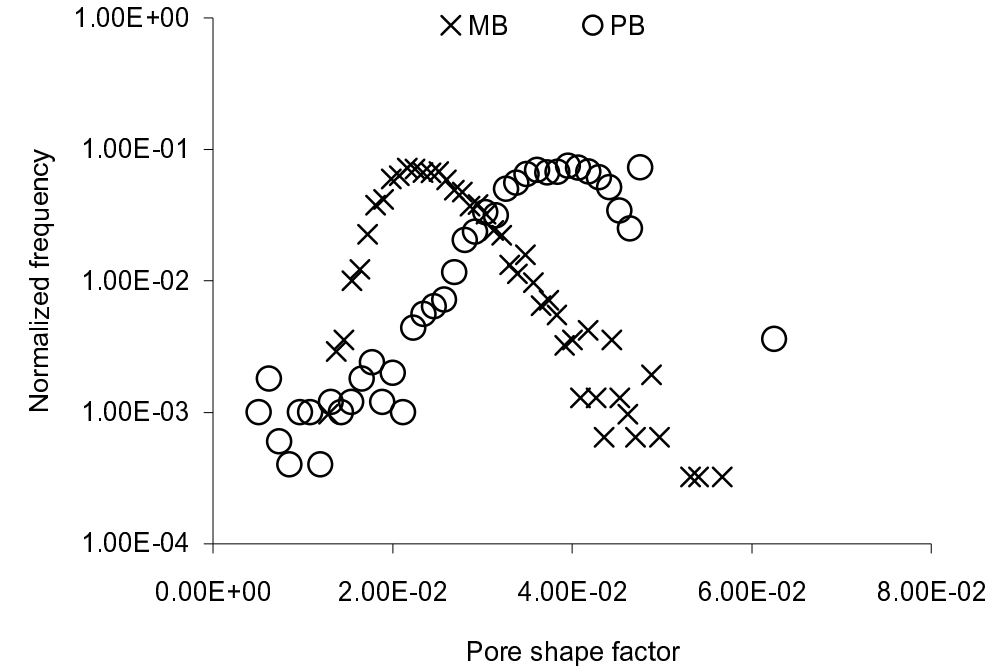

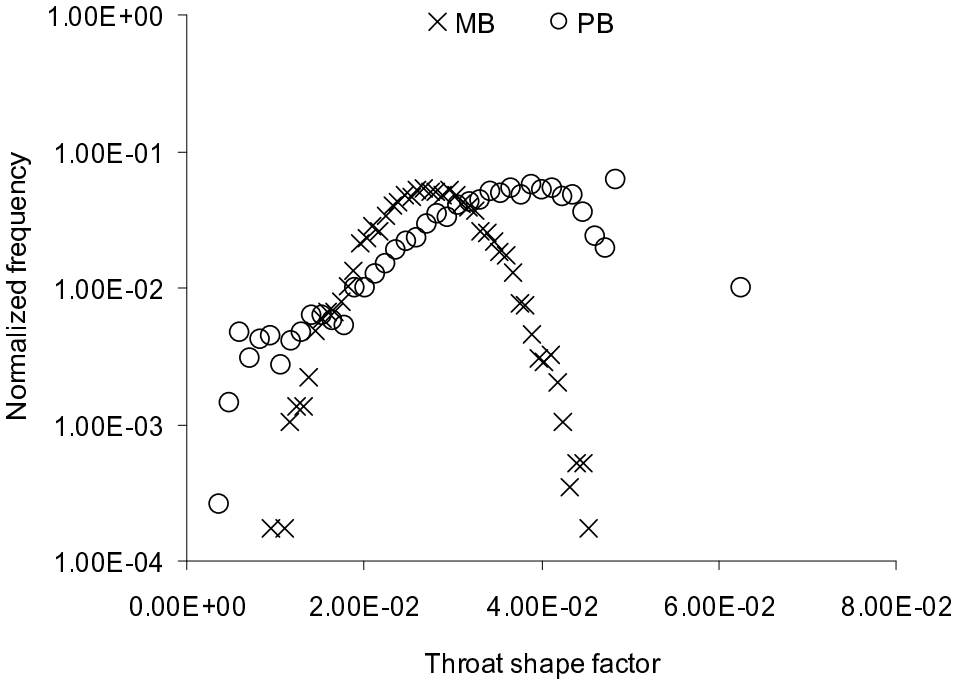

Figure 6.17. Comparison of pore and throat shape factor distributions of MB and PB networks extracted from reconstructed Fontainebleau sandstone.

6.2.7 Aspect ratios

The aspect ratio is the ratio of pore radius to the linked throat radius. The aspect ratio distributions are compared in Fig. 6.18. MB defines higher aspect ratios than the PB method. This is because we assign some very small throat radii. As we show later, aspect ratio has a large impact on multi-phase flow simulation, so this discrepancy is something that should be studied for future work.

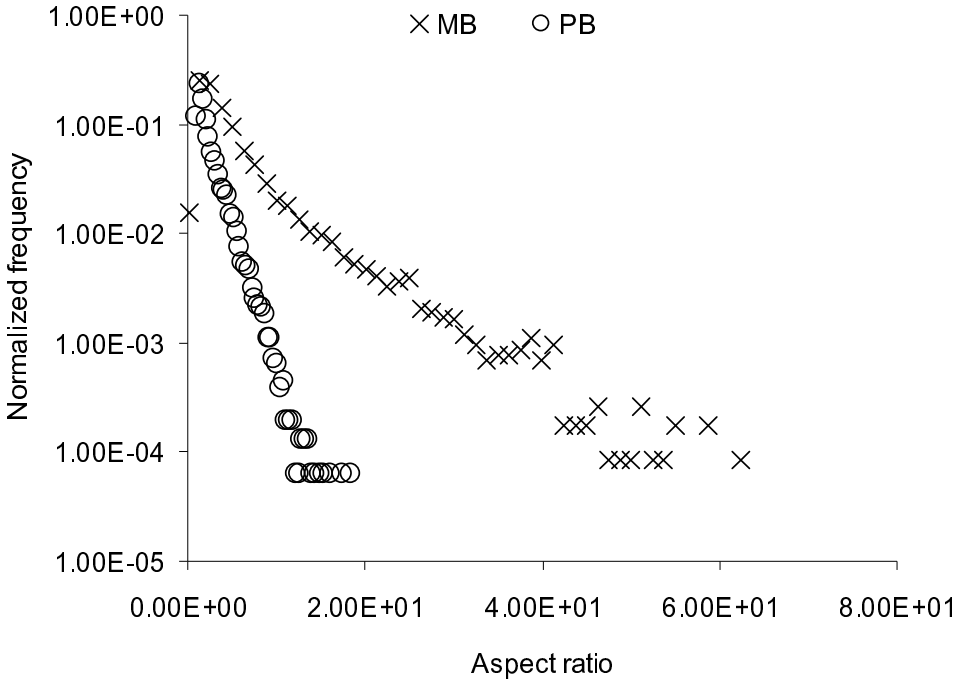

Figure 6.18. Comparison of aspect ratio distributions of MB and PB networks extracted from reconstructed Fontainebleau sandstone.

6.3 Validation on a Berea sandstone micro-CT image

The classic Berea network that was generated by Øren and Bakke (2003) and used by Valvatne and Blunt (2004) and Piri and Blunt (2005 a; b) has a net porosity of 18.3% and clay porosity of 5.7% representing 27 mm^3 rock volume. We selected from our image library a Berea sandstone imaged at Imperial College with a porosity of 19% and voxel length of 5.345 µm covering a rock volume of 9.77 mm^3. The network extracted using the MB method is compared to this classic Berea network in this section.

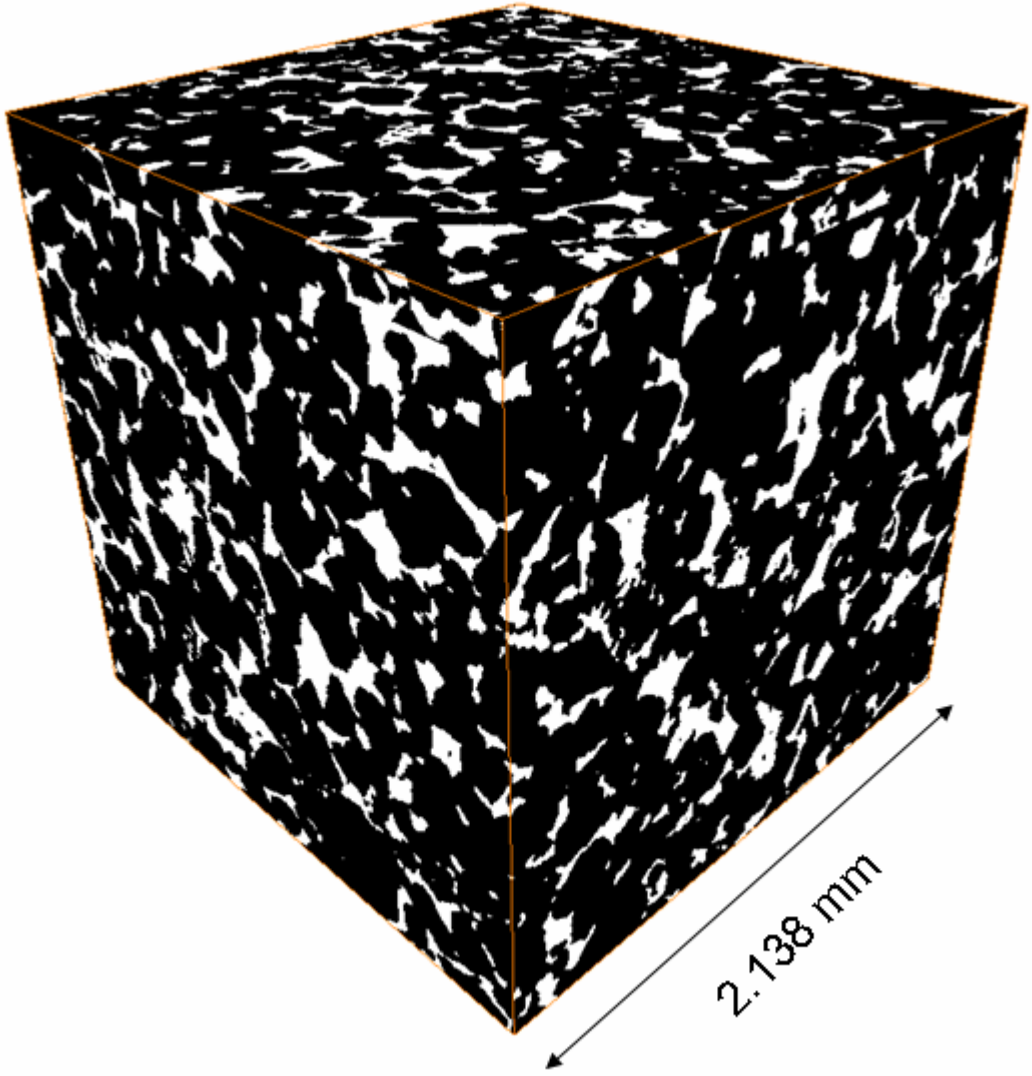

Figure 6.19. The 3D micro-CT image of Berea sandstone.

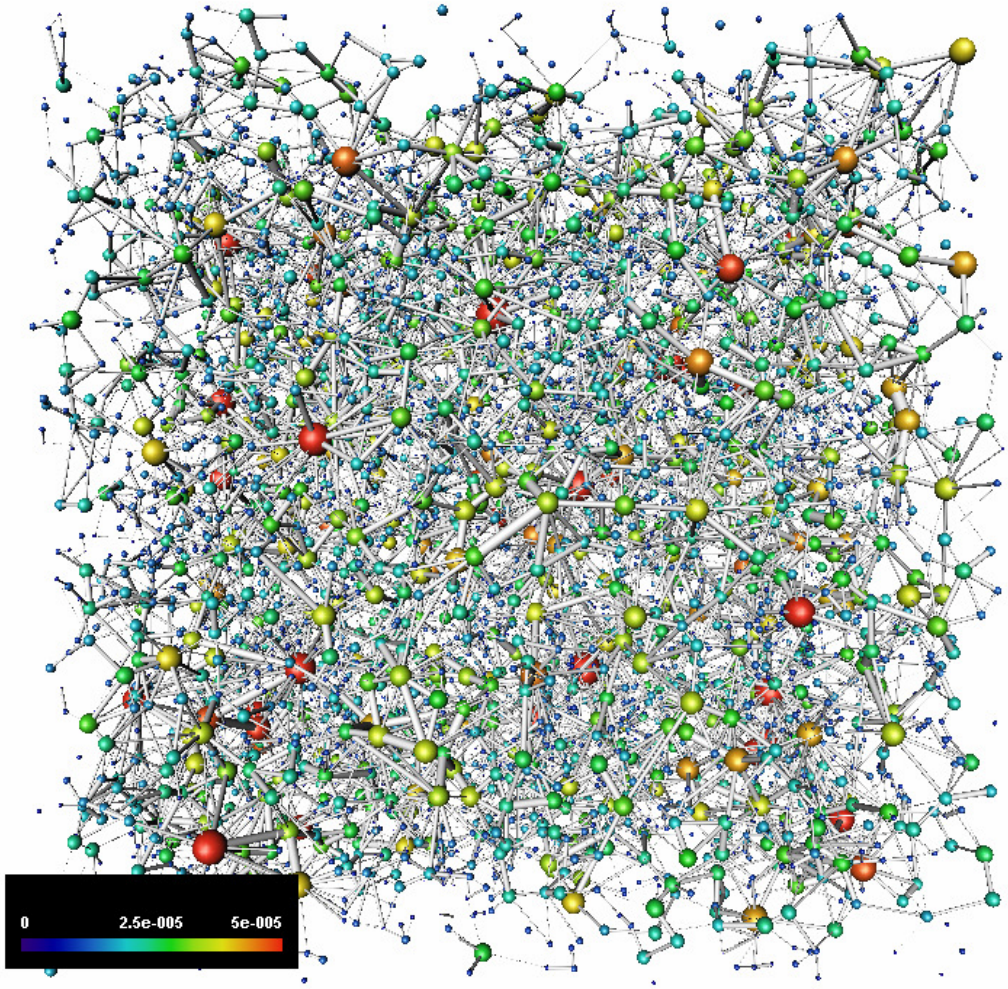

Figure 6.20. The extracted Berea network using the maximal ball algorithm. The color map shows the size of the pores in the network in meters.

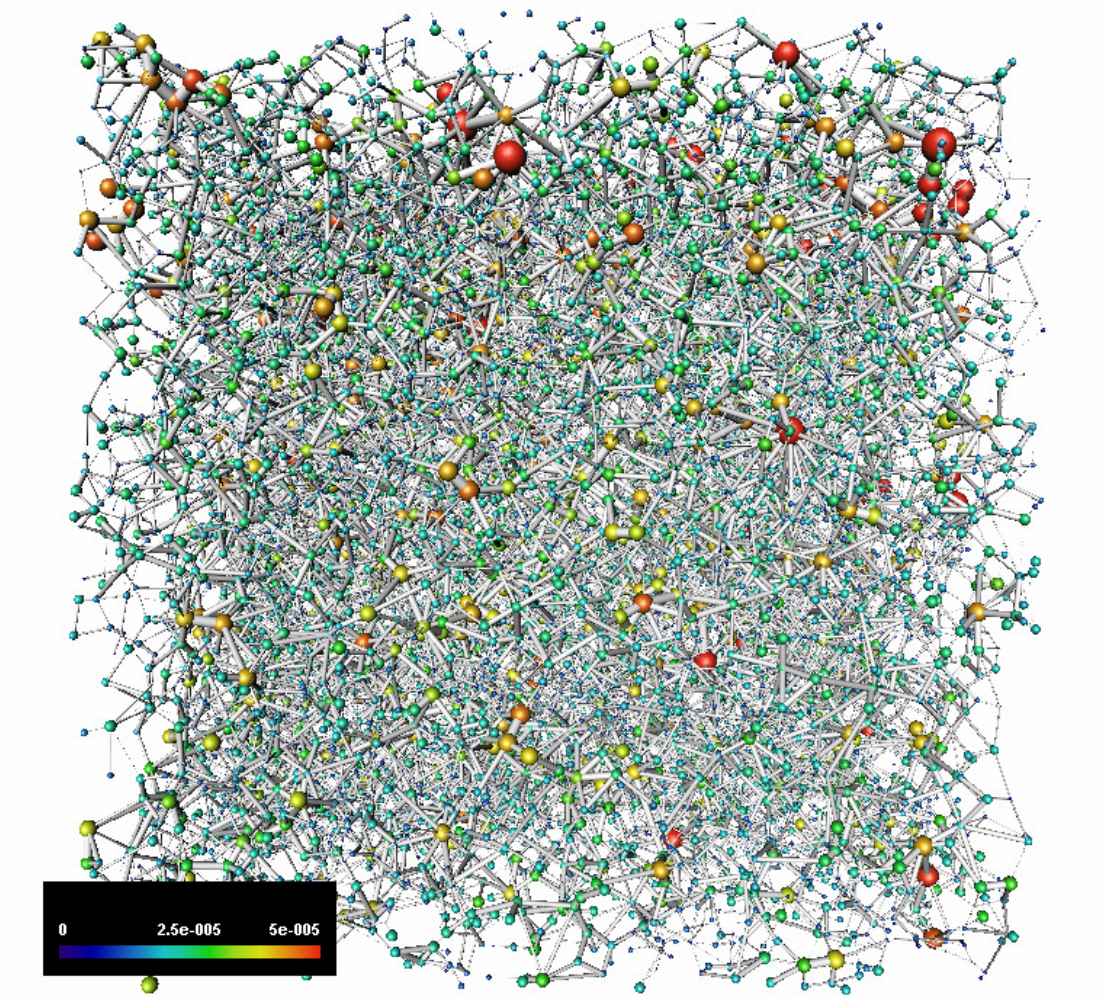

Figure 6.21. The classic PB Berea network. The color map shows the size of the pores in the network in meters.

6.3.1 Number of pores

First, the numbers of pores and throats are compared. In this case we define more pores per unit volume in the MB (644 pores/mm^3) than in the PB network (457 pores/mm^3) even though a more aggressive merging criterion is used in the MB method. This could be because the resolution of the micro-CT image is higher than the PB image; however, our methods should be independent of image resolution as long as all the relevant pore-space features are captured. Alternatively, the grain size in the PB image could be coarser. As we show later, this is the more likely

explanation of the difference.

Table 6.8. Properties of Berea networks: number of elements.

Number of elements	PB	MB
No. of pores	12349	6298
No. of throats	26146	12545
No. of surface pores	433	447

6.3.2 Connectivity

The coordination number distributions are compared in Fig. 6.22 and the statistics are summarized in Table 6.9.

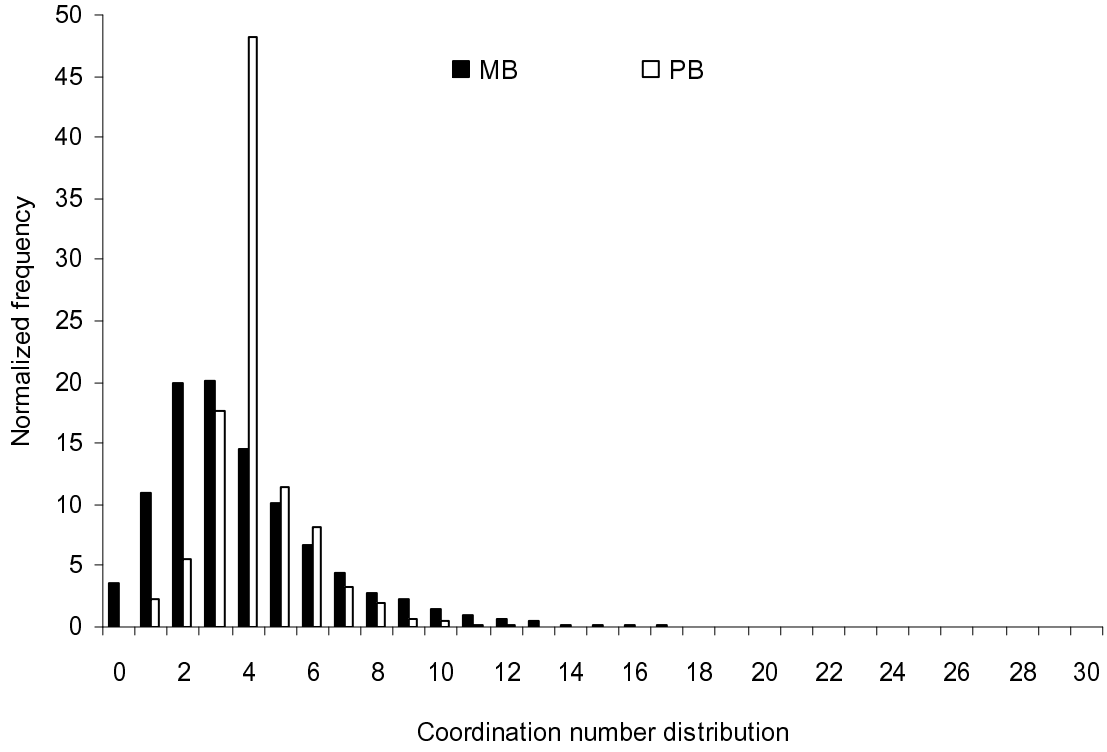

Figure 6.22. Comparison of coordination number distributions for PB and MB Berea networks.

Table 6.9. Properties of Berea networks: Connectivity.

Connectivity	**PB**	**MB**
Average connection number	4.19	3.91
Minimum connection number	1	0
Maximum connection number	19	30
No. of connections to inlet	254	201
No. of connections to outlet	267	246
No. of isolated elements	9	290

The average coordination numbers are similar although the peak values are different. More pores with high coordination numbers are found in the MB network. The reason is that the MB network is derived from a micro-CT image; and the high noise level in the micro-CT image (compared to the reconstructed image) increases the possibility to find more smaller satellite pores (sometimes only artefacts due to imaging) around big pores. On the other hand the mean coordination number is lower for the MB network. This is the opposite of what is found for the Fontainebleau networks. In this case we assign a large number of poorly connected pores, with a coordination number of only 0, 1 or 2.

6.3.3 Pore and throat sizes

Inscribed radii of pores and throats of the MB and PB networks are compared in Table 6.10.

Table 6.10. Properties of Berea networks: pore size.

Pore size statistics	**PB**	**MB**
Average pore radius	19.17 μm	15.36 μm
Minimum pore radius	3.62 μm	2.27 μm
Maximum pore radius	73.54 μm	70.25 μm

Table 6.11. Properties of Berea networks: throat size.

Throat size statistics	**PB**	**MB**
Average throat radius	10.87 μm	7.01 μm
Minimum throat radius	0.90 μm	0.54 μm
Maximum throat radius	56.85 μm	40.06 μm

For the pore sizes, both the maximum and minimum values are close although the two images have different resolution. The average pore size is slightly smaller in the MB network, nevertheless good agreement is obtained in the pore size distribution in Fig 6.23. The throat sizes of MB network are smaller than PB network in terms of maximum and average radius since the minimum value for both networks is just a matter of the post-processing method. Again these results are consistent with the PB image having a slightly larger grain size.

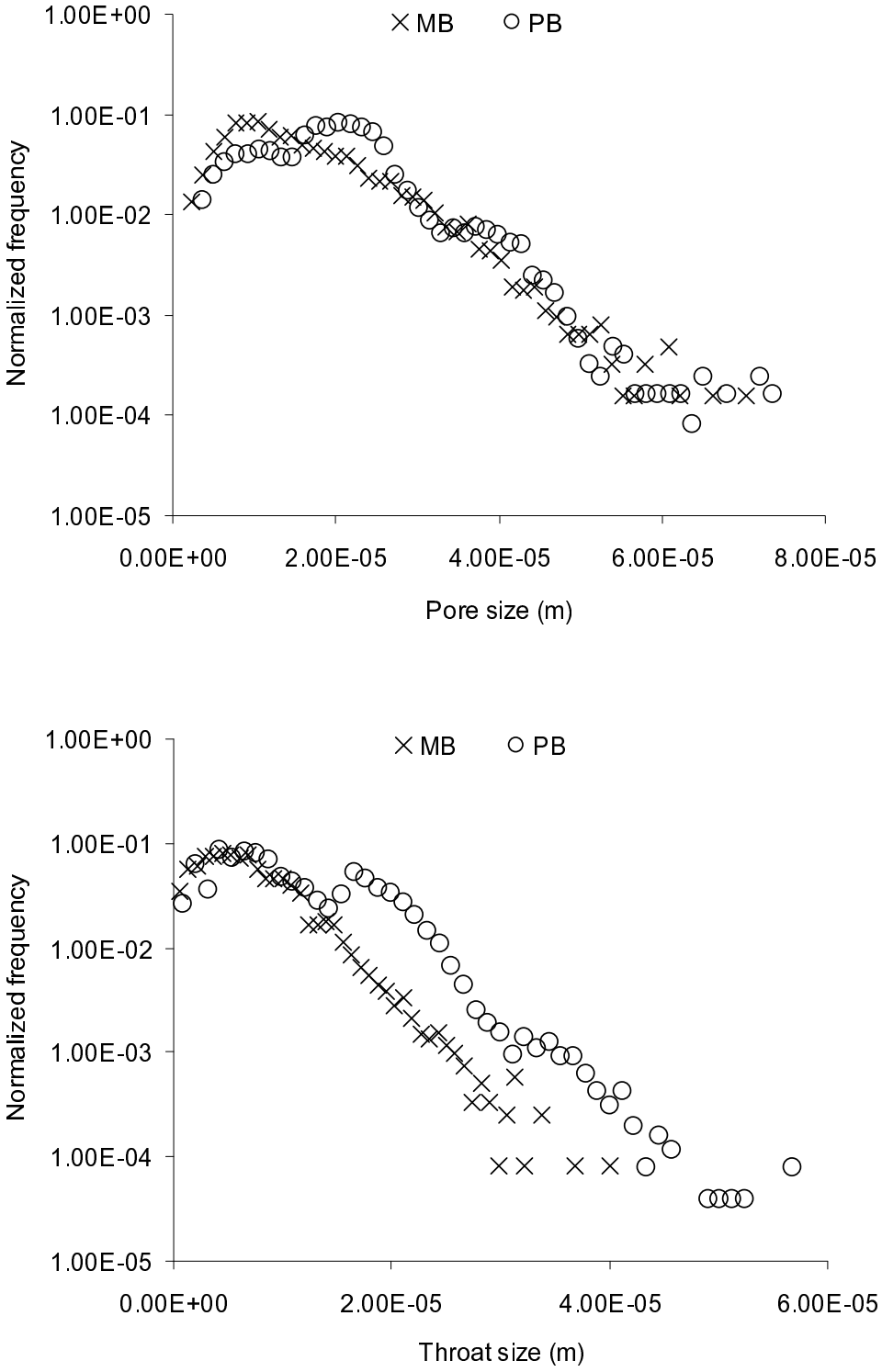

Figure 6.23. Comparisons of pore and throat size distributions of PB and MB Berea networks.

6.3.4 Pore and throat volumes

Fig. 6.24 compares the pore and throat volumes for the two Berea networks.

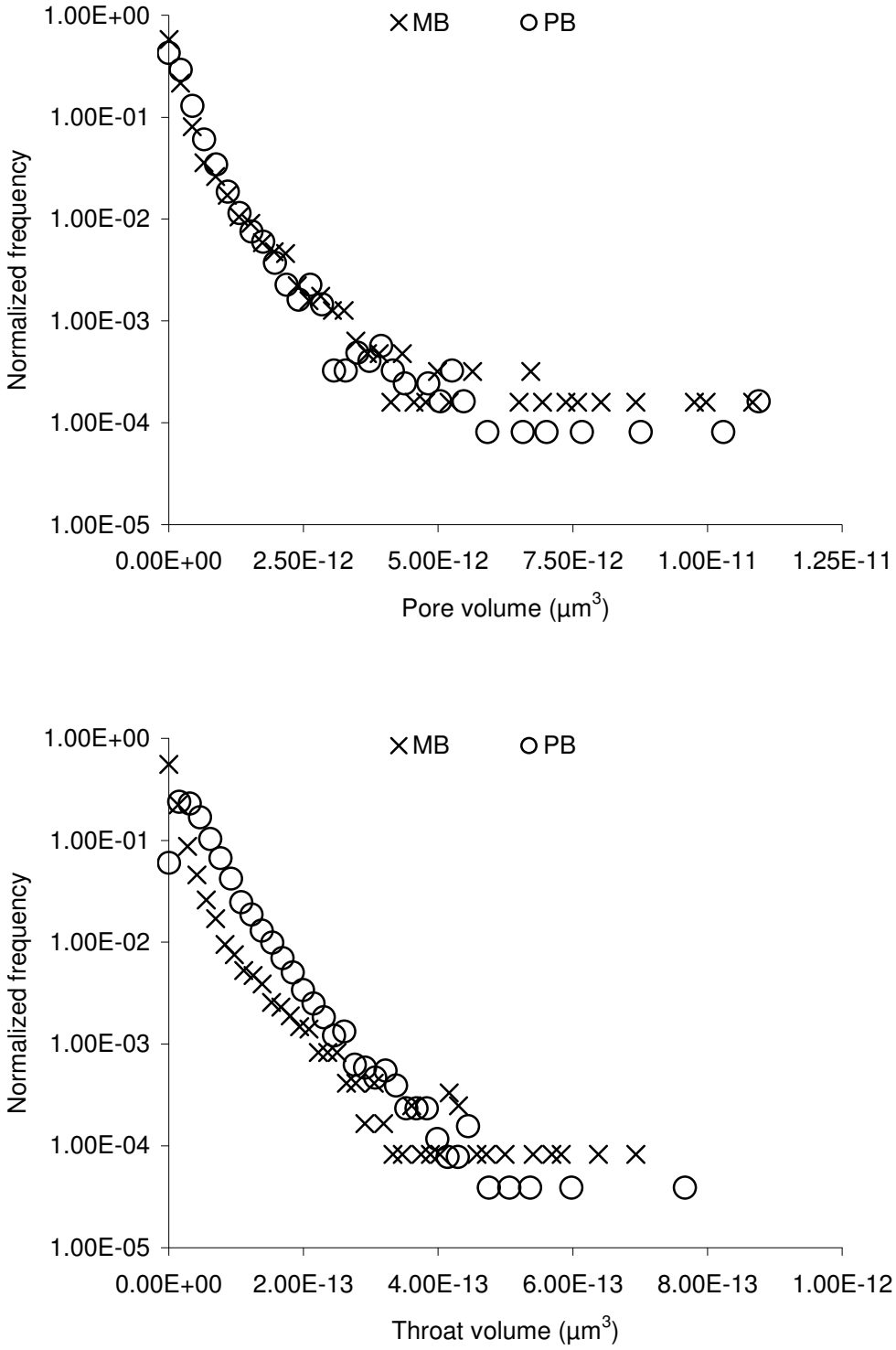

Figure 6.24. Comparisons of pore and throat volume distributions of PB and MB Berea networks.

The volumes of pores are similar in both networks except MB network has slightly higher frequency for pores larger than 6.0×10^{-12} μm^3. Moreover, the MB defines more big throats and fewer small throats in terms of volume compared to the PB network.

6.3.5 The lengths of elements

Similar to Fontainebleau networks, MB methods tend to define long distance links in terms of throat total length (pore to pore center) and throat length (the length of a pure throat) as shown in Figs. 6.25 and 6.26.

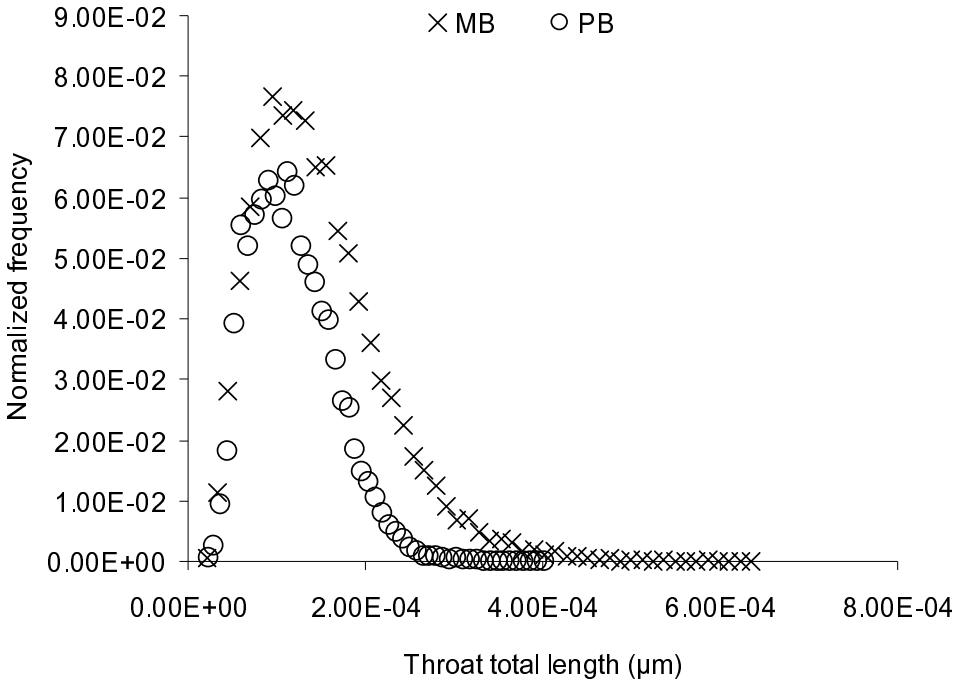

Figure 6.25. Comparisons of throat total length distributions of PB and MB Berea networks.

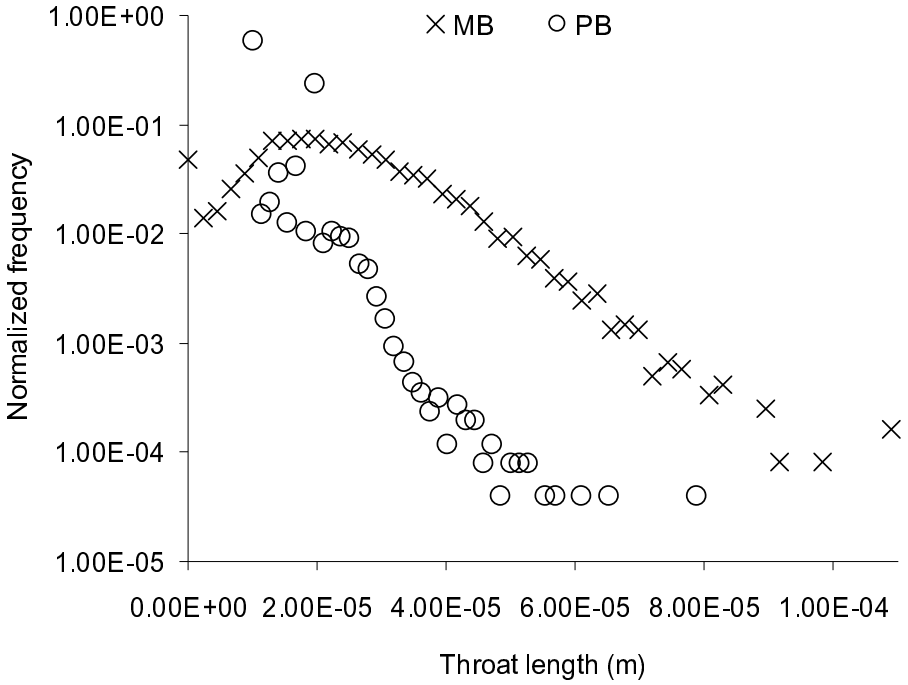

Figure 6.26. Comparisons of throat length distributions of PB and MB Berea networks.

6.3.6 Shape factors of pores and throats

We calculate the shape factors for pores using Equation 4.8 and assign the shape factors for throats using a normal distribution between (0, 0.0625] as before. Although the MB defines more triangular elements than the PB method (see Table 6.12), they are in good agreement statistically on the angularity of the network elements seen in Fig. 6.27.

Table 6.12. Properties of Berea networks: number of shaped pores and throats.

Number of elements	**PB**	**MB**
No. of triangular shaped elements	35518	18771
No. of square shaped elements	2506	74
No. of circular shaped elements	473	0

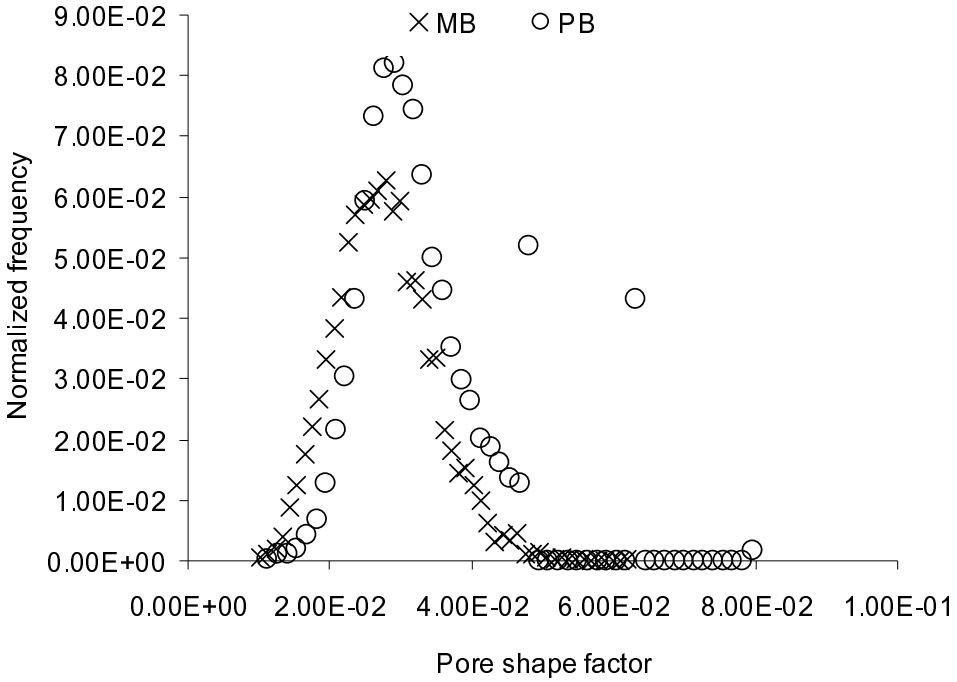

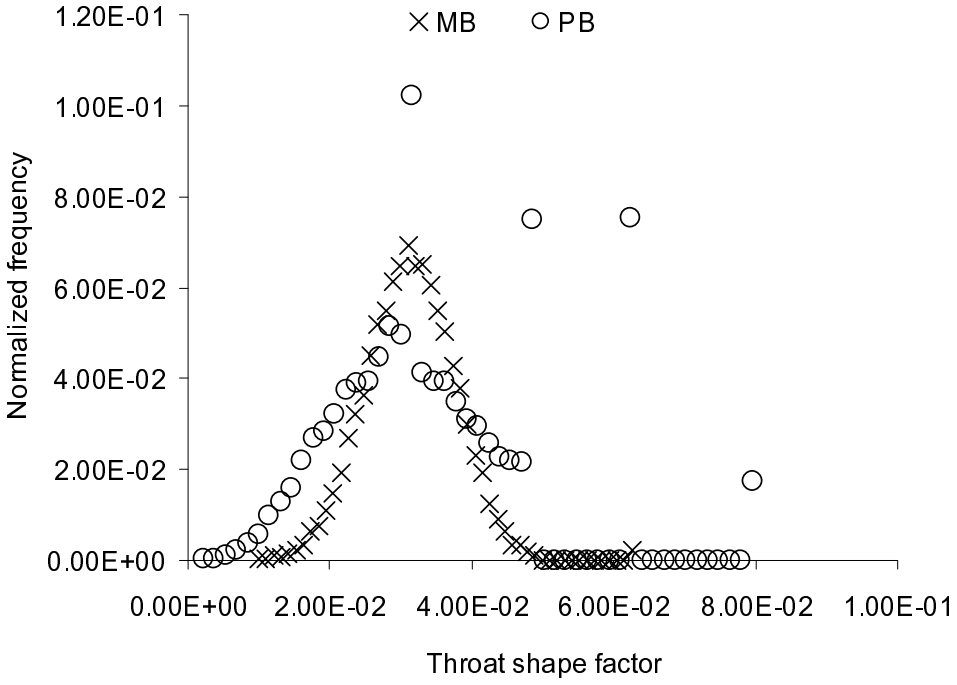

Figure 6.27. Comparisons of the shape factor distributions of pores and throats of PB and MB Berea networks.

6.3.7 Aspect ratios

Fig. 6.28 compares the aspect ratios of the two Berea networks.

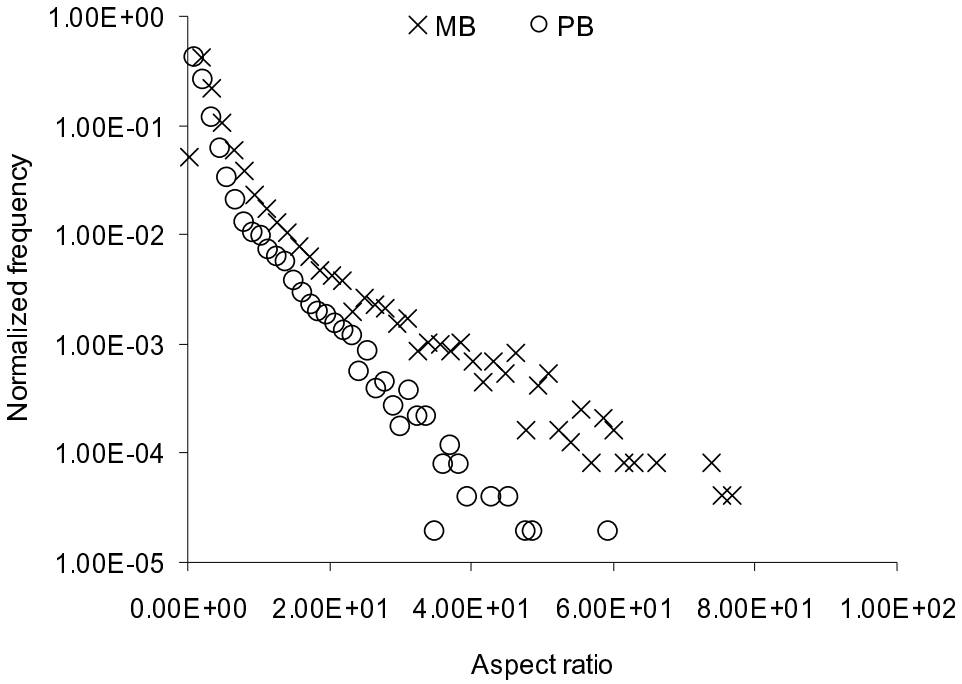

Figure 6.28. Comparisons of aspect ratio distributions of PB and MB Berea networks.

Similar to the Fontainebleau MB network, the Berea MB network has higher aspect ratios than the PB network.

6.4 Validation on other test samples

The network extraction algorithm was applied to all the samples imaged. The average and distributions of coordination numbers, the pore size and throat size distributions of the networks are presented in this section – Figs 6.29-6.40. Their cross-sections of micro-CT images, image resolution, pictures of pore networks and two-point correlation functions can be found in Section 5.2. The petrophysical properties calculated on both voxel images and pore networks can be found in Table 7.3 in Section 7.3.3.

For the coordination number distribution, it is found that some samples have large fractions of pores with a coordination number of 0 (isolated pores) or 1 (dead ends), which indicates that the image resolution can be insufficient to identify the throats smaller than a voxel for the samples.

Similarly, if a large fraction of pores and throats are found with a size around the voxel size of the image, a better image resolution is required to capture more detailed pore-space features.

It is also found from the validations that a resolution of a few microns is sufficient to image most of the sandstone rocks, but it cannot resolve the features of carbonate rocks (sample C1 and C2) and some low permeability sandstone (sample S4); this is evident by comparing the calculated absolute permeability in Table 7.3.

We find that most of the sandstone samples have an average coordination numbers in the range 3.15-4.77 which is similar to that obtained from our two benchmark sandstones, while sandstone sample S4 has a low average coordination number (2.72) due to the poor connectivity caused by the insufficient resolution as discussed earlier. The synthetic silica sample A1 with high porosity (42.9%) and high

permeability (8076 mD) has a high average coordination number (6.65) indicating its eximious connectivity. More heterogeneous media – such as the carbonates C1 and C2 (see the pictures in Table 3.1 and Section 5.2.) are characterized by relatively low coordination numbers (3.0 and 2.37 respectively) because of a large number of poorly connected pores.

On the other hand, some heterogeneous samples, such as S7 and S8, have high coordination numbers (5.23 and 5.94 respectively) because we have relatively large pores connected to many throats. There is clearly a large disparity between pore and throat size and the relatively open structure leads to lots of connections in the pore space. Overall though, there is no simple way to relate qualitative, visual features of the images to the computed coordination number distribution. Similarly, while the typical pore radius can easily be inferred from the images, the segmentation into pores and throats is sufficiently subtle to elude quantitative assessment from visual inspection alone. What matters are the transport properties of the networks and this is discussed in the next Chapter.

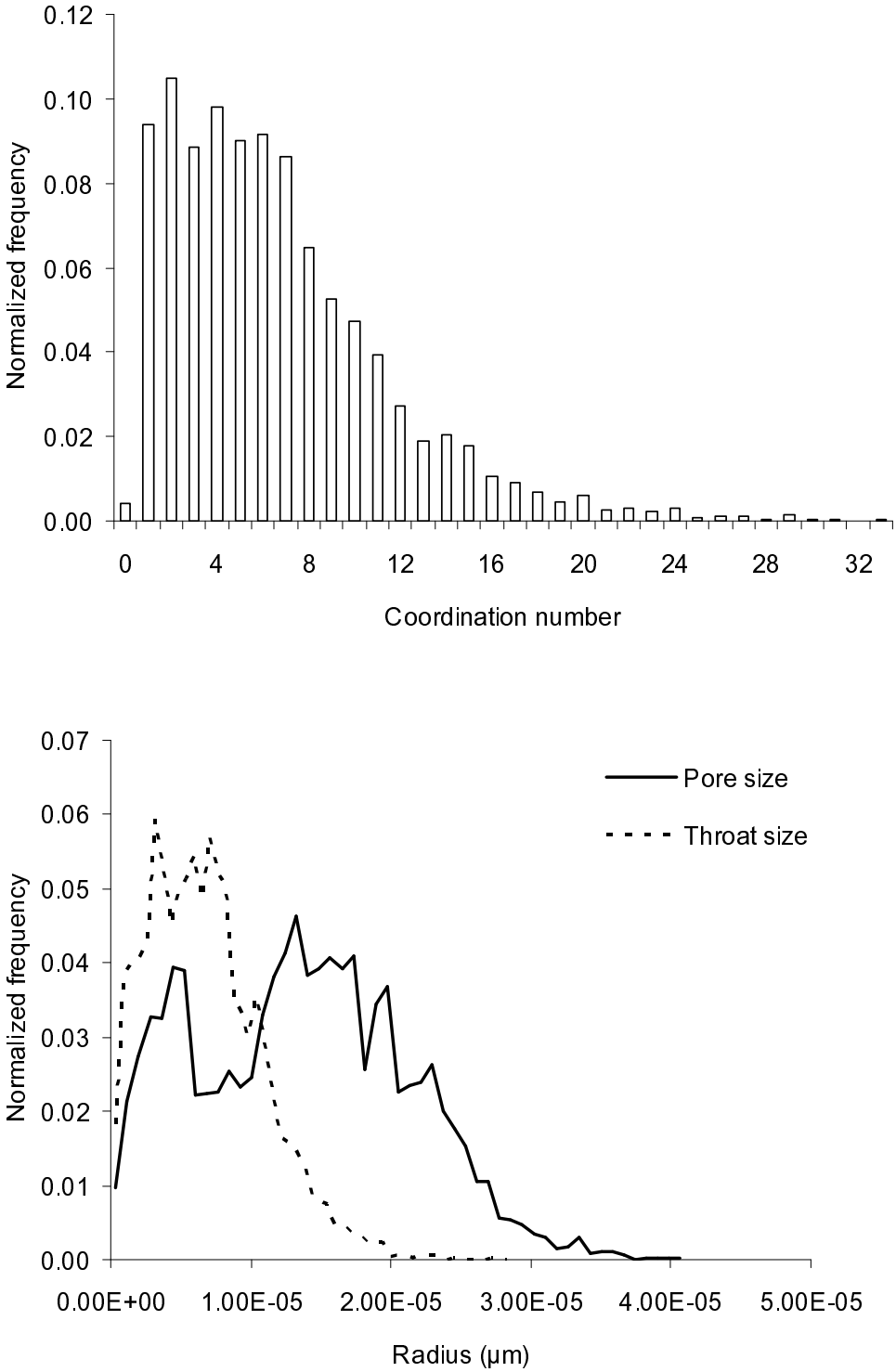

Figure 6.29. Distributions of coordination number (top) and pore size and throat size (bottom) of sample A1. The network porosity is 42.9% and the average coordination number is 6.65.

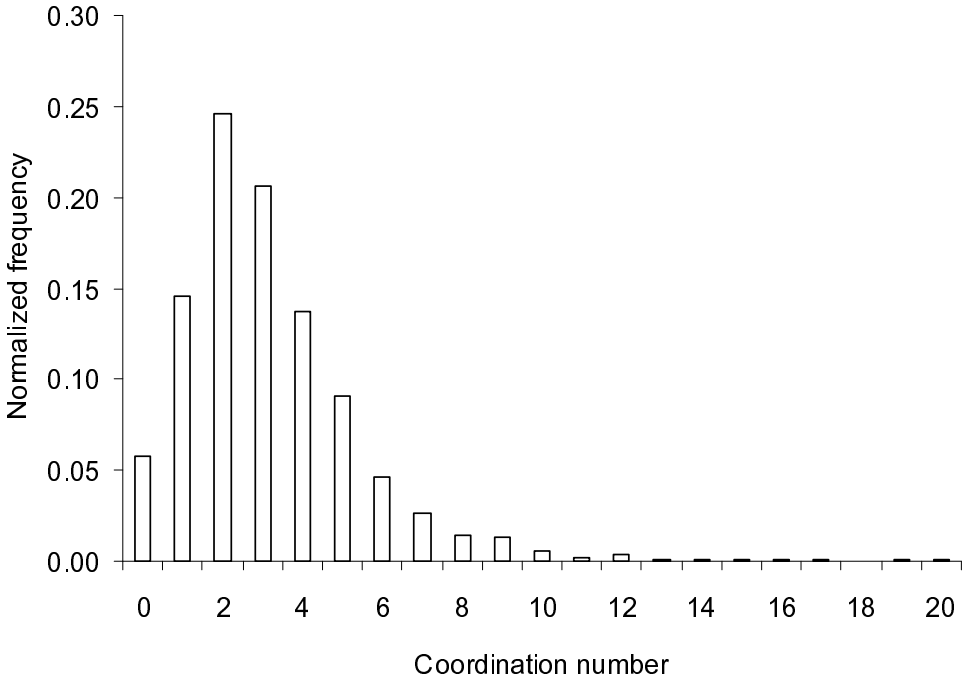

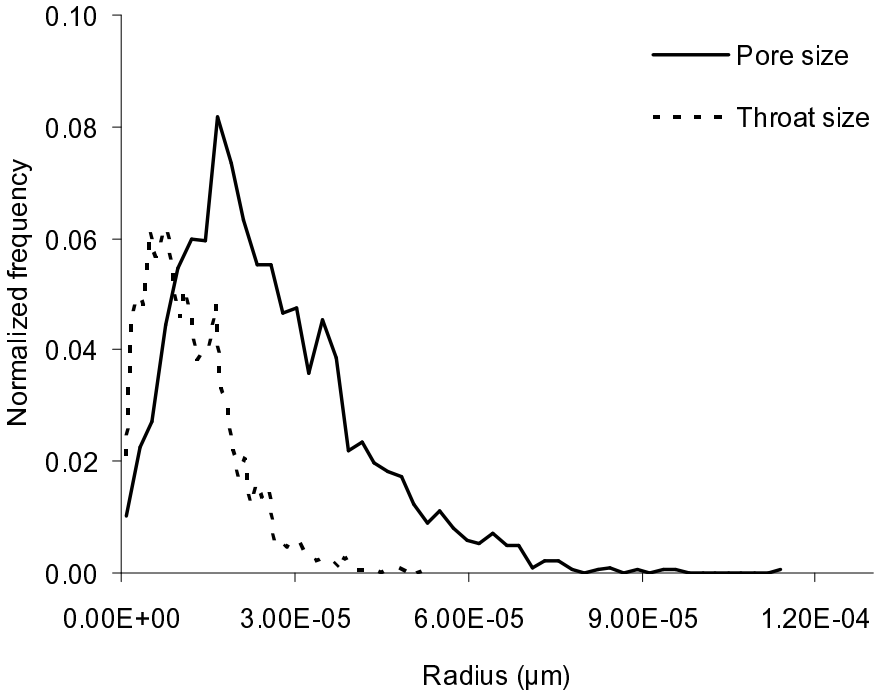

Figure 6.30. Distributions of coordination number (top) and pore size and throat size (bottom) for sample S1. The network porosity is 14.1% and the average coordination number is 3.15.

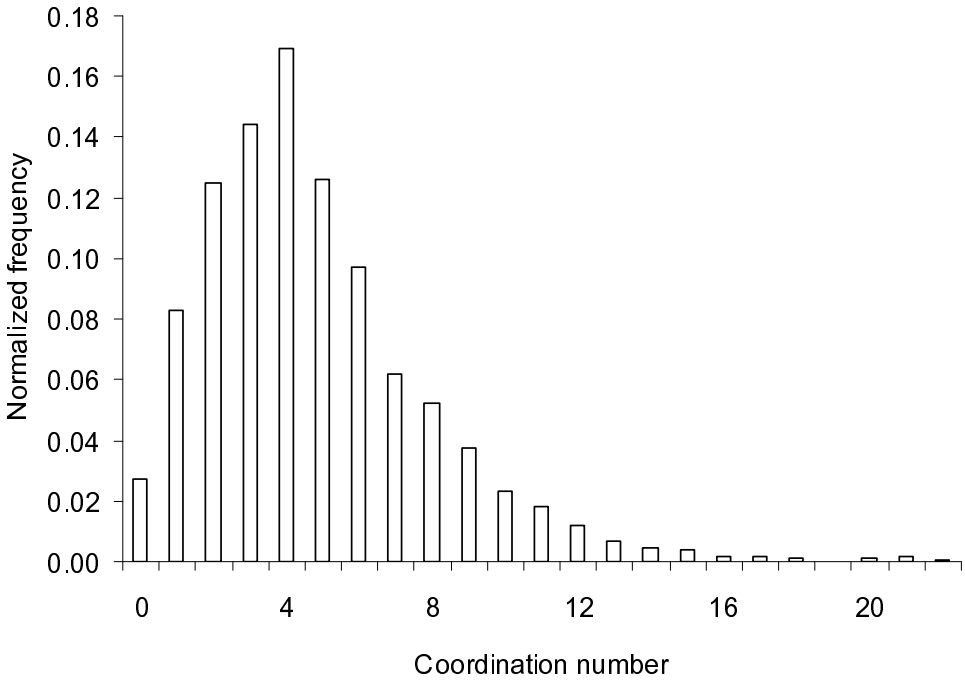

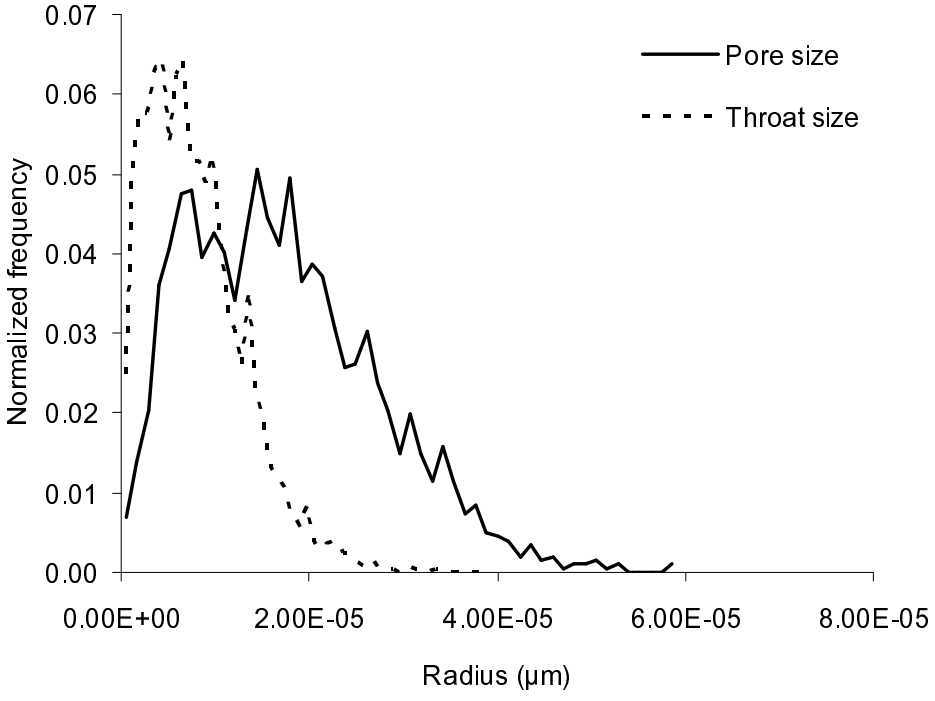

Figure 6.31. Distributions of coordination number (top) and pore size and throat size (bottom) of sample S2. The network porosity is 24.6% and the average coordination number is 4.77.

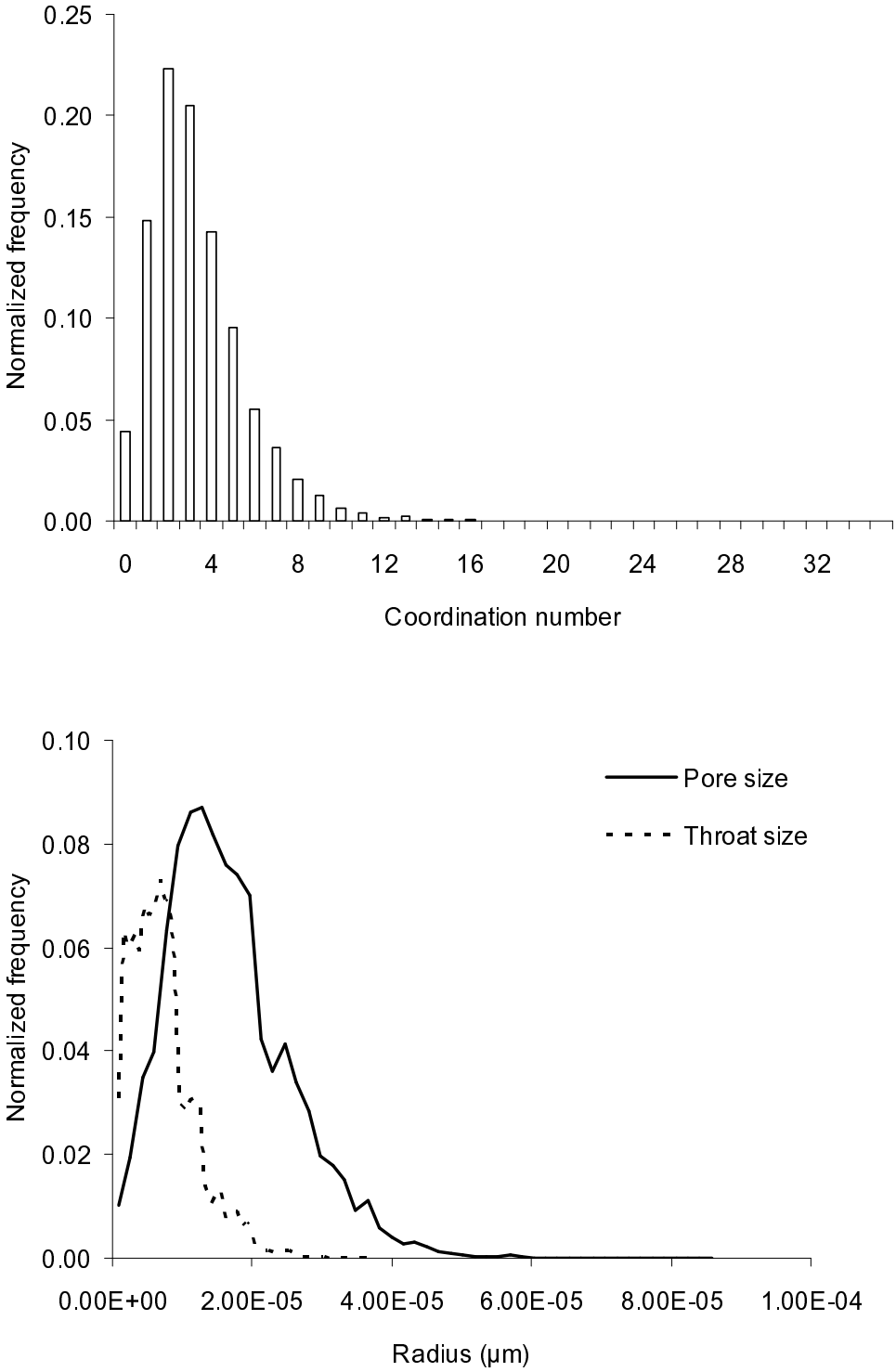

Figure 6.32. Distributions of coordination number (top) and pore size and throat size (bottom) of sample S3. The network porosity is 16.9% and the average coordination number is 3.32.

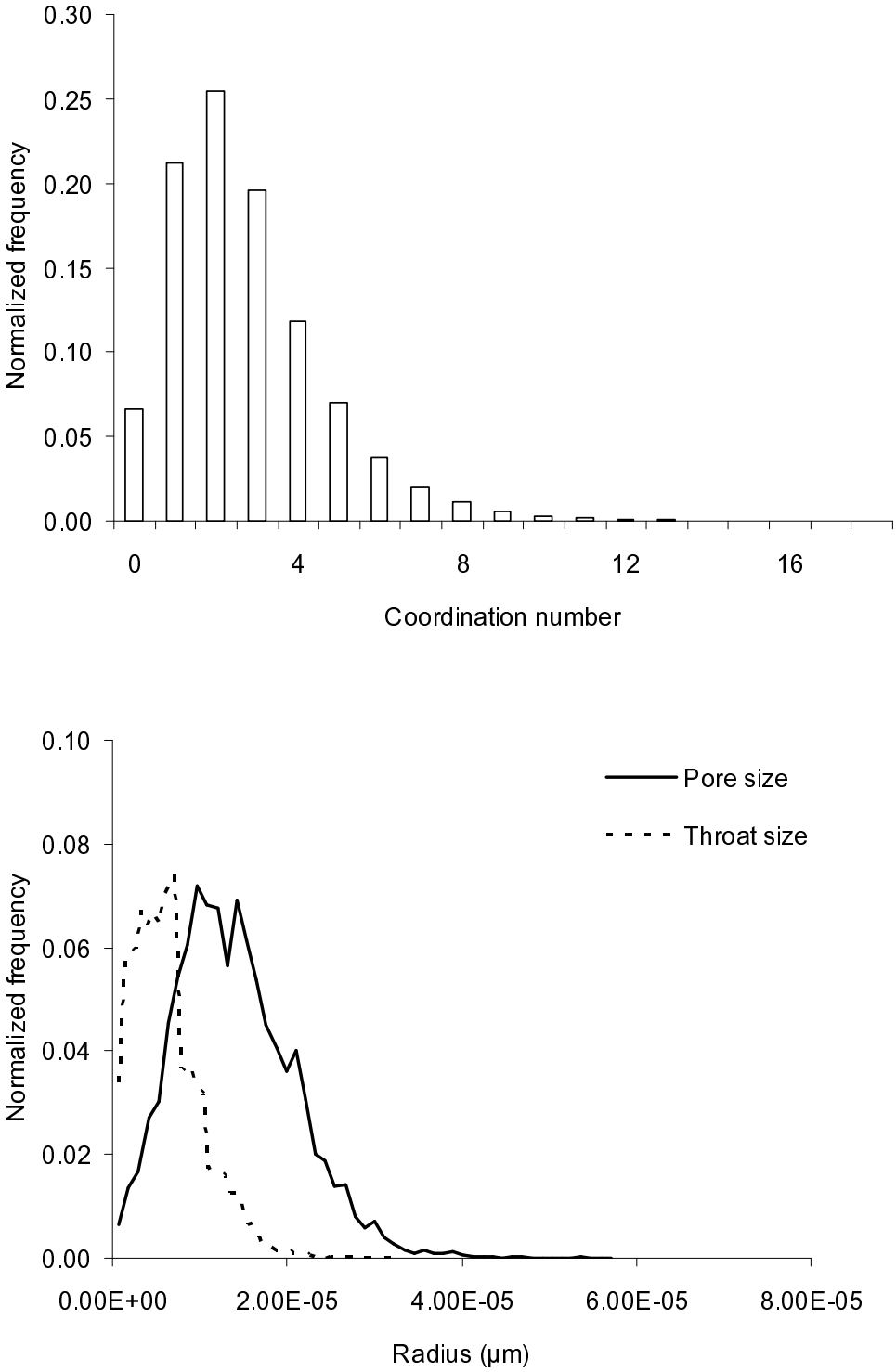

Figure 6.33. Distributions of coordination number (top) and pore size and throat size (bottom) of sample S4. The network porosity is 17.1% and the average coordination number is 2.72.

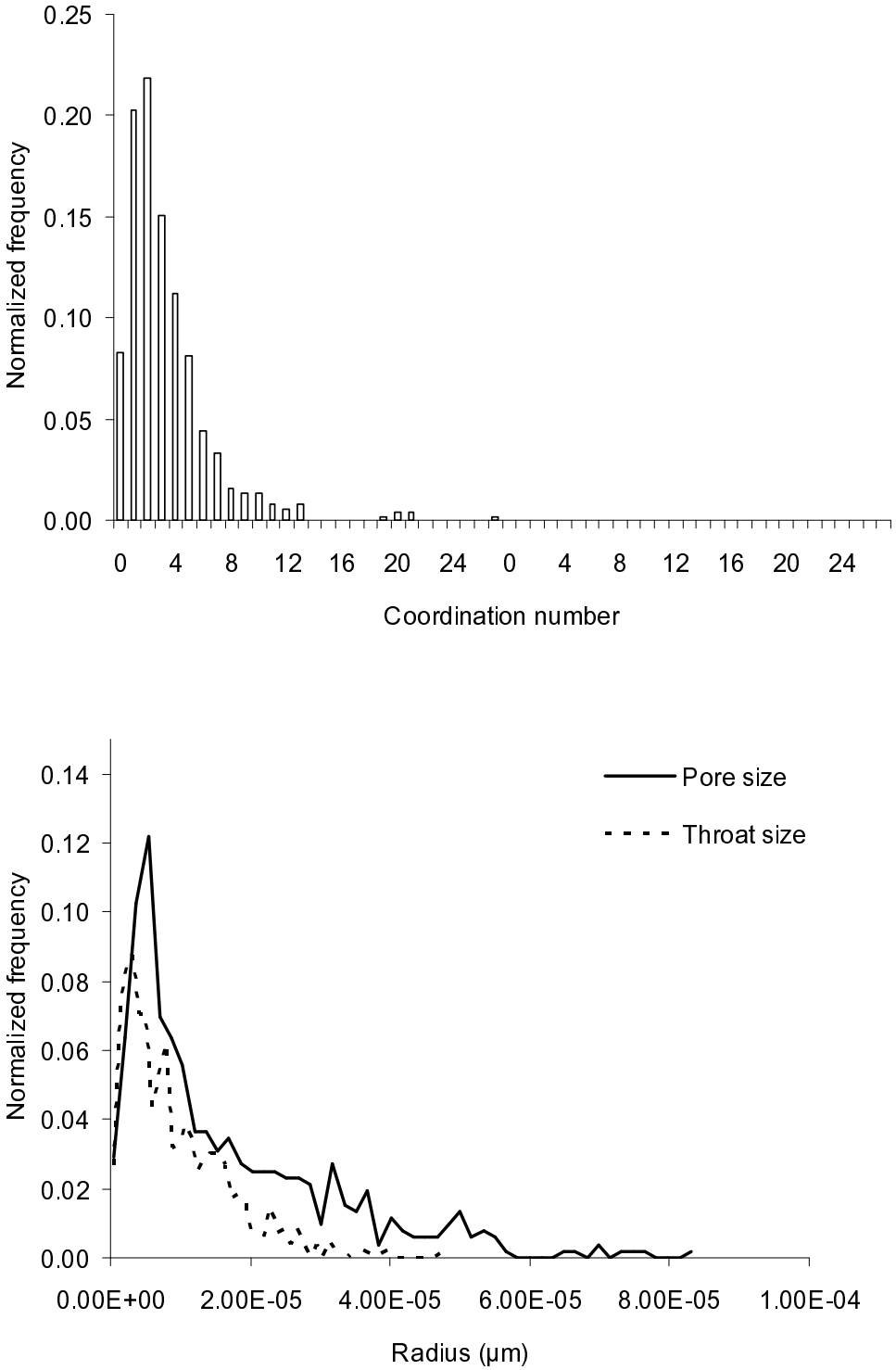

Figure 6.34. Distributions of coordination number (top) and pore size and throat size (bottom) of sample S5. The network porosity is 21.1% and the average coordination number is 3.32.

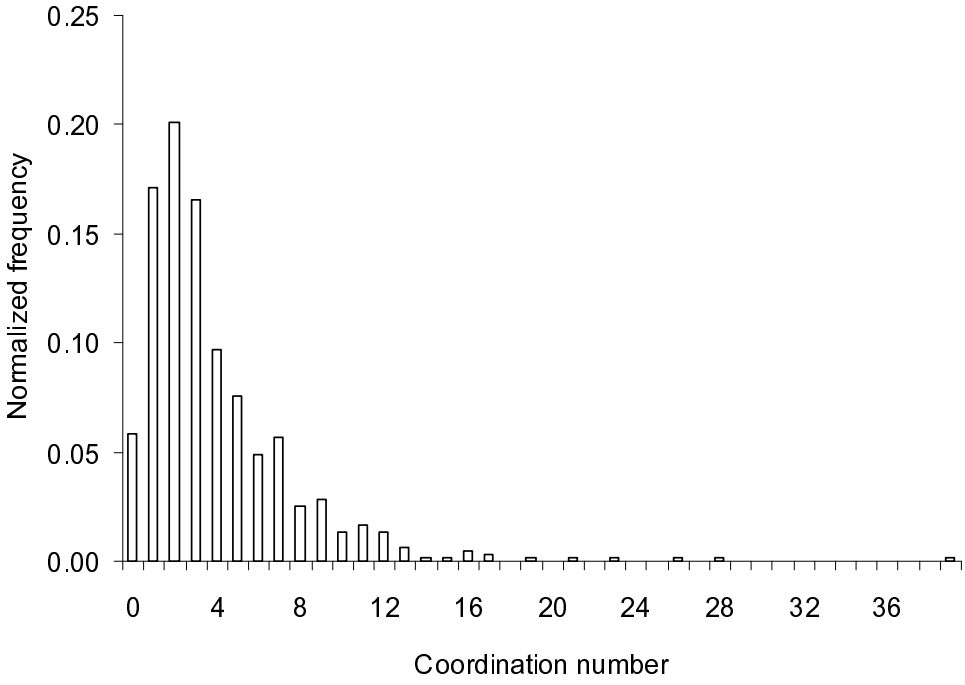

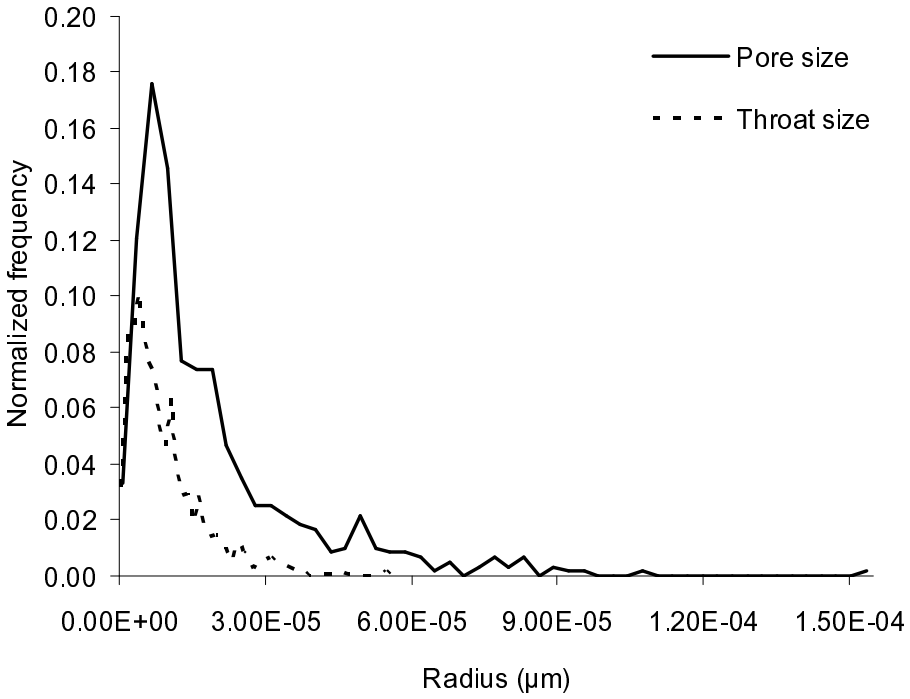

Figure 6.35. Distributions of coordination number (top) and pore size and throat size (bottom) of sample S6. The network porosity is 24.0% and the average coordination number is 4.0.

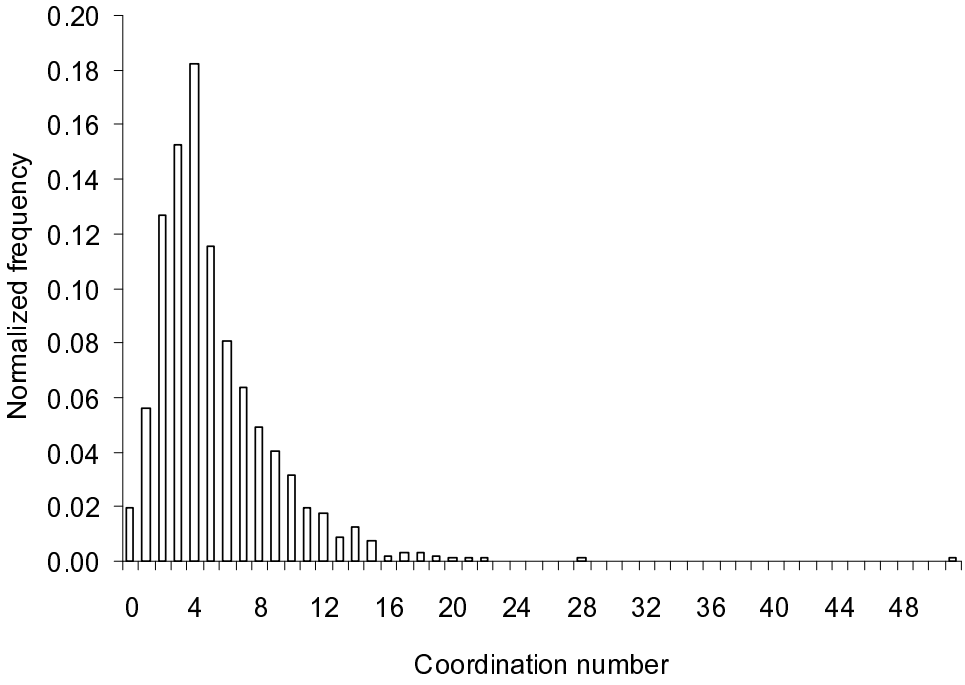

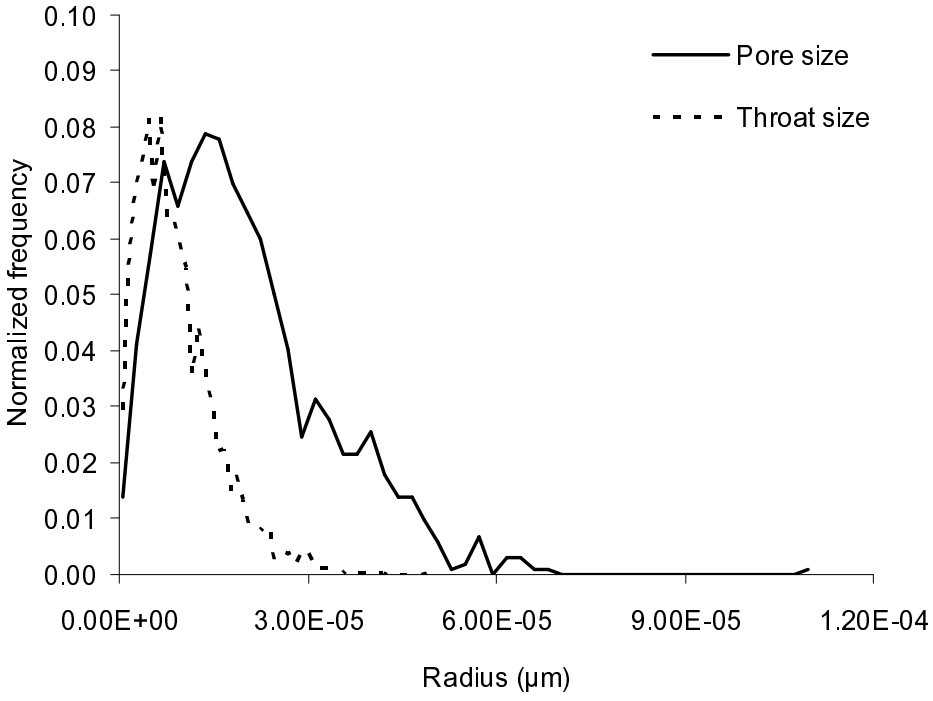

Figure 6.36. Distributions of coordination number (top) and pore size and throat size (bottom) of sample S7. The network porosity is 25.1% and the average coordination number is 5.23.

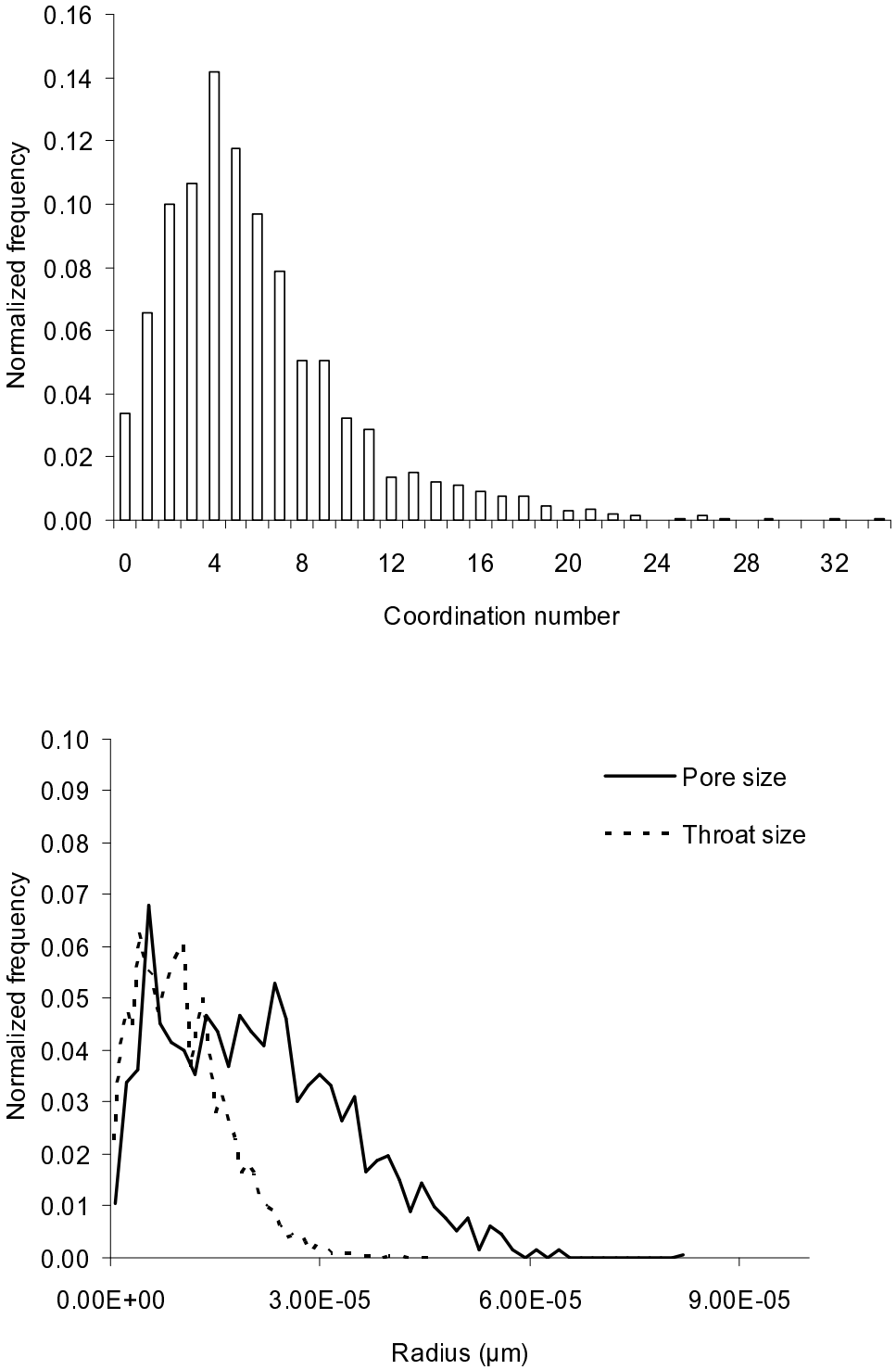

Figure 6.37. Distributions of coordination number (top) and pore size and throat size (bottom) of sample S8. The network porosity is 34.0% and the average coordination number is 5.94.

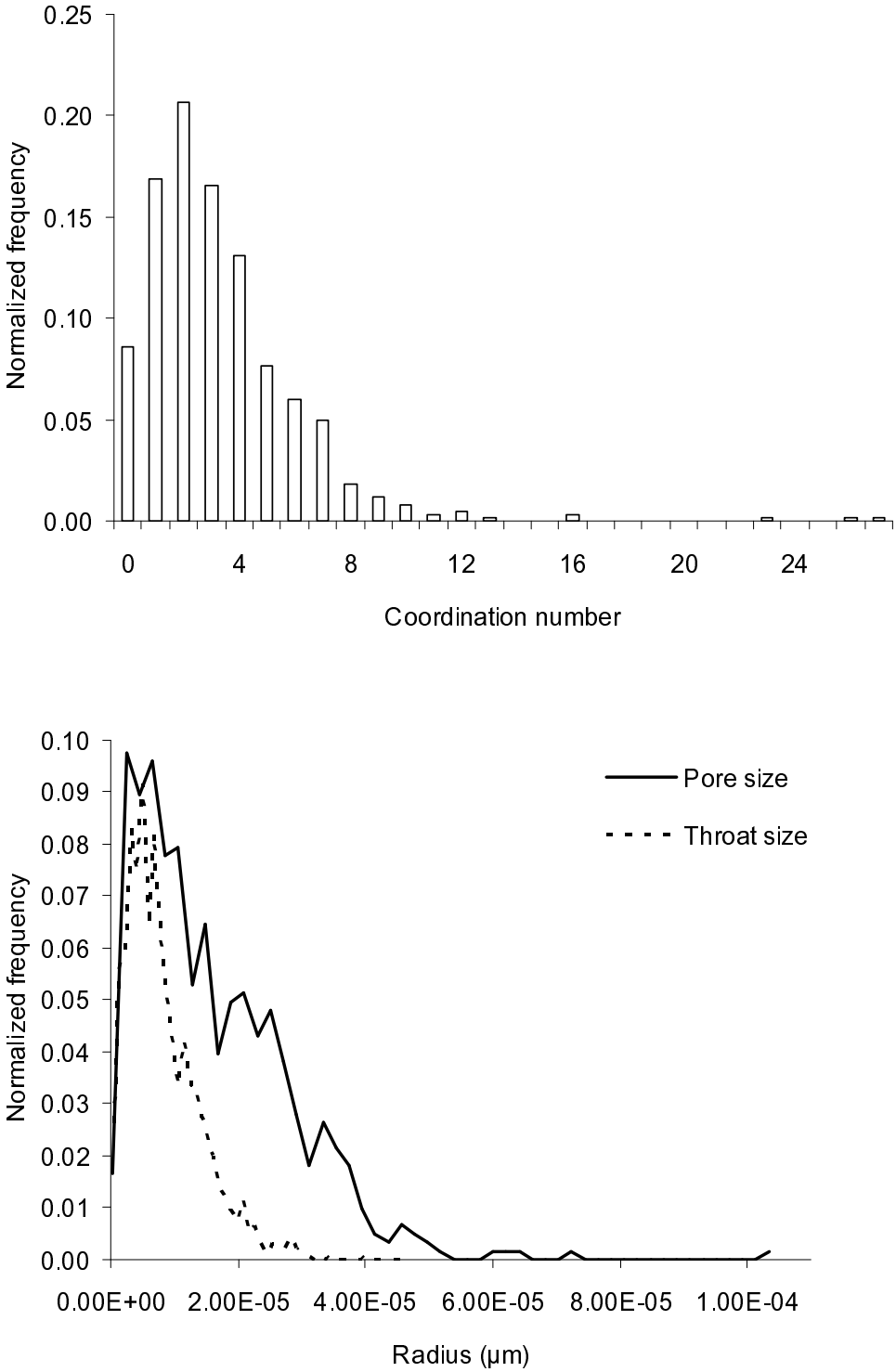

Figure 6.38. Distributions of coordination number (top) and pore size and throat size (bottom) of sample S9. The network porosity is 22.2% and the average coordination number is 3.32.

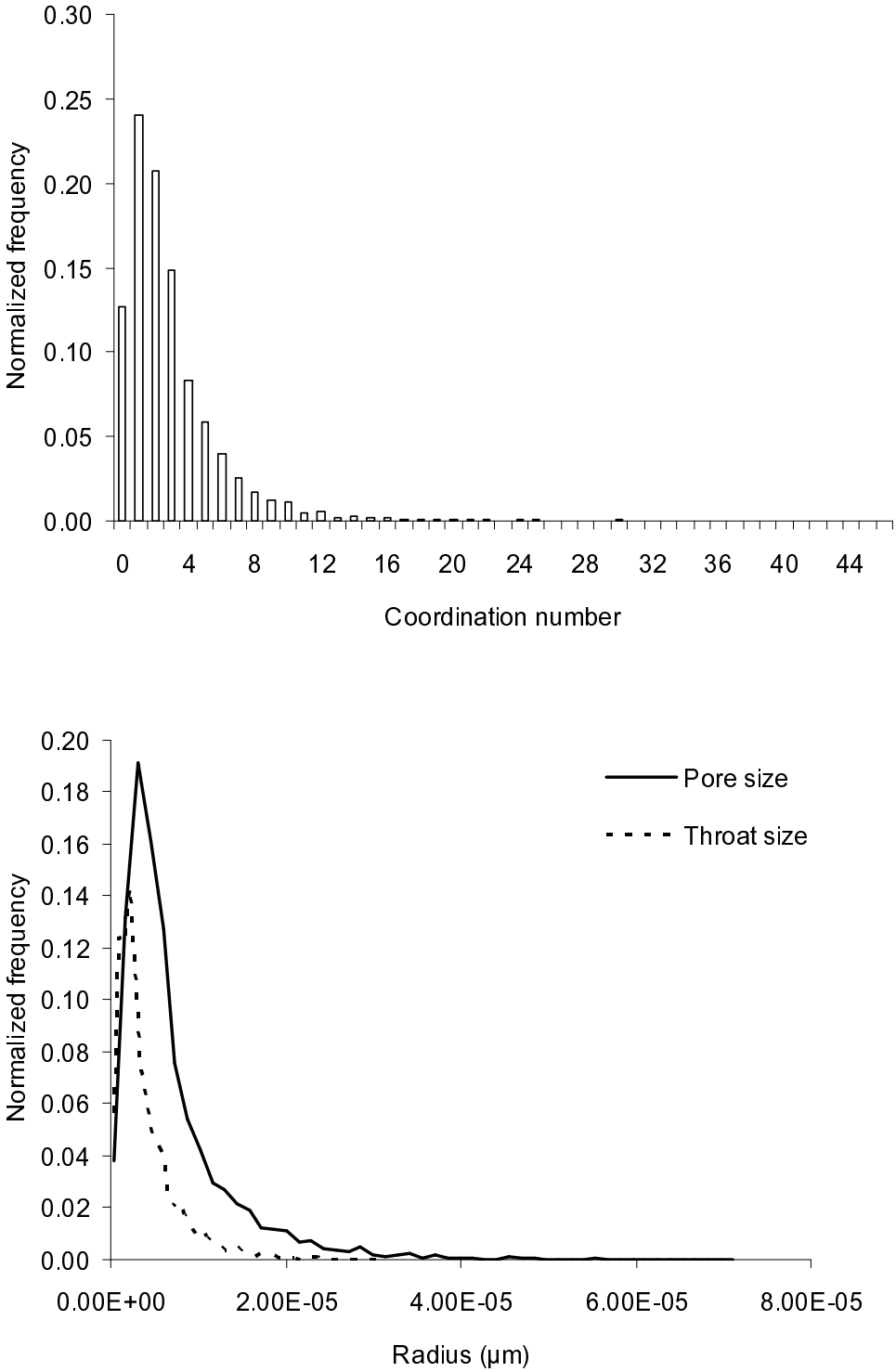

Figure 6.39. Distributions of coordination number (top) and pore size and throat size (bottom) of sample C1. The network porosity is 23.3% and the average coordination number is 3.0.

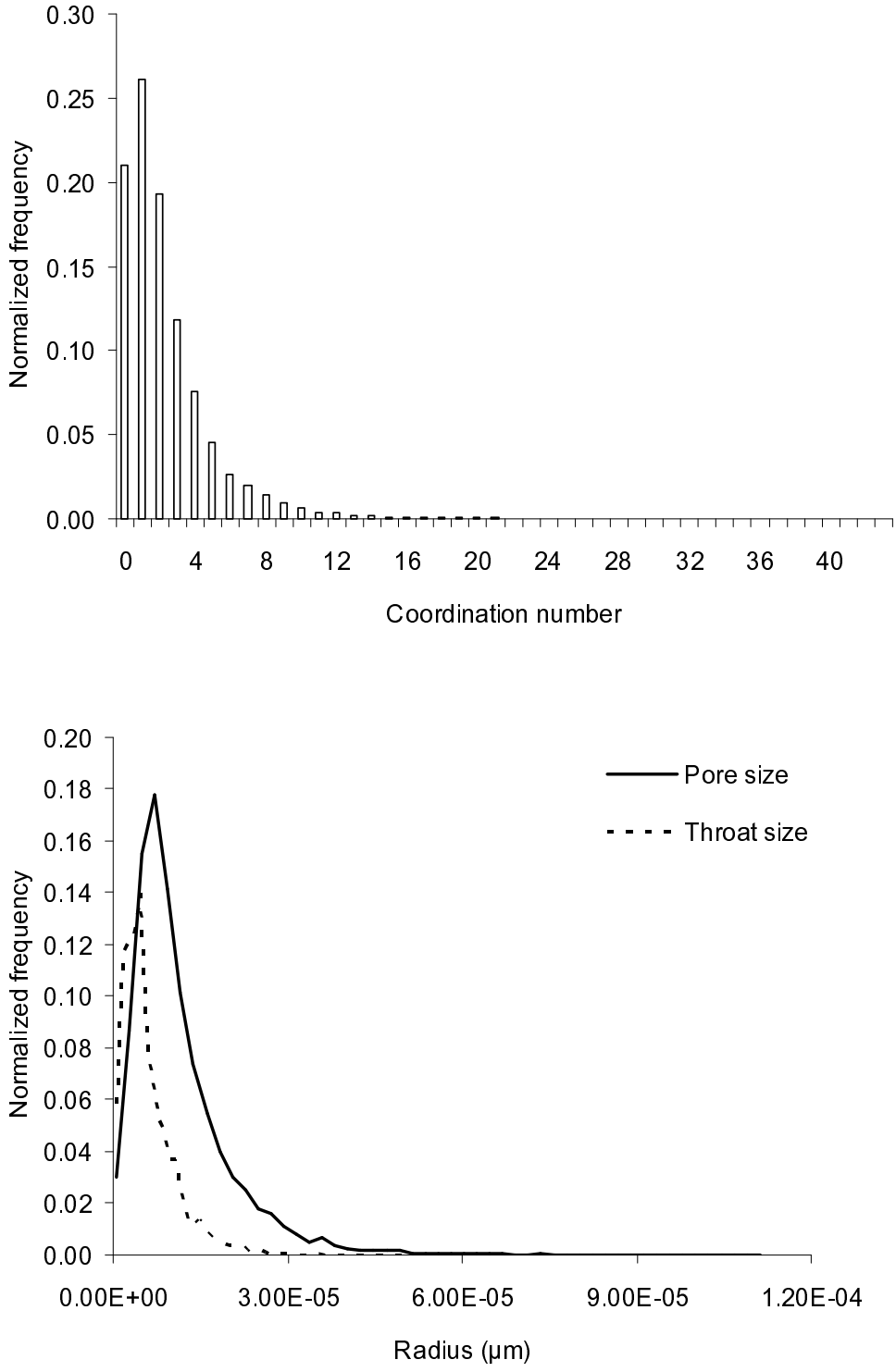

Figure 6.40. Distributions of coordination number (top) and pore size and throat size (bottom) of sample C2. The network porosity is 16.8% and the average coordination number is 2.37.

7 Transport predictions

To assess the quality of the network extraction method, we validate our algorithm on selected samples from our image library to extract pore networks. The two-phase pore-scale simulator developed at Imperial College London by Valvantne and Blunt (2004) was used to predict single and two-phase flow through these networks.

Single-phase flows are simulated across all the extracted networks and the absolute permeability and formation factors are calculated on the networks and compared to the results computed directly on the images using Lattice Boltzmann simulation for absolute permeability (Chen and Doolen, 1998; Manwart et al., 2002) and solving the Laplace equation on the image grid for the formation factor (Øren and Bakke, 2002) by Øren and Bakke at Numerical Rocks AS.

Two-phase flow was simulated and the capillary pressure curves and relative permeability were computed across the networks of Fontainebleau sandstone (PB reconstructed image) and Berea sandstone (micro-CT imaged at Imperial College). The results of multi-phase properties are compared against the PB networks (Øren and Bakke, 2002; 2003) and experimental data (Oak, 1990).

7.1 Calculation of absolute permeability

The single-phase absolute permeability was calculated on both pore networks using the pore-scale simulator and on the voxel based 3D pore space images using a lattice Boltzmann simulation.

7.1.1 Calculating absolute permeability of pore networks

The two-phase pore-scale simulator developed at Imperial College London (Valvatne and Blunt, 2004) was used to predict the transport properties of the networks extracted. The saturation was calculated using the prevailing maximum in capillary pressure (or minimum in the case of water injection) to compute the radius of curvature of the fluid interfaces. The absolute permeability *K* of the network is derived from Darcy's law,

$$K = \frac{\mu_p q_{tsp} L}{A(\Phi_{inlet} - \Phi_{outloet})} \tag{7.1}$$

where the network is fully saturated with a single phase *p* of viscosity μ_p. q_{tsp} is the total single phase flow rate through the pore network of length *L* with the potential drop $(\Phi_{inlet} - \Phi_{outloet})$. A is the cross-sectional area of the model.

The relative permeability k_{rp} is given by

$$k_{rp} = \frac{q_{tmp}}{q_{tsp}} \tag{7.2}$$

where q_{tmp} is the total flow rate of phase *p* in multiphase conditions with the same imposed pressure drop.

The flow rate q_p between two pores *i* and *j* is given by

$$q_{p,ij} = \frac{g_{p,ij}}{L_{ij}}(\Phi_{p,i} - \Phi_{p,j}) \tag{7.3}$$

where g_p is the fluid conductance, L is the length between the pore centers (throat total length) and Φ is the phase potential.

The conductance between two pore bodies (*i, j*) via throat (*t*) is given as the harmonic mean of each individual conductance,

$$\frac{l_{ij}}{g_{p,ij}} = \frac{l_i}{g_{p,i}} + \frac{l_t}{g_{p,t}} + \frac{l_j}{g_{p,j}} \tag{7.4}$$

where l_{ij} is the distance from pore *i* center to pore *j* center (throat total length); l_i and l_j are the pore body lengths (i.e. *pore-i* length and *pore-j* length defined in Section 4.4), which are the lengths from the pore-throat interface to the pore centers, as illustrated in Fig. 7.1; l_t is the throat length that is the length of purely the throat.

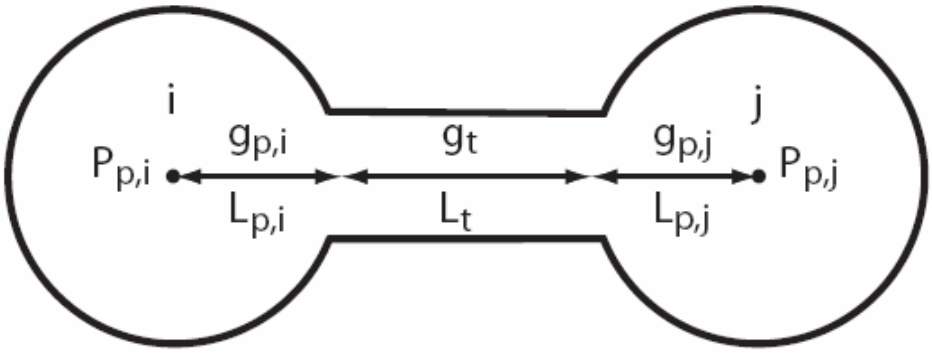

Figure 7.1. Conductance between two pore bodies *i* and *j*. (Valvatne, 2004)

For single-phase laminar flow in a given shape tube, the conductance g_p is given analytically by the Hagen-Poiseuille formula,

$$g_p = k\frac{A^2 G}{\mu_p} \tag{7.5}$$

For a circular, an equilateral and a square tube, the constant k is 0.5, 0.6 and 0.5623 respectively (Patzek and Silin, 2001).

7.1.2 Calculation of absolute permeability on voxelized images

Instead of solving the Navier-Stokes equations to calculate the absolute permeability, the discrete Boltzmann equation is solved to simulate the flow of Newtonian fluid with collision models(Chen and Doolen, 1998; Manwart et al., 2002). The advantage of the lattice Boltzmann method (LBM) compared to the traditional Computational fluid dynamics (CFD) method is that the LBM models the fluid as consisting of fictitious particles performing consecutive propagation and collision processes on the discrete lattice mesh (voxel grids) rather than solving numerically for the conservation equations of mass and momentum. In other words, the LBM captures the essential physics at the micro- or meso-scopic scale in order to satisfy the macroscopic dynamics from the averaged particles behavior (Okabe, 2004). The lattice Boltzmann simulation is fully parallelized and capable to deal with complex boundary conditions.

In this study, we used LBM to simulate single-phase flow for the absolute permeability. The Boltzmann equation is discretized by limiting the space to a lattice and the velocity space to a discrete set of velocities $\vec{e}_i$, therefore the lattice Boltzmann equation is:

$$f_i(\vec{x}+\vec{e}_i, t+1) - f_i(\vec{x}, t) = \Omega_i(f_i(\vec{x}, t)) \tag{7.6}$$

where $f_i(\vec{x},t)$ is the particle distribution function at location $\vec{x}$ and time *t* along the *i*-th direction (*i*=0,1,2…18) using three-dimensional nineteen velocity model (Qian et al., 1992) which considers three velocity types as shown in Fig.7.2. $\Omega_i(f_i(\vec{x},t))$ is the collision operator and $\vec{e}_i$ is the local particle velocity.

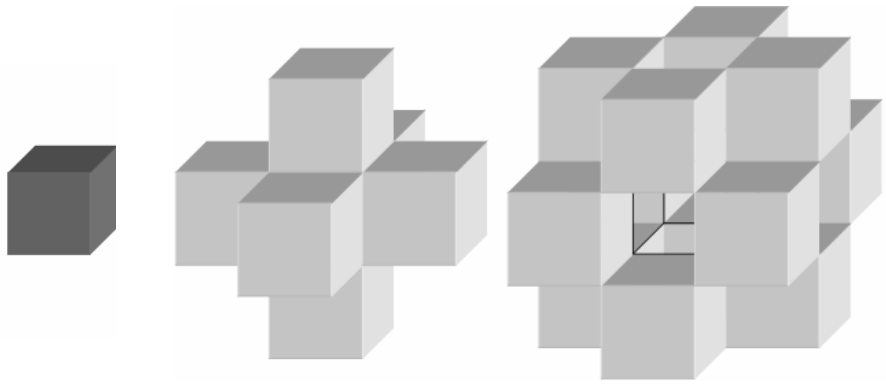

Figure 7.2. 19 velocity vectors (directions along the neighboring voxels in three velocity types — the central (1), lateral (6) and diagonal (12) directions, in the picture from left to right respectively).

The collision operator represents the relaxation proccess to local equilibrium, which is often approximated by a BGK collision operator (Bhatnagar et al., 1954) and widely used due to its simplicity (Qian et al., 1992).

$$\Omega_i = \frac{1}{\tau}(f_i^{\,0} - f_i) \tag{7.7}$$

where τ is the single time relaxation parameter and $f_i^{\,0}$ is the local equilibrium state depending on the local density and velocity. The conserved quantities are the mass and momentum described below

$$\rho = \sum_i f_i = \sum_i f_i^{\,0} \tag{7.8}$$

$$\rho\vec{u} = \sum_i f_i \vec{e}_i = \sum_i f_i{}^0 \tag{7.9}$$

where ρ and $\boldsymbol{u}$ are the density and the local velocity respectively.

Thus, the 3D single-phase LB model is

$$f_i(\vec{x} + \vec{e}_i, t+1) - f_i(\vec{x}, t) = \frac{1}{\tau}(f_i{}^0 - f_i) \tag{7.10}$$

7.2 Calculation of formation factors

Similarly, the formation factors were calculated on both pore networks and the voxelized 3D pore space images to compare the results.

7.2.1 Calculation of formation factors of pore networks

Fatt (1956c) used electrical circuit to calculate relative permeability curves across a pore network, because Poiseuille's law can be closely related to Ohm's law, $a = g_e V$, where pressure can be replaced by voltage V, fluid flow replaced by electrical current a and hydraulic conductance replaced by electrical conductance g_e. Fluid flow is analogous to electrical current and the electrical analogy to absolute permeability is formation factor F,

$$F = \frac{R_0}{R_w} \tag{7.11}$$

where R_0 is the resistivity of the network elements when fully saturated by water and R_w is the resistivity of water . The resistivity of the network is found from Ohm's

law,

$$R_0 = \frac{A\Delta V}{a_{ts} L} \tag{7.12}$$

where A is the cross-sectional area, ΔV is the voltage drop, a_{ts} is the total single phase flow of current and L is the length of the network. The electrical conductance between two pore bodies is assumed a function of the cross-sectional area occupied by the conducting water (Valvatne, 2004),

$$g_e = \frac{A_w}{R_w} \tag{7.13}$$

The potential field is analogous to the pressure field in the calculation. Since the rock matrix is non-conductive, formation factor will decrease with increasing absolute permeability.

7.2.2 Calculation of formation factors on voxelized images

Similarly, the work done in Numerical Rocks AS to calculate formation factor on voxel based images uses the same conceptual basis. The details of the method are described by Øren and Bakke (2002).

The directional formation factor, F_i, is expressed as the inverse of the macroscopic electrical conductance σ_i in the direction i,

$$F_i = \frac{\sigma_w}{\sigma_i} \tag{7.14}$$

where σ_w is the macroscopic electrical conductance of the fluid phase filling the pore space. σ_i can be derived from the linear relation between the total electrical flux and the applied potential gradient,

$$E = -\sigma_x \frac{\Delta\Phi}{L} A \tag{7.15}$$

where E is the total electrical flux; $\Delta\Phi$ is the total potential drop over the distance L in the flow direction x; A is the total cross-sectional area normal to flow direction; the electrical potential is determined by solving the Laplace equation,

$$\nabla \cdot (\sigma \nabla \Phi) = 0 \tag{7.16}$$

$$\nabla \Phi \cdot \vec{n} = 0 \text{ on } S_p \tag{7.17}$$

where $\vec{n}$ is the unit vector normal to the wall S_p. It is assumed the solid phase is insulating which is well verified for sandstones without clay content so the conductance is distributed as $\sigma(\vec{x}) = \sigma_w Z(\vec{x})$ where $Z(\vec{x})$ equals one if $\vec{x}$ is inside the pore space and zero if in the solid.

The flux E can be determined from

$$E = -\int_{\Omega_x} \sigma_w \frac{\partial \Phi}{\partial x} dydz \tag{7.18}$$

where Ω_x is the cross-section normal to the flow direction x.

From the equations above, the electrical conductivity can be derived,

$$\sigma_x = \frac{1}{A}\frac{\Delta x}{\Delta \Phi}\int_{\Omega_x} \sigma_w \frac{\partial \Phi}{\partial x} dydz \tag{7.19}$$

thus the formation factor along the *x* direction is

$$F_x = \frac{1}{\sigma_x} \tag{7.20}$$

The average formation factor is the harmonic mean of three directions,

$$\frac{1}{F} = \frac{1}{3}\left(\frac{1}{F_x} + \frac{1}{F_y} + \frac{1}{F_z}\right) \tag{7.21}$$

To calculate the formation factors on the voxelized images, Equation 7.16 is solved by a finite volume method on the voxels, which is written as below

$$\int_{\partial V} \sigma_w \nabla \Phi \cdot \vec{n} dA = 0 \tag{7.22}$$

for all (open) control volumes *V*; for the closed control volumes (solid phase), the boundary condition is set to $\Phi = 0$.

7.3 Results for single-phase flow simulations

Pore networks are extracted from the Berea sandstone μCT and reconstructed Fontainebleau images as well as other 12 samples selected from the image library. The petrophysical properties, i.e. the porosity, absolute permeability and formation factors are calculated through all these networks. The results for Fontainebleau and Berea sandstone will be discussed in Section 7.3.1 and 7.3.2. The results from the rest

of networks is summarized in Table 7.3.

7.3.1 Single phase results for reconstructed Fontainebleau sandstone

The porosity of the image is measured by counting the number of voxels in the void space from the whole image. The pore network preserves the porosity of the image by translating the pore space into pore and throat elements. The absolute permeability and formation factors of these networks are computed (see Section 7.1.1 & 7.2.1) using Valvatne and Blunt's simulator (2004) and compared to the results derived by solving numerically the local equations governing the transport on the 3D micro-CT images directly (Øren and Bakke, 2002; 2003, see Section 7.1.2 & 7.2.2).

Table 7.1. Properties of Fontainebleau networks.

Petrophysical properties	**PB**	**MB**
Net porosity	0.136	0.136
Clay bound porosity	0.0	0.0
Absolute permeability (mD)	582	380
Absolute permeability (m^2)	5.75×10^{-13}	3.75×10^{-13}
Formation factor	34.93	30.57

From the comparison, we found both the permeability and formation factor of the two networks are in good agreement. The absolute permeability of MB network is even closer compared to that calculated on the voxel image (345 mD) listed in Table 7.3. The absolute permeability of the two networks are both low compared to 862 mD for the experimental data (Bourbie and Zinszner, 1985, Equation 5.1).

7.3.2 Single-phase results for Berea sandstone

Since we do not distinguish the clay content in the micro-CT image, we distribute clay that remains water-filled during the simulations uniformly to each element of the pore network to match the connate water saturation. The two networks (PB and MB) have similar porosity but different absolute permeability. The absolute permeability of the PB image is 2668 mD compared to an experimental value of 1100 mD. The permeability of the MB network is 1111 mD compared to an experimental measurement of of 650 mD on a core plug (provided by the sample owner). Again these results are consistent with the PB sample representing a slightly coarser-grained, more permeable sample. However, both networks over-predict permeability. This may be due to the heterogeneity of the sample, since we only study 9.77 mm^3 of the rock volume, and the uncertainty associated in the course of imaging and image processing. It is also noted that the prediction made by the network is close to that calculated on the voxel image directly (1286 mD). This implies that the network extraction algorithm preserves permeability and that any errors are due to sample size and the image processing.

Table 7.2. Properties of Berea networks.

Petrophysical properties	**PB**	**MB**
Net porosity	0.183	0.197
Clay bound porosity	0.057	0.07
Absolute permeability (mD)	2668	1111
Absolute permeability (m^2)	2.63×10^{-12}	1.10×10^{-12}
Formation factor	14.33	14.58

7.3.3 Single-phase results for various samples

Pore networks have been extracted from a series of images selected in Chapter 5. Single phase flow has been simulated across the networks and the results are compared to that computed from voxel-based micro-CT images. From Table 7.3, it is found the MB networks predict the absolute permeability successfully with an average overestimation factor of 1.11. However, the MB networks tend to underestimate the formation factors by a factor of 1.73, which needs further investigation. Formation factor is the inverse of conductivity; hence we over-estimate the conductivity of the system. This is consistent with our error in permeability. Conductivity is proportional to the cross-sectional area, while permeability is proportional to area squared. That we better predict permeability is consistent with the MB algorithm estimating the larger pore and throat sizes accurately, while over-estimating the average pore sizes. What is more, the pore networks underestimated absolute permeability for some samples, such as carbonate sample C1 and a consolidated sandstone sample S4 due to uncertainty associated to their relatively low image resolutions that may lead to the extraction of a poorly connected network.

Table 7.3. Computed transport properties for the samples studied.

Sample name	**A1**	**S1**	**S2**	**S3**	**S4**	**S5**	**S6**	**S7**	**S8**	**S9**	**C1**	**C2**	**B.**	**F.**	**AVG**
Rock type	P[1]	S	S	S	S	S	S	S	S	S	C	C	S	S	
Resolution (μm)	3.9	8.7	5.0	9.1	9.0	4.0	5.1	4.8	4.9	3.4	2.9	5.3	5.3	7.5	
Porosity(%)	42.9	14.1	24.6	16.9	17.1	21.1	24.0	25.1	34.0	22.2	23.3	16.8	19.6	13.5	
Kx (mD)	8272	1969	4318	143	273	4638	11289	7268	13063	2735	785	38	1360	292	
Ky (mD)	7977	1752	3983	420	289	4874	10683	7594	13507	2093	1469	161	1304	321	
Kz (mD)	5412	1312	3394	109	215	4440	10951	6037	12936	1844	1053	18	1193	422	
Avg. K (mD) [2]	7220	1678	3898	224	259	4651	10974	6966	13169	2224	1102	72.333	1286	345	
Network K (mD) [2]	8076	1486	3950	281	169	5369	11282	7926	13932	3640	556	158	1111	380	
K overestimation factor[3]	1.12	0.89	1.01	1.25	0.65	1.15	1.03	1.14	1.06	1.64	0.50	2.18	0.86	1.10	1.11
FFx	4.47	36.32	10.85	52.16	74.50	14.08	10.26	9.58	6.02	16.42	33.74	185.83	23.12	53.86	
FFy	4.57	37.89	11.32	41.89	71.01	14.59	11.17	9.28	5.97	19.85	21.94	120.96	23.99	53.03	
FFz	5.73	53.47	12.55	70.32	114.44	15.90	12.92	11.17	6.53	18.10	27.18	248.69	25.22	46.81	
Avg. FF[2]	4.86	41.31	11.53	52.40	82.77	14.82	11.35	9.94	6.16	18.02	26.78	169.78	24.08	51.03	
Network FF[2]	2.36	26.00	6.53	37.40	59.40	8.04	6.68	5.41	3.39	8.69	22.00	78.71	14.86	30.57	
FF underestimation factor[3]	2.06	1.59	1.77	1.40	1.39	1.84	1.70	1.84	1.82	2.07	1.22	2.16	1.65	1.67	1.73

[1] P=sandpack; S=sandstone; C= carbonate; B.= Berea sandstone; F.= Fontainebleau sandstone;

[2] Kx, Ky, Kz, FFx, FFy and FFz are the directional absolute permeability and formation factors in X, Y and Z directions respectively; network K and FF are the absolute permeability and formation factors measured on the pore networks; AVG K is the average absolute permeability; AVG FF is the harmonic mean of the formation factors of the three directions;

[3] K overestimation factor is the ratio of network K to avg. K; FF underestimation factor is the ratio of avg. FF to network FF.

7.4 Results of multi-phase flow simulations

In this section, we predict two-phase flow transport properties for Fontainebleau sandstone and Berea sandstone using MB networks. We assume both samples are water-wet and simulate the primary drainage (oil invading) and secondary imbibition (water flooding) cycles through the pore networks.

For the benchmark purpose, the results of Fontainebleau sandstone are compared to the simulation results at the same condition using the PB network; for the Berea sandstone, the results are compared against both the simulation results across a PB network and experimental data (Oak, 1990).

7.4.1 Relative permeability of reconstructed Fontainebleau sandstone

During the primary drainage, the networks are assumed strongly water-wet with a receding contact angle of 0 degrees.

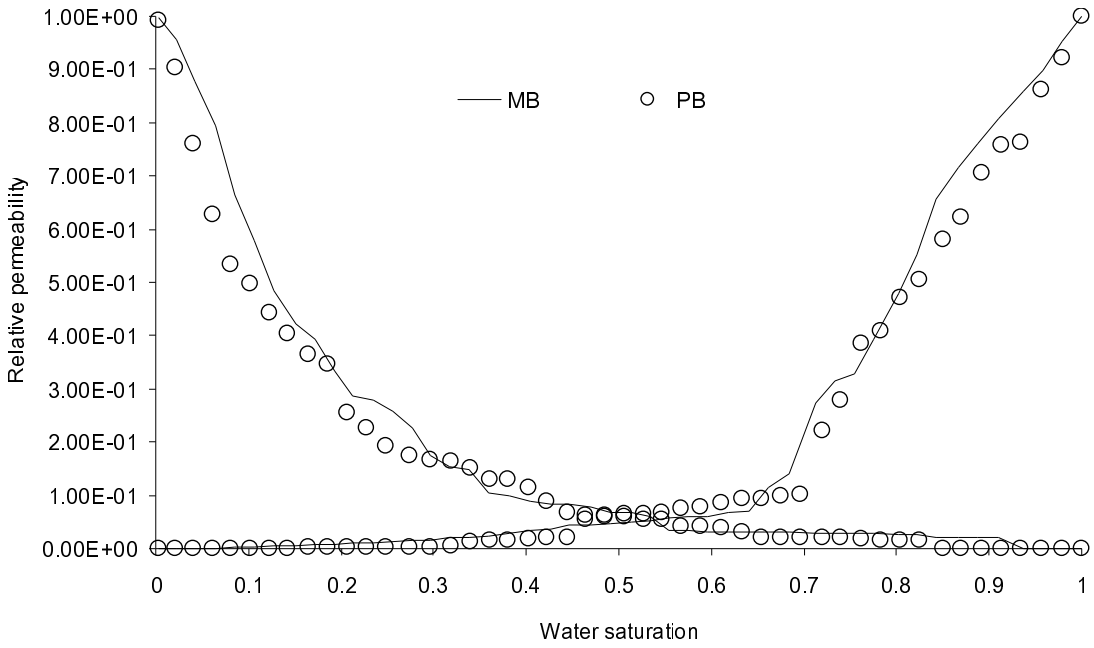

Figure 7.3. Predicted primary oil flooding for reconstructed Fontainebleau sandstone using PB and MB networks.

The similarity in the drainage relative permeability curves indicates that the two networks are in good agreement in terms of topology and element geometry. The slightly less curving MB relative permeability may be consistent with a broader pore size distribution shown in Section 6.2.3.

To predict the imbibition data, we assumed a uniform distribution of intrinsic contact angles between 50-60 degrees (same as the range used by Valvatne and Blunt for water-wet Berea sandstone predictions). The corresponding advancing contact angles can be found in Fig. 7.4 (Valvatne and Blunt, 2004; Morrow, 1975).

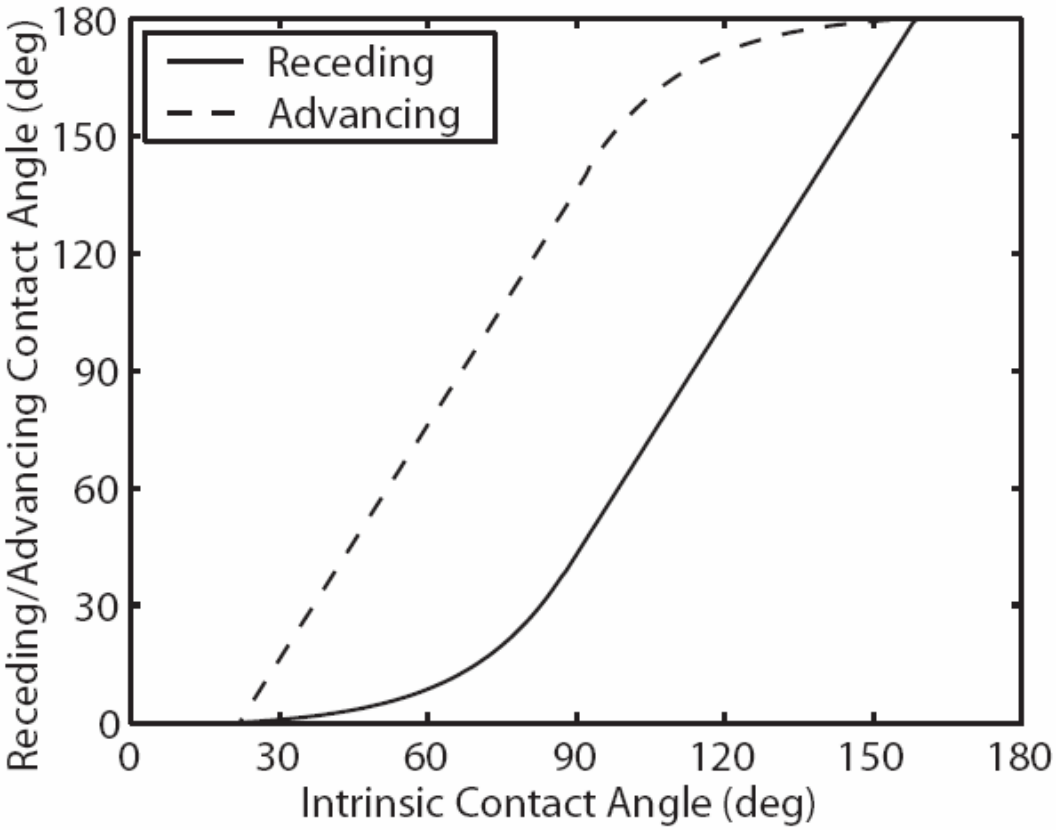

Figure 7.4. Relationship of the receding and advancing contact angles on a rough surface as a function of intrinsic contact angles measured at rest on a smooth surface [Morrow, 1975].

The two networks yield similar oil relative permeability and the same residual oil saturation (Fig. 7.5). The water relative permeability of MB network is higher than for the PB network. This is due to the smaller shape factors in the MB networks, which allows the wetting phase (water) to be better connected in the corners of the

pores and throats. While there is no direct experimental data to compare against, the very low water relative permeability for the PB network is unlikely to be correct.

Table 7.4. Fluid properties used in predictions of Fontainebleau sandstone.

Properties	
Surface tension (10^{-3} N/m)	30
Water viscosity (10^{-3} Pa/s)	1.05
Oil viscosity (10^{-3} Pa/s)	1.39

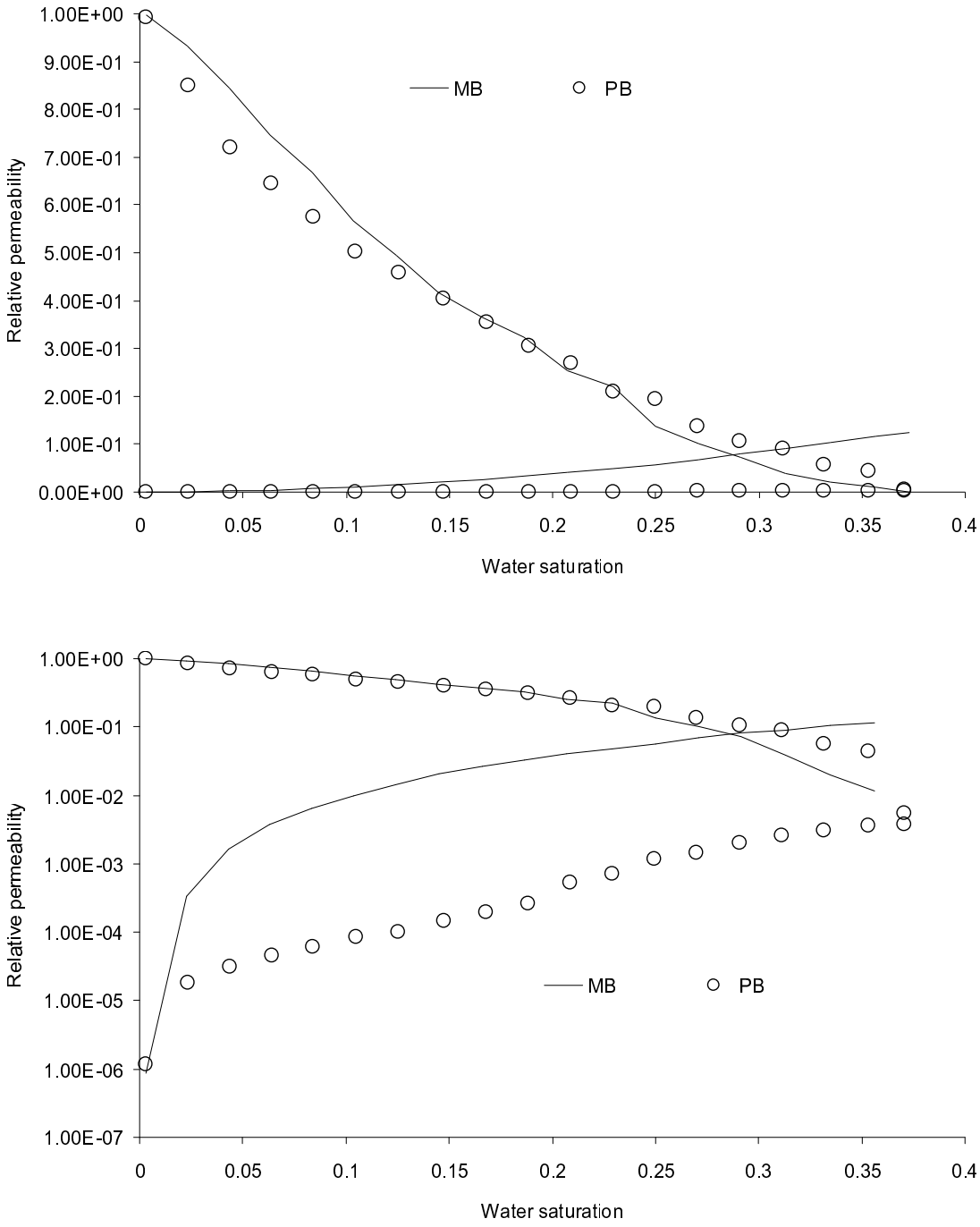

Figure 7.5. Predicted secondary water flooding cycle for reconstructed Fontainebleau sandstone using PB and MB networks. The lower figure shows the relative permeability on a logarithmic axis.

7.4.2 Relative permeability of Berea sandstone

Valvatne and Blunt (2004) used a PB Berea pore network generated by Øren and Bakke (2003) to predict the two-phase behavior of water-wet Berea sandstone observed experimentally by Oak (1990). In the experiment, 1800 steady-state two-phase and three-phase relative permeability data had been collected using three fired Berea sandstone with variety of absolute permeability (Sample 6: 200mD; Sample 13: 1000mD; and Sample 14: 800mD). Valvatne and Blunt used Sample 13 data for the predictions since this sample has a similar permeability of 1100 mD (Hazlett, 1995; Øren and Bakke, 2002).

The original sample imaged at Imperial College has a porosity of 22% and a permeability of 650 mD that is closer to Sample 14 (see Table 7.5). We use the extracted MB network to predict for both samples. The rock and fluid properties listed in Table 7.5 were used by Oak in the experiment. We use the same properties for the simulation. The only input parameters we change for the predictions are the contact angles.

Table 7.5. Rock and fluid properties used in Oak (1990) experiment for sample 13 and 14.

Properties	Sample 13	Sample 14
Absolute permeability (mD)	1000	800
Surface tension (10^{-3} N/m)	30	30
Water viscosity (10^{-3} Pa/s)	1.05	1.05
Oil viscosity (10^{-3} Pa/s)	1.39	1.43

Predictions for Sample 13:

To predict the transport properties for Sample 13 for the water-oil system, Valvatne and Blunt used receding contact angle of 0 degrees for the primary drainage; for the secondary imbibition, they uniformly distributed the intrinsic contact angles between 50 and 60 degrees. The corresponding advancing contact angles can be found using the relationship shown in Fig. 7.4. In our simulation, to match the connate water

saturation, we introduced clay uniformly into each network element as immobile volumes in the pores and throats. We used the same receding contact angle of 0 degrees for the primary drainage and uniformly distributed intrinsic contact angles between 50 to 70 degrees to match the experimental residual oil saturation in the secondary imbibition.

The predictions (in Fig. 7.6) in general are in good agreement with both the experimental data and Valvatne and Blunt's prediction results. During primary drainage, the water relative permeability matches the experimental data very well. However, the oil relative permeability is low especially at the low water saturation end, which indicates that the larger elements in the network are poorly connected. This is consistent with the slightly lower average coordination number and the large number of poorly connected pores in the MB network. The water relative permeability during the water flooding cycle again matches the experimental data well. But the oil relative permeability is rather low compared to the experiment and PB network prediction. The lower shape factors and higher aspect ratios in the MB network allows more snap-off, or the filling of small throats by water, disconnecting the oil phase. However, since the primary drainage curve, when all the oil is connected, is lower, this is more likely to be due to under-estimating the oil conductance.

Other possibilities for the discrepancy include the dissimilarity in the original samples, the heterogeneity intrinsic to the samples and the finite pore network size.

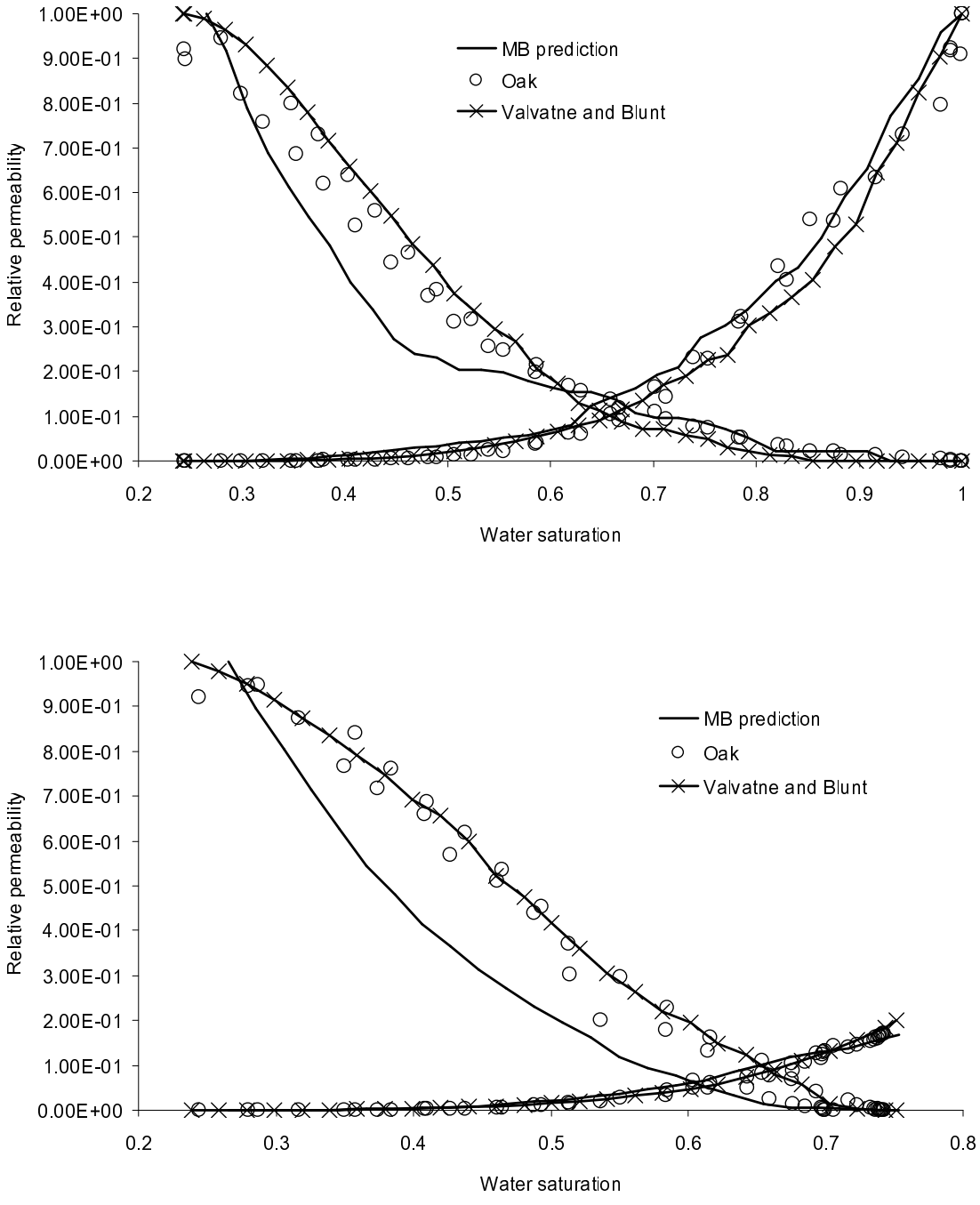

Figure 7.6. Predicted primary oil flooding (top) and secondary water flooding (bottom) relative permeability for water-wet Berea sandstone compared to Oak experimental data and Valvatne and Blunt's predictions (2004) using a PB network.

Predictions for Sample 14:

We use the same method to introduce the clay and the same properties for predicting the experimental results for sample 14. The same receding contact angles (0 degrees) are used for primary drainage. The intrinsic contact angles are chosen randomly between 50 to 75 degrees to match the residual oil saturation. The relative permeability curves are shown in Fig. 7.7.

The relative permeability of primary drainage is better predicted using sample 14 than sample 13, although the MB network predicts more curvature in the oil relative permeability indicating again poor connectivity of the oil phase. Low oil relative permeability is also seen for water flooding indicating more snap-off trapping oil in the pores. On the other hand, the samples are not exactly the same and the network is rather small to present the whole core plug.

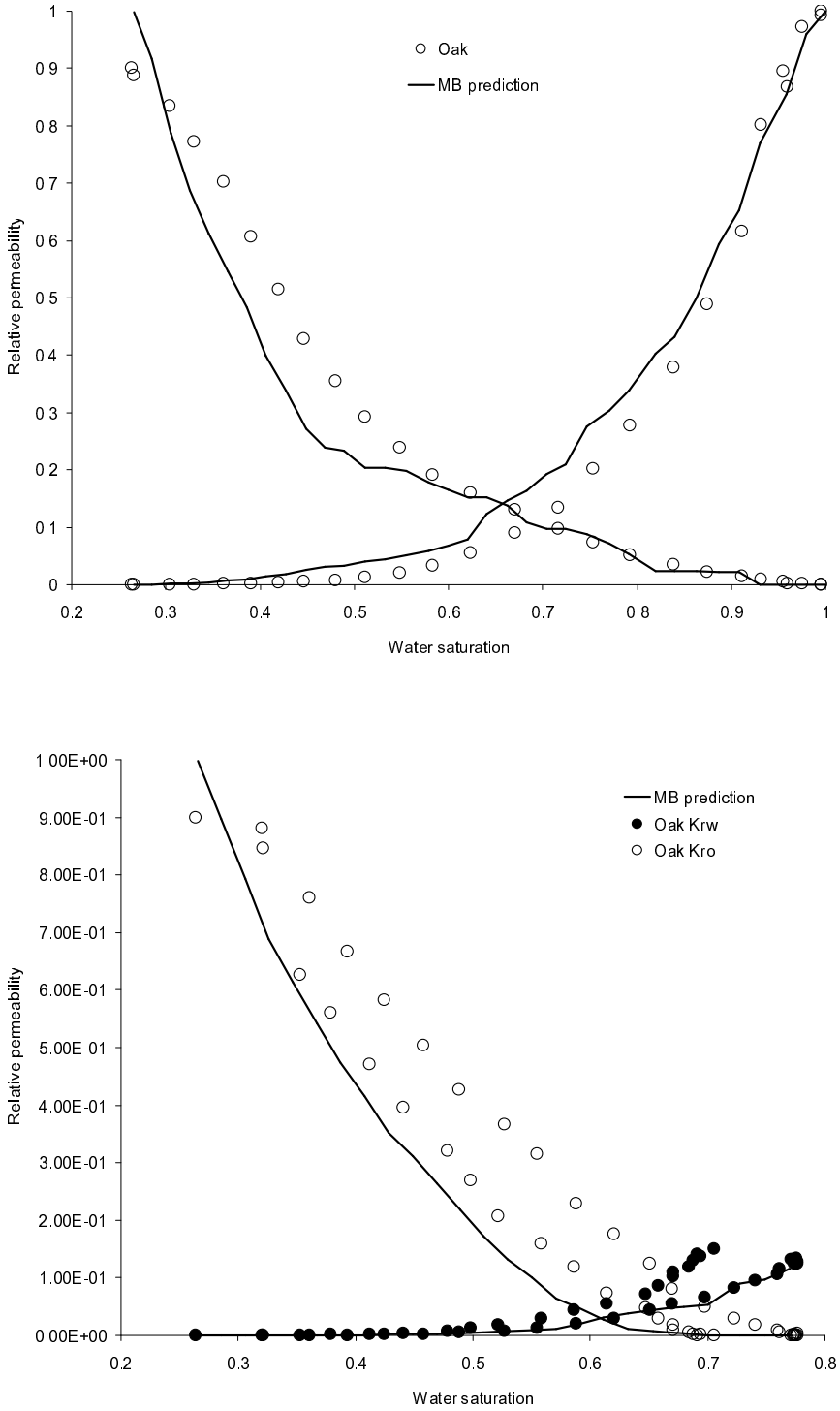

Figure 7.7. Predicted primary oil flooding (top) and secondary water flooding (bottom) relative permeability for water-wet Berea sandstone compared to experimental data by Oak (1990).

8 Conclusions and future directions

8.1 Conclusions

A preliminary study on micro-CT imaging porous rocks has been carried out and a series of micro-CT images on sandstone, carbonate and sand packs have been acquired during this project as part of the image library for the Consortium on Pore-Scale Modelling at Imperial College London.

A methodology has been developed to extract pore networks from generic 3D images as the input of the pore-scale models to predict single- and multi- phase flow in porous media. Micro-CT imaging, image processing and a maximal ball (MB) algorithm which includes the subroutines of constructing maximal balls, clustering balls into family trees and organizing voxels into pore and throat blocks with parameterized topology and geometries have been presented in this thesis.

The method has been tested on a series of samples from simple sphere packings to real rock images and compared to networks generated using process-based modeling (PB networks) and experimental data. The number of interior pores has been compared to theoretical solutions and PB networks. Both MB and PB methods define the correct number of pores in simple structures. When testing complex material structures, the MB method defines fewer pores than PB method due to different merging process and boundary considerations. The geometry and topology of the two types of networks are found similar by comparing the statistics of networks extracted from the same and similar images. There are two main aspects of difference. First, the segmentation of pore space into pore and throat blocks after the principal maximal balls are found representing nodes and links is dissimilar. The current MB network code tends to assign more volume to pores. Second, the size post-processing is different.

Full networks have been extracted to predict transport properties on a series of micro-CT images. For single-phase flow, MB pore networks yield good prediction of absolute permeability but underestimate the formation factors by an average factor of

1.7 compared to the calculation on voxelized images directly. The prediction of multi-phase properties, such as relative permeability, is promising, although for Berea the relative permeability of the oil phase is under-estimated.

In comparison to the method of Al-Kharusi and Blunt (2007), our approach avoids forming pores with very high coordination numbers and is more efficient in terms of memory requirements and computational time, allowing larger images to be analyzed; our method required only 325 s CPU time (Intel Core 2 6600 @ 2.4 GHz) and 655 MB memory to analyze images with 400^3 voxels. This allows larger samples to be analyzed more representative of core plugs and reducing the uncertainty associated with the finite images.

8.2 Future directions

Our current pore network generation algorithm captures the positions and sizes of the pores and throats as well as their connectivity. However, the MB method tends to find too many small throats especially when the image resolution is insufficient. The current MB method finds throats by protruding ends of family trees to detect connectedness but cannot guarantee every link to be located where the hydraulic restriction is strictly defined, since the ambiguity commonly exists in the discrete image in terms of distances and sizes. Medial axis methods can be used to determine cross-sections to find the local hydraulic minima as throats. What is more, even though the lengths and shape factors of pores and throats have been corrected by testing different cases yielding good predictions, the algorithm of pore space segmentation could be improved to avoid the need for such corrections.

The post-processing on sizes (pore and throat radius) currently aids good predictions, especially for single-phase flow. However, the size treatment influences the aspect ratio of the network which increases the amount of snap-off displacements during imbibition. It is suggested to improve the processing method caring for both single and multi-phase predictions by studying benchmarking data systematically.

The next stage in this research is to use the library of networks generated to

study the influence of structure on multi-phase flow properties, particularly relative permeability. This should enable us to determine what controls multi-phase flow and to make good predictions of properties for a variety of rock types. The impact of pore structure and wettability, benchmarked against experimental data, needs to be performed to improve our current assignment of properties for field-scale reservoir simulation.

We could also extend the present scope of the study to relate pore structure to pore and throat size distribution and coordination number distribution for a wide variety of rock types. This could enable us to estimate these distributions and their variation for samples where a direct three-dimensional image is not available.

Bibliography

Adler, P.M., Jacquin, C.G. and Thovert, J.F., 1992. The formation factor of reconstructed porous-media. Water Resources Research, 28: 1571-1576.

Adler, P.M. and Thovert, J.F., 1998. Real porous media: Local geometry and macroscopic properties. Applied Mechanics Review, 51: 537-585.

Al-Harthy, S., 1999. Laboratory investigation of petrophysical properties of sandstone rocks under true triaxial stress. PhD thesis, Imperial College London.

Al-Kharusi, A.S. and Blunt, M.J., 2007. Network extraction from sandstone and carbonate pore space images. Journal of Petroleum Science and Engineering 56: 219-231.

Alberts, L.J.H., 2005. Initial porosity of random packing. PhD thesis, Delft University of Technology, the Netherlands.

Arns, C.H., Bauget, F., Limaye, A., Sakellariou, A., Senden, T.J., Sheppard, A.P., Sok, R.M., Pinczewski, W.V., Bakke, S., Berge, L.I., Øren, P.-E. and Knackstedt, M.A., 2005. Pore-scale characterization of carbonates using X-ray microtomography. SPE Journal, 10(4): 475-484, doi:10.2118/90368-PA.

Arns, C.H., Knackstedt, M.A., Pinczewski, W.V. and Martys, N.S., 2004a. Virtual permeametry on microtomographic images. Journal of Petroleum Science and Engineering, 45: 41-46.

Arns, J.-Y., Robins, V., Sheppard, A.P., Sok, R.M., Pinczewski, W.V. and Knackstedt, M.A., 2004b. Effect of network topology on relative permeability transport in porous media, 55(1): 21-46. doi: 10.1023/B:TIPM.0000007252.68488.43.

Bakke, S. and Øren, P.-E., 1997. 3-D pore-scale modelling of sandstones and flow simulations in the pore networks. SPE Journal, 2: 136-149.

Baldwin, C.A., Sederman, A.J., Mantle, M.D., Alexander, P. and Gladden, L.F., 1996. Determination and characterization of the structure of a pore space from 3D volume images. Journal of Colloid and Interface Science, 181: 79-92.

Bekri, S., Xu, K., Yousefian, F., Adler, P.M., Thovert, J.F., Muller, J., Iden, K., Psyllos, A., Stubos, A.K. and Ioannidis, M.A., 2000. Pore geometry and transport properties in North Sea chalk. Journal of Petroleum Science and Engineering, 25: 107-134.

Bhatnagar, P.L., Gross, E.P. and Krook, M., 1954. A model for collision processes in gases. I: small amplitude processes in charged and neutral one-component system. Physical Review, 94: 511-525.

Blunt, M.J., 2001. Flow in porous media pore-network models and multiphase flow. Current Opinion in Colloid & Interface Science, 6: 197-207

Blunt, M.J., Jackson, M.D., Piri, M. and Valvatne, P.H., 2002. Detailed physics, predictive capabilities and macroscopic consequences for pore-network models of multiphase flow. Advances in Water Resources, 25: 1069-1089.

Bourbie, T., Coussy, O. and Zinszner, B., 1987. Acoustics of Porous Media. Gulf Publishing Company, Paris.

Bourbie, T. and Zinszner, B., 1985. Hydraulic and acoustic properties as a function of porosity in Fontainebleau sandstone. Journal of Geophysical Research, 90: 11524-11532.

Bryant, S. and Blunt, M., 1992. Prediction of relative permeability in simple porous media. Physical Review A, 46(4): 2004-2012.

Bryant, S. and Raikes, S., 1995. Prediction of elastic-wave velocities in sandstones using structural models. Geophysics, 60: 437-446.

Bryant, S.L., King, P.R. and Mellor, D.W., 1993a. Network model evaluation of permeability and spatial correlation in a real random sphere packing. Transport in Porous Media, 11: 53-70.

Bryant, S.L., Mellor, D.W. and Cade, C.A., 1993b. Physically representative network models of transport in porous media. AIChE Journal, 39(3): 387-396.

Celia, M.A., Reeves, P.C. and Ferrand, L.A., 1995. Recent advances in pore scale models for multiphase flow in porous media. Review of Geophysics, 33, Supplement: 1049-1057.

Chatzis, I. and Dullien, F.A.L., 1977. Modeling pore structure by 2-D and 3-D networks with application to sandstones. Journal of Canadian Petroleum Technology, 16: 97-108.

Chawla, N., Sidhu, R.S. and Ganesh, V.V., 2006. Three-dimensional visualization and microstructure-based modeling of deformation in particle-reinforced composites. Acta Materialia, 54(6): 1541-1548.

Chen, S. and Doolen, G.D., 1998. Lattice Boltzmann method for fluid flows. Annual Review of Fluid Mechanics, 30: 329-364.

Churcher, P.L., French, P.R., Shaw, J.C. and Schramm, L.L., 1991. Rock properties of

Berea sandstone, Baker dolomite, and Indiana limestone. Paper SPE 21044, Proceedings of the SPE International Symposium on Oilfiled Chemistry held in Anaheim, California.

Coenen, J., Tchouparova, E. and Jing, X., 2004. Measurement parameters and resolution aspects of micro X-ray tomography for advanced core analysis. Proceedings of International Symposium of the Society of Core Analysts, Abu Dhabi, UAE.

Coker, D.A., Torquato, S. and Dunsmuir, J.H., 1996. Morphology and physical properties of Fontainebleau sandstone via a tomographic analysis. Journal of geophysical research, 101(B8): 17497-17506.

Delerue, J.-F.-C. and Perrier, E., 2002. DXSoil, a library for 3D image analysis in soil science. Computers & Geosciences, 28: 1041-1050.

Dixit, A.B., McDougall, S.R., and K.S.Sorbie, 1997. Pore-level investigation of relative permeability hysteresis in water-wet systems. Paper SPE 37233, Proceedings of the 1997 SPE International Symposium on Oilfield Chemistry held in Houston.

Dullien, F.A.L., 1992. Porous Media: Fluid transport and pore structure. Academic Press, San Diego.

Dunsmuir, J.H., Ferguson, S.R., D'Amico, K.L. and Stokes, J.P., 1991. X-ray microtomography: a new tool for the characterization of porous media, Paper SPE 22860, Proceedings of 66th Annual Technical Conference and Exhibition of the Society of Petroleum Engineers, Dallas, TX.

Elliott, J.C. and Dover, S.D., 1982. X-ray micro-tomography. Journal of Microscopy, 126: 211-213.

Fatt, I., 1956a. The network model of porous media I. Capillary characteristics. Pet. Trans. AIME, 207: 144-159.

Fatt, I., 1956b. The network model of porous media II. Dynamic properties of a single size tube network. Pet. Trans. AIME, 207: 160-163.

Fatt, I., 1956c. The network model of porous media III. Dynamic properties of networks with tube radius distribution. Pet. Trans. AIME, 207: 164-181.

Fredrich, J.T., Menendez, B. and Wong, T.-F., 1995. Imaging the pore structure of geomaterials. Science, 268: 276-279.

Hazlett, R.D., 1995. Simulation of capillary-dominated displacements in microtomographic images of reservoir rocks. Transport in Porous Media, 20:

21-35.

Hilfer, R., 1991. Geometric and dielectric characterization of porous-media. Physical Review B, 44: 60-75.

Ioannidis, M.A. and Chatzis, I., 2000. On the geometry and topology of 3D stochastic porous media. Journal of Colloid and Interface Science, 229: 323-334.

Ioannidis, M.A., Chatzis, I. and Kwiecien, M.J., 1999. Computer enhanced core analysis for petrophysical properties. Journal of Canadian Petroleum Technology, 38: 18-24.

Jerauld, G.R. and Salter, S.J., 1990. The effects of pore-structure on hysteresis in relative permeability and capillary pressure: pore-level modeling. Transport in Porous Media, 5(2): 103-151.

Kak, A.C. and Slaney, M., 2001. Principles of computerized tomographic imaging. SIAM, New York.

Levitz, P., 1998. Off-lattice reconstruction of porous media: critical evaluation, geometrical confinement and molecular transport. Advances in Colloid and Interface Science, 77: 71-106.

Liang, Z., Ioannidis, M.A. and Chatzis, I., 2000. Geometric and topological analysis of three-dimensional porous media: pore space partitioning based on morphological skeletonization. Journal of Colloid and Interface Science, 221: 13-24.

Liang, Z.R., Fernandes, C.P., Magnani, F.S. and Philippi, P.C., 1998. A reconstruction technique for three-dimensional porous media using image analysis and Fourier transforms. Journal of Petroleum Science and Engineering, 21: 273-283.

Liang, Z.R., Philippi, P.C., Fernandes, C.P. and Magnani, F.S., 1999. Prediction of permeability from the skeleton of three-dimensional pore structure. SPE Reservoir Evaluation and Engineering, 2: 161-168.

Lindquist, W.B., Lee, S.M., Coker, D., Jones, K. and Spanne, P., 1996. Medial axis analysis of void structure in three-dimensional tomographic images of porous media. Journal of Geophysical Research, 101B: 8297.

Lindquist, W.B. and Venkatarangan, A., 1999. Investigating 3D Geometry of Porous Media from High Resolution Images. Phys. Chem. Earth (A), 25(7): 593-599.

Lowry, M.I. and Miller, C.T., 1995. Pore-scale modeling of nonwetting-phase residual in porous media. Water Resources Research, 31(3): 455-473.

Lymberopoulos, D.P. and Payatakes, A.C., 1992. Derivation of topological, geometrical, and correlational properties of porous media from pore-chart analysis of serial section data Journal of Colloid and Interface Science, 150(1): 61-80, doi:10.1016/0021-9797(92)90268-Q

Mahmud, W., Arns, J., Sheppard, A., Knackstedt, M. and Pinczewski, W., 2007. Effect of network topology on two-phase imbibition relative permeability. Transport in Porous Media, 66(3): 481-493. doi: 10.1007/s11242-006-0026-8.

Manwart, C., Torquato, S. and Hilfer, R., 2000. Stochastic reconstruction of sandstones. Physical Review E, 62: 893-899.

Manwart, C., Aaltosalmi, U., Koponen, A., Hilfer, R. and Timonen, J., 2002. Lattice-Boltzmann and finite-difference simulations for the permeability for three-dimensional porous media. Physical Review E, 66: doi:10.1103/PhysRevE.66.016702.

Mason, G. and Morrow, N.R., 1991. Capillary behavior of a perfectly wetting liquid in irregular triangular tubes. Journal of Colloid and Interface Science, 141: 262-274.

Morrow, N. R., 1975. Effects of surface roughness on contact angle with special reference to petroleum recovery, Journal of Canadian Petroleum Technology, 14: 42-53.

Oak, M.J., 1990. Three-phase relative permeability of water-wet Berea. Paper SPE 20183, Proceedings of the SPE/DOE Seventh Symposium on Enhanced Oil Recovery, Society of Petroleum Engineers, Tulsa.

Okabe, H., 2004. Pore-scale modelling of carbonates. PhD thesis, Department of Earth Science and Engineering, Imperial College London.

Okabe, H. and Blunt, M.J., 2004. Prediction of permeability for porous media reconstructed using multiple-point statistics. Physical Review E, 70: 066135.

Okabe, H. and Blunt, M.J., 2005. Pore space reconstruction using multiple-point statistics. Journal of Petroleum Science and Engineering, 46: 121-137.

Øren, P.-E. and Bakke, S., 2002. Process Based Reconstruction of Sandstones and Prediction of Transport Properties. Transport in Porous Media, 46: 311-343.

Øren, P.-E. and Bakke, S., 2003. Reconstruction of Berea Sandstone and Pore-Scale Modeling of Wettability Effects. Journal of Petroleum Science and Engineering, 39: 177-199.

Øren, P.-E., Bakke, S. and Arntzen, O.J., 1998. Extending Predictive Capabilities to

Network Models. SPE Journal, 3: 324-336.

Patzek, T.W., 2001. Verification of a complete pore network simulator of drainage and imbibition. SPE Journal, 6: 144-156

Patzek, T.W. and Silin, D.B., 2001. Shape factor and hydraulic conductance in noncircular capillaries I. One-phase creeping flow. Journal of Colloid and Interface Science, 236: 295-304.

Piri, M. and Blunt, M.J., 2005a. Three-dimensional mixed-wet random pore-scale network modeling of two- and three-phase flow in porous media. I. Model description. Physical Review E, 71: 026301, doi:10.1103/PhysRevE.71.026301.

Piri, M. and Blunt, M.J., 2005b. Three-dimensional mixed-wet random pore-scale network modeling of two- and three-phase flow in porous media. II. Results. Physical Review E, 71: 026302, doi:10.1103/PhysRevE.71.026302.

Prodanović, M., Lindquist, W.B. and Seright, R.S., 2006. Porous structure and fluid partitioning in polyethylene cores from 3D X-ray microtomographic imaging. Journal of Colloid and Interface Science, 298: 282-297.

Qian, Y.H., Dhumieres, D. and Lallemand, P., 1992. Lattice BGK models for Navier-Stokes equation. Europhysics Letters, 17: 479-484.

Quiblier, J.A., 1984. A new three-dimensional modeling technique for studying porous-media. Journal of Colloid and Interface Science, 98: 84-102.

Ridler, T.W. and Calvard, S., 1978. Picture thresholding using an iterative selection method. IEEE Trans. System, Man and Cybernetics, SMC-8: 630-632.

Roberts, A.P., 1997. Statistical reconstruction of three-dimensional porous media from two-dimensional images. Physical Review E, 56: 3203-3212.

Roberts, A.P. and Torquato, S., 1999. Chord-distribution functions of three-dimensional random media: approximate first-passage times of Gaussian processes. Physical Review E, 59: 4953-4963.

Serra, J., 1982. Image analysis and mathematical morphology. Academic Press, New York.

Sheppard, A.P., Sok, R.M. and Averdunk, H., 2005. Improved pore network extraction methods. Proceedings of International Symposium of the Society of Core Analysts, Toronto, Canada.

Shin, H., Lindquist, W.B., Sahagian, D.L. and Song, S.R., 2005. Analysis of the vesicular structure of basalts. Computers and Geosciences, 31: 473-487.

Silin, D. and Patzek, T., 2006. Pore space morphology analysis using maximal inscribed spheres. Physica A, 371: 336-360.

Silin, D.B., Jin, G. and Patzek, T.W., 2003. Robust Determination of Pore Space Morphology in Sedimentary Rocks, Paper SPE 84296, Proceedings of SPE Annual Technical Conference and Exhibition, Denver, Colorado, U.S.A.

Saadatfar, M., Turner, M.L., Arns, C.H., Averdunk, H., Senden, T.J., Sheppard, A.P., Sok, R.M., Pinczewski, W.V., Kelly, J. and Knackstedt, M.A., 2005. Rock fabric and texture from digital core analysis. Proceedings of SPWLA 46th Annual Logging Symposium, New Orleans, Louisiana, United States.

Tomutsa, L. and Radmilovic, V., 2003. Focussed ion beam assisted three-dimensional rock imaging at submicron-scale. Proceedings of International Symposium of the Society of Core Analysts, Pau, France.

Tomutsa, L. and Silin, D., 2004. Nanoscale Pore Imaging and Pore Scale Fluid Flow Modeling in Chalk. Lawrence Berkeley National Laboratory: Paper LBNL-56266. http://repositories.cdlib.org/lbnl/LBNL-56266.

Tomutsa, L., Silin, D. and Radmilovic, V., 2007. Analysis of chalk petrophysical properties by means of submicron-scale pore imaging and modeling. SPE Reservoir Evaluation & Engineering, 10: 285-293.

Torquato, S. and Lu, B., 1993. Chord-length distribution function for 2-phase random-media. Physical Review E, 47: 2950-2953.

Turner, M.L., Knung, L., Arns, C.H., Sakellariou, A., Senden, T.J., Sheppard, A.P., Sok, R.M., Limaye, A., Pinczewski, W.V. and Knackstedt, M.A., 2004. Three-dimensional imaging of multiphase flow in porous media. Physica A, 339: 166-172.

Valvatne, P.H., 2004. Predictive pore-scale modelling of multiphase flow. PhD thesis, Department of Earth Science and Engineering, Imperial College London.

Valvatne, P.H. and Blunt, M.J., 2004. Predictive Pore-scale Modeling of Two-phase Flow in Mixed Wet Media. Water Resources Research, 40: W07406, doi:10.1029/2003WR002627

Venkatarangan, A.B., 2000. Geometric and statistical analysis of porous media. PhD thesis, Department of Applied Mathematics and Statistics, State University of New York at Stony Brook.

Vogel, H.-J. and Roth, K., 2001. Quantitative morphology and network representation of soil pore structure. Advances in Water Resources 24(3-4): 233-242.

Wu, K., Dijke, M.I.J.V., Couples, G.D., Jiang, Z., Ma, J., Sorbie, K.S., Crawford, J., Young, I. and Zhang, X., 2006. 3D stochastic modelling of heterogeneous porous media – applications to reservoir rocks Transport in Porous Media, 65(3): 443-467. doi:10.1007/s11242-006-0006-z.

Wu, K., Nunan, N., Crawford, J.W., Young, I.M. and Ritz, K., 2004. An efficient Markov Chain model for the simulation of heterogeneous soil structure. Soil Science Society of America journal, 68: 346-351.

Yeong, C.L. and Torquato, S., 1998a. Reconstructing random media. Physical Review E, 57: 495-506.

Yeong, C.L. and Torquato, S., 1998b. Reconstructing random media. II. Three-dimensional media from two-dimensional cuts. Physical Review E, 58: 224-233.

Yu, Z.Y., Delerue, J.-F. and Ma, S.D., 1998. 3D Euclidean distance transformation. Proceedings of International symposium on image, speech, signal and robotics, Hong Kong.

Zhao, H.Q., Macdonald, I.F. and Kwiecien, M.J., 1994. Multi-orientation scanning: a necessity in the identification of pore necks in porous media by 3-D computer reconstruction from serial section data. Journal of Colloid and Interface Science, 162(2): 390-401.

Appendices

Appendix A

Micro-CT image processing

The original image output from micro-CT scanners are commonly in two formats, a series of 2D cross-sections or a unitary 3D array as a volumetric dataset. To view and process the data into a usable format as input of the pore-scale simulators developed in Imperial College London, a software ImageJ is used. ImageJ is a public domain, Java-based image processing program developed at the National Institutes of Health. ImageJ has an open architecture that provides extensibility via Java plugins and recordable macros.

A.1 Data format of micro-CT images

Phoenix v|tome|x system outputs the projection shadow images, the configuration files and the micro-CT datasets, among which the most important data to the end users are two files. One is *.vgi file that is an ascii text with description of the micro-CT data. The most useful information contained in *.vgi files are the dimensions of the 3D image and the resolution of the image. The other is *.vol file consists of 32 bit real type data that is the 3D array of gray scale reflecting the volumetric information of the inspected specimen. Although it is 32 bit data type, the gray scale is only 16 bit due to the resolution of detector.

A.2 Importing and saving data

The typical output 3D image is about 1~1.2 GB from Phoenix v|tome|x system depending on the image size and datatype. To enable ImageJ to view the whole image, the maximum memory usage of ImageJ is suggested to be set to 1500 MB through the menu: Edit->Options->Memory. Restart the program after the configuration to valid the modification.

To import the *.vol data, go to File->Import->Raw, input the dimensions and

choose the proper datatype 32 bit real.

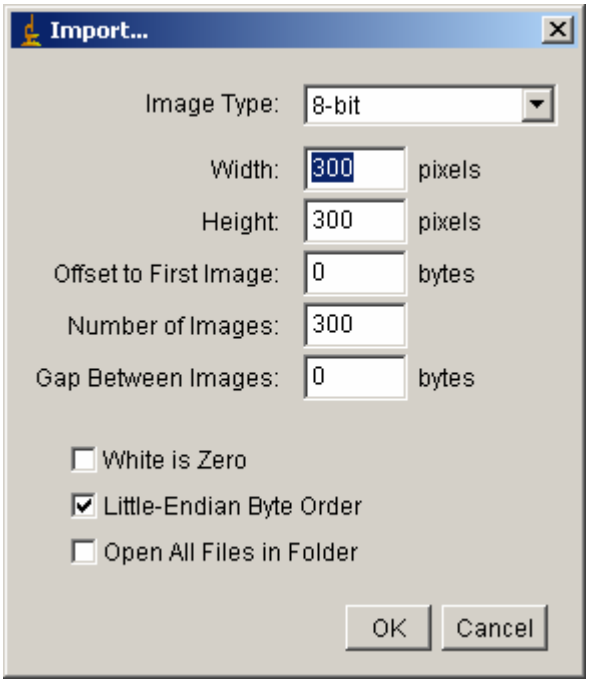

Figure A.1. Dialogue box of importing data.

To import a series of 2D cross-sections, go to File->Import->Image Sequence.

To save the processed images, go to File->Save as->Raw data.

During the import, there is an option of 'Little-Endian Byte Order'. In computing, endianness is the byte (and sometimes bit) ordering in memory used to represent some kind of data, which is system dependent. To keep the data format consistency, please go to Edit->Options->Input/Output and tick 'Export Raw in Intel Byte Order" on.

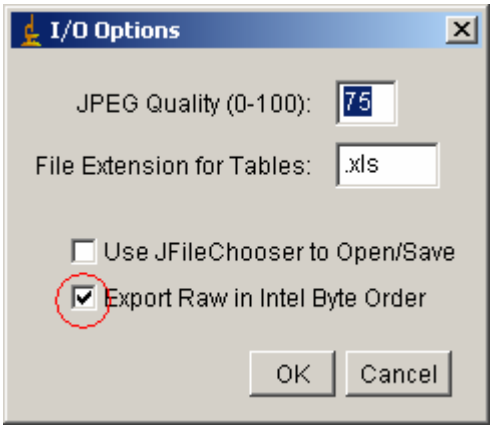

Figure A.2. Change the byte order.

A.3 Processing images

1. Cropping

To obtain the desired sub-section of the whole image, the plug-in of 'TransformJ' is used to crop the data in 3D with user defined dimensions.

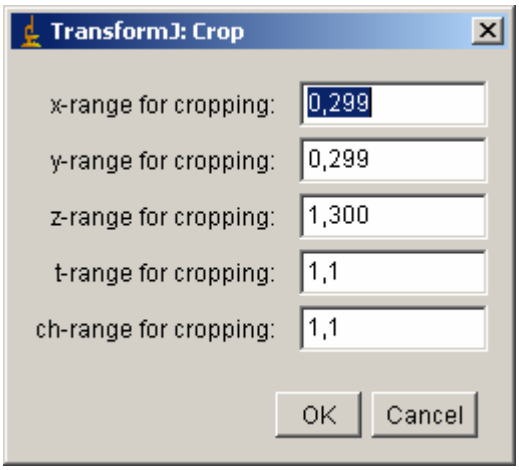

Figure A.3. Dialogue box of cropping data.

2. Rescaling

Since the useful gray scale is only in 16 bit, it is necessary to subsample the gray scale to save the memory usage and harddisk storage by transforming the 32 bit real data to 16 bit. Go to Image->Type and choose 16 bit.

3. Filtering

To apply a median filter to the image, go to Process->Filters->Median, choose a radius that is the neighborhood range to judge the median value. Please note that, this median filter of ImageJ is a 2D filter. To apply a 3D median filter, it is suggested to use another freeware VolView (http://www.kitware.com/products/volview.html). More professional filters can be found in the software packages VGS Studio Max and Amira in the XMT lab in Imperial College London.

4. Segmentation

To transform the gray scale into black and white image (pore space and solid phase), go to Image->Adjust->Threshold. A threshold value is selected automatically by Image based on an *isodata* algorithm (Ridler and Calvard, 1978). Visual inspection is required to make sure the segmentation is roughly correct before applying the value to the global image. The resultant image is black (0) and white (255).

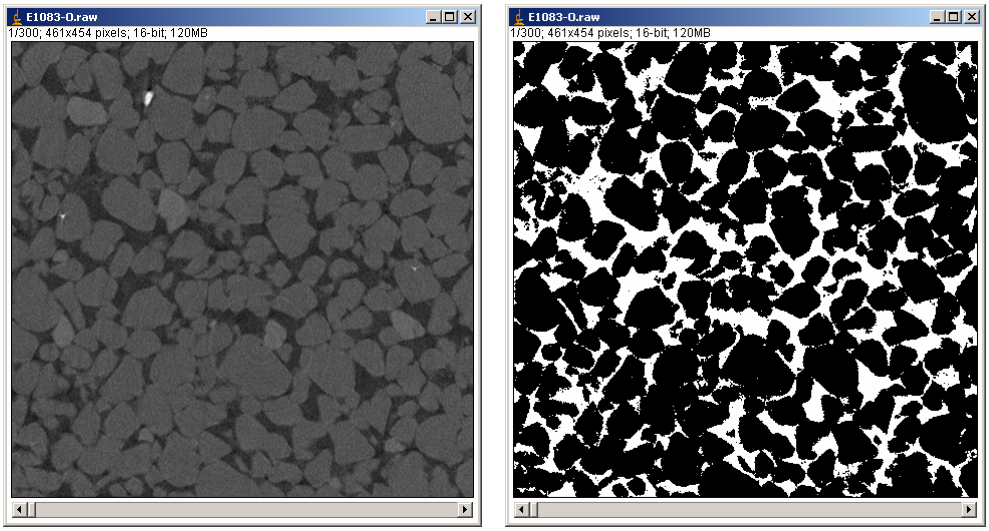

Figure A.4. Segmentation.

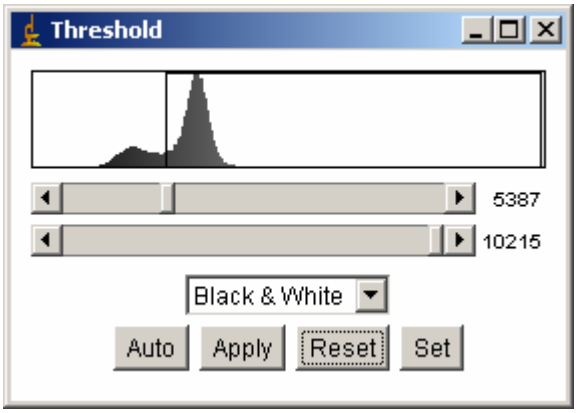

Figure A.5. Thresholding window.

5. Normalization

Since the desired input data for porenet.exe (the program to extract a network

from any generic 3D images) consists only 0s (pore space) and 1s (solid phase), we set the maximum value of the global image to 1 by visiting Process->Math->Max. Go to Image ->Adjust->B&C->Auto to obtain the best view condition whenever the contrast and brightness are uncomfortable.

Appendix B

How to execute pore network extraction program

B.1 Description of the input file

The pore network extraction program requires an input file containing necessary information about the source image.

Keywords:

1. Datatype:

Three types of data can be recognized as the source image.

a. Binary: Binary data is a 3D array consists of 1s and 0s as 8 bit in a binary file.

b. Raw: Raw data consists of only 1s and 0s in an ascii text file.

c. MicroCT: MicroCT data is similar to raw but contains a header. An example of the header is given below in four lines:

ascii
3 uc
128 128 128
0.0 1280.0 0.0 1280.0 0.0 1280.0

2. File name:

Specify the file name of your data in this line without suffix name. However, the suffix name of the data should be *.dat* and placed in the same folder with executive files

3. **Size of the image:**

   Specify the size of your data in voxels in three dimensions.

4. **Voxel side length:**

Specify the voxel size length in μm.

5. **Minimum pore size:**

Specify the minimum squared pore size (in voxels).

B.2 Run the program

There are two executive files in the package of pore network extraction program.

1.PPD.exe

PPD is the data preparation program. We use a Running Length Encoding (RLE) algorithm (http://en.wikipedia.org/wiki/Run-length_encoding) to compress the data to save their memory occupation during the calculation. To run this program:

PPD.exe *input_ file*

2. Porenet.exe

This is the main program of pore network extraction. To run this program:

Porenet.exe *input_file*